Numerical Simulation Of Three-Dimensional Free Surface Film Flow Over Or Around Obstacles On An Inclined Plane

Steven J. Baxter, MMath (Hons).

Thesis submitted to the University of Nottingham

for the degree of Doctor of Philosophy

July 2010

Abstract

Within the bearing chamber of a gas turbine aero-engine, lubrication of the shaft and other bearings is achieved by an oil film which may become significantly disturbed by interacting with a range of chamber geometries which protrude from the chamber wall. Minimizing these disturbances and preventing possible dry areas is crucial in optimizing a bearing chambers design. In addition, multiple obstructions may be located close to one another, resulting in a more complex disturbed film profile than by individual obstacles. Prediction of the disturbance of the film is an important aspect of bearing chamber design.

For analysis of the film profile over or around a local obstacle, typical bearing chamber flows can be approximated as an incompressible thin film flow down an inclined wall driven by gravity. The Reynolds number of thin film flows is often small, and for the bulk of this thesis a Stokes flow assumption is implemented. In addition, thin films are often dominated by surface tension effects, which for accurate modelling require an accurate representation of the free surface profile. Numerical techniques such as the volume of fluid method fail to track the surface profile specifically, and inaccuracies will occur in applying surface tension in this approach. A numerical scheme based on the boundary element method tracks the free surface explicitly, alleviating this potential error source and is applied throughout this thesis. The evaluation of free surface quantities, such as unit normal and curvature is achieved by using a Hermitian radial basis function interpolation. This hermite interpolation can also be used to incorporate the far field

boundary conditions and to enable contact line conditions to be satisfied for cases where the obstacle penetrates the free surface.

Initial results consider a film flowing over an arbitrary hemispherical obstacle, fully submerged by the fluid for a range of flow configurations. Comparison is made with previously published papers that assume the obstacle is small and / or the free surface deflection and disturbance velocity is small. Free surface profiles for thin film flows over hemispherical obstacles that approach the film surface are also produced, and the effects of near point singularities considered. All free surface profiles indicate an upstream peak, followed by a trough downstream of the obstacle with the peak decaying in a "horseshoe" shaped surface deformation. Flow profiles are governed by the plane inclination, the Bond number and the obstacle geometry; effects of these key physical parameters on flow solutions are provided.

The disturbed film profiles over multiple obstacles will differ from the use of a single obstacle analysis as their proximity decreases. An understanding of the local interaction of individual obstacles is an important aspect of bearing chamber design. In this thesis the single obstacle analysis is extended to the case of flow over multiple hemispheres. For obstacles that are separated by a sufficiently large distance the flow profiles are identical to those for a single obstacle. However, for flow over multiple obstacles with small separation, variations from single obstacle solutions maybe significant. For flow over two obstacles placed in-line with the incident flow, variations with flow parameters are provided. To identify the flexibility of this approach, flows over three obstacles are modelled.

The calculation of flows around obstacles provides a greater challenge. Notably, a static contact line must be included such that the angle between the free surface and the obstacle is introduced as an extra flow parameter that will depend both on the fluid and the obstacle surface characteristics. The numerical models used for flow over hemispheres can be developed to consider film flow around circular cylinders. Numerical simulations

are used to investigate flow parameters and boundary conditions. Solutions are obtained where steady flow profiles can be found both over and around a cylindrical obstacle raising the awareness of possible multiple solutions.

Flow around multiple obstacles is also analyzed, with profiles produced for flow around two cylinders placed in various locations relative to one another. As for flow over two hemispheres, for sufficiently large separations the flow profiles are identical to a single obstacle analysis. For flow around two obstacles spaced in the direction of the flow, effects of altering the four governing parameters; plane inclination angle, Bond number, obstacle size, and static contact angle are examined. The analysis of flow around three cylinders in two configurations is finally considered. In addition, for two obstacles spaced in-line with the incident flow, the numerical approaches for flow over and flow around are combined to predict situations where flow passes over an upstream cylinder, and then around an identical downstream cylinder.

The final section of this thesis removes the basic assumption of Stokes flow, through solving the full Navier-Stokes equations at low Reynolds number and so incorporating the need to solve nonlinear equations through the solution domain. An efficient numerical algorithm for including the inertia effects is developed and compared to more conventional methods, such as the dual reciprocity method and particular integral techniques for the case of a three-dimensional lid driven cavity. This approach is extended to enable calculation of low Reynolds number film profiles for both flow over and around a cylinder. Results are compared to the analysis from previous Stokes flow solutions for modest increases in the Reynolds number.

List Of Publications

S. J. Baxter, H. Power, K. A. Cliffe and S. Hibberd. Simulation of thin film flow around a cylinder on an inclined plane using the boundary element method. In *Boundary Elements and Other Mesh Reduction Methods XXX*. Maribor, Slovenia (WIT Press, 2008) ISBN: 978-1-84564-121-4

S. J. Baxter, H. Power, K. A. Cliffe and S. Hibberd. Three-Dimensional Thin Film Flow Over and Around an Obstacle on an Inclined Plane. *Physics of Fluids*. (3) 21 (2009)

S. J. Baxter, H. Power, K. A. Cliffe and S. Hibberd. Free surface Stokes flows obstructed by multiple obstacles. Published Online; *International Journal for Numerical Methods in Fluids* DOI:10.1002/fld.2029. (2009)

S. J. Baxter, H. Power, K. A. Cliffe and S. Hibberd. Numerical Simulation Of A Free Surface Stokes Flow Around Multiple Cylinders On An Inclined Plane Using A Boundary Element Method And Radial Basis Function Approach. In *Grand Review in the State-of-the-Art in the Numerical Simulation of Fluid Flow* London, United Kingdom (IMechE, 2009)

S. J. Baxter, H. Power, K. A. Cliffe and S. Hibberd. An Efficient Numerical Scheme For A Low Reynolds Number Flow In A Three-Dimensional Lid-Driven Cavity. In *Seventh UK conference on Boundary Integral Methods*. Nottingham, United Kingdom (University of Nottingham, 2009) ISBN: 978-0-9563221-0-4

Award for best poster by a PhD student: Numerical Simulation of Thin Films Over and Around Obstacles. *50th British Applied Mathematics Colloquium* (University of Manchester, 2008).

Acknowledgements

I gratefully acknowledge my supervisors, Henry Power, Andrew Cliffe and Stephen Hibberd, for their guidance and hard work throughout this project. Without their support, this PhD would not have been possible.

I would also like to thank the EPSRC and Rolls-Royce, for the financial support they have provided throughout this project.

The PhD was carried out at the University Technology Centre in Gas Turbine Transmission Systems at the University of Nottingham, and I am grateful to all my friends and colleagues for contributing to my time at the University.

I wish to thank my parents and the rest of my family for their continuous encouragement and support. Finally, to Charlotte, thank you for your unwavering love and patience, and for keeping me sane.

Contents

Chapter 1

Introduction

A bearing chamber of a gas-turbine aero-engine is used to constrain and collect oil injected to lubricate the shaft and other bearings. The oil is also required to cool the chamber walls by convective transport of heat within the oil system. If the oil film does not sufficiently cover the chamber wall then the reduced local cooling may result in oil degradation, coking and potentially oil fires could occur. Thus for design, thermal studies, and evaluation of oil quality, it is important to predict the film height and volume flux of oil at each point in the chamber. However computation of such flows is made difficult because bearing chambers have complex geometries and can include obstacles that locally significantly affect the film behaviour.

Figure 1.1 illustrates a schematic of a simplified aero-engine bearing chamber. A jet of oil is introduced to the bearing through the injector block, and the airflow within the chamber, generated by a highly rotating central shaft, may cause the jet to break down into small droplets which are incident on the chamber wall. On the chamber wall, the droplets collect, forming a film, with the oil finally removed from the bearing chamber through oil collected at the scavenge at the bottom of the chamber.

A schematic from experimental observation for a film profile around an obstacle piercing the free surface is shown in figure 1.2. The film flow is incident on the upstream edge of the obstacle, and then passes around the obstruction. Behind the obstacle recirculation is possible, with the flow merging back to the inlet flow profile further downstream.

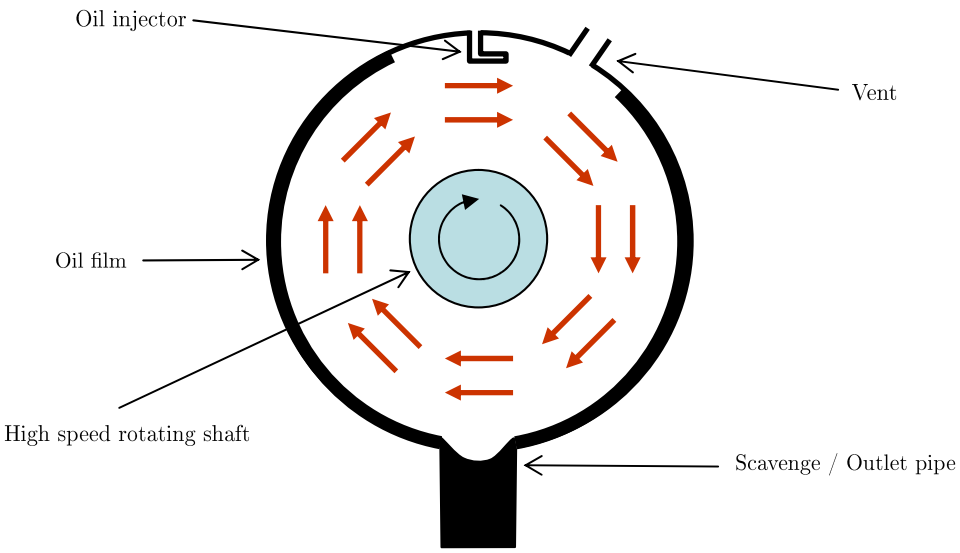

Figure 1.1: Schematic showing a typical bearing chamber configuration.

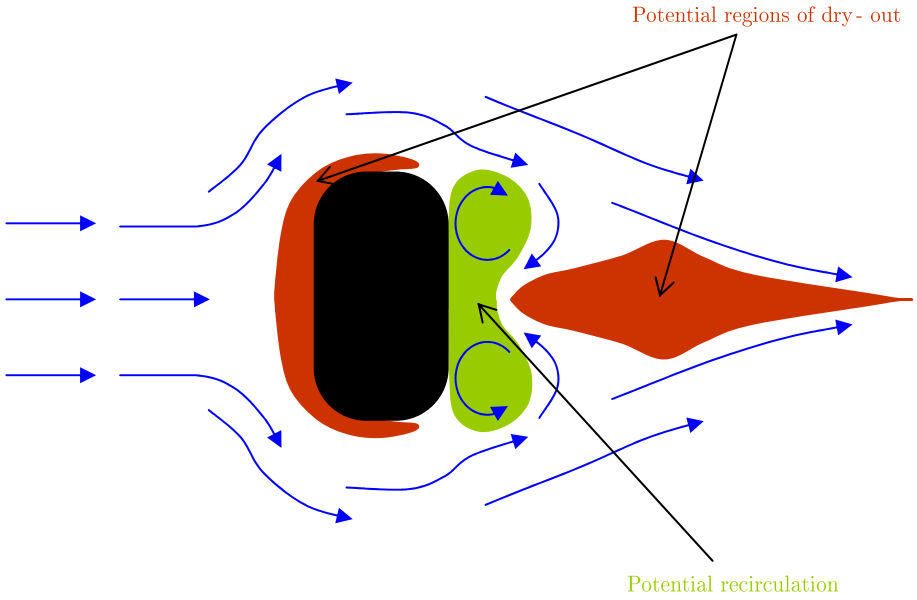

Figure 1.2: Schematic showing a typical film profile around an obstacle.

Experimental results from Eastwick et al. [1] have shown the possibility of fluctuating and stable dry-out regions both upstream and downstream of the obstruction as indicated.

Due to its influence on the optimal design of commercial aero-engines, flow behaviour in a bearing chamber has been analyzed by many authors. Experimentally, Wittig et al. [2] consider the film thickness and heat transfer characteristics for two-phase oil / air flows. Glahn and Wittig [3] used a high speed bearing chamber rig to experimentally measure the oil film velocity profile, and compare results to a theoretical analysis outlined. For film flows obstructed by a typical chamber support, Eastwick et al. [1] experimentally established the conditions for stable and fluctuating dry-out to occur both upstream and downstream of an obstruction. Further, they plotted a regime map in terms of liquid and gas Reynolds numbers to indicate where each dry-out regime occurs. Results included measured film thicknesses for a range of liquid flow rates at a fixed air flow rate.

Numerically, Farrall et al. [4] considers the exit flows within a bearing chamber, specifically focusing on the composition of liquid and gas within these flows. The split in oil removal between the scavenge and vent was extensively considered for three shaft speeds. By altering the vent design, so that it protrudes into the bearing chamber, the percentage of oil removed through the vent was found to be substantially lower than when using a flush vent design. Farrall et al. [5] numerically evaluated the motion of an oil film within a bearing chamber along with the effects of various boundary conditions applied at both the vent and scavenge of the chamber. Solutions are found to be sensitive to the boundary conditions applied within the numerical model, and by comparison with experimental data, the most physical boundary conditions are determined. Recently, Farrall et al. [6] numerically examined the oil film behaviour and its generation from oil droplets shed from the central shaft. Analysis indicates that the location at which the oil is eventually deposited on the chamber wall is significantly affected by the the initial droplet size of the oil.

Thesis Aims

The main aim of this thesis is to develop a numerical technique to analyze the interaction of a thin film oil flow with obstacles, similar to those found within the bearing chamber of an aero-engine. The numerical approaches developed are to be used as a design tool for bearing chambers, and thus efficiency along with accuracy of the numerical algorithms is all-important. In addition, many current simulations consider a two-dimensional approximation to the flow problem, and in these cases the possibility of flow around an obstacle penetrating the fluid film is not possible. Thus, a three-dimensional analysis will be implemented throughout this thesis.

Flows driven by gravity will be considered along with both fully submerged and protruding obstacles in a range of configurations. In designing a bearing chamber, the film disturbance for flows over or around multiple obstacles is as important as the analysis of a single obstruction. Flow profiles will be examined locally to the obstacles under consideration and the curvature of the bearing chamber wall will be neglected (i.e. the flow will be assumed down an inclined flat plane).

In summary, the objectives of this thesis are:

- Development of three-dimensional models for zero Reynolds number flow (Stokes flow) down an inclined plane, driven by gravity and obstructed by both single and multiple obstacles either fully submerged, or penetrating the film.
- Obtaining numerical solutions for
  - flow over hemispherical obstacles fully submerged by the film;
  - flow around circular cylinders penetrating the film.
- Development of the model to enable analysis of more complex chamber conditions by incorporating inertial effects for film flows over and around obstacles.

1.1 Literature Overview

Free surface film flows occur regularly during coating and cooling processes in a wide range of industrial applications, and as such are considered extensively by a range of authors. This literature review is divided into two sections, initially giving an overview of experimental work, providing an understanding of the fluid dynamics, and the physical effects with respect to the free surface and geometry within the flow problem. The final section of the literature review considers the numerical analysis of free surface film flows, relating the solutions obtained within the literature to the experimental results previously discussed.

1.1.1 Physical Observation Of Film Flows

Experimental analysis give an important insight into the physical effects caused by film flows in a range of problems, with results allowing analysis of flow solutions and the validation of numerical solutions.

Film flows over heterogeneously heated surfaces have been considered by a wide range of authors, examining the effects of heat exchange between the wall and a fluid film. Kabov [7] considered film flow falling freely down a vertical plane over a local heat source of two different lengths. When the longer heated regions were considered, instabilities in the fluid film were formed, and the potential for dry patches on the lower part of the heater found. This analysis of gravity driven film flow down a vertical plane and over a local heating unit was extended by Kabov and Marchuk [8]. Temperature gradients on the film surface were recorded, along with film disturbances caused by the heating unit. The breakdown of the film is extensively analyzed for a range of Reynolds numbers, with anything from one to three "horseshoe" shape film deformations formed for the different Reynolds numbers and heat flux densities considered. Recently, Kabov et al. [9] reconsidered the falling liquid film down a vertical, locally heated plane. Methods for

measuring the surface velocity were introduced, and the 'horseshoe" shape deformation reconsidered. It was found that a stagnation point exists at the top of the "horseshoe" deformation, a phenomenon predicted by earlier numerical analysis.

A closely related topic to film flow over topographies is that of film flow down a wavy inclined plane with experimental research conducted by Shetty and Cerro [10] and Argyriadi et al. [11], amongst others. Shetty and Cerro [10] considers the spreading of a fluid from a point source over a range of periodic surface corrugations on a vertical plane. A film evolution equation is also derived and gives good agreement with experimental results for transverse corrugations. Further experimental analysis of periodic corrugations was considered by Argyriadi et al. [11], who considered the corrugated wall at shallow inclinations ($< 15^o$). Variations in the ratio of corrugation height to length are tested with the effects on the flow profile reported.

Experimental analysis investigating the interaction of liquid films with obstacles has been conducted by a range of authors. Flow profiles over microscopic topography using spin coating has been considered by both Stillwagon and Larson [12] and Peurrung and Graves [13]. Stillwagon and Larson [12] experimentally consider flow over a trench, comparing results to those predicted by lubrication theory and producing good quantitative agreement, with the free surface shown to form a dip as the film passes over the trench. In addition as the ratio of centrifugal to capillary forces is increased, the film profile forms an upstream ridge as it enters the trench. Peurrung and Graves [13] continued the spin coating experiments, analyzing film profiles for flow over an underlying substrate, and again comparing results with lubrication theory.

Decré and Baret [14] generated full two-dimensional maps of the free-surface profile of a water film on an inclined plane with topography. One-dimensional topographies of a step up, step down and trenches were considered that cross the whole plate width, along with flow over four different rectangular, and one square two-dimensional topography. The case of flow over a square is of particular interest, allowing qualitative comparison with

numerical results considered in the following section. The flow profile exhibits a typical "horseshoe" disturbance of a large upstream peak before the obstacle, decaying around the obstruction, and returning to the undisturbed film height further downstream.

The experimental study of the onset of dry-out in a film has been considered by Shiralkar and Lahey [15] and Eastwick et al. [1] amongst others. Shiralkar and Lahey [15], considered two-phase air-water flow to assess problems in nuclear reactors upstream of flow obstacles. Both rectangular and cylindrical obstructions were used in the experiment and their effects discussed. More recently, Eastwick et al. [1] considered film flows around bearing chamber supports. This paper focused on the determination of the conditions necessary for dry-out to occur, both upstream and downstream of an obstacle using a water-glycerol liquid and shearing air flow. Both studies [15] and [1] consider the effects of varying the flow rate of the shearing air flow over the liquid film. Shiralkar and Lahey [15] observed two types of dry-out, which they categorized as Type I and Type II. Type I occur upstream of the obstacle, and Type II is located behind the obstacle. Eastwick et al. [1] extended these definitions of Type I and Type II dry-out to cover both stable and fluctuating dry-outs. This paper concluded with a regime map of dry-out conditions for both the liquid and air Reynolds numbers. Although numerical formulations presented in this thesis are not looking to capture the occurrence of dry-out, regions of minimum film depth are identified.

1.1.2 Numerical Simulation Of Film Flows

The industrial processes in which film flows occur are often complex, with hostile environments, and thus the cost and time involved with obtaining accurate experimental results is prohibitive. Numerical simulations of these complex film flows are an important design tool for optimization of industrial processes.

Numerical models are used to describe the dynamics of liquid films falling down a vertical plane and under the action of gravity when subjected to a local heat source. Skotheim

et al. [16] considered the stability of these film flows with numerical results illustrating an upstream ridge at the beginning of the heater as found in experimental investigations. Whereas [16] considered flow over a locally heated plate, Scheid et al. [17] considers the case of film flow over a plate of non-uniform temperature distribution.

Numerical simulation of film flows down wavy or periodic inclines have been considered extensively by a wide range of authors. For example, Wang [18] determined the velocity and film profiles of low Reynolds number flows down a wavy incline. It was determined that the transport properties of the film flow where effected by the presence of wall corrugations, with fluid particles having a tendency to flow in the direction of the corrugations. The extent of this effect was found to depend on the geometry of the corrugations, inclination of the wall and surface tension. Pozrikidis [19] used a two-dimensional Stokes flow formulation along with the corresponding boundary integrals to formulate film flow over a periodic wall. Free surface profiles are found over both a sinusoidal wall and a rectangular corrugated wall. Solutions found were dependent on the flow rate of the film, inclination angle of the wall, the wave amplitude of the corrugations and the surface tension of the fluid. This work was extended by Pozrikidis [20], analyzing the effects of surfactants on the film flow. The formulation is again based on Stokes equations, with solutions obtained numerically using a combined boundary element / finite volume scheme. Solutions found the surfactants to slightly exaggerate deformations of the film flow compared to earlier analysis. Malamataris and Bontozoglou [21] used a finite element method (FEM) to solve the full Navier-Stokes equations for film flow at a range of Reynolds numbers. For small amplitude undulations on the wavy wall, the free surface was shown to resonate for Reynolds numbers $Re \sim 200$.

Film flow over two-dimensional obstructions have been modelled by an extensive range of numerical methods. Generally, modelling and analysis is taken from approximate governing equations based on either the thin film lubrication approximation, or the equations of Stokes flow (zero Reynolds number). Fewer numerical computations of thin film flows with obstacles have been reported utilizing a fully three-dimensional analysis;

the majority implementing a boundary element method (BEM) for the solution of Stokes flows.

A lubrication approximation is implemented by Kalliadasis et al. [22] for a two-dimensional viscous thin film flow moving slowly over both trenches and mounds. By using the lubrication approximation to describe the flow, the film dynamics are shown to be governed by feature depth, feature width and capillary scale. However, the paper notes the limitations of a lubrication approximation in the vicinity of a sharp step where an alternative formulation, such as Stokes flow should be used. Mazouchi and Homsy [23] continue the earlier work of [22] by addressing these limitations by implementing a Stokes flow analysis for flow over an obstacle (step or trench) under the action of gravity, or some other body force. Solutions for Stokes flow in [23] are sought by formulating the governing flow equations in terms of the stream function - vorticity variables and solving using the boundary integral method (BIM).

Kalliadasis et al. [22] does not address issues with regards to the use of Stokes equations and whether they would produce solely quantitative corrections to the solutions obtained by the lubrication approximation or if fundamentally new features are produced. This motivated the extended work by Mazouchi and Homsy [23] that shows that despite the lubrication approximations lack of validity for steep features, when the capillary number is small, the lubrication approximation in [22] gave good correlation with the Stokes flow analysis presented in [23]. This was despite the substrate not being the required "small sloped topograph". After an extensive analysis, Kalliadasis et al. [22] concluded that thin films over topography are "most likely to rupture over corners or in advance of a step-up". The paper included two-dimensional profiles of the free surface over both trench and mound obstacles of various width.

The papers by Hansen [24, 25], analyze a Stokes flow in two dimensions on an inclined plane over a cylindrical obstacle of one or two ridges. The use of the boundary integral equations (BIE) to solve Stokes flow over an obstacle is widely regarded to have been

pioneered in [24, 25]. The BIE is formulated in terms of the stream function and the system solved for the free surface position and any unknown field variables. Free surface profiles are shown for a range of values of surface tension. For the case of the single obstacle in [24] velocity on the free surface and tangential stress on the obstacle surface are also shown.

The extended work of Hansen [25] also produced streamlines for film flow over obstacle(s), which for larger obstacles showed the formation of eddies either side of the obstruction. As the obstacle size grew, a distinct asymmetry of the eddy sizes was found, with the larger eddy upstream of the obstacle. When multiple obstacles are considered, the region between the obstacles is filled by circulating flow, and for large distances between obstacles this region comprises of one eddy. For shorter distances two eddies occur, stretching between the two obstacles, and located one above the other. The formation of this second eddy as the obstacle separation is decreased is analogous to the case of flow over a cavity, where the cavities depth-to-width ratio is increased. For flow over a relatively wide, shallow rectangular cavity a single eddy is formed. As the aspect ratio is increased, then progressively more eddies occur, and are located above each other within the cavity region. It is noted that for cases of flow over very shallow and wide cavities, multiple eddies are also formed. However in these cases, the eddies occur in the corners of the cavity. The paper by Hansen [25] does not show results corresponding to these corner recirculations when considering obstacles with large separations.

The thesis of Shuaib [26] simulates thin film flows in two-dimensions. Initially two numerical methods are compared, namely a direct boundary integral formulation and the volume of fluid method (VOF). This boundary integral formulation is based upon the physical flow variables, unlike the stream function - vorticity analysis of [23] and the stream function analysis of [24, 25]. As volume based methods do not track the free surface position explicitly, issues arise with the application of surface boundary conditions such as surface tension forces. Shuaib shows that for cases where surface tension is dominant, the VOF is inaccurate and the rest of the work presented is formulated around

the BEM. The flow was assumed to be governed by the two-dimensional Stokes flow equations. Constant shear stress has been applied to the thin film and results produced for film flow down an inclined plane, flow over a rectangular cavity, and flow into an outlet. For more realistic calculations, variable shear stress was used to recalculate results for some of the previous scenarios. Finally the dual reciprocity method (DRM) was implemented to extend the Stokes approximation to include inertia effects.

A steady, three-dimensional thin viscous liquid film driven by gravity down an inclined plane and over small topographies was considered by Hayes et al. [27] and Gaskell et al. [28]. Both formulations are based on the lubrication approximation, with Hayes et al. [27] deriving a single linear inhomogeneous evolution equation and obtaining the disturbed free surface profile by formulating the appropriate Green's function. Hayes et al. [27] consider an obstacle based on the dirac delta distribution, a point defect on the inclined plane, despite the lubrication approximation not being directly applicable in this case (as acknowledged by the authors). Results using this lubrication approximation are reported to give qualitatively similar results to the Stokes flow analysis of Pozrikidis and Thoroddsen [29] for flow over a spherical obstacle. The accuracy of modelling film flows over steep sided topographies using the lubrication approximation was considered by Gaskell et al. [28] by comparison of results with solutions to the full Navier-Stokes equations found using a finite element method. Solutions produced by the two methods reported good agreement. Thin film flows over both single and multiple obstacles using the lubrication approximation was considered by Lee et al. [30]. Film profiles for a single square, diamond and circular trench were all produced along with solution of the complex multiple obstacle configuration of a central diamond trench with two circular trenches downstream and two circular struts upstream.

Due to the added complexity in solving the full three-dimensional flow problem, restricted approaches are available for analysis, with a lubrication approximation the most popular technique. However, due to the additional simplification, problems arise with validity of this assumption where the flow profiles become steep. This problem is not present with

a Stokes flow analysis but such analysis are not yet well developed.

Several authors have considered a three-dimensional Stokes formulation for film flows driven by gravity down an inclined plane and over an obstacle. The use of a direct BIE for solution of this Stokes flow has been implemented by both Pozrikidis and Thoroddsen [29] and Blyth and Pozrikidis [31]. Pozrikidis and Thoroddsen [29] considered film flows over spherical obstacles in the asymptotic limit where the obstacle size was much smaller than the undisturbed film depth. Film profiles are obtained by solution of the appropriate BIEs using the BEM. Both Decré and Baret [14] and Hayes et al. [27] consider their film deformations to be qualitatively similar to the numerical work by Pozrikidis and Thoroddsen [29]

The formulation of Pozrikidis and Thoroddsen [29] includes an error in the jump condition of the BIE, which is corrected in the later work of Blyth and Pozrikidis [31]. However, this error is shown to produce only a small effect on the free surface profile, with the correct qualitative behaviour predicted. Blyth and Pozrikidis [31] extend the work of Pozrikidis and Thoroddsen [29] by removing the constraint of asymptotically small obstacles, and analyzing the effect of larger obstructions.

Both the simulations in [29, 31] simplify the numerical problem by linearizing the free surface deflection. Thus, even with the removal of the asymptotic constraint in [29], the accuracy of the results in [31] for significant deformations caused by large obstacles is unknown. Comparison between the corrected asymptotic and complete obstacle analysis is also presented, although problems in obtaining results for the complete obstacle analysis in the asymptotic limit led to difficulties in finding exact agreement.

Results from Pozrikidis and Thoroddsen [29], Blyth and Pozrikidis [31] along with the disturbance produced by the dirac delta topography in Hayes et al. [27] all show similar flow features of a pronounced upstream peak, decaying in a "horseshoe" fashion, with a trough formed immediately downstream of the obstacle, and decaying slowly. Qualitatively, this is in agreement with the experimental results for flow over a square

topography by Decré and Baret [14]. Interestingly, in [27] and the experimental work of [14], a slight upstream dip is depicted before the formation of the substantial peak on the free surface. This small dip does not feature in the Stokes flow analysis of [29] and [31].

Consideration of film flows around obstacles has not been widely considered. Sellier [32] and Sellier et al. [33] used the lubrication approximation to consider flows around obstructions. However, the lubrication theory makes it impossible to fully impose the no-slip boundary condition, and instead zero flux is specified on the obstacle wall. Thus results are expected to be more relevant in the far field. Sellier [32] consider flows around a circular cylinder with Sellier et al. [33] considering flow around a range of geometrical obstructions, including single and multiple circular cylinders.

1.2 Thesis Structure

Thin film flows occur in a wide range of industrial processes, with this thesis focusing on flows within the bearing chambers of a gas turbine aero-engine. These thin films can often be approximated as a Stokes flow analysis and it is this approach that will be initially implemented. Heat transfer effects from the bearing chamber wall to the thin film will be neglected throughout this thesis. Using a Stokes flow analysis, film profiles over or around a single obstacle may be modelled, with solutions considered for variations in the flow parameters. Results are produced numerically using the boundary element method (BEM) and a radial basis function (RBF) interpolation for generation of free surface parameters. However, within industrial processes, the film disturbance in the presence of multiple obstacles is often as important as the film deflection caused by a single obstruction. Using the Stokes flow analysis, film profiles for flows down an inclined plane over and around up to three obstacles are considered. Finally, the case of non-zero Reynolds numbers is considered, including inertia within the formulation, and analyzing the effects on the film disturbance generated by single obstacles.

This chapter has considered an overview of the literature discussing the physical behaviour of film flows along with their numerical simulation, and below a detailed description of the following chapters of this thesis is presented.

Chapter 2 overviews the theory of viscous flows, and the formulation of the corresponding boundary integral equations (BIEs). The end of chapter 2 discusses solution of the integral equations by the BEM, a numerical scheme. In addition, thin films are often dominated by surface tension effects, and thus for accurate evaluation of these forces, an accurate representation of the free surface and its derivatives are required. This is achieved by using a radial basis function (RBF) interpolation and more details are given in chapter 3. The extension of Stokes flow analysis to the full Navier-Stokes solutions for flows at finite Reynolds number is modelled in chapter 7 and also requires RBF interpolations.

Chapter 4 considers Stokes flow down an inclined plane, and driven by gravity over a single obstacle. Duplication of the methods introduced in the publications of Pozrikidis and Thoroddsen [29] and Blyth and Pozrikidis [31] provides an initial milestone to generate numerical codes and provide a base case for later qualitative comparisons. Assumptions of small free surface deflections are implemented by both [29] and [31] with [29] also imposing the constraint of asymptotically small obstacles. The small free surface deflection assumption allows linearization of the unknown free surface location, and the film profile can be found directly by the solution of a system of equations. Development of the analysis from [31] is aimed at obtaining solution methods for modelling flow over more general obstacles and flow conditions, with the model developed to relax the small deflection restrictions of the governing equations. The removal of the small free surface deflection requires solution of a non-linear problem, and an iterative solution technique has been developed.

A further extension to film flow over a single obstacle considers the film disturbance for flow over multiple obstacles located close to one another. The interaction between

multiple obstacles fully submerged by the film is considered in chapter 5. Two and three hemispheres in a range of relative locations are analyzed with the effects of the wake from one obstacle, on the film deformation caused by a subsequent obstacle discussed. In addition, effects of flow parameters on the film disturbance are considered.

Thin film flows around obstacles have been less widely considered in the literature, with Sellier [32] and Sellier et al. [33] the only reported works. However in using the lubrication theory, the no slip boundary condition on the obstacle wall is not fully imposed, with no flux specified instead. By using a Stokes flow analysis, film flows around obstructions using the full no-slip boundary condition on the wetted obstacle surface can be accurately modelled. The consideration of both single and multiple obstacles that penetrate the free surface are considered in chapter 6. For this analysis the incorporation of a contact line condition in the problem formulation is required. This is a non-trivial extension to the flow over analysis, and the contact angle at the contact line of the film is constrained using the RBF interpolation of the free surface. Circular cylinders are considered throughout, again with the relative positioning of obstacles assessed. The incorporation of the additional contact line constraint yields the possibility of multiple solutions. This is where for identical flow parameters, and far field conditions, the profile can exist both over, or around an identical obstacle.

The Reynolds number of thin film flows is often small and the Stokes flow assumption implemented up until Chapter 6 is often an appropriate approximation. However, even at low Reynolds numbers, the effects of inertia on the film profile may be significant. Chapter 7 considers the effects of the convective term from the Navier-Stokes equations on the film profile. An efficient numerical algorithm is developed for incorporating inertia effects, with the case of a three-dimensional lid driven cavity used to benchmark the algorithms. Incorporation of these numerical techniques into the film model allows the effects of low, finite Reynolds number to be considered.

In the final chapter, development of the theory and numerical aspects of this work are

reviewed, along with a discussion of the key results obtained. A particularly important aspect is the new insight into thin film flows around obstacles. Future developments and applications of this work are also discussed.

Chapter 2

Viscous Flows

This chapter considers the development of Stokes flow as an approximation to the Navier-Stokes equations for viscous fluid flow. The fundamental solution will be used to form the boundary integral equation (BIE) that will be the basis of the numerical solver utilizing the boundary element method (BEM). Initially, the Navier-Stokes equations are non-dimensionalized, and used to obtain the governing equations of Stokes flow (see § 2.1), and similar derivations are shown in [34–37]. The use of a direct formulation of the BIEs for Stokes flow is then analyzed in § 2.3 with the BEM, a numerical technique used to obtain solutions of the BIEs discussed in § 2.4

2.1 Introduction To Viscous Flows

The flow of an incompressible Newtonian fluid under the influence of a body force is governed by the Navier-Stokes equations, a vector equation for the conservation of momentum (2.1.1), and the scalar continuity equation for the conservation of mass (2.1.2). Although not presented here, full derivations of these equations can be found in [34, 35, 38, 39]. For a fluid whose motion is dominated by viscous effects, the Navier-Stokes equations can be approximated by the simpler Stokes equations using certain assumptions which will be discussed in some detail.

Non-dimensionalizing the Navier-Stokes equation allows simplification by means of a constraint on the non-dimensional quantity - the Reynolds number, *Re*. The Reynolds number is a representative value of the ratio of inertia forces to viscous forces acting within the fluid flow, and for the case of low *Re*, i.e. $Re \ll 1$ fluid inertia forces are negligible compared to the viscous forces. The viscous forces are balanced with the remaining terms in the Navier-Stokes equations, i.e. pressure and external body forces. The main benefit of this simplification is the removal of the non-linear term from (2.1.1) and results in Stokes equation. The equation for mass conservation (2.1.2) is unaltered. Typically, the Reynolds number is generally small when either the characteristic velocity or length scale of the flow is very small or the kinematic viscosity of the fluid is very large. Correspondingly these flows are also referred to as *creeping flows* or *slow flows*, and are associated with the limit of the Reynolds number tending to zero.

Stokes Flow

Consider the flow of an incompressible Newtonian fluid under the influence of a gravitational body force $\bar{\mathbf{g}}$, with velocity $\bar{\mathbf{u}} = (\bar{u}_1, \bar{u}_2, \bar{u}_3)$, pressure $\bar{p}$, density ρ, and dynamic viscosity μ. Over bars are used to denote dimensional quantities, with the non-dimensional variables plain. The fluid flow is governed by the Navier-Stokes equations (2.1.1) and the continuity equation (2.1.2),

$$\rho\left(\frac{\partial \bar{\mathbf{u}}}{\partial \bar{t}} + \bar{\mathbf{u}} \cdot \bar{\nabla}\bar{\mathbf{u}}\right) = -\bar{\nabla}\bar{p} + \mu\bar{\nabla}^2\bar{\mathbf{u}} + \rho\bar{\mathbf{g}}, \tag{2.1.1}$$

$$\bar{\nabla} \cdot \bar{\mathbf{u}} = 0. \tag{2.1.2}$$

Gravitational body forces are conservative, and thus the gravitational force can be rewritten as the gradient of a second function, i.e. $\bar{\mathbf{g}} = \bar{\nabla}\bar{G}$. As such the gravitational body force can be combined with the pressure term from the Navier-Stokes equations, producing,

$$\rho\left(\frac{\partial \bar{\mathbf{u}}}{\partial \bar{t}} + \bar{\mathbf{u}} \cdot \bar{\nabla}\bar{\mathbf{u}}\right) = -\bar{\nabla}\bar{p}^{mod} + \mu\bar{\nabla}^2\bar{\mathbf{u}} \tag{2.1.3}$$

where $\bar{p}^{mod} = \bar{p} - \rho\bar{G}$. For a fluid whose motion is dominated by viscous effects, the Navier-Stokes equations can be reduced to the simpler Stokes equations using certain assumptions which will be discussed in some detail.

The equations for a Stokes flow subject to gravitational body forces are obtained by simplifying the full Navier-Stokes equations (2.1.3) for an incompressible fluid. The derivation in this section recreates in full detail that presented in [34]. To proceed, flow quantities in equation (2.1.3) are non-dimensionalized based on representative values of velocity U, length L and time T for the flow. In cases of thin films the length scale L is often taken as the characteristic thickness of the film. A representative pressure is obtained by scaling the pressure term with the dominant viscous term in (2.1.3). Hence the following dimensionless variables can now be defined,

$$\mathbf{u} \equiv \frac{\bar{\mathbf{u}}}{U}, \quad x \equiv \frac{\bar{x}}{L}, \quad \nabla \equiv L\bar{\nabla}, \quad t \equiv \frac{\bar{t}}{T}, \quad p^{mod} \equiv \frac{\bar{p}^{mod}L}{\mu U}. \tag{2.1.4}$$

Substituting expressions (2.1.4) into (2.1.3) yields the non-dimensional equations for mass conservation and Navier-Stokes,

$$\frac{L^2}{T\nu}\frac{\partial \mathbf{u}}{\partial t} + \frac{LU}{\nu}\mathbf{u}\cdot\nabla\mathbf{u} = -\nabla p^{mod} + \nabla^2\mathbf{u}, \tag{2.1.5}$$

$$\frac{U}{L}\nabla\cdot\mathbf{u} = 0, \tag{2.1.6}$$

where the kinematic viscosity is given by ν where $(\mu = \nu\rho)$.

Two dimensionless parameters are now introduced. The first is the Reynolds number, denoted Re, which expresses the ratio between inertia and viscous forces and is given by

$$Re = \frac{LU}{\nu}. \tag{2.1.7}$$

The next is the unsteadiness parameter and represents the ratio of inertial acceleration body forces and the viscous forces. It is denoted by β and is expressed as,

$$\beta = \frac{L^2}{\nu T} = Re\ \frac{L}{UT}, \tag{2.1.8}$$

and in cases where the typical velocity, length and time scales are interlinked (i.e. $U = \frac{L}{T}$), β reduces to the Reynolds number Re.

Using dimensionless parameters (2.1.7) - (2.1.8), (2.1.5) and (2.1.6) reduce to

$$\beta\frac{\partial \mathbf{u}}{\partial t} + Re\ \mathbf{u}\cdot\nabla\mathbf{u} = -\nabla p + \nabla G + \nabla^2\mathbf{u}, \tag{2.1.9}$$

$$\nabla\cdot\mathbf{u} = 0. \tag{2.1.10}$$

For steady flows, or flows with a relatively long time scale, the frequency parameter β is approximated by $\beta \ll 1$ and the time derivative term in (2.1.9) can be neglected, resulting in the equations for steady Navier-Stokes flow,

$$Re\ \mathbf{u}\cdot\nabla\mathbf{u} = -\nabla p + \nabla G + \nabla^2\mathbf{u}. \tag{2.1.11}$$

In terms of the Reynolds number there are three broad cases,

- $Re \ll 1$ - Inertia forces are dominated by viscous forces and pressure forces.
- $Re \sim O(1)$ - Inertial, viscous and pressure forces are all of the same magnitude and thus are all equally important to the motion of the fluid.
- $Re \gg 1$ - Viscous forces are dominated by inertia and pressure forces. Note for consistency in this case, the assumed scaling for pressure would be changed to balance the inertia terms.

Thus in the case of $Re \ll 1$, (2.1.11) simplifies to the steady Stokes equation,

$$-\nabla p + \nabla G + \nabla^2\mathbf{u} = 0. \tag{2.1.12}$$

2.2 An Overview Of The Boundary Integral Formulation

A wide range of engineering problems are governed by linear partial differential equations (PDEs) which require solving. The governing equation can be re-written exactly as an integral equation and is often referred to as the boundary integral equation (BIE). The

BIE is obtained by using the corresponding Green's function appropriate for the case of interest. This imposes restrictions due to the difficulty in finding the Green's function required for creating the BIE from the original PDE.

The BIE formulations can take two forms, direct and indirect. The indirect approach formulates integral equations in terms of fictitious sources with no physical meaning. The integral equation is solved for these fictitious source densities and physical variables can be computed afterwards. The need to introduce the fictitious densities can be eliminated by use of a Direct approach which formulates the integral equations in terms of the physical quantities (for example tractions and velocities). Solely the direct formulation is focused on here and thus in future the distinction will not always be made.

For non-linear cases, the problem is formulated in terms of the boundary integrals corresponding to the linear case, with an additional domain integral incorporating the non-linear term. Early works required the discretization of the full domain, eliminating one of the major benefits of the boundary integral formulation. More recent work has considered methods of keeping the boundary-only nature of the formulation, and details are presented in chapter 7.

The boundary element method (BEM) is a numerical computational method used to solve the BIE, by applying the specified boundary conditions and introducing three approximations. Initially a geometric approximation is made, where the boundary is discretized into a set of elements. The BIE is then re-written as the sum of the integrals over each of the elements. The boundary distributions of the surface variables (i.e. boundary tractions and velocities) are then approximated on each of the previously defined boundary elements. Finally the integrals defined over each element are evaluated by an appropriate numerical scheme. Values for the unknown surface variables can then be found on the contours of the problem domain. Using the BIE and BEM again, these surface values can be used to find the values for the variables anywhere within the flow domain.

The major advantage of the BEM over volume-discretization methods such as the finite element method (FEM) or finite volume method (FVM) is obvious, that only the bounding surface requires discretization and the dimension of the solution space is reduced by one when compared to the dimension of the physical variable space. For problems with a solution domain with a large volume/surface ratio the BEM can offer significant performance advantages over volume-meshing based solution methods. However, one disadvantage of the BEM is its formation of fully populated matrices. Memory requirements for BEM problems grow with the square of the number of elements, whereas for a typical FEM analysis, the matrix is banded and the growth relationship linear. Additionally, for cases where surface properties (e.g. surface tension) are important, the BIE formulation can offer significant improvement in accuracy when compared with the volume of fluid (VOF) method, a more typical numerical scheme for fluid problems. More details in the comparison of these two methods was conducted in the PhD Thesis by Shuaib [26].

The following section gives a detailed account of the formation of the BIE for Stokes flow using the direct formulation. This is followed by details of the BEM, describing typical approximations that may be utilized in its application.

2.3 Direct Boundary Integral Equations For Stokes Flow

Formulation of the direct boundary integral equations (BIE) for Stokes flow requires the Lorentz reciprocal identity, calculation of the relevant Green's functions and formulation of the governing integral equations. Derivations of the direct BIE are produced in many texts, for example [34, 35, 37]. For consistency, notation wherever possible is kept the same as [34], however, the derivation shown throughout is non-dimensional.

2.3.1 Derivation Of The Lorentz Reciprocal Relation

Stokes flow in the absence of gravitational body forces is given by (2.3.1)

$$-\nabla p + \nabla^2 \mathbf{u} = 0. \tag{2.3.1}$$

By defining the non-dimensional stress tensor σ_{ij} as follows,

$$\sigma_{ij} = -p\delta_{ij} + \left(\frac{\partial u_i}{\partial x_j} + \frac{\partial u_j}{\partial x_i}\right), \tag{2.3.2}$$

the Stokes equation (2.3.1) can be rewritten as

$$\nabla \cdot \boldsymbol{\sigma} = 0. \tag{2.3.3}$$

Consider two solutions $\mathbf{u}$, $\mathbf{u}'$ corresponding to stress tensors $\boldsymbol{\sigma}$, $\boldsymbol{\sigma}'$ of a Stokes flow governed by (2.3.3) and (2.1.10). Taking the inner product of $\mathbf{u}'$ and the divergence of the stress tensor $\nabla \cdot \boldsymbol{\sigma}$, and substituting (2.3.2) for the stress tensor yields,

$$u_j' \frac{\partial \sigma_{ij}}{\partial x_i} = \frac{\partial}{\partial x_i}(u_j' \sigma_{ij}) - \left(-p\delta_{ij} + \left(\frac{\partial u_i}{\partial x_j} + \frac{\partial u_j}{\partial x_i}\right)\right) \frac{\partial u_j'}{\partial x_i}. \tag{2.3.4}$$

By the standard properties of the Kronecker's delta function and noting that by mass conservation $\frac{\partial u_i'}{\partial x_i} = 0$,

$$u_j' \frac{\partial \sigma_{ij}}{\partial x_i} = \frac{\partial}{\partial x_i}(u_j' \sigma_{ij}) - \left(\frac{\partial u_i}{\partial x_j} + \frac{\partial u_j}{\partial x_i}\right) \frac{\partial u_j'}{\partial x_i}. \tag{2.3.5}$$

Interchanging the flow solutions, i.e. $\mathbf{u}' \leftrightarrow \mathbf{u}$ and $\boldsymbol{\sigma}' \leftrightarrow \boldsymbol{\sigma}$ the following identity is obtained,

$$u_j \frac{\partial \sigma_{ij}'}{\partial x_i} = \frac{\partial}{\partial x_i}(u_j \sigma_{ij}') - \left(\frac{\partial u_i'}{\partial x_j} + \frac{\partial u_j'}{\partial x_i}\right) \frac{\partial u_j}{\partial x_i}. \tag{2.3.6}$$

The penultimate step of the derivation involves subtracting (2.3.6) from (2.3.5). By manipulating the indices of the viscous term on the right hand side of (2.3.6), it can be shown to cancel with the corresponding term in (2.3.5) to give,

$$u_j' \frac{\partial \sigma_{ij}}{\partial x_i} - u_j \frac{\partial \sigma_{ij}'}{\partial x_i} = \frac{\partial}{\partial x_i}(u_j' \sigma_{ij} - u_j \sigma_{ij}'). \tag{2.3.7}$$

By the initial statement that both flows satisfy the equations of Stokes flow,

$$\nabla \cdot \boldsymbol{\sigma}' \equiv \frac{\partial \sigma'_{ij}}{\partial x_i} = 0, \qquad \nabla \cdot \boldsymbol{\sigma} \equiv \frac{\partial \sigma_{ij}}{\partial x_i} = 0, \tag{2.3.8}$$

the expression (2.3.7) reduces to the Lorentz reciprocal relation,

$$\frac{\partial}{\partial x_i}(u'_j \sigma_{ij} - u_j \sigma'_{ij}) = 0, \tag{2.3.9}$$

or in vector notation

$$\nabla \cdot (\mathbf{u}' \cdot \boldsymbol{\sigma} - \mathbf{u} \cdot \boldsymbol{\sigma}') = 0. \tag{2.3.10}$$

2.3.2 Fundamental Solutions And Their Properties

The analysis of Stokes flow involves two key terms, a *fundamental solution* and *Green's function*. A fundamental solution of Stokes flow is one that satisfies the singularly forced Stokes equation (2.3.11) or (2.3.12) and the continuity equation (2.1.10). A Green's function for Stokes flow is a fundamental solution that also satisfies suitable boundary conditions for the specific problem modelled. In three-dimensions, the singularly forced Stokes equation is,

$$-\nabla p + \nabla^2 \mathbf{u} + \delta(\mathbf{x} - \mathbf{x}_0)\mathbf{b} = \mathbf{0}, \tag{2.3.11}$$

or

$$\nabla \cdot \boldsymbol{\sigma} + \delta(\mathbf{x} - \mathbf{x}_0)\mathbf{b} = \mathbf{0}, \tag{2.3.12}$$

where δ is Dirac's delta function, $\mathbf{x}_0$ is some arbitrary location of the singularity, $\mathbf{x}$ is the field point, and $\mathbf{b}$ is some constant vector. The fundamental solutions of Stokes flow correspond to the solutions of (2.3.11) or (2.3.12) along with mass conservation (2.1.10) and they describe the flow caused by a point force (or pole) at $\mathbf{x}_0$, with orientation and strength given by $\mathbf{b}$.

Solutions of (2.3.11) or (2.3.12) are conventionally written in the form (see [34, 37]),

$$u_i(\mathbf{x}) = \frac{1}{8\pi} G_{ij}(\mathbf{x}, \mathbf{x}_0) b_j \tag{2.3.13}$$

$$p_i(\mathbf{x}) = \frac{1}{8\pi} P_j(\mathbf{x}, \mathbf{x}_0) b_j \tag{2.3.14}$$

$$\sigma_{ik}(\mathbf{x}) = \frac{1}{8\pi} T_{ijk}(\mathbf{x}, \mathbf{x}_0) b_j \tag{2.3.15}$$

Green's Function In Free-Space And Bounded Domains

The free-space Green's function (fundamental solution) for a three-dimensional Stokes flow are well known, e.g.[34, 37], and are,

$$G_{ij}(\hat{\mathbf{x}}) = \frac{\delta_{ij}}{r} + \frac{\hat{x}_i \hat{x}_j}{r^3}, \tag{2.3.16}$$

$$P_j(\hat{\mathbf{x}}) = 2\frac{\hat{x}_i}{r^3}, \tag{2.3.17}$$

$$T_{ijk}(\hat{\mathbf{x}}) = -6\frac{\hat{x}_i \hat{x}_j \hat{x}_k}{r^5}, \tag{2.3.18}$$

where

$$\hat{\mathbf{x}} \equiv \mathbf{x} - \mathbf{x}_0, \qquad r = |\hat{\mathbf{x}}|. \tag{2.3.19}$$

The Green's function (2.3.16) corresponding to the velocity field (2.3.13) is also referred to as the *Stokeslet*. The choice of Green's functions for bounded and periodic domains may involve requirements on the domain boundaries. For example, if for a given problem, a section of boundary requires the fluid velocity to be zero, then it is often convenient to choose a Green's function that is also zero on this surface. The Lorentz-Blake Green's functions can be used to model problems bounded by a plane wall with details given in Appendix A.

Fundamental Solutions: Symmetry And Other Properties

Here the form of the fundamental solutions shown in equations (2.3.16) - (2.3.18) are analyzed, with six symmetry relations or integral properties defined. Before proceeding

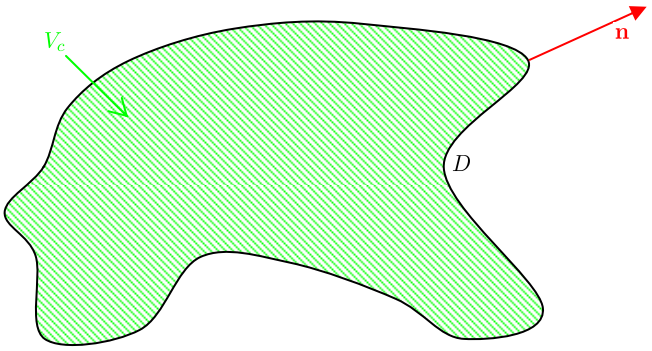

Figure 2.1: Schematic of a typical domain for which the Green's functions are applied.

with the derivation of these properties an arbitrary control volume V_c , bounded by the surface D is defined with the surface having unit normal vector $\mathbf{n}$, pointing out of the control volume V_c. For a detailed schematic see figure 2.1

(i) Due to the inherent symmetry of the stress tensor ($\sigma_{ik} = \sigma_{ki}$ - see equation (2.3.2)) it is obvious that the corresponding fundamental solution will also have the symmetry property,

$$T_{ijk} = T_{kji}. \tag{2.3.20}$$

(ii) The fundamental solution associated with the velocity field has symmetry property,

$$G_{ij}(\mathbf{x}, \mathbf{x}_0) = G_{ji}(\mathbf{x}_0, \mathbf{x}), \tag{2.3.21}$$

and a proof is given in [37]. Hence a swap of the location of the field point and pole in conjunction with an exchange in the order of the indices is allowed.

(iii) By mass conservation, equation (2.1.10) must be satisfied and substituting from (2.3.13) gives,

$$\nabla \cdot \mathbf{G}(\mathbf{x}, \mathbf{x}_0) \equiv \frac{\partial G_{ij}(\mathbf{x}, \mathbf{x}_0)}{\partial x_i} = 0. \tag{2.3.22}$$

Integration of (2.3.22) over the control volume V_c yields,

$$\int_{V_c} \frac{\partial G_{ij}(\mathbf{x}, \mathbf{x}_0)}{\partial x_i} \mathrm{d}V(\mathbf{x}) = 0, \tag{2.3.23}$$

and by applying the divergence theorem becomes,

$$\int_D G_{ij}(\mathbf{x},\mathbf{x}_0)n_i(\mathbf{x})\mathrm{d}S(\mathbf{x}) = 0. \tag{2.3.24}$$

(iv) Substituting equations (2.3.13) and (2.3.14) into (2.3.11) results in the relation,

$$-\frac{\partial}{\partial x_i}(P_j(\mathbf{x},\mathbf{x}_0)b_j) + \frac{\partial^2}{\partial x_k \partial x_k}(G_{ij}(\mathbf{x},\mathbf{x}_0)b_j) + 8\pi\delta(\mathbf{x}-\mathbf{x}_0)b_i = 0. \tag{2.3.25}$$

Introducing the Kronecker's delta function enables cancelling of the b_j terms that appear throughout the expression and yields the result,

$$-\frac{\partial P_j(\mathbf{x},\mathbf{x}_0)}{\partial x_i} + \frac{\partial^2}{\partial x_k \partial x_k}G_{ij}(\mathbf{x},\mathbf{x}_0) + 8\pi\delta(\mathbf{x}-\mathbf{x}_0)\delta_{ij} = 0. \tag{2.3.26}$$

(v) Substituting from (2.3.15) into (2.3.12) yields the relation,

$$\left(\frac{\partial T_{kji}(\mathbf{x},\mathbf{x}_0)}{\partial x_k}\right) b_j + 8\pi\delta(\mathbf{x}-\mathbf{x}_0)b_i = 0. \tag{2.3.27}$$

Switching the indices of the fundamental stress solution and repeating the previous analysis by introducing the Kronecker's delta function and again cancelling the terms b_j, gives

$$\frac{\partial T_{ijk}(\mathbf{x},\mathbf{x}_0)}{\partial x_k} + 8\pi\delta(\mathbf{x}-\mathbf{x}_0)\delta_{ij} = 0. \tag{2.3.28}$$

Integrating (2.3.28) over the control volume V_c, yields

$$\int_{V_c} \frac{\partial T_{ijk}(\mathbf{x},\mathbf{x}_0)}{\partial x_k}\mathrm{d}V(\mathbf{x}) = -8\pi\delta_{ij}\int_{V_c}\delta(\mathbf{x}-\mathbf{x}_0)\mathrm{d}V(\mathbf{x}), \tag{2.3.29}$$

and applying the divergence theorem to the integral on the left hand side of (2.3.29) gives,

$$-\frac{1}{8\pi}\int_D T_{ijk}(\mathbf{x},\mathbf{x}_0)n_k(\mathbf{x})\mathrm{d}S(\mathbf{x}) = \delta_{ij}\int_{V_c}\delta(\mathbf{x}-\mathbf{x}_0)\mathrm{d}V(\mathbf{x}). \tag{2.3.30}$$

By the properties of Dirac's delta function, the right hand side integral in (2.3.30) is unity if $\mathbf{x}_0$ is contained in V_c and zero if $\mathbf{x}_0$ is outside of V_c. If $\mathbf{x}_0$ lies on the locally smooth surface D (bounding V_c), then the integral equals a half. For a

brief explanation of the last result see Appendix B. Thus (2.3.30) can be written piecewise as,

$$-\frac{1}{8\pi}\int_D T_{ijk}(\mathbf{x},\mathbf{x}_0)n_k(\mathbf{x})\mathrm{d}S(\mathbf{x}) = \begin{cases} \delta_{ij} & \text{when } \mathbf{x}_0 \text{ is inside } D. \\ \frac{1}{2}\delta_{ij} & \text{when } \mathbf{x}_0 \text{ is on } D. \\ 0 & \text{when } \mathbf{x}_0 \text{ is outside } D. \end{cases} \tag{2.3.31}$$

The piecewise relation (2.3.31) can be used to form an expression for integrals with $\mathbf{x}_0$ taken interior and exterior to the domain V_c, denoted by a superscript (i) and (e) above the integral symbol. Integrals for cases where $\mathbf{x}_0$ is contained exactly on surface D are denoted by $\mathbf{x}_0 \in D$ superscript to the integral symbol. Thus for an integral with $\mathbf{x}_0$ external to the domain, (2.3.31) becomes,

$$\begin{aligned} -\frac{1}{8\pi}\int_D^{(e)} T_{ijk}(\mathbf{x},\mathbf{x}_0)n_k(\mathbf{x})\mathrm{d}S(\mathbf{x}) = \\ -\frac{1}{8\pi}\int_D^{\mathbf{x}_0\in D} T_{ijk}(\mathbf{x},\mathbf{x}_0)n_k(\mathbf{x})\mathrm{d}S(\mathbf{x}) - \frac{1}{2}\delta_{ij}, \end{aligned} \tag{2.3.32}$$

and for $\mathbf{x}_0$ internal to the domain,

$$\begin{aligned} -\frac{1}{8\pi}\int_D^{(i)} T_{ijk}(\mathbf{x},\mathbf{x}_0)n_k(\mathbf{x})\mathrm{d}S(\mathbf{x}) = \\ -\frac{1}{8\pi}\int_D^{\mathbf{x}_0\in D} T_{ijk}(\mathbf{x},\mathbf{x}_0)n_k(\mathbf{x})\mathrm{d}S(\mathbf{x}) + \frac{1}{2}\delta_{ij}. \end{aligned} \tag{2.3.33}$$

The effect of a singular point occurring at a corner of a domain results in the slightly different form of equation in (2.3.31)

$$-\frac{1}{8\pi}\int_D T_{ijk}(\mathbf{x},\mathbf{x}_0)n_k(\mathbf{x})\mathrm{d}S(\mathbf{x}) = \begin{cases} \delta_{ij} & \text{when } \mathbf{x}_0 \text{ is inside } D. \\ \frac{\Omega}{4\pi}\delta_{ij} & \text{when } \mathbf{x}_0 \text{ is at corner of } D. \\ 0 & \text{when } \mathbf{x}_0 \text{ is outside } D. \end{cases} \tag{2.3.34}$$

where Ω is the solid angle of the boundary corner. The solid angle is evaluated by drawing a unit sphere around the singularity, and extending the shape of boundary D infinitely close to the corner out into free-space. The intersection of the two

surfaces defines a contour on the sphere, whose area within the original domain is the solid angle Ω. Note that $\Omega = 2\pi$ is effectively the earlier case of a locally smooth boundary D, and Ω can take any value between 0 and 4π. The form of the right hand side of (2.3.34) is also considered in Appendix B.

The corresponding equation to (2.3.32) when $\mathbf{x}_0$ is exterior to the domain D is,

$$-\frac{1}{8\pi}\int_D^{(e)} T_{ijk}(\mathbf{x},\mathbf{x}_0)n_k(\mathbf{x})\mathrm{d}S(\mathbf{x}) = \\ -\frac{1}{8\pi}\int_D^{\mathbf{x}_0\in D} T_{ijk}(\mathbf{x},\mathbf{x}_0)n_k(\mathbf{x})\mathrm{d}S(\mathbf{x}) - \frac{\Omega}{4\pi}\delta_{ij}, \tag{2.3.35}$$

and when $\mathbf{x}_0$ is interior to the domain,

$$-\frac{1}{8\pi}\int_D^{(i)} T_{ijk}(\mathbf{x},\mathbf{x}_0)n_k(\mathbf{x})\mathrm{d}S(\mathbf{x}) = \\ -\frac{1}{8\pi}\int_D^{\mathbf{x}_0\in D} T_{ijk}(\mathbf{x},\mathbf{x}_0)n_k(\mathbf{x})\mathrm{d}S(\mathbf{x}) + \left(1-\frac{\Omega}{4\pi}\right)\delta_{ij}, \tag{2.3.36}$$

corresponding to (2.3.33) for a smooth boundary.

(vi) The fundamental solution $\mathbf{T}$ is related to the fundamental solution for pressure $\mathbf{P}$, and velocity $\mathbf{G}$, by substituting (2.3.13) - (2.3.15) into (2.3.2) to give,

$$\frac{1}{8\pi}T_{ijk}(\mathbf{x},\mathbf{x}_0)b_j = -\frac{1}{8\pi}P_j(\mathbf{x},\mathbf{x}_0)\delta_{ik}b_j \\ + \frac{1}{8\pi}\left(\frac{\partial G_{ij}(\mathbf{x},\mathbf{x}_0)}{\partial x_k} + \frac{\partial G_{kj}(\mathbf{x},\mathbf{x}_0)}{\partial x_i}\right)b_j. \tag{2.3.37}$$

Notice that for direct substitution, the indices j need to be changed to k in (2.3.2). Cancelling wherever possible, the following relation (for which the symmetry condition (i), clearly still holds) is obtained,

$$T_{ijk}(\mathbf{x},\mathbf{x}_0) = -P_j(\mathbf{x},\mathbf{x}_0)\delta_{ik} + \frac{\partial G_{ij}(\mathbf{x},\mathbf{x}_0)}{\partial x_k} + \frac{\partial G_{kj}(\mathbf{x},\mathbf{x}_0)}{\partial x_i}. \tag{2.3.38}$$

2.3.3 Derivation Of The Direct Boundary Integral Equations

The derivation of the direct BIEs for the velocity $\mathbf{u}$ of a three-dimensional Stokes flow is shown below. Consider a specific Stokes flow of interest with velocity $\mathbf{u}$ and stress tensor $\boldsymbol{\sigma}$, satisfying (2.3.1) or (2.3.3), and define the singularly forced Stokes flow satisfying (2.3.11) or (2.3.12) as having solutions of the form shown in (2.3.39) - (2.3.41),

$$u_i'(\mathbf{x}) = \frac{1}{8\pi} G_{im}(\mathbf{x}, \mathbf{x}_0) b_m, \tag{2.3.39}$$

$$\sigma_{ij}'(\mathbf{x}) = \frac{1}{8\pi} T_{imj}(\mathbf{x}, \mathbf{x}_0) b_m, \tag{2.3.40}$$

$$\frac{\partial \sigma_{ij}'}{\partial x_i} = -\delta(\mathbf{x} - \mathbf{x}_0) b_j, \tag{2.3.41}$$

where $\mathbf{b}$ is some arbitrary constant vector and (2.3.39) - (2.3.40) are of similar form to (2.3.13) and (2.3.15).

By equation (2.3.7) of the derivation of the Lorentz reciprocal relation,

$$\frac{\partial}{\partial x_i}(u_j' \sigma_{ij} - u_j \sigma_{ij}') = u_j' \frac{\partial \sigma_{ij}}{\partial x_i} - u_j \frac{\partial \sigma_{ij}'}{\partial x_i}. \tag{2.3.42}$$

The solution of the specific Stokes flow satisfies $\frac{\partial \sigma_{ij}}{\partial x_i} = 0$ and the scalar equation (2.3.42) becomes,

$$\frac{\partial}{\partial x_i}\left(\frac{1}{8\pi} G_{jm}(\mathbf{x}, \mathbf{x}_0) b_m \sigma_{ij}(\mathbf{x}) - u_j(\mathbf{x}) \frac{1}{8\pi} T_{imj}(\mathbf{x}, \mathbf{x}_0) b_m\right) = u_m(\mathbf{x}) \delta(\mathbf{x} - \mathbf{x}_0) b_m, \tag{2.3.43}$$

or as $\mathbf{b}$ is arbitrary,

$$u_m(\mathbf{x})\delta(\mathbf{x} - \mathbf{x}_0) = \frac{\partial}{\partial x_i}\left(\frac{1}{8\pi} G_{jm}(\mathbf{x}, \mathbf{x}_0) \sigma_{ij}(\mathbf{x}) - u_j(\mathbf{x}) \frac{1}{8\pi} T_{imj}(\mathbf{x}, \mathbf{x}_0)\right). \tag{2.3.44}$$

Introduce a control volume V_c such as in figure 2.1, that is bounded by a surface D which has an outward unit normal vector $\mathbf{n}$. Equation (2.3.44) can be integrated over this volume and simplification made as the integral on the right hand side reduces to a

surface integral by the divergence theorem to give,

$$\int_{V_c} u_m(\mathbf{x})\delta(\mathbf{x}-\mathbf{x}_0)\mathrm{d}V(\mathbf{x}) = \int_D \left(\frac{1}{8\pi}G_{jm}(\mathbf{x},\mathbf{x}_0)\sigma_{ij}(\mathbf{x}) - u_j(\mathbf{x})\frac{1}{8\pi}T_{imj}(\mathbf{x},\mathbf{x}_0)\right) n_i(\mathbf{x})\mathrm{d}S(\mathbf{x}). \tag{2.3.45}$$

By re-labelling the indices as

$$m \to j, \qquad j \to i, \qquad i \to k, \tag{2.3.46}$$

equation (2.3.45) becomes

$$\int_{V_c} u_j(\mathbf{x})\delta(\mathbf{x}-\mathbf{x}_0)\mathrm{d}V(\mathbf{x}) = \frac{1}{8\pi}\int_D G_{ij}(\mathbf{x},\mathbf{x}_0)\sigma_{ik}(\mathbf{x})n_k(\mathbf{x})\mathrm{d}S(\mathbf{x}) - \frac{1}{8\pi}\int_D u_i(\mathbf{x})T_{ijk}(\mathbf{x},\mathbf{x}_0)n_k(\mathbf{x})\mathrm{d}S(\mathbf{x}). \tag{2.3.47}$$

Note the use of the stress tensor and fundamental stress solution symmetry conditions.

By the properties of Dirac's delta function, if $\mathbf{x}_0$ is not contained in V_c, then the left hand integral in (2.3.47) is zero, whereas when $\mathbf{x}_0$ is within V_c, the integral becomes $u_j(\mathbf{x}_0)$. Introducing, the boundary traction $\mathbf{f}$, given by,

$$f_i(\mathbf{x}) \equiv \sigma_{ik}(\mathbf{x})n_k(\mathbf{x}), \tag{2.3.48}$$

and by taking $\mathbf{x}_0$ inside V_c (2.3.47) becomes

$$u_j(\mathbf{x}_0) = \frac{1}{8\pi}\overset{(i)}{\int_D} G_{ij}(\mathbf{x},\mathbf{x}_0)f_i(\mathbf{x})\mathrm{d}S(\mathbf{x}) - \frac{1}{8\pi}\overset{(i)}{\int_D} u_i(\mathbf{x})T_{ijk}(\mathbf{x},\mathbf{x}_0)n_k(\mathbf{x})\mathrm{d}S(\mathbf{x}), \tag{2.3.49}$$

where the superscript (i) to the integrals denotes $\mathbf{x}_0$ is interior to V_c.

The terms on the right hand side of (2.3.49) are referred to as the single-layer and double-layer potential respectively, and are discussed in depth in [37]. The following two subsections give a brief overview of each potential in the direct formulation of the BIE.

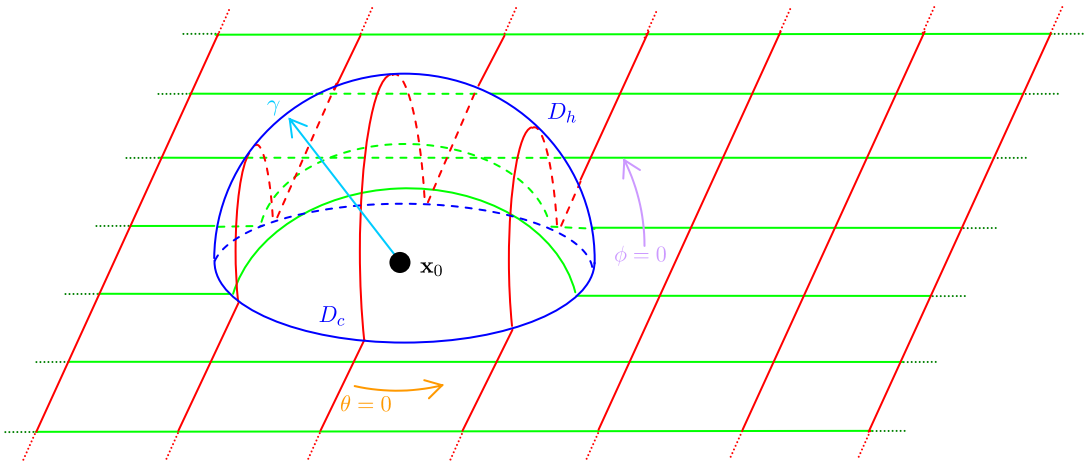

Figure 2.2: An illustration of the modified boundary including a hemisphere around the location of singularity in the integrand of (2.3.50).

Single Layer Potential

Denote the single layer potential V_j as,

$$V_j = \frac{1}{8\pi} \int_D G_{ij}(\mathbf{x}, \mathbf{x}_0) f_i(\mathbf{x}) \mathrm{d}S(\mathbf{x}), \tag{2.3.50}$$

in a three-dimensional formulation with surface D. When the singular point $\mathbf{x}_0$ tends to a field point $\mathbf{x}$ on a locally smooth surface D, then the velocity Green's function (and hence the integrand of (2.3.50)) exhibits a singularity of the form $1/r$, where r is defined as in equation (2.3.19). For an example consider the free-space velocity Green's function given by equation (2.3.16). The surface of integration D is distorted to include the point $\mathbf{x}_0$ in a hemispherical shell, with radius γ, and the limit $\gamma \to 0$ taken to recover the original boundary - see Figure 2.2. Thus integration is now conducted over the surface $D - D_c$ (where D_c is the circular region defined by the contour where the hemisphere intersects with D) and the surface of the hemisphere D_h.

In this limit the single layer potential (2.3.50) becomes

$$V_j = \frac{1}{8\pi} \lim_{\gamma \to 0} \left[\int_{D - D_c} G_{ij}(\mathbf{x}, \mathbf{x}_0) f_i(\mathbf{x}) \mathrm{d}S(\mathbf{x}) + \int_{D_h} G_{ij}(\mathbf{x}, \mathbf{x}_0) f_i(\mathbf{x}) \mathrm{d}S(\mathbf{x}) \right]. \tag{2.3.51}$$

The first integral in (2.3.51) tends to the original integral (2.3.50) in the limit defined. The second integral of (2.3.51) can be rewritten as,

$$\lim_{\gamma\to 0}\int\limits_{D_h} G_{ij}(\mathbf{x},\mathbf{x}_0)f_i(\mathbf{x})\mathrm{d}S(\mathbf{x}) = \lim_{\gamma\to 0}\int\limits_0^{\frac{\pi}{2}}\int\limits_0^{2\pi} G_{ij}(\mathbf{x},\mathbf{x}_0)f_i(\mathbf{x})\gamma^2\sin\phi\,\mathrm{d}\theta\mathrm{d}\phi, \tag{2.3.52}$$

where

$$G_{ij}(\mathbf{x},\mathbf{x}_0) \sim \frac{1}{\gamma}. \tag{2.3.53}$$

Provided $f_i(\mathbf{x})$ is non-singular over the entire boundary, the integral in (2.3.52) can be shown to tend to zero. Expression (2.3.51) becomes identical to (2.3.50) as $\mathbf{x}_0$ tends to the surface, and the single-layer potential shows no discontinuity as $\mathbf{x}_0$ is moved onto the boundary D. This result holds even for $\mathbf{x}_0$ placed at a corner of the boundary D, although the analysis requires the hemisphere to be replaced by a portion of a sphere dependent on the solid angle prescribed by the boundary shape at the corner.

Double Layer Potential

Consider the double-layer potential W_j from (2.3.49), with $\mathbf{x}_0$ interior to the domain,

$$W_j = -\frac{1}{8\pi}\int\limits_D^{(i)} u_i(\mathbf{x})T_{ijk}(\mathbf{x},\mathbf{x}_0)n_k(\mathbf{x})\mathrm{d}S(\mathbf{x}), \tag{2.3.54}$$

which can be rewritten as

$$\begin{aligned} W_j = -\frac{1}{8\pi}\int\limits_D^{(i)} &[u_i(\mathbf{x}) - u_i(\mathbf{x}_0)]T_{ijk}(\mathbf{x},\mathbf{x}_0)n_k(\mathbf{x})\mathrm{d}S(\mathbf{x}) \\ &- \frac{1}{8\pi}u_i(\mathbf{x}_0)\int\limits_D^{(i)} T_{ijk}(\mathbf{x},\mathbf{x}_0)n_k(\mathbf{x})\mathrm{d}S(\mathbf{x}), \end{aligned} \tag{2.3.55}$$

and note that the integrand of the first integral in (2.3.55) is no longer singular (i.e. the singularity of $T_{ijk}(\mathbf{x},\mathbf{x}_0)n_k(\mathbf{x})$ is countered by its preceding term tending to zero). Manipulating (2.3.55) and applying (2.3.33) (due to taking the singularity point initially

within V_c and then moving to the boundary), allows expression (2.3.56) for the double-layer potential to be derived when $\mathbf{x}_0$ lies directly on the locally smooth boundary D of control volume V_c,

$$W_j = -\frac{1}{8\pi} \int_D^{\mathbf{x}_0 \in D} [u_i(\mathbf{x}) - u_i(\mathbf{x}_0)] T_{ijk}(\mathbf{x}, \mathbf{x}_0) n_k(\mathbf{x}) \mathrm{d}S(\mathbf{x}) \\ - \frac{1}{8\pi} u_i(\mathbf{x}_0) \int_D^{\mathbf{x}_0 \in D} T_{ijk}(\mathbf{x}, \mathbf{x}_0) n_k(\mathbf{x}) \mathrm{d}S(\mathbf{x}) + \frac{1}{2} \delta_{ij} u_i(\mathbf{x}_0). \tag{2.3.56}$$

Rewriting (2.3.56) in the more convenient form using the standard properties of the Kronecker delta yields

$$W_j = -\frac{1}{8\pi} \int_D^{\mathbf{x}_0 \in D} u_i(\mathbf{x}) T_{ijk}(\mathbf{x}, \mathbf{x}_0) n_k(\mathbf{x}) \mathrm{d}S(\mathbf{x}) \\ + \frac{1}{8\pi} \int_D^{\mathbf{x}_0 \in D} u_i(\mathbf{x}_0) T_{ijk}(\mathbf{x}, \mathbf{x}_0) n_k(\mathbf{x}) \mathrm{d}S(\mathbf{x}) \\ + \frac{1}{2} u_j(\mathbf{x}_0) - \frac{1}{8\pi} \int_D^{\mathbf{x}_0 \in D} u_i(\mathbf{x}_0) T_{ijk}(\mathbf{x}, \mathbf{x}_0) n_k(\mathbf{x}) \mathrm{d}S(\mathbf{x}), \tag{2.3.57}$$

and with $\mathbf{x}_0$ located on the boundary D, the middle and last integrals in (2.3.57) cancel and the following important equation is obtained,

$$\lim_{\mathbf{x}_0 \to D} \left[-\frac{1}{8\pi} \int_D^{(i)} u_i(\mathbf{x}) T_{ijk}(\mathbf{x}, \mathbf{x}_0) n_k(\mathbf{x}) \mathrm{d}S(\mathbf{x}) \right] = \\ \frac{1}{2} u_j(\mathbf{x}_0) - \frac{1}{8\pi} \int_D^{\mathbf{x}_0 \in D} u_i(\mathbf{x}) T_{ijk}(\mathbf{x}, \mathbf{x}_0) n_k(\mathbf{x}) \mathrm{d}S(\mathbf{x}). \tag{2.3.58}$$

The double-layer potential exhibits a discontinuity as the point $\mathbf{x}_0$ is moved onto the boundary. The corresponding equation to (2.3.58) for the case of the singularity point being located at a corner on the boundary D can be derived by similar means to those shown. Using (2.3.36) in place of (2.3.33) in the above manipulation and following all

the steps shown gives,

$$\lim_{\mathbf{x}_0 \to D} \left[-\frac{1}{8\pi} \overset{(i)}{\int_D} u_i(\mathbf{x}) T_{ijk}(\mathbf{x}, \mathbf{x}_0) n_k(\mathbf{x}) \mathrm{d}S(\mathbf{x}) \right] = \left(1 - \frac{\Omega}{4\pi} \right) u_j(\mathbf{x}_0) - \frac{1}{8\pi} \overset{\mathbf{x}_0 \in D}{\int_D} u_i(\mathbf{x}) T_{ijk}(\mathbf{x}, \mathbf{x}_0) n_k(\mathbf{x}) \mathrm{d}S(\mathbf{x}) \tag{2.3.59}$$

The case of $\Omega = 2\pi$ corresponds to $\mathbf{x}_0$ placed on a locally smooth boundary and equation (2.3.59) reduces to (2.3.58)

Direct Boundary Integral Equations

A general form for the BIE is found by (2.3.49), and using the continuous and discontinuous properties of the single and double layer potentials as $\mathbf{x}_0$ approaches the surface,

$$c_{ij}(\mathbf{x}_0) u_i(\mathbf{x}_0) = \frac{1}{8\pi} \int_D G_{ij}(\mathbf{x}, \mathbf{x}_0) f_i(\mathbf{x}) \mathrm{d}S(\mathbf{x}) - \frac{1}{8\pi} \int_D u_i(\mathbf{x}) T_{ijk}(\mathbf{x}, \mathbf{x}_0) n_k(\mathbf{x}) \mathrm{d}S(\mathbf{x}), \tag{2.3.60}$$

where $c_{ij}(\mathbf{x}_0)$ defines the jump condition and is given by

$$c_{ij}(\mathbf{x}_0) = \begin{cases} \delta_{ij} & \text{when } \mathbf{x}_0 \text{ is inside } D, \\ \frac{1}{2}\delta_{ij} & \text{when } \mathbf{x}_0 \text{ is on } D, \\ 0 & \text{when } \mathbf{x}_0 \text{ is outside } D, \end{cases} \tag{2.3.61}$$

for a smooth surface, and

$$c_{ij}(\mathbf{x}_0) = \begin{cases} \delta_{ij} & \text{when } \mathbf{x}_0 \text{ is inside } D, \\ \frac{\Omega}{4\pi}\delta_{ij} & \text{when } \mathbf{x}_0 \text{ is on } D, \\ 0 & \text{when } \mathbf{x}_0 \text{ is outside } D, \end{cases} \tag{2.3.62}$$

at a corner point. Again, the case of $\Omega = 2\pi$ corresponds to $\mathbf{x}_0$ placed on a locally smooth boundary and (2.3.62) reduces to (2.3.61).

The BIE (2.3.60) relates the governing boundary velocities and tractions for a Stokes flow. Solutions of the BIE require boundary conditions suitable for the flow being analyzed.

Three general possibilities of boundary conditions are described briefly below. For more details see [34, 37].

(i) If the boundary velocity $\mathbf{u}$ is specified over D, then the BIE becomes an equation for the surface traction $\mathbf{f}$ only. This is called a *Fredholm integral equation of the first kind.*

(ii) If the surface traction $\mathbf{f}$ is specified over D, then the BIE becomes an equation for the boundary velocity $\mathbf{u}$ only. This is called a *Fredholm integral equation of the second kind.*

(iii) A *Fredholm integral equation of mixed type* involves specifying the boundary velocity $\mathbf{u}$ over a part of D and for the remainder of D specifying the surface traction $\mathbf{f}$. Each of the resulting BIE is then solved for the unknown values on each section of the boundary.

2.4 The Boundary Element Method

The boundary integral equation (BIE) for a singularity $\mathbf{x}_0$, located on a smooth boundary D was derived in § 2.3 and is given by equation (2.3.60). The boundary element method (BEM) is used as a means to solving the BIE on the boundary by implementing three approximations. For suitable boundary conditions, the boundary elements are collocated, resulting in a matrix problem to be solved for unknown boundary tractions f_i or velocities u_i. These approximations along with the collocation of the boundary elements are discussed in this section. Finally an example BEM implementation utilizing a constant boundary distribution is described.

2.4.1 Approximation And Collocation

The aim of the BEM is to reduce the BIE (2.3.60) to a matrix problem which can be solved. To do this, three approximations are implemented. First of all the boundary is discretized into elements by means of a *geometrical approximation*. Then the physical variables are approximated on each of the previously defined elements by a chosen *boundary distribution*. Finally, using an *integral approximation*, the integrals over each element are evaluated using an appropriate numerical technique. Finally the resulting equation can be *collocated* over all boundary elements to produce a system of equations that can be solved. Each of these three approximations along with the collocation technique are discussed in turn below.

Geometric Approximation

The boundary D of domain V_c over which the integrals of (2.3.60) are to be evaluated often have complex geometries. It is appropriate to discretize the boundary D into geometrically simpler boundary elements, denoted by E_ν, $\nu = 1, \ldots, N$. The integrals in (2.3.60) can then be rewritten as the sum of the integrals over each boundary elements as shown in (2.4.1).

$$\begin{aligned}\frac{1}{2}u_j(\mathbf{x}_0) = \frac{1}{8\pi}\sum_{\nu=1}^{N}\int_{E_\nu} G_{ij}(\mathbf{x},\mathbf{x}_0)f_i(\mathbf{x})\mathrm{d}S(\mathbf{x}) \\ - \frac{1}{8\pi}\sum_{\nu=1}^{N}\int_{E_\nu} u_i(\mathbf{x})T_{ijk}(\mathbf{x},\mathbf{x}_0)n_k(\mathbf{x})\mathrm{d}S(\mathbf{x}).\end{aligned} \tag{2.4.1}$$

Various forms of boundary discretization may be implemented, with the most common cases comprising of either linear or quadratic triangular elements.

Boundary Distribution

Values are required for the boundary traction f_i and velocity u_i on each of the boundary elements E_ν. The simplest approximation is to take the boundary tractions and velocities constant over each element. However to improve accuracy, a variety of higher-ordered polynomials, or other kinds of interpolation function can be used to represent the boundary distributions.

Integral Approximation

The integrals in equation (2.4.1) need evaluating on each element that discretizes the boundary. These integrals can be classified as,

- *Non-Singular*: The element over which the integration is to be conducted does not contain the singularity $\mathbf{x}_0$ and the integrands are non-singular in this case.
- *Singular*: The element over which the integration is to be conducted contains the singularity $\mathbf{x}_0$ and the integrands are singular in this case.

In general the integrals will be evaluated using a range of numerical methods for both non-singular and singular integrands. Non-singular integrands are evaluated numerically using appropriate Gaussian quadrature techniques. For cases of near-point singularities, refinement of the integration is made by a combination of an adaptive Gaussian integration algorithm and an element subdivision approach. Further details of this method are given in chapter 4. Singularities of the single layer potential are evaluated using polar integration, with details omitted here but shown in [34]. Flat elements are considered throughout this thesis, causing the singularity of the double layer potential to vanish due to the tangent vector of a flat element always being perpendicular to the normal.

Collocation Of Boundary Elements

When suitable boundary conditions are applied, which define either the boundary traction f_i or velocity u_i on each element, then it is left for the BEM to calculate the unknown values of f_i or u_i on each element. This is achieved by collocation of the discretized equation in a bid to generate the same number of equations as unknowns. A matrix problem is formulated and solved for the unknown values associated with the Stokes flow.

2.4.2 Implementation Of A Constant Boundary Distribution

This section considers the BEM formulation outlined above for a constant boundary distribution. Details of the geometrical approximation and the type of numerical techniques used for the evaluation of the integrals are not required per se as they will have no effect on the formulation shown below.

Consider a geometric approximation, used to discretize the boundary into N elements. As described in the previous section, the integral (2.3.60) is simplified to the sum of the integrals over each element, as shown in (2.4.1). In addition a constant or uniform boundary distribution implies a constant value for boundary traction f_i and velocity u_i be defined over each element. These are written as $f_i|_{E_\nu}$ and $u_i|_{E_\nu}$ for element E_ν. Also note that from here on $\mathrm{d}S \equiv \mathrm{d}S(\mathbf{x})$. Substituting these values into equation (2.4.1) yields,

$$\begin{aligned}\frac{1}{2}u_j(\mathbf{x}_0) = \frac{1}{8\pi}\sum_{\nu=1}^{N} f_i|_{E_\nu} \int_{E_\nu} G_{ij}(\mathbf{x},\mathbf{x}_0)\mathrm{d}S \\ - \frac{1}{8\pi}\sum_{\nu=1}^{N} u_i|_{E_\nu} \int_{E_\nu} T_{ijk}(\mathbf{x},\mathbf{x}_0)n_k(\mathbf{x})\mathrm{d}S.\end{aligned} \tag{2.4.2}$$

Equation (2.4.2) can be rewritten such that the summation used for the evaluation of

$u_j(\mathbf{x}_0)$ is via the multiplication of vectors,

$$\begin{aligned}\frac{1}{2}u_j(\mathbf{x}_0) = \frac{1}{8\pi}\left(f_i|_{E_\nu=1} \quad ,\cdots, \quad f_i|_{E_\nu=N}\right)\begin{pmatrix}\int_{E_\nu=1} G_{ij}(\mathbf{x},\mathbf{x}_0)\mathrm{d}S \\ \vdots \\ \int_{E_\nu=N} G_{ij}(\mathbf{x},\mathbf{x}_0)\mathrm{d}S\end{pmatrix} \\ -\frac{1}{8\pi}\left(u_i|_{E_\nu=1} \quad ,\cdots, \quad u_i|_{E_\nu=N}\right)\begin{pmatrix}\int_{E_\nu=1} T_{ijk}(\mathbf{x},\mathbf{x}_0)n_k\mathrm{d}S \\ \vdots \\ \int_{E_\nu=N} T_{ijk}(\mathbf{x},\mathbf{x}_0)n_k\mathrm{d}S\end{pmatrix}.\end{aligned} \tag{2.4.3}$$

By placing the singularity point $\mathbf{x}_0$ at the middle of element ζ, denoted $\mathbf{x}_\zeta^M$ and recalling the values of f_i and u_i are taken constant over each element, the left hand side of (2.4.3) becomes,

$$\frac{1}{2}u_j(\mathbf{x}_\zeta^M) = \frac{1}{2}u_j|_{E_\zeta}. \tag{2.4.4}$$

By collocating over all the elements, (2.4.2) becomes a system of $3N$ equations comprising of the 3 components of u_i, f_i on each of the N elements. Two $3N \times 3N$ matrices are formed, which can be thought of as $N \times N$ arrays where each component is the 3×3 matrix G_{ij} or $T_{ijk}n_k$ (where i is the local row number and j is the local column number of each component within the $N \times N$ array). Thus the collocated system of equations determined by the BEM is given by.

$$\frac{1}{2}U_d = \frac{1}{8\pi}F_cA_{cd} - \frac{1}{8\pi}U_cB_{cd}, \tag{2.4.5}$$

where

$$F_c = \left(f_i|_{E_\nu=1} \quad \cdots \quad f_i|_{E_\nu=N}\right), \tag{2.4.6}$$

$$U_c = \left(u_i|_{E_\nu=1} \quad \cdots \quad u_i|_{E_\nu=N}\right), \tag{2.4.7}$$

$$A_{cd} = \begin{pmatrix}\int_{E_\nu=1} G_{ij}(\mathbf{x},\mathbf{x}_{\zeta=1}^M)\mathrm{d}S & \cdots & \int_{E_\nu=1} G_{ij}(\mathbf{x},\mathbf{x}_{\zeta=N}^M)\mathrm{d}S \\ \vdots & \ddots & \vdots \\ \int_{E_\nu=N} G_{ij}(\mathbf{x},\mathbf{x}_{\zeta=1}^M)\mathrm{d}S & \cdots & \int_{E_\nu=N} G_{ij}(\mathbf{x},\mathbf{x}_{\zeta=N}^M)\mathrm{d}S\end{pmatrix}, \tag{2.4.8}$$

$$B_{cd} = \begin{pmatrix}\int_{E_\nu=1} T_{ijk}(\mathbf{x},\mathbf{x}_{\zeta=1}^M)n_k\mathrm{d}S & \cdots & \int_{E_\nu=1} T_{ijk}(\mathbf{x},\mathbf{x}_{\zeta=N}^M)n_k\mathrm{d}S \\ \vdots & \ddots & \vdots \\ \int_{E_\nu=N} T_{ijk}(\mathbf{x},\mathbf{x}_{\zeta=1}^M)n_k\mathrm{d}S & \cdots & \int_{E_\nu=N} T_{ijk}(\mathbf{x},\mathbf{x}_{\zeta=N}^M)n_k\mathrm{d}S\end{pmatrix}, \tag{2.4.9}$$

for $i, j, k = 1, \ldots, 3$, and $\nu, \zeta = 1, \ldots, N$. Indices c and d take values $c, d = 1, \ldots, 3N$ and are defined by.

$$c = 3(\nu - 1) + i, \tag{2.4.10}$$

$$d = 3(\zeta - 1) + j. \tag{2.4.11}$$

Rewritten (2.4.5) becomes

$$\frac{1}{8\pi} F_c A_{cd} = U_c \left(\frac{1}{2} \delta_{cd} + \frac{1}{8\pi} B_{cd} \right). \tag{2.4.12}$$

The solution of (2.4.12) involves calculating the integrals of each element, and forming the components of the two matrices. By specifying suitable boundary conditions the system of equations is solved for unknown tractions and/or velocities.

Chapter 3

Radial Basis Functions

Solutions of film flows down an inclined plane over and around obstacles require a range of efficient numerical techniques. These film profiles are often dominated by surface forces such as surface tension, and require an accurate representation of the free surface. The evaluation of the free surface traction, incorporating these effects, is achieved by using a radial basis function (RBF). In addition by using a Hermitian RBF, far field and contact line constraints imposed on the free surface can also be included in the interpolation. A RBF interpolation is also used in Chapter 7 when implementing numerical techniques to extend a Stokes flow formulation to the non-linear problem of finite Reynolds number flows. This chapter considers an overview of RBFs, along with implementation of local and global interpolations.

3.1 Introduction To Radial Basis Function Interpolations

The interpolation of a discrete set of data points, such as those obtained by mesh based schemes, (e.g. the boundary element method (BEM)), is a common problem. Conventional methods such as polynomial and spline interpolations have been applied to a wide range of engineering problems. Alternatively a radial basis function (RBF) interpolation can be used for such a purpose. An extensive study of interpolation methods available at the time was conducted by Franke [40], and concluded that RBF interpolations were

Generalized Thin Plate Spline (2D)	$r^{2m-2}\log r$
Generalized Thin Plate Spline (3D)	r^m (m odd)
Generalized Multiquadric	$\left(r^2+c^2\right)^{\frac{m}{2}}$ (m odd)
Gaussian	$\exp\left(-\frac{r}{c}\right)$

Table 3.1: Common radial basis functions

the most accurate techniques evaluated.

The theory of RBFs originated as a means to provide a continuous interpolation of scattered data values. However, in recent years RBFs have been extensively researched and applied in a wider range of analysis. Partial differential equations (PDEs) have been solved using RBFs with recent work in this field conducted by La Rocca et al. [41] and La Rocca and Power [42]. The RBF interpolation has also been used in the implementation of the dual reciprocity method (DRM) (see Nardini and Brebbia [43]), a method used to transform the domain integrals present in the boundary integral equations (BIEs) for non-linear problems. In this thesis the original application of RBFs is used as a means of interpolating the surface data for film flow over or around an obstacle. In addition, chapter 7 considers the non-linear problem of film flows at finite Reynolds number, using a RBF interpolation within the numerical techniques implemented.

A RBF $\psi(\|\mathbf{x}-\boldsymbol{\xi}^j\|)$ depends on the separation between a field point $\mathbf{x}$ and the data centres $\boldsymbol{\xi}^j$, for $j=1,\ldots,N$, and N data points. The interpolants are classed as radial due to their spherical symmetry around centres $\boldsymbol{\xi}^j$, with $\|\mathbf{x}-\boldsymbol{\xi}^j\|$ the Euclidean norm. The most popular RBFs are listed in table 3.1 where $r=\|\mathbf{x}-\boldsymbol{\xi}^j\|$, m is an integer, and c is a free parameter, often referred to as the shape parameter, to be specified by the user. In addition, for the multiquadric and the three-dimensional thin plate spline, only odd values of m are permitted.

The inverse multiquadric ($m<0$ in the generalized multiquadric) and Gaussian are functions which form positive definite interpolation matrices, whilst the thin plate spline

and multiquadric ($m > 0$ in the generalized multiquadric) are functions which generate conditionally positive definite matrices of order m. By standard theory, positive definite matrices are never singular, and guarantee solution to the interpolation problem. However, the conditionally positive definite matrices which are formed by RBFs such as the thin plate spline may be singular for certain selections of data centres. These conditionally positive definite matrices are conditionate of a polynomial of order $m-1$ along with homogeneous constraint condition. If these are included within the interpolation, a positive definite matrix is formed, and solution to the interpolation is guaranteed. For further details, see Golberg and Chen [44].

The shape parameter c within the Gaussian and multiquadric RBFs requires fine tuning and can dramatically alter the quality of the interpolation. Despite being considered as optimal for interpolating multivariate data, Franke [40] found that the thin plate spline was marginally outperformed by the multiquadric RBF with regards to the test criteria. In fact Powell [45] indicated that the thin plate spline RBF only converges linearly compared to the multiquadrics which converge exponentially, producing a minimal semi-norm error (see Madych and Nelson [46]). However, the multiquadric RBF is disadvantaged by the presence of the shape parameter c whose choice significantly effects the interpolation. In addition, Schaback [47] states that numerical experiments show that the condition number of the resulting interpolation matrix is large for smooth interpolants such as the gaussian or multiquadric RBF when compared to non-smooth functions such as thin plate splines for low m. Thus a thin plate spline RBF is used throughout this thesis.

Typical interpolation problems involve taking the known data centres $\left(\boldsymbol{\xi}^j, F(\boldsymbol{\xi}^j)\right)$, for $j = 1, \ldots, N$ of the unknown function F and interpolating it by the function f. Thus for a conditionally positive definite function, the interpolation takes the form,

$$f(\mathbf{x}) = \sum_{j=1}^{N} \lambda_j \psi\left(\|\mathbf{x} - \boldsymbol{\xi}^j\|\right) + P_{m-1}(\mathbf{x}), \tag{3.1.1}$$

and for arbitrary order m, the polynomial P_{m-1} contains N_p terms and in two-dimensions

has the expanded form

$$P_{m-1}(\mathbf{x}^i) = \lambda_{N+1}(x_1^i)^{m-1} + \lambda_{N+2}(x_2^i)^{m-1} + \lambda_{N+3}(x_1^i)^{m-2}x_2^i + \dots \\ + \lambda_{N+N_p-2}x_1^i + \lambda_{N+N_p-1}x_2^i + \lambda_{N+N_p}. \tag{3.1.2}$$

Collocation of (3.1.1) over the N data centres yields N equations for the $N + N_p$ unknowns λ_j. The homogeneous constraint condition,

$$\sum_{j=1}^{N} \lambda_j P_k(\mathbf{x}^j) = 0, \qquad 1 \le k \le m-1, \tag{3.1.3}$$

gives another N_p equations to close the system. Thus, by collocation over the data centres, a matrix problem $A_{ij}\lambda_j = b_i$ is formed, where A_{ij} is defined by,

$$A_{ij} = \begin{pmatrix} \psi & P_{m-1} \\ (P_{m-1})^T & 0 \end{pmatrix}, \tag{3.1.4}$$

and b_i is given by,

$$b_i = \begin{pmatrix} F & 0 \end{pmatrix}^T. \tag{3.1.5}$$

The matrix problem can be solved for λ_j, and thus the function $f(\mathbf{x})$ can be reconstructed at any point by (3.1.1).

Hermitian Interpolations And Double Collocation

When the problem specifies additional constraints (for example far field conditions), they can be incorporated by use of a Hermite RBF interpolation. Consider the linear partial differential operator $L_x(f(\mathbf{x})) = G$ to be applied at n points which may or may not correspond to locations used in the original interpolation (3.1.1). Then the Hermitian interpolation takes the form

$$f(\mathbf{x}) = \sum_{j=1}^{N} \lambda_j \psi\left(\|\mathbf{x} - \boldsymbol{\xi}^j\|\right) + \sum_{j=N+1}^{N+n} \lambda_j L_\xi \psi\left(\|\mathbf{x} - \boldsymbol{\xi}^j\|\right) + P_{m-1}(\mathbf{x}), \tag{3.1.6}$$

where L_ξ is the differential operator defined above but acting on $\boldsymbol{\xi}$.

For the Hermite interpolation (3.1.6), a matrix problem $A_{ij}\lambda_j = b_i$ is formed, where A_{ij} is now defined by,

$$A_{ij} = \begin{pmatrix} \psi & L_\xi(\psi) & P_{m-1} \\ L_x(\psi) & L_xL_\xi(\psi) & L_x(P_{m-1}) \\ (P_{m-1})^T & (L_x(P_{m-1}))^T & 0 \end{pmatrix}, \tag{3.1.7}$$

and b_i is given by,

$$b_i = \begin{pmatrix} F & G & 0 \end{pmatrix}^T. \tag{3.1.8}$$

The matrix (3.1.7) is non-singular as long as ψ is chosen appropriately. For cases of double collocation, ψ, $L_x(\psi)$ and any further differential operators can be applied simultaneously at the same collocation points as long as they are linearly independent.

When modelling film flow over an obstacle, an accurate method for generating the free surface and deducing the unit normal and curvature is required. By supplying a discrete set of data points (surface heights), a Hermitian RBF can be used to find a smooth function through all of the points, allowing the derivative of the free surface and hence the unit normal and mean curvature to be found.

3.2 Local And Global Interpolations

The radial basis function (RBF) interpolation outlined in section 3.1 is described in a global sense. The interpolation matrix involves solving a system of equations that incorporate all data points. For an $N \times N$ interpolation matrix, this requires $O(N^3)$ operations when using Gaussian elimination to solve the system of equations. For large systems the amount of CPU time and RAM necessary can become prohibitive. In addition, as the system becomes large, the resulting matrix becomes ill-conditioned. The local RBF can offer substantial improvements with regards to the CPU time and RAM requirements,

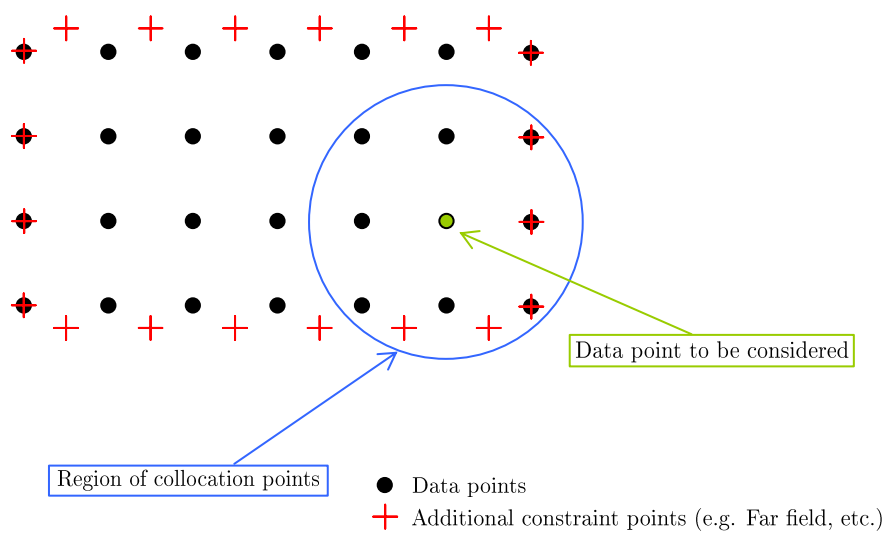

Figure 3.1: A sketch indicating how the local elements are chosen.

and avoid this ill-conditioning problem. At each data point, a local approach involves solving an interpolation matrix that only incorporates the collocation points within a certain range of the data point under consideration. The upshot of this method is to reduce computation time to $O(NM^3)$, where M is the $M \times M$ local interpolation matrix, and N is the number of global data points considered. Thus, for M sufficiently smaller than N, this will offer significant benefits in terms of run-time and memory requirement.

In two-dimensions, the local points are found by drawing a circular region in the x_1x_2 plane of a chosen radius around each data point in turn, and recording the collocation points that fall within this region. Obviously the more points chosen for the interpolation, the more accurate it will be, although the CPU time and RAM required is also increased. Care needs to be taken as to whether any of the points caught require derivative conditions to be applied (for example in the far field). This technique is illustrated in Figure 3.1

The generation and solution of the local system is conducted by identical means to the global approach outlined in section 3.1, and for a sufficiently large inclusion zone, the results should be virtually identical. This is due to the ever decreasing effect data points

will have on the interpolation further away from the point under consideration. The efficiency gains from using a local interpolation will be evaluated for each case implemented. In general when interpolating the free surface, a global technique is optimum. However, when considering the effects of inertia using the method of particular solutions in chapter 7, a local approach is often beneficial.

Chapter 4

Stokes Flow Over A Single Obstacle

Thin film flows driven by gravity down an inclined plane and over an obstacle is an important, well studied generic flow problem. Efficient and accurate solution techniques are developed in this chapter based on a Stokes flow formulation. In § 1.1 a thorough overview of published works in this field are considered, with this chapter starting by considering the formulation and numerical schemes to be used in solving the problem, outlined in § 4.1 and § 4.2 respectively. Finally, solutions for Stokes flow over a single obstacle are considered in § 4.3, validating results with those previously published by other authors.

4.1 Mathematical Formulation

This section considers the Stokes flow formulation of a thin film driven by gravity down an inclined plane over an obstacle attached to the plane. The flow variables are solved for disturbance and undisturbed components in a manner similar to Blyth and Pozrikidis [31]. Two subsections outline the simplification of the formulation for consideration of small free surface deflections as in [31] and consideration of asymptotically small obstacles as implemented by Pozrikidis and Thoroddsen [29].

A two-dimensional schematic of a typical film flow of undisturbed thickness H, driven

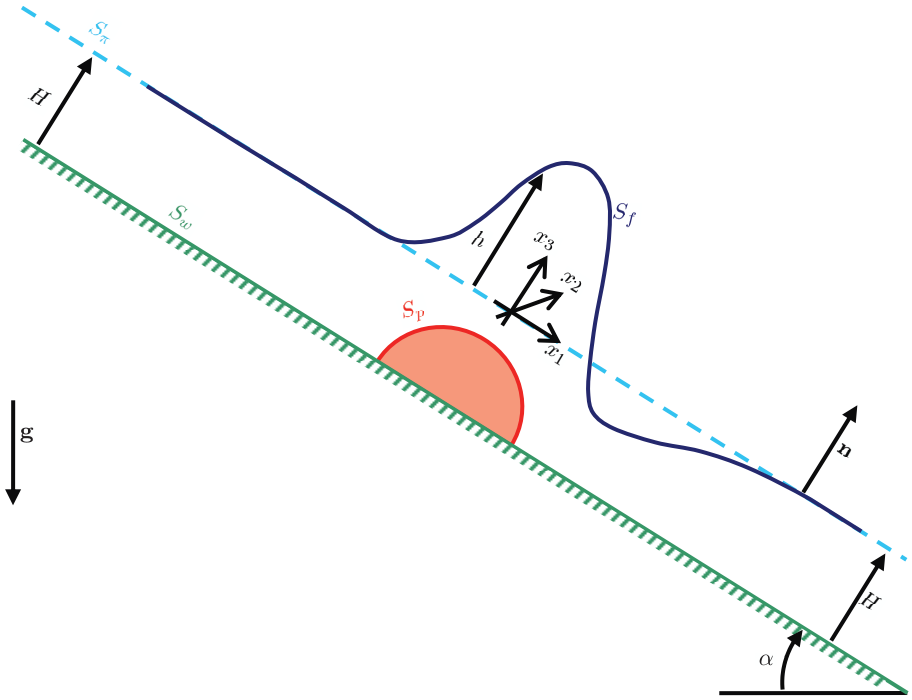

Figure 4.1: Two-dimensional cross section of a typical film profile.

Table 4.1: Reference Quantities

Reference Length	H
Reference Velocity	$U_s = \frac{H^2 \rho g \sin\alpha}{2\mu}$
Reference Stress	$\frac{\mu U_s}{H}$

by a component of gravity **g** down an inclined plane at angle α and over an obstacle is shown in Figure 4.1. The wetted obstacle surface is denoted S_p and is attached to the inclined plane S_w. A fluid travels down the inclined plane, completely submerging the obstacle, with free surface denoted S_f. The corresponding undisturbed film surface is given by S_π. The distance from the undisturbed film S_π to the disturbed film surface S_f is given by h, and the outward unit normal is denoted by **n**. A cartesian co-ordinate system is aligned such that the undisturbed plane S_π is defined by the x_1x_2-plane, with x_1 in the direction of the undisturbed flow. Axis x_3 is perpendicular to S_π, pointing away from the inclined wall S_w.

For mathematical convenience, physical variables are non-dimensionalized using the three

reference quantities shown in table 4.1. The reference length is taken as the undisturbed film height H, with reference velocity given by the free stream surface velocity U_s for film flow down an inclined plane in the absence of an obstacle. Finally, a viscous scaling is used for the reference stress. The associated Bond number is

$$Bo = \frac{\rho g H^2 \sin\alpha}{\gamma}, \tag{4.1.1}$$

where γ is the surface tension, ρ the fluid density and $g = |\mathbf{g}|$ the acceleration due to gravity.

The film flow is governed by the standard incompressible equations for mass conservation (4.1.2) and steady Stokes flow (4.1.3)

$$\frac{\partial u_i}{\partial x_i} = 0, \tag{4.1.2}$$

$$-\frac{\partial p}{\partial x_i} + \frac{\partial G}{\partial x_i} + \frac{\partial^2 u_i}{\partial x_j^2} = 0, \tag{4.1.3}$$

where G is defined by (4.1.4),

$$G = -2(x_3 \cot\alpha - x_1). \tag{4.1.4}$$

Far field constraints involve the flow velocity and pressure returning to values associated with a gravity driven film flow down an inclined plane in the absence of an obstacle, and denoted by a superscript ∞. In addition, the free surface deflection, along with the gradient of the free surface should decay to zero. These conditions are shown in (4.1.5),

$$\left.\begin{array}{c} u_i \to u_i^\infty \\ p \to p^\infty \\ h \to 0 \\ \frac{\partial h}{\partial x_1} \to 0 \\ \frac{\partial h}{\partial x_2} \to 0 \end{array}\right\} \text{as } \mathbf{x} \to \pm\infty. \tag{4.1.5}$$

Several boundary conditions are also applied within the flow domain. No slip (zero velocity) is specified on the inclined wall S_w, and wetted obstacle surface S_p, given by

(4.1.6). In addition a dynamic (4.1.7) and kinematic (4.1.8) condition are applied on the free surface S_f, and expressed as,

$$u_i = 0 \qquad \mathbf{x} \in S_w \cup S_p, \tag{4.1.6}$$

$$f_i = \sigma_{ij} n_j = -\frac{4}{Bo}\kappa n_i \qquad \mathbf{x} \in S_f, \tag{4.1.7}$$

$$\frac{\partial h}{\partial t} = -u_1 \frac{\partial h}{\partial x_1} - u_2 \frac{\partial h}{\partial x_2} + u_3 \qquad \mathbf{x} \in S_f, \tag{4.1.8}$$

where f_i is the boundary traction. The curvature of the free surface is denoted by κ, σ_{ij} is the stress tensor, and time is given by t. The curvature and the stress tensor are expressed by (4.1.9) and (4.1.10):

$$\kappa = \frac{1}{2}\frac{\partial n_i}{\partial x_i}, \tag{4.1.9}$$

$$\sigma_{ij} = -p\delta_{ij} + \left(\frac{\partial u_i}{\partial x_j} + \frac{\partial u_j}{\partial x_i}\right). \tag{4.1.10}$$

In (4.1.9) and (4.1.10) n_i is the components of the outward unit normal to the free surface S_f. The outward unit normal n_i of the free surface can be evaluated as,

$$\mathbf{n} = \frac{1}{\sqrt{1 + \left(\frac{\partial h}{\partial x_1}\right)^2 + \left(\frac{\partial h}{\partial x_2}\right)^2}} \left(-\frac{\partial h}{\partial x_1}, -\frac{\partial h}{\partial x_2}, 1\right). \tag{4.1.11}$$

The form of the curvature κ can also be expanded as,

$$\begin{aligned} \kappa = &-\frac{1}{2}\left(1 + \left(\frac{\partial h}{\partial x_1}\right)^2 + \left(\frac{\partial h}{\partial x_2}\right)^2\right)^{-\frac{3}{2}} \\ &\times \left[\frac{\partial^2 h}{\partial x_1^2}\left(1 + \left(\frac{\partial h}{\partial x_2}\right)^2\right) + \frac{\partial^2 h}{\partial x_2^2}\left(1 + \left(\frac{\partial h}{\partial x_1}\right)^2\right) - 2\frac{\partial^2 h}{\partial x_1 \partial x_2}\frac{\partial h}{\partial x_1}\frac{\partial h}{\partial x_2}\right]. \end{aligned} \tag{4.1.12}$$

Film Flow In The Absence Of Obstacles

The governing equations for film flow in the absence of obstacles, is given by

$$\frac{\partial u_i^\infty}{\partial x_i} = 0, \tag{4.1.13}$$

$$-\frac{\partial p^\infty}{\partial x_i} + \frac{\partial G}{\partial x_i} + \frac{\partial^2 u_i^\infty}{\partial x_j^2} = 0, \tag{4.1.14}$$

where superscript ∞ on the flow variables corresponds to the far field asymptotic case. Solutions to the equations (4.1.13) and (4.1.14) can be readily shown to be,

$$p^{\infty} = -2x_3 \cot\alpha, \tag{4.1.15}$$

$$u_i^{\infty} = (1 - x_3^2)\delta_{i1}. \tag{4.1.16}$$

The expressions (4.1.15) and (4.1.16) satisfy the following boundary conditions for the asymptotic flow:

$$u_i^{\infty} = 0 \qquad \mathbf{x} \in S_w, \tag{4.1.17}$$

$$f_i^{\infty} = 0 \qquad \mathbf{x} \in S_\pi. \tag{4.1.18}$$

The asymptotic boundary traction is given by $f_i^{\infty} = \sigma_{ij}(p^{\infty}, u_k^{\infty})n_j$, and using (4.1.10) becomes

$$f_i^{\infty} = 2x_3(\cot\alpha n_i - n_3\delta_{i1} - n_1\delta_{i3}). \tag{4.1.19}$$

Expressions for (4.1.15), (4.1.16) and (4.1.19) govern Stokes flow down an inclined plane in the absence of obstacles, corresponding to the asymptotic far field flow configuration where obstacles are present. This film flow is used as the basis for determining conditions for a disturbance flow due to the obstacle.

Disturbance Components For Film Flow Over An Obstacles

Disturbance flow quantities are denoted by superscript δ, with velocities and pressures related to the asymptotic and complete flow variables by:

$$u_i = u_i^{\delta} + u_i^{\infty}, \tag{4.1.20}$$

$$p = p^{\delta} + p^{\infty}. \tag{4.1.21}$$

The governing equations for the disturbance regime are obtained by comparing (4.1.2) - (4.1.3) with (4.1.13) - (4.1.14) and are

$$\frac{\partial u_i^{\delta}}{\partial x_i} = 0, \tag{4.1.22}$$

$$-\frac{\partial p^{\delta}}{\partial x_i} + \frac{\partial^2 u_i^{\delta}}{\partial x_j^2} = 0. \tag{4.1.23}$$

Far field conditions for the disturbance regime require the variables to decay to zero, and flow velocity and pressure to return to the values associated with the asymptotic regime, as seen in (4.1.5). Thus u_i^δ and p^δ are subject to the following conditions in the far field:

$$\left.\begin{array}{l} u_i^\delta \to 0 \\ p^\delta \to 0 \end{array}\right\} \text{as } \mathbf{x} \to \pm\infty. \tag{4.1.24}$$

No-slip boundary conditions for the disturbance velocity u_i^δ can also be specified on the wall S_w and wetted obstacle boundary S_p by comparing (4.1.6) with (4.1.17) and requires:

$$u_i^\delta = \quad 0 \qquad\qquad \mathbf{x} \in S_w, \tag{4.1.25}$$

$$u_i^\delta = \quad -u_i^\infty \qquad\qquad \mathbf{x} \in S_p. \tag{4.1.26}$$

Finally an expression for the boundary traction associated with the disturbance flow f_i^δ can be defined on the free surface S_f by comparing (4.1.7) and (4.1.19). The expression for f_i^δ is

$$f_i^\delta = -\frac{4}{Bo}\kappa n_i - 2x_3(\cot\alpha n_i - n_3\delta_{i1} - n_1\delta_{i3}), \tag{4.1.27}$$

where κ is the curvature associated with the disturbed free surface.

Boundary Integral Formulation For Flow Over An Obstacle

For the disturbance regime, the governing equations for Stokes flow (4.1.22) - (4.1.23) can be expressed exactly as a boundary integral equation (BIE) over the fluid domain (4.1.28)

$$\begin{aligned} c_{ij}(\mathbf{x}_0)u_i^\delta(\mathbf{x}_0) = \frac{1}{8\pi}&\int\limits_{S_f\cup S_p} G_{ij}^*(\mathbf{x},\mathbf{x}_0)f_i^\delta(\mathbf{x})\mathrm{d}S(\mathbf{x}) \\ &- \frac{1}{8\pi}\int\limits_{S_f\cup S_p} u_i^\delta(\mathbf{x})T_{ijk}^*(\mathbf{x},\mathbf{x}_0)n_k(\mathbf{x})\mathrm{d}S(\mathbf{x}), \end{aligned} \tag{4.1.28}$$

where $\mathbf{x}$ is the field point within the analysis, and $\mathbf{x}_0$ any collocation point. The Green's functions $G_{ij}^*(\mathbf{x},\mathbf{x}_0)$, $T_{ijk}^*(\mathbf{x},\mathbf{x}_0)$ in (4.1.28) are the Lorentz-Blake Green's function for

velocity and stress respectively and details of their form are given in the appendix A. The flow is solved for disturbance components u_i^δ, f_i^δ and due to $f_i^\delta \to 0$ and $u_i^\delta \to 0$ as $\mathbf{x} \to \pm\infty$, it is possible to omit the edges of the flow domain from the integrations in (4.1.28). Finally, direct omission of the wall boundary S_w from the integral domains in (4.1.28) is also justified subject to the conditions,

$$\left.\begin{array}{c} G_{ij}^*(\mathbf{x},\mathbf{x}_0) = 0 \\ u_i^\delta = 0 \end{array}\right\} \mathbf{x} \in S_w. \tag{4.1.29}$$

Thus by solving for disturbance components, the solution domain is considerably reduced. Finally within (4.1.28), the coefficient $c_{ij}(\mathbf{x}_0)$ is the jump parameter and defined by

$$c_{ij}(\mathbf{x}_0) = \begin{cases} 0 & \mathbf{x}_0 \text{ outside the domain,} \\ \frac{1}{2}\delta_{ij} & \mathbf{x}_0 \text{ on the boundary of the domain,} \\ \delta_{ij} & \mathbf{x}_0 \text{ within the domain.} \end{cases} \tag{4.1.30}$$

For the obstacle domain, enclosed by a section of S_w and the wetted surface S_p, the Stokes flow (4.1.13) - (4.1.14) associated with the asymptotic regime $u_i^\infty, f_i^\infty + Gn_i$ can be satisfied by the BIE expression,

$$\begin{aligned} c_{ij}(\mathbf{x}_0)u_i^\infty(\mathbf{x}_0) = -\frac{1}{8\pi}\int_{S_p} G_{ij}^*(\mathbf{x},\mathbf{x}_0)(f_i^\infty(\mathbf{x}) + Gn_i)\mathrm{d}S(\mathbf{x}) \\ +\frac{1}{8\pi}\int_{S_p} u_i^\infty(\mathbf{x})T_{ijk}^*(\mathbf{x},\mathbf{x}_0)n_k(\mathbf{x})\mathrm{d}S(\mathbf{x}), \end{aligned} \tag{4.1.31}$$

where the unit normal is defined outward of the fluid domain, i.e. inward to the obstacle domain. Again the wall S_w is omitted by use of the Lorentz-Blake Green's functions and $u_i^\infty = 0$ for $\mathbf{x} \in S_w$. Thus the disturbance and asymptotic flow regimes are satisfied exactly by the two BIEs (4.1.28) and (4.1.31).

When the collocation point $\mathbf{x}_0$ lies outside of the obstacle domain and boundary (i.e.

$\mathbf{x}_0 \notin S_p, \Omega_p$), (4.1.31) and (4.1.30) gives,

$$\begin{aligned}\frac{1}{8\pi}\int_{S_p} G^*_{ij}(\mathbf{x},\mathbf{x}_0)(f_i^\infty(\mathbf{x}) + Gn_i)\mathrm{d}S(\mathbf{x}) \\ = \frac{1}{8\pi}\int_{S_p} u_i^\infty(\mathbf{x})T^*_{ijk}(\mathbf{x},\mathbf{x}_0)n_k(\mathbf{x})\mathrm{d}S(\mathbf{x}).\end{aligned} \tag{4.1.32}$$

The BIE (4.1.28) associated with the disturbance regime can be modified by taking collocation on the free surface ($\mathbf{x}_0 \in S_f$), and applying (4.1.26), yielding

$$\begin{aligned}\frac{1}{2}u_j^\delta(\mathbf{x}_0) = \frac{1}{8\pi}\int_{S_f} G^*_{ij}(\mathbf{x},\mathbf{x}_0)f_i^\delta(\mathbf{x})\mathrm{d}S(\mathbf{x}) \\ -\frac{1}{8\pi}\int_{S_f} u_i^\delta(\mathbf{x})T^*_{ijk}(\mathbf{x},\mathbf{x}_0)n_k(\mathbf{x})\mathrm{d}S(\mathbf{x}) \\ \frac{1}{8\pi}\int_{S_p} G^*_{ij}(\mathbf{x},\mathbf{x}_0)f_i^\delta(\mathbf{x})\mathrm{d}S(\mathbf{x}) \\ + \frac{1}{8\pi}\int_{S_p} u_i^\infty(\mathbf{x})T^*_{ijk}(\mathbf{x},\mathbf{x}_0)n_k(\mathbf{x})\mathrm{d}S(\mathbf{x}).\end{aligned} \tag{4.1.33}$$

Combining (4.1.32) and (4.1.33) gives a BIE with collocation over the free surface:

$$\begin{aligned}\frac{1}{2}u_j^\delta(\mathbf{x}_0) + \frac{1}{8\pi}\int_{S_f} u_i^\delta(\mathbf{x})T^*_{ijk}(\mathbf{x},\mathbf{x}_0)n_k(\mathbf{x})\mathrm{d}S(\mathbf{x}) \\ = \frac{1}{8\pi}\int_{S_p} G^*_{ij}(\mathbf{x},\mathbf{x}_0)\tilde{f}_i(\mathbf{x})\mathrm{d}S(\mathbf{x}) \\ +\frac{1}{8\pi}\int_{S_f} G^*_{ij}(\mathbf{x},\mathbf{x}_0)f_i^\delta(\mathbf{x})\mathrm{d}S(\mathbf{x}) \qquad \mathbf{x}_0 \in S_f,\end{aligned} \tag{4.1.34}$$

where $\tilde{f}_i(\mathbf{x}) = f_i(\mathbf{x}) + Gn_i$.

Collocating the BIE for the asymptotic regime (4.1.31) at the wetted obstacle surface $\mathbf{x}_0 \in S_p$ yields,

$$\begin{aligned}\frac{1}{2}u_j^\infty(\mathbf{x}_0) = -\frac{1}{8\pi}\int_{S_p} G^*_{ij}(\mathbf{x},\mathbf{x}_0)\tilde{f}_i^\infty(\mathbf{x})\mathrm{d}S(\mathbf{x}) \\ + \frac{1}{8\pi}\int_{S_p} u_i^\infty(\mathbf{x})T^*_{ijk}(\mathbf{x},\mathbf{x}_0)n_k(\mathbf{x})\mathrm{d}S(\mathbf{x}),\end{aligned} \tag{4.1.35}$$

where $\tilde{f}_i^{\infty}(\mathbf{x}) = f_i^{\infty}(\mathbf{x}) + Gn_i$. The disturbance BIE (4.1.28) can be collocated over the wetted obstacle surface $\mathbf{x}_0 \in S_p$, with the no slip condition (4.1.26) to form,

$$\begin{aligned} -\frac{1}{2}u_j^{\infty}(\mathbf{x}_0) = \frac{1}{8\pi}\int_{S_f} G_{ij}^*(\mathbf{x},\mathbf{x}_0) f_i^{\delta}(\mathbf{x})\mathrm{d}S(\mathbf{x}) \\ -\frac{1}{8\pi}\int_{S_f} u_i^{\delta}(\mathbf{x}) T_{ijk}^*(\mathbf{x},\mathbf{x}_0) n_k(\mathbf{x})\mathrm{d}S(\mathbf{x}) \\ +\frac{1}{8\pi}\int_{S_p} G_{ij}^*(\mathbf{x},\mathbf{x}_0) f_i^{\delta}(\mathbf{x})\mathrm{d}S(\mathbf{x}) \\ +\frac{1}{8\pi}\int_{S_p} u_i^{\infty}(\mathbf{x}) T_{ijk}^*(\mathbf{x},\mathbf{x}_0) n_k(\mathbf{x})\mathrm{d}S(\mathbf{x}). \end{aligned} \tag{4.1.36}$$

Combining (4.1.35) and (4.1.36) yields (4.1.37), a BIE for collocation over the wetted obstacle surface S_p:

$$\begin{aligned} \frac{1}{8\pi}\int_{S_p} G_{ij}^*(\mathbf{x},\mathbf{x}_0)\tilde{f}_i(\mathbf{x})\mathrm{d}S(\mathbf{x}) \\ = -u_j^{\infty}(\mathbf{x}_0) - \frac{1}{8\pi}\int_{S_f} G_{ij}^*(\mathbf{x},\mathbf{x}_0) f_i^{\delta}(\mathbf{x})\mathrm{d}S(\mathbf{x}) \\ +\frac{1}{8\pi}\int_{S_f} u_i^{\delta}(\mathbf{x}) T_{ijk}^*(\mathbf{x},\mathbf{x}_0) n_k(\mathbf{x})\mathrm{d}S(\mathbf{x}) \qquad \mathbf{x}_0 \in S_p. \end{aligned} \tag{4.1.37}$$

In summary the steady, gravity driven Stokes flow down an inclined plane over an obstacle is governed exactly by solutions satisfying the BIEs (4.1.37) and (4.1.34). The flow is subject to a kinematic condition (4.1.8), a dynamic condition (4.1.7), and far field constraints (4.1.5). Flow over a single obstacle are governed by, plane inclination angle α, the obstacle geometry, and the Bond number Bo.

4.1.1 Small Free Surface Deflections

Pozrikidis and Thoroddsen [29] and Blyth and Pozrikidis [31] simplified flow over a hemisphere through the assumption of a small free surface deflection. By assuming the free surface disturbance remains small, when compared to the undisturbed film thickness, and

the disturbance velocities at the free surface are small when compared to the undisturbed film speed at the same point then

$$h \ll 1, \qquad u_i^\delta \ll 1, \ i = 1, 2, 3. \tag{4.1.38}$$

Assuming asymptotically small disturbances, the unit normal on the free surface is approximated by

$$\mathbf{n} = (0, 0, 1) + \left(-\frac{\partial h}{\partial x_1}, -\frac{\partial h}{\partial x_2}, 0 \right), \tag{4.1.39}$$

where the components in the x_1x_2-plane are considered small. Thus,

$$\frac{\partial n_i}{\partial x_i} \approx -\frac{\partial^2 h}{\partial x_1^2} - \frac{\partial^2 h}{\partial x_2^2} \equiv -\nabla^2_{x_1x_2} h. \tag{4.1.40}$$

The disturbance boundary traction (4.1.27) approximates to,

$$f_i^\delta = 2h\delta_{i1} + \left(\frac{2}{Bo} \nabla^2_{x_1x_2} h - 2h \cot \alpha \right) \delta_{i3}, \tag{4.1.41}$$

at leading order. To the same order of approximation the kinematic condition (4.1.8) becomes

$$\frac{\partial h}{\partial t} = -\frac{\partial h}{\partial x_1} + u_i^\delta \delta_{i3}. \tag{4.1.42}$$

Finally the BIEs for flow over an obstacle,(4.1.34) and (4.1.37) simplify to integrals over the undisturbed surface S_π ($x_3 = 0$) and become,

$$\begin{aligned} \frac{1}{2} u_j^\delta(\mathbf{x}_0) + \frac{1}{8\pi} \int_{S_\pi} & u_i^\delta(\mathbf{x}) T^*_{ijk}(\mathbf{x}, \mathbf{x}_0) n_k(\mathbf{x}) \mathrm{d}S(\mathbf{x}) \\ &= \frac{1}{8\pi} \int_{S_p} G^*_{ij}(\mathbf{x}, \mathbf{x}_0) \tilde{f}_i(\mathbf{x}) \mathrm{d}S(\mathbf{x}) \\ &\quad + \frac{1}{8\pi} \int_{S_\pi} G^*_{ij}(\mathbf{x}, \mathbf{x}_0) f_i^\delta(\mathbf{x}) \mathrm{d}S(\mathbf{x}) \qquad \mathbf{x}_0 \in S_\pi, \end{aligned} \tag{4.1.43}$$

and

$$\begin{aligned} \frac{1}{8\pi} \int_{S_p} & G^*_{ij}(\mathbf{x}, \mathbf{x}_0) \tilde{f}_i(\mathbf{x}) \mathrm{d}S(\mathbf{x}) \\ &= -u_j^\infty(\mathbf{x}_0) - \frac{1}{8\pi} \int_{S_\pi} G^*_{ij}(\mathbf{x}, \mathbf{x}_0) f_i^\delta(\mathbf{x}) \mathrm{d}S(\mathbf{x}) \\ &\quad + \frac{1}{8\pi} \int_{S_\pi} u_i^\delta(\mathbf{x}) T^*_{ijk}(\mathbf{x}, \mathbf{x}_0) n_k(\mathbf{x}) \mathrm{d}S(\mathbf{x}) \qquad \mathbf{x}_0 \in S_p. \end{aligned} \tag{4.1.44}$$

Pozrikidis and Thoroddsen [29] and Blyth and Pozrikidis [31] consider this small deflection simplification in combination with finite difference approximations (FDAs) for evaluating all derivatives. However, this assumption is not relevant for finite free surface deflections as of interest here, with the small deflection analysis used only for verification with the previously published work.

4.1.2 Flow Over Asymptotically Small Obstacles

A further simplification to the boundary integral analysis can be made when the obstacle is asymptotically small. Asymptotic analysis of the obstacle is conducted by following Blyth and Pozrikidis [31] which reproduced the earlier work of Pozrikidis and Thoroddsen [29]. A brief summary of the method is reproduced here, and the reader is referred to [29, 31] for full details.

The aim of the asymptotic analysis is to produce an expression for the obstacle integral S_p, in (4.1.43), eliminating the need for solving (4.1.44). This first term of the right hand side of (4.1.43) can be rewritten using the symmetry property (2.3.21) as,

$$\frac{1}{8\pi}\int_{S_p} G^*_{ij}(\mathbf{x},\mathbf{x}_0)\tilde{f}_i(\mathbf{x})\mathrm{d}S(\mathbf{x}) = \frac{1}{8\pi}\int_{S_p} G^*_{ji}(\mathbf{x}_0,\mathbf{x})\tilde{f}_i(\mathbf{x})\mathrm{d}S(\mathbf{x}). \tag{4.1.45}$$

We consider a small spherical obstacle, with radius a and in contact with a plane wall and assume that the obstacle is much smaller than the undisturbed, non-dimensionalized film height, $a \ll 1$. Then it is possible to expand the velocity Green's function G^*_{ji} using a Taylor series with respect to d, where $d = x_3 - x_{3_{wall}} = x_3 + 1$ is the vertical distance from the point x_3 on the obstacle to the plane wall, and is illustrated in figure 4.2. The Lorentz-Blake Green's function are shown in appendix A (where h_0 is equivalent to d here), with the order of the indices and arguments shown in reverse to (4.1.45). The

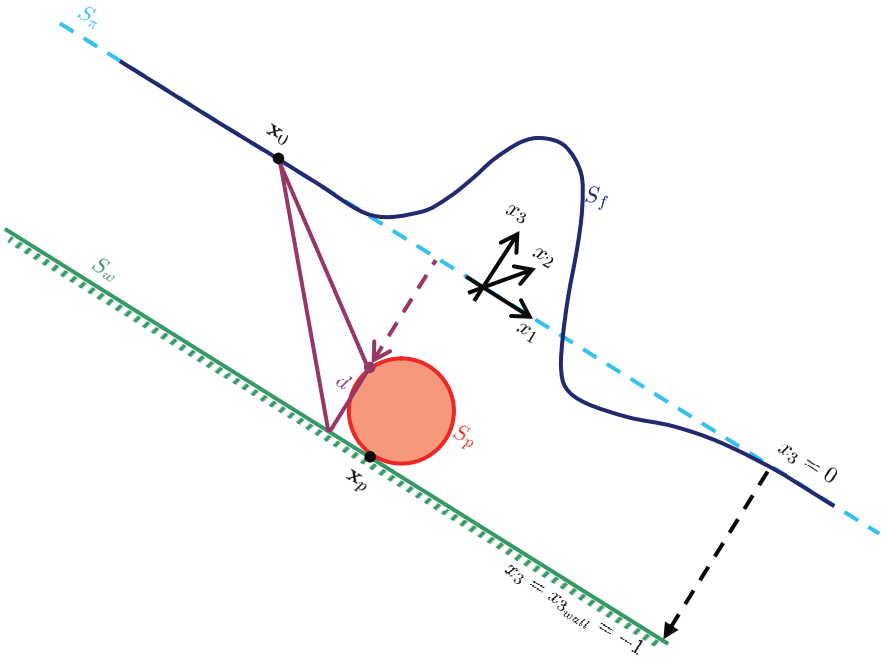

Figure 4.2: Two-dimensional cross section indicating the asymptotic formulation of the film profile.

Taylor series is written as,

$$G^*_{ji}(\mathbf{x}_0,\mathbf{x}) \approx G^*_{ji}(\mathbf{x}_0,\mathbf{x}_p) + d\,\frac{\partial}{\partial x_3}\left(G^*_{ji}(\mathbf{x}_0,\mathbf{x})\right)\Big|_{\mathbf{x}=\mathbf{x}_p} + \frac{d^2}{2}\,\frac{\partial^2}{\partial x_3^2}\left(G^*_{ji}(\mathbf{x}_0,\mathbf{x})\right)\Big|_{\mathbf{x}=\mathbf{x}_p} + \ldots, \tag{4.1.46}$$

where the non-dimensional point $\mathbf{x}_p$ is defined as

$$\mathbf{x}_p = (0,0,-1). \tag{4.1.47}$$

The case of $i = 3$ requires separate consideration to $i = 1, 2$ with the Taylor series shown to give to leading order,

$$G^*_{jm}(\mathbf{x}_0,\mathbf{x}) \approx dM_{jm}(\tilde{\mathbf{X}}) \qquad m = 1,2, \tag{4.1.48}$$

$$G^*_{j3}(\mathbf{x}_0,\mathbf{x}) \approx d^2 M_{j3}(\tilde{\mathbf{X}}), \tag{4.1.49}$$

where

$$\tilde{\mathbf{X}} = \mathbf{x}_0 - \mathbf{x}_p, \tag{4.1.50}$$

$$M_{jm}(\tilde{\mathbf{X}}) = 12\frac{\tilde{X}_m\tilde{X}_j\tilde{X}_3}{|\tilde{\mathbf{X}}|^5}, \qquad m = 1,2 \tag{4.1.51}$$

$$M_{j3}(\tilde{\mathbf{X}}) = -6\tilde{X}_3\left(\frac{2\tilde{X}_j}{|\tilde{\mathbf{X}}|^5} + \frac{\delta_{j3}\tilde{X}_3}{|\tilde{\mathbf{X}}|^5} - \frac{5\tilde{X}_3^2\tilde{X}_j}{|\tilde{\mathbf{X}}|^7}\right). \tag{4.1.52}$$

The integral (4.1.45) becomes

$$\begin{aligned}\frac{1}{8\pi}\int_{S_p} G^*_{ji}(\mathbf{x}_0,\mathbf{x})\tilde{f}_i(\mathbf{x})\mathrm{d}S(\mathbf{x}) \approx &\frac{1}{8\pi}M_{jm}(\tilde{\mathbf{X}})\int_{S_p} d\tilde{f}_m(\mathbf{x})\mathrm{d}S(\mathbf{x}) \\ &+ \frac{1}{8\pi}M_{j3}(\tilde{\mathbf{X}})\int_{S_p} d^2\tilde{f}_3(\mathbf{x})\mathrm{d}S(\mathbf{x}) \qquad m = 1,2.\end{aligned} \tag{4.1.53}$$

This is analogous to the work in [29] when the difference in the definition of the co-ordinate axis is taken into account.

From [29], the following scalings are introduced,

$$\int_{S_p} d\tilde{f}_m(\mathbf{x})\mathrm{d}S(\mathbf{x}) = -8\pi a^3 c_m \left.\frac{\partial u_x^\infty}{\partial x_3}\right|_{x_3=-1}, \qquad m = 1,2 \tag{4.1.54}$$

$$\int_{S_p} d^2\tilde{f}_3(\mathbf{x})\mathrm{d}S(\mathbf{x}) = -8\pi a^4 c_3 \left.\frac{\partial u_x^\infty}{\partial x_3}\right|_{x_3=-1}, \tag{4.1.55}$$

where the sign on the right hand side is generated from taking the outward unit normal instead of inward as specified in [29] resulting in an opposite sign for the boundary traction $\tilde{f}_i$. In (4.1.54) - (4.1.55), the distance d is taken to scale like the radius a, and the traction $\tilde{f}_i$, scales like the shear stress $\left.\frac{\partial u_x^\infty}{\partial x_3}\right|_{x_3=-1}$. Both of these are independent of the integration, which as a result yields the surface area of a sphere $4\pi a^2$. For equality, a constant vector $2c_3$ and $2c_m$, $m = 1,2$ is required and depends on the geometry of the obstacle. For the case of a spherical obstacle the terms of $\mathbf{c}$ are given by the work of [29], which extracts them from O'Neill [48] and gives them to be,

$$c_1 = -\frac{1}{6}\int_0^\infty A(s)\left(3 - 8s\coth s + 7\frac{s^2}{\sinh^2 s} - 2\frac{s^3}{\sinh^2 s}\coth s\right)\mathrm{d}s, \tag{4.1.56}$$

$$c_2 = 0, \tag{4.1.57}$$

$$c_3 = 0, \tag{4.1.58}$$

where values of $A(s)$ are tabulated in [48]. From [29], the constant c_1 is given as 1.8. However, when considering results produced using this asymptotic method, flow profiles appear sensitive to small changes in the parameter c_1. The value of $c_1 = 1.8$ in Pozrikidis and Thoroddsen [29] is likely to be rounded, and as a result the value of c_1 has been recalculated. The calculation involved truncating the domain of integration of (4.1.56) and used the trapezium rule. Values for $A(s)$ are tabulated in [48] where they were obtained numerically. It is found here that,

$$c_1 = 1.760677101. \tag{4.1.59}$$

For an asymptotically small, spherical obstacle with non-dimensional radius $a \ll 1$, it is clear that the right hand side of equation (4.1.55) is small compared to the corresponding term in (4.1.54). In addition the values for $\mathbf{c}$ are defined in (4.1.57) - (4.1.59), and equation (4.1.53) is approximated by,

$$\frac{1}{8\pi}\int\limits_{S_p} G^*_{ji}(\mathbf{x}_0,\mathbf{x})\tilde{f}_i(\mathbf{x})\mathrm{d}S(\mathbf{x}) \approx -M_{j1}(\tilde{\mathbf{X}})a^3c_1\left.\frac{\partial u^\infty_x}{\partial x_3}\right|_{x_3=-1}, \tag{4.1.60}$$

with the derivative on the right hand side of (4.1.60) evaluated as,

$$\left.\frac{\partial u^\infty_x}{\partial x_3}\right|_{x_3=-1} = 2, \tag{4.1.61}$$

using (4.1.16). Therefore substituting back into the original BIE for collocation over the free surface (4.1.43) yields,

$$\begin{aligned}\frac{1}{2}u^\delta_j(\mathbf{x}_0) =& -2a^3c_1M_{j1}(\mathbf{x}_0-\mathbf{x}_p)\\ &+\frac{1}{8\pi}\int\limits_{S_f} G^*_{ij}(\mathbf{x},\mathbf{x}_0)f^\delta_i(\mathbf{x})\mathrm{d}S(\mathbf{x})\\ &-\frac{1}{8\pi}\int\limits_{S_f} u^\delta_i(\mathbf{x})T^*_{ijk}(\mathbf{x},\mathbf{x}_0)n_k(\mathbf{x})\mathrm{d}S(\mathbf{x}) \qquad \mathbf{x}_0\in S_f.\end{aligned} \tag{4.1.62}$$

4.2 Numerical Schemes

This section considers the numerical schemes implemented to obtain solutions to the flow problem outlined in §4.1. The formulation of the film flow takes three possible forms:

(i) A "full" film profile analysis.

(ii) A small free surface deflection approach.

(iii) An asymptotically small obstacle analysis using the small free surface deflection approach.

For case (i) the flow problem is to be evaluated numerically for u_i^δ on S_f and $\tilde{f}_i$ on S_p. The necessary equations to be solved involve the kinematic and dynamic conditions (4.1.8) and (4.1.7) on the free surface S_f, and the two boundary integral equations (BIEs) (4.1.37) and (4.1.34) for flow over a single obstacle. In addition the the far field boundary conditions (4.1.5) are also required.

For case (ii) when the free surface deflection is limited, a finite difference approximation (FDA) is used for evaluation of the free surface quantities [29, 31]. The numerical scheme can be formulated into a completely closed system, to be solved once for the free surface displacement h, disturbance velocity components u_1^δ, u_2^δ and the obstacle tractions $\tilde{f}_i$. This is similar to Blyth and Pozrikidis [31], where the formulation generates two matrix problems, one for solution of the free surface variables u_1^δ, u_2^δ and h, the other for obstacle tractions $\tilde{f}_i$. The final solution can then be found by iterating between them.

When the free surface deflection is limited, results analyzing the effects of an asymptotically small obstacle on the film profile can be found. In this case (iii) a limited free surface deflection analysis is implemented throughout, with the system of BIEs (4.1.43) and (4.1.44) reduced by approximating the integral over the obstacle within the free surface BIE (4.1.43) by an analytical expression (see (4.1.62)).

Unlike the linearized free surface film flow problem, which can be solved once for all unknowns, case (i) requires solution in a transient manner. A Hermitian radial basis function (RBF) is introduced and evaluated for the surface quantities, with more details given later. It is found that it is more efficient to solve the coupled system of BIEs iteratively, although they could be solved in one calculation for each time-step. The

iterative sequence used was:

(i) Guess an initial film profile and disturbance velocities for the free surface.

(ii) Calculate the disturbance boundary traction using the dynamic condition (4.1.7).

(iii) Use the obstacle BIE (4.1.37) to calculate the boundary tractions on the obstacle, $\tilde{f}_i$.

(iv) Use the free surface BIE (4.1.34) to calculate a new set of disturbance velocities on the film surface.

(v) Via the kinematic condition (4.1.8) and using a forward finite difference, the free surface position is iterated in time.

(vi) Repeat from step 2 using the new film profile and disturbance velocity profile for the free surface, until the surface has reached a steady profile.

The BIEs were solved using a boundary element method (BEM) on the discretized surfaces and the implementation of this method is discussed below. In addition through the remainder of this section, the use of FDAs and a Hermitian RBF for evaluating the free surface curvature and outward unit normal are considered.

4.2.1 Surface Discretizations And The Boundary Element Method

For numerical solutions, the obstacle boundary and free surface require discretizing and in this chapter, hemispherical and spherical objects were considered. The hemispherical obstacle mesh is generated by a method of successive subdivision and consists of linear triangular elements. Spherical obstacles were meshed by reflective symmetry of the hemispherical discretization. Figure 4.3 indicates typical meshes for the hemispherical obstacles considered throughout this work.

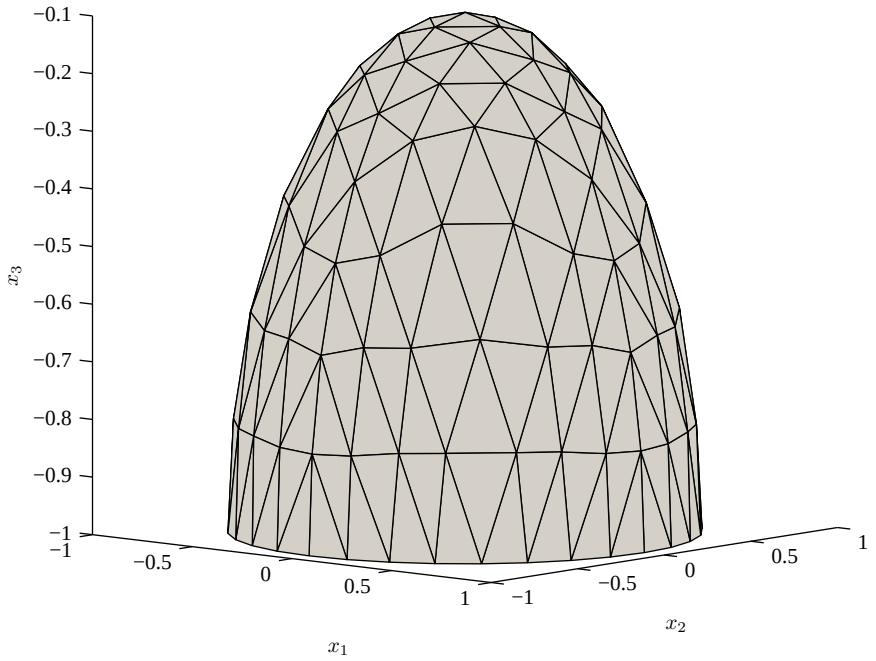

Figure 4.3: Typical mesh for a hemispherical obstacle of radius $a = 0.9$.

For the simplest case of small film deflection, the free surface is discretized using a set of uniform, linear rectangular elements. However, when the free surface requires discretizing fully, rectangular elements are insufficient for the mesh and linear triangular elements are used. Triangular elements were formed by first subdividing the free surface domain into a set of rectangular elements, and then for each element connecting the diagonal vertices to form four sub-triangular linear elements. Free surface elements are referred to as $m \times n$, where for a rectangular mesh m is the number of elements in the x_1 direction and n the number of elements in the x_2 direction. For a triangular mesh of $m \times n$, the free surface is first divided into a $m/2 \times n/2$ rectangular mesh and further subdivisions to create the triangular elements are carried out as described above. A schematic of typical free surface discretizations using rectangular and triangular elements are shown in figure 4.4.

The BEM was used to solve each of the BIEs within the problem. The velocity and traction variables were assumed constant over each element, and values assigned at the

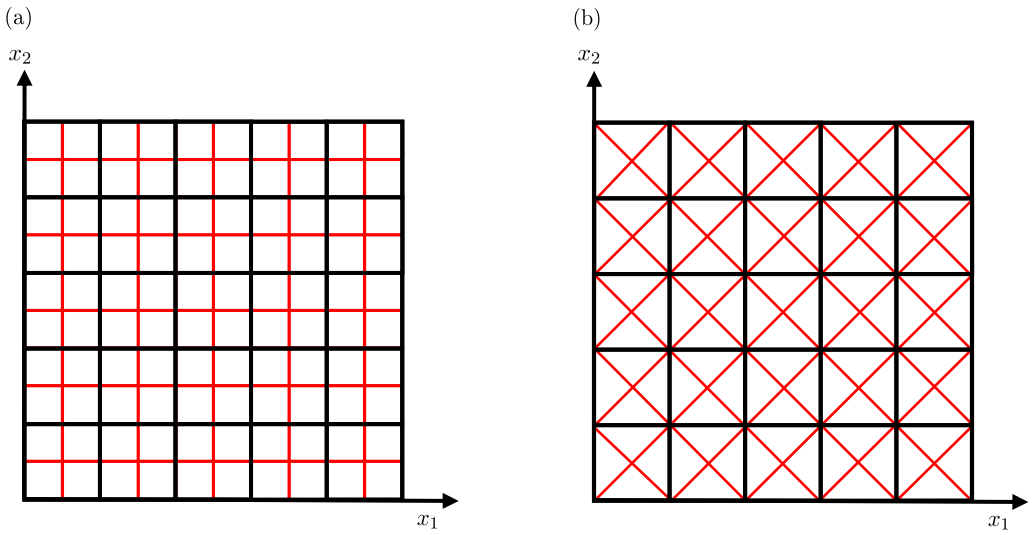

Figure 4.4: Typical mesh for the free surface using (a) rectangular elements, and (b) triangular elements.

midpoint of the elements. To avoid difficulty in the re-meshing of the surface with every time-step the velocities and tractions were found at the element midpoints and these midpoints are repositioned in the x_3 direction at every time step. Movement of the element nodal points was achieved by fitting a Hermitian RBF through the new midpoints and finding the corresponding new nodal locations for each element. It is noted that the data point is displaced from the new linear elements midpoint and a small error occurs within the BEM approximation. Globally the accurate midpoint heights are used when evaluating the kinematic and dynamic boundary conditions, but the approximated midpoint heights (from the linear element mesh) are used for collocation within the BEM.

4.2.2 Integration Techniques And Near Point Singularities

Standard numerical integration regimes for the stress and velocity Green's functions over the linear elements were conducted. A 4-point Gaussian quadrature scheme was used for the rectangular elements and 3-point for the triangular elements. The velocity Green's

function on singular elements was integrated using the polar integration rule. For larger obstacles that approach the free surface, the BIEs eventually fail numerically due to near-point singularities. This problem is common when modelling thin structures and gaps using conventional BEMs. As outlined by Krishnasamy et al. [49], two difficulties arise from the standard BIEs when considering thin bodies. These are,

(i) As the gap between two surfaces reduces, the BIEs tend to form an ill condition coefficient matrix.

(ii) The integrals become nearly singular and difficult to evaluate accurately using standard numerical integration schemes.

Krishnasamy et al. [49] notes that achieving a suitable integration technique to solve the problem of nearly singular integrals allows limited success with thin shapes. For very thin shapes, the ill conditioning eventually becomes too severe for the conventional BIE to be applicable in solving the problem. However for the film flows considered in this paper, the severity of reduced thickness necessary to cause ill-conditioning effects are physically unrealistic.

Several techniques are reported in the literature to deal with near-singular integration. They include element subdivision Lachat and Watson [50], adaptive Gaussian integration Hayami [51], variable transformation techniques and semi-analytical integration based on series expansions and removal of singularities, Mi and Aliabadi [52], besides others. In this work, the effects of ill conditioning are not considered and improvements in the numerical integration scheme follow a method similar to that outlined in Cutanda et al. [53], and consists of a combination of the adaptive Gaussian integration algorithm and the element subdivision approach. The approach of Cutanda et al. [53] to deal with near-singular integrals was chosen due to its simplicity of formulation, although it is known that some other approaches, such as variable transformation and semi-analytical integration, are numerically more efficient.

The distance, d, between the singular point and the linear triangular element of integration was first evaluated. Standard integration was conducted via a 3-point triangular Gaussian quadrature method. Integration refinement was used depending on the distance d and the successive threshold distances as shown in table 4.2. If the distance was below a certain threshold, d_1, then 6-point triangular Gaussian quadrature was used. If the distance was less than d_2, 9-point Gaussian integration was used and if the distance was less than d_3, 13-point Gaussian integration was used.

However, increasing the order of integration gives only limited improvement on the thinness of gap that can be modelled [53]. Using the 13-point integration technique, a method of subdivision is required. The method chosen followed a similar manner to the geometrical successive sub-division used in discretizing the hemispherical and spherical obstacles. If the distance between the integration element and singularity was less than d_4, then the element was split into four theoretical sub elements. The distance between each sub element and the singularity was then tested and if less than a distance d_5, then the sub element is split into four theoretical sub-sub triangular elements. This method is repeated for up to five consecutive sub divisions and if the whole element was discretized to the maximum it would be sub-divided into 4^5 integration regions. This has the added benefit of only increasing the numerical computation in the required regions.

This approach requires finding suitable values for the distances d_i where $i = 1, \ldots, 8$ and the values used are shown in table 4.2 after an extensive convergence analysis has been conducted. The computational time associated with calculating the distance between element and singularity and subsequent adjustments was not excessive on the computational run-time of the simulation and is significantly advantageous over using a high order integration technique applied for all elements.

Bounding Point	d_1	d_2	d_3	d_4	d_5	d_6	d_7	d_8
Bounding Value	0.6	0.45	0.3	0.2	0.15	0.1	0.0316	0.01

Table 4.2: Boundary values used to determine which numerical integration approach to implement.

4.2.3 Finite Difference Approximations

The FDAs are used solely for the small free surface disturbance to describe the surface derivatives needed for calculation of the unit normal and curvature. The FDAs utilized are identical to those implemented in Blyth and Pozrikidis [31]. When calculating the free surface curvature, (4.1.40) will be evaluated using a central difference about the midpoint values and is given by

$$\begin{aligned}\nabla^2_{x_1x_2}(x_1^i, x_2^j) =& \frac{h(x_1^{i+1}, x_2^j) - 2h(x_1^i, x_2^j) + h(x_1^{i-1}, x_2^j)}{(\Delta x_1)^2} \\ &+ \frac{h(x_1^i, x_2^{j+1}) - 2h(x_1^i, x_2^j) + h(x_1^i, x_2^{j-1})}{(\Delta x_2)^2},\end{aligned} \tag{4.2.1}$$

where superscripts i,j are associated with the x_1,x_2 distribution of the element midpoints.

The spacial derivative associated with (4.1.42) should be evaluated using a backward difference to avoid spurious oscillations [31] and is

$$\frac{\partial h(x_1^i, x_2^j)}{\partial x_1} = \frac{h(x_1^i, x_2^j) - h(x_1^{i-1}, x_2^j)}{(\Delta x_1)}. \tag{4.2.2}$$

Special care is required for any midpoint height used outside the discretized domain. Two options are available, implementing the far field condition for h from (4.1.5) will take a value of zero for any imaginary node outside the domain, whereas implementing conditions for $\frac{\partial h}{\partial x_1}$ and $\frac{\partial h}{\partial x_2}$ from (4.1.5), takes any node outside the domain to have the same height as its image node within the domain.

4.2.4 Finite Free Surface Deflections And Radial Basis Functions

For finite free surface deflections, accurate evaluation of the unit normal and curvature as defined in equations (4.1.11) and (4.1.12) using FDAs is difficult. Thus a RBF can be used to interpolate a set of data points contained within a domain, and by use of a Hermite RBF the boundary conditions also applied. At any point on the free surface, the height is given by $h(x_1, x_2)$, and takes values h^i at data point i for a total of N points. The surface can then be interpolated using the RBF $\psi(\|\mathbf{x} - \boldsymbol{\xi}^j\|)$, where $j = 1, \ldots, N$ and $\boldsymbol{\xi}^j$ are the x_1, x_2 co-ordinates of the data points h^j.

A choice of thin plate splines was used for the RBF. The addition of a polynomial is required to guarantee invertibility when using a thin plate spline since it is known that the generalized thin plate spline of power $(2m-2)$ is a conditionally positive definite function of order m. Thus it requires the addition of a polynomial term of order $m-1$, together with a homogeneous constraint condition, in order to obtain an invertible interpolation matrix. In our case, we are using $m = 3$ requiring a second order polynomial and the thin plate spline RBF takes the form

$$\psi = r^{2m-2} \log r, \tag{4.2.3}$$

where

$$r = \|\mathbf{x} - \boldsymbol{\xi}\|. \tag{4.2.4}$$

A value of $m = 3$ avoids singularities at $r = 0$ for up to and including the third order derivatives of ψ and as stated in La Rocca et al. [41] minimizes the interpolation matrix becoming more ill-conditioned.

The values of $\frac{\partial h}{\partial x_1}$ and $\frac{\partial h}{\partial x_2}$ can be constrained at a selected set of n data points (such as the far field locations where the gradients are set to zero), whilst still defining h on the original N data points. A solution for h can be obtained using the differential operators $\frac{\partial}{\partial x_1}$ and $\frac{\partial}{\partial x_2}$ but acting on the thin plate splines second argument $\boldsymbol{\xi}$, i.e. $\frac{\partial}{\partial \xi_1}$ and $\frac{\partial}{\partial \xi_2}$. A

representation for the surface displacement becomes,

$$h(x_1^i, x_2^i) = \sum_{j=1}^{N} \lambda_j \psi + \sum_{j=1}^{n} \lambda_{N+j} \frac{\partial \psi}{\partial \xi_1} + \sum_{j=1}^{n} \lambda_{N+n+j} \frac{\partial \psi}{\partial \xi_2} + P_2(\mathbf{x}), \tag{4.2.5}$$

where $\psi = \psi(\|\mathbf{x}^i - \boldsymbol{\xi}^j\|)$ and

$$\begin{aligned} P_2(\mathbf{x}^i) = \lambda_{N+n+n+1}(x_1^i)^2 + \lambda_{N+n+n+2} x_1^i x_2^i + \lambda_{N+n+n+3}(x_2^i)^2 + \\ + \lambda_{N+n+n+4} x_1^i + \lambda_{N+n+n+5} x_2^i + \lambda_{N+n+n+6}, \end{aligned} \tag{4.2.6}$$

is a polynomial which also satisfies a homogeneous constraint condition.

The first order derivatives of h with respect to x_1 and x_2 are required for constraining the far field conditions and given by

$$\begin{aligned} \frac{\partial h}{\partial x_1} = \sum_{j=1}^{N} \lambda_j \frac{\partial \psi}{\partial x_1} + \sum_{j=1}^{n} \lambda_{N+j} \frac{\partial^2 \psi}{\partial \xi_1 \partial x_1} \\ + \sum_{j=1}^{n} \lambda_{N+n+j} \frac{\partial^2 \psi}{\partial \xi_2 \partial x_1} + \frac{\partial P_2(\mathbf{x})}{\partial x_1}, \end{aligned} \tag{4.2.7}$$

$$\begin{aligned} \frac{\partial h}{\partial x_2} = \sum_{j=1}^{N} \lambda_j \frac{\partial \psi}{\partial x_2} + \sum_{j=1}^{n} \lambda_{N+j} \frac{\partial^2 \psi}{\partial \xi_1 \partial x_2} \\ + \sum_{j=1}^{n} \lambda_{N+n+j} \frac{\partial^2 \psi}{\partial \xi_2 \partial x_2} + \frac{\partial P_2(\mathbf{x})}{\partial x_2}. \end{aligned} \tag{4.2.8}$$

Expressions (4.2.5) - (4.2.8) can be used to formulate a matrix representation $\tilde{h}_i = A_{ij}\lambda_j$ given by,

$$A_{ij} = \begin{pmatrix} \psi & \frac{\partial \psi}{\partial \xi_1} & \frac{\partial \psi}{\partial \xi_2} & P_2 \\ \frac{\partial \psi}{\partial x_1} & \frac{\partial^2 \psi}{\partial \xi_1 \partial x_1} & \frac{\partial^2 \psi}{\partial \xi_2 \partial x_1} & \frac{\partial P_2}{\partial x_1} \\ \frac{\partial \psi}{\partial x_2} & \frac{\partial^2 \psi}{\partial \xi_1 \partial x_2} & \frac{\partial^2 \psi}{\partial \xi_2 \partial x_2} & \frac{\partial P_2}{\partial x_2} \\ (P_2)^T & (\frac{\partial P_2}{\partial x_1})^T & (\frac{\partial P_2}{\partial x_2})^T & 0 \end{pmatrix} \tag{4.2.9}$$

where $\tilde{h}_i$ is given by,

$$\tilde{h}_i = \begin{pmatrix} h & \frac{\partial h}{\partial x_1} & \frac{\partial h}{\partial x_2} & 0 \end{pmatrix}^T. \tag{4.2.10}$$

This system must be solved to find the vector λ_j.

Once the system has been solved for λ_j, the RBF can be evaluated for the outward unit normal and mean curvature of the free surface. Evaluation of the unit normal will require derivatives $\frac{\partial h}{\partial x_1}$ and $\frac{\partial h}{\partial x_2}$, with the mean curvature needing in addition, $\frac{\partial^2 h}{\partial x_1^2}$, $\frac{\partial^2 h}{\partial x_2^2}$, and $\frac{\partial^2 h}{\partial x_1 \partial x_2}$ on the surface. The evaluation of these derivatives simply involve the finding of specific derivatives of ψ. The values of h, $\frac{\partial h}{\partial x_1}$ and $\frac{\partial h}{\partial x_2}$ are determined by (4.2.5) - (4.2.8). The corresponding second order derivatives are given by

$$\begin{aligned}\frac{\partial^2 h}{\partial x_1^2} = &\sum_{j=1}^{N} \lambda_j \frac{\partial^2 \psi}{\partial x_1^2} + \sum_{j=1}^{n} \lambda_{N+j} \frac{\partial^3 \psi}{\partial \xi_1 \partial x_1^2} \\ &+ \sum_{j=1}^{n} \lambda_{N+n+j} \frac{\partial^3 \psi}{\partial \xi_2 \partial x_1^2} + \frac{\partial^2 P_2(\mathbf{x})}{\partial x_1^2},\end{aligned} \tag{4.2.11}$$

$$\begin{aligned}\frac{\partial^2 h}{\partial x_2^2} = &\sum_{j=1}^{N} \lambda_j \frac{\partial^2 \psi}{\partial x_1^2} + \sum_{j=1}^{n} \lambda_{N+j} \frac{\partial^3 \psi}{\partial \xi_1 \partial x_2^2} \\ &+ \sum_{j=1}^{n} \lambda_{N+n+j} \frac{\partial^3 \psi}{\partial \xi_2 \partial x_2^2} + \frac{\partial^2 P_2(\mathbf{x})}{\partial x_2^2},\end{aligned} \tag{4.2.12}$$

$$\begin{aligned}\frac{\partial^2 h}{\partial x_1 \partial x_2} = &\sum_{j=1}^{N} \lambda_j \frac{\partial^2 \psi}{\partial x_1 \partial x_2} + \sum_{j=1}^{n} \lambda_{N+j} \frac{\partial^3 \psi}{\partial \xi_1 \partial x_1 \partial x_2} \\ &+ \sum_{j=1}^{n} \lambda_{N+n+j} \frac{\partial^3 \psi}{\partial \xi_2 \partial x_1 \partial x_2} + \frac{\partial^2 P_2(\mathbf{x})}{\partial x_1 \partial x_2}.\end{aligned} \tag{4.2.13}$$

When implementing the thin plate spline RBF (4.2.3) for the interpolation of the free surface, the following derivatives of ψ are required

$$\frac{\partial \psi}{\partial \xi_1} = -r^2(2\log(r^2)+1)(x_1-\xi_1), \tag{4.2.14}$$

$$\frac{\partial \psi}{\partial \xi_2} = -r^2(2\log(r^2)+1)(x_2-\xi_2), \tag{4.2.15}$$

$$\frac{\partial \psi}{\partial x_1} = r^2(2\log(r^2)+1)(x_1-\xi_1), \tag{4.2.16}$$

$$\frac{\partial \psi}{\partial x_2} = r^2(2\log(r^2)+1)(x_2-\xi_2), \tag{4.2.17}$$

$$\frac{\partial^2 \psi}{\partial \xi_1 \partial x_1} = -(x_1-\xi_1)^2(4\log(r^2)+6) - r^2(2\log(r^2)+1), \tag{4.2.18}$$

$$\frac{\partial^2\psi}{\partial\xi_2\partial x_1} = -(x_1-\xi_1)(x_2-\xi_2)(4\log(r^2)+6), \tag{4.2.19}$$

$$\frac{\partial^2\psi}{\partial\xi_1\partial x_2} = -(x_1-\xi_1)(x_2-\xi_2)(4\log(r^2)+6), \tag{4.2.20}$$

$$\frac{\partial^2\psi}{\partial\xi_2\partial x_2} = -(x_2-\xi_2)^2(4\log(r^2)+6) - r^2(2\log(r^2)+1), \tag{4.2.21}$$

$$\frac{\partial^2\psi}{\partial x_1^2} = r^2(2\log(r^2)+1) + (x_1-\xi_1)^2(4\log(r^2)+6), \tag{4.2.22}$$

$$\frac{\partial^2\psi}{\partial x_2^2} = r^2(2\log(r^2)+1) + (x_2-\xi_2)^2(4\log(r^2)+6), \tag{4.2.23}$$

$$\frac{\partial^2\psi}{\partial x_1\partial x_2} = (x_2-\xi_2)(x_1-\xi_1)(4\log(r^2)+6), \tag{4.2.24}$$

$$\frac{\partial^3\psi}{\partial\xi_1\partial x_1^2} = -3(x_1-\xi_1)(4\log(r^2)+6) - 8\frac{(x_1-\xi_1)^3}{r^2}, \tag{4.2.25}$$

$$\frac{\partial^3\psi}{\partial\xi_2\partial x_1^2} = -(x_2-\xi_2)\left(4\log(r^2)+6+8\frac{(x_1-\xi_1)^2}{r^2}\right), \tag{4.2.26}$$

$$\frac{\partial^3\psi}{\partial\xi_1\partial x_2^2} = -(x_1-\xi_1)\left(4\log(r^2)+6+8\frac{(x_2-\xi_2)^2}{r^2}\right), \tag{4.2.27}$$

$$\frac{\partial^3\psi}{\partial\xi_2\partial x_2^2} = -3(x_2-\xi_2)(4\log(r^2)+6) - 8\frac{(x_2-\xi_2)^3}{r^2}, \tag{4.2.28}$$

$$\frac{\partial^3\psi}{\partial\xi_1\partial x_1\partial x_2} = -(x_2-\xi_2)\left(4\log(r^2)+6+8\frac{(x_1-\xi_1)^2}{r^2}\right), \tag{4.2.29}$$

$$\frac{\partial^3\psi}{\partial\xi_2\partial x_1\partial x_2} = -(x_1-\xi_1)\left(4\log(r^2)+6+8\frac{(x_2-\xi_2)^2}{r^2}\right). \tag{4.2.30}$$

4.3 Solution Profiles For Flow Over An Obstacle

Simulations of flow computations over single obstacles and corresponding numerical details are described in this section, each identifying different aspects of the numerical method.

Results are initially produced illustrating the effects of implementing a Hermitian radial basis function (RBF) for the free surface compared with the finite difference approximations (FDAs) used in [29, 31]. Blyth and Pozrikidis [31] produced figures for an inverse

Bond number B, related to Bo by

$$Bo = \frac{\sin^{1/3}\alpha}{B}, \tag{4.3.1}$$

and to allow comparison of results, appropriate solutions are given in terms of the inverse Bond number B. Results are also reproduced from Blyth and Pozrikidis [31], using a global RBF with the limitation of a small amplitude free surface deflection and the asymptotic obstacle analysis where appropriate. Consistency of results is found between the full obstacle and asymptotic analysis.

The assumption of small free surface deflection is then removed and results for the finite deflection approach presented for significant film deformations generated by large hemispherical obstacles. An example of particular interest is where the fluid film can fully contain an obstacle that is taller than the undisturbed film height.

4.3.1 Small Free Surface Deflections

This section considers implementation of a global Hermitian RBF for finding the unit normal and curvature of the free surface. Comparisons are made with the FDAs used in the published work by Pozrikidis and Thoroddsen [29] and Blyth and Pozrikidis [31]. Flow down an inclined plane over a hemispherical obstacle is considered using the small free surface deflection restriction. The RBF analysis is to be solved transiently, to converge to a steady state profile. For illustration, calculation is taken for flow over hemispherical obstacles of radius $a = 0.2$, a Bond number of $Bo = 0.89$, ($B = 1$) and the plane is inclined at $\alpha = 45^o$. A suitable choice for the size of the free surface domain is required such that the far field conditions (4.1.5) are accurately represented on the edges of the domain. The choice of free surface domain was made by initially solving the problem for large far field distances, and progressively reducing these truncation points. The optimum free surface domain was one that minimized the area that required discretization, whilst maintaining accurate representation of the free surface profile. For this flow problem, it was found that the free surface should be solved within the domain

$-6 \leq x_1 \leq 8$, $-6 \leq x_2 \leq 6$. Similar analysis are conducted to find suitable far field truncation values when other flow parameters are chosen. The hemispherical obstacle was discretized using 256 linear triangular elements in all cases, with the level of free surface discretization varied between results. The far field boundary condition of zero gradients was imposed throughout. For consistency with the FDAs, the far field condition was applied at the element midpoints within the RBF of any element containing a boundary node. This implementation will be improved for later results. Solutions are interpolated to the centre line using a cubic spline for the FDA implementation and the global RBF interpolation when implemented for the normal and curvature. A 4-point Gaussian quadrature is used for the numerical integration over rectangular elements, with a 3-point scheme implemented over triangular elements.

Figure 4.5a illustrates the centre line solutions for a free surface mesh resolution of 56×48. The solutions are produced using both a RBF and FDA analysis for the free surface normal and curvature. The main difference between the RBF and FDA solution is the difference in peak height and trough depth. In addition, there is a marginal shift of the centre line profile downstream when using the RBF interpolation. Figure 4.5b illustrates the difference in surface position along the centre line for two free surface rectangular mesh resolutions, 56×48 and 28×24. The solutions for the two RBF meshes seem to compare more favourably than the corresponding solutions found when implementing FDAs. The RBF interpolation predicts the surface almost identically (especially in the far field), regardless of which resolution of mesh is used for the BIEs. The FDA solution seems to exhibit a marginal shift downstream with increase in mesh resolution, with the peak slightly higher.

Corresponding to Figure 4.5, a full three-dimensional profile for the RBF solution of flow over a hemisphere using the more refined mesh of 56×48 elements is shown in Figure 4.6. As expected the flow profile is symmetric, producing a large upstream peak, which collapses into a shallow trough downstream of the obstacle. The peak decays in a "horseshoe" shape fashion.

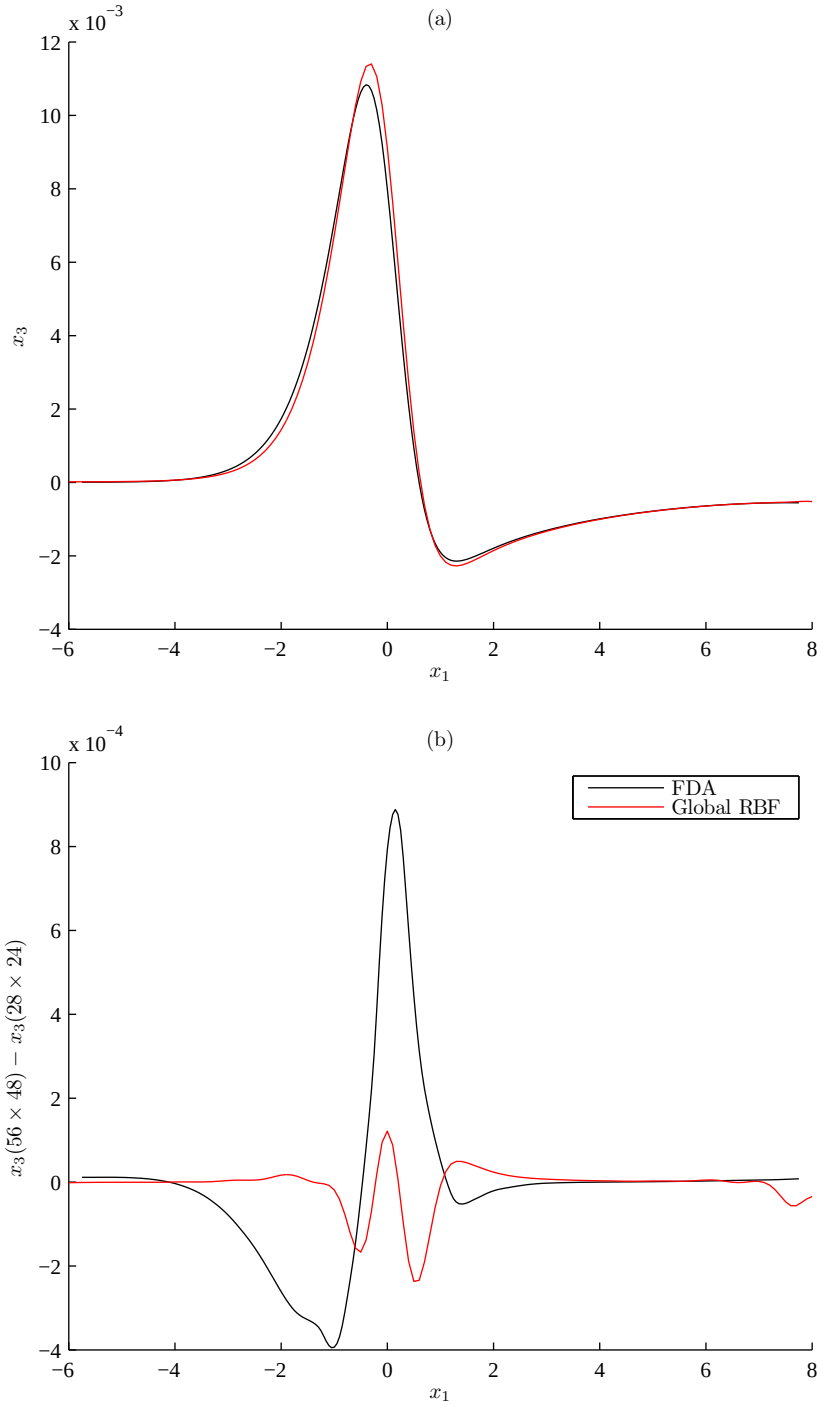

Figure 4.5: Centre line solutions produced by the small deflection assumption for the free surface comparing (a) results for the RBF interpolation compared with a FDA approximation for a 56×48 mesh and (b) the relative errors between using a 56×48 and a 28×24 for the free surface mesh.

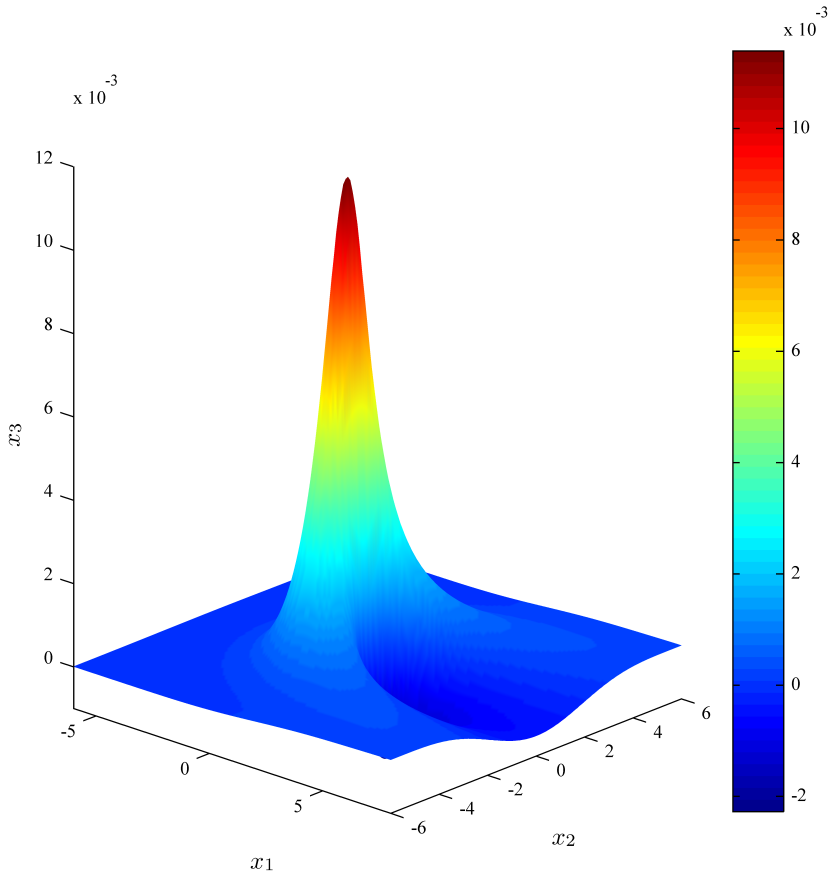

Figure 4.6: The full three-dimensional flow profile for film flow over a hemisphere of radius $a = 0.2$. The flow has a Bond number of $Bo = 0.89$, $(B = 1)$ and the plane is inclined at $\alpha = 45^o$.

Results corresponding to Blyth and Pozrikidis [31] (their Fig 10 and Fig 8) are shown in the centre line solutions ($x_2 = 0$) of figures 4.7 - 4.9 utilizing a free surface discretized by 49×49 elements for the domain $-8 \leq x_1 \leq 10$ and $-9 \leq x_2 \leq 9$. The free surface profiles are smoothed by the RBF interpolation implemented for the free surface curvature and unit normal. Solution variations caused by the obstacle mesh were found to be sufficiently eliminated after four successive subdivisions, resulting in 256 elements for the hemispherical obstacle and 512 for the spherical obstacle. This is identical to the number of quadratic elements used by Blyth and Pozrikidis [31]. Again, the far field condition of zero gradients was imposed throughout at the element midpoints within the RBF.

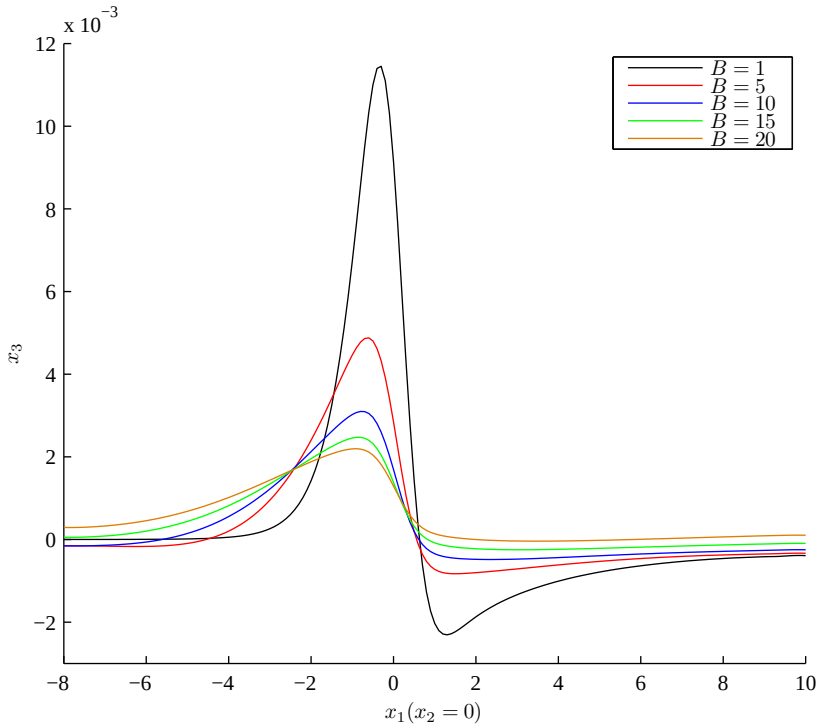

Figure 4.7: Centre line solutions for a selection of inverse Bond numbers, using the assumption of small free surface deflection. The plane is inclined at 45^o and the hemispherical obstacle has radius $a = 0.2$.

Figure 4.7 allows comparison with Blyth and Pozrikidis [31] (their Fig 10a) for flow down an inclined plane at 45^o over a hemisphere of radius $a = 0.2$. As the inverse Bond number is increased, surface tension forces are increased in comparison to the gravitational forces and acts to flatten any surface deformation. With this increase in the value of B the peak of the flow appears to migrate slightly upstream. A comparison to the results of Blyth and Pozrikidis [31] (their Fig 10a) shows that, although the qualitative behaviour is the same, current results exhibit a larger peak. Taking $B = 1$, the percentage difference of peak heights between the FDA and RBF models is approximately 24% as estimated from the FDA solution presented in [31]. It is thought that this difference in the film profile is caused by the differing far field conditions used within the FDA of [31] and the RBF analysis presented in this Thesis. Within [31] the zero deflection far field condition is implemented, which can cause irregularities of the film profile at the far field truncation

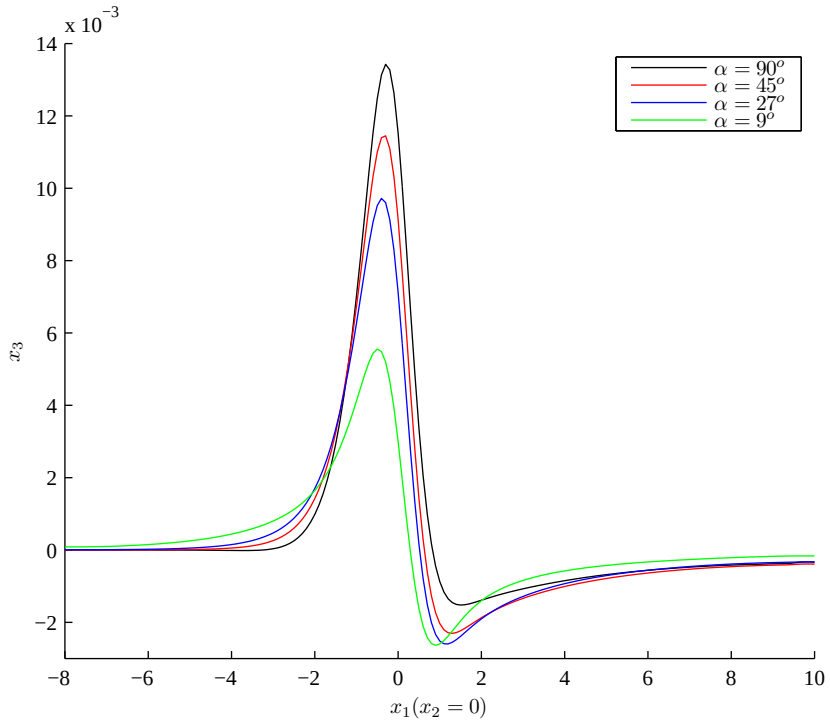

Figure 4.8: Centre line solutions for a selection of wall inclinations, using the assumption of small free surface deflection. The flow has an inverse Bond number $B = 1$ and the hemispherical obstacle has radius $a = 0.2$.

point if the condition is not sufficiently satisfied. This problem is eliminated by using the zero derivative condition within the RBF analysis, which offers a more consistent approximation in the far field. Implementing the zero derivative far field condition within both the FDA and RBF method, yields more consistent results as can be seen in figure 4.5a.

Figure 4.8 illustrates solutions for a selection of inclination angles for a flow with an inverse Bond number $B = 1$ and hemispherical obstacle of radius $a = 0.2$. Increasing the inclination angle has the effect of increasing the peak size and decreasing the trough size behind the obstacle. Although the peak location is relatively unaffected by the inclination angles, the downstream trough is seen to migrate upstream as the angle is reduced. This is in agreement with Blyth and Pozrikidis [31] (their Fig10b) as a direct comparison with this work. Again it is seen that results in figure 4.8 using the RBF interpolation exhibit

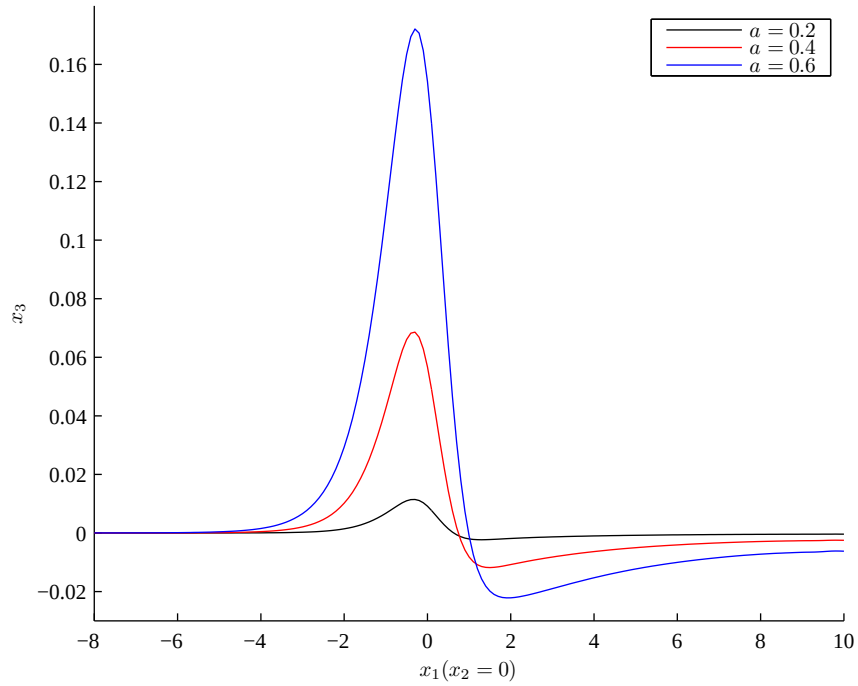

Figure 4.9: Centre line solutions for a selection of hemisphere radii, using the assumption of small free surface deflection. The flow has an inverse Bond number $B = 1$ and is along an inclined plane at 45^o.

a larger peak then those in [31]. The percentage difference of peak heights for $\alpha = 90^o$ between the RBF and FDA models is approximately 18%, obtained by estimation of the FDA film profile from [31]. As for figure 4.7, these differences are likely to be caused by the different far field conditions implemented in [31] and this Thesis. In particular, where the zero deflection approximation is used [31], possible irregularities in the film profile can occur in the far field. These irregularities are not seen when using the zero derivative far field constraint as used within the RBF interpolation.

Figure 4.9 illustrates solutions for small to large obstacle sizes for a flow with an inverse Bond number $B = 1$ on an inclined plane at an angle of 45^o. Here, as expected, a larger obstacle will generate a larger deformation. Again results are in direct comparison with the plot by Blyth and Pozrikidis [31] (their Fig 8). The peaks of the RBF analysis appear larger than those using FDAs, and the percentage difference of peak height between the

RBF and FDA results is approximately 19% for $a = 0.6$, as estimated from the FDA solution in [31]. As discussed previously, these differences are likely to be caused by the different far field conditions implemented, and specifically irregularities in the film profile caused by the zero deflection condition implemented in [31]. For flow over an obstacle of radius $a = 0.6$, the RBF analysis shown in figure 4.9 has a smooth continuation in the far field, unlike that displayed at the downstream truncation point for the FDA analysis of [31]. This arises due to use of a zero gradient far field condition compared to the zero deflection far field implemented in [31].

To quantify the difference between the FDA and global RBF analysis, figure 4.10 shows the centre line values for $\frac{\partial h}{\partial x_1}$ and curvature by both the FDA and global RBF evaluations for a 56×48 mesh. The slight upstream shift of the FDA free surface relative to the RBF profile is caused by the use of a backward difference FDA, utilized by the $\frac{\partial h}{\partial x_1}$ term present in the kinematic condition. Values of $\frac{\partial h}{\partial x_1}$ along the centre line of the free surface are shown in figure 4.10a. Figure 4.10b shows the comparison in curvature between the FDA and global RBF interpolation. Due to the higher peaks and lower troughs of the RBF interpolation, these regions are more compacted and thus require a more rapid change of direction of the free surface for a given horizontal displacement as illustrated by the higher magnitudes of curvature at these locations for the RBF interpolation. These differences yield the larger peak-height-to-trough-depth for flow profiles generated using the RBF interpolation when compared to a FDA analysis. These trends have been seen in figure 4.5a, and through the comparisons of figures 4.7 - 4.9 with results in Blyth and Pozrikidis [31].

Comparison can be made with results obtained from numerically and asymptotically modelling a spherical obstacle. The work in Blyth and Pozrikidis [31] found difficulties in comparing free surface profiles as they were unable to obtain results for spherical obstacles with radius less than $a = 0.05$. The case shown in Blyth and Pozrikidis [31] (their Fig 9a) has been calculated and is shown in Figure 4.11. The free surface was discretized identically to Blyth and Pozrikidis [31] using a mesh of 47×47 square elements

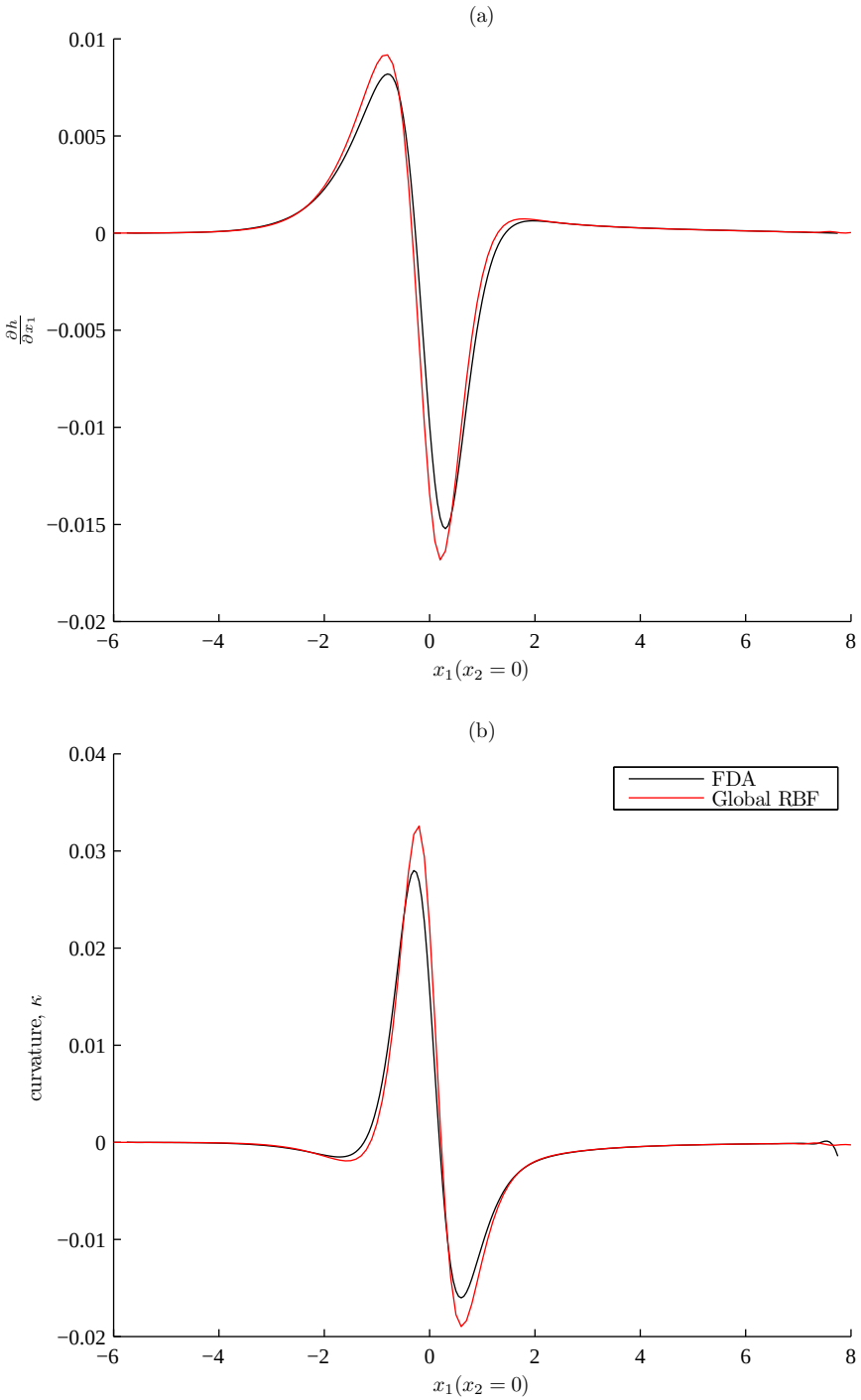

Figure 4.10: Centre line solutions comparing (a) $\frac{\partial h}{\partial x_1}$ and (b) the curvature κ, for the flow profiles with a 56×48 mesh as shown in figure 4.5. Both cases utilize the small free surface deflection assumption.

for the asymptotic results and 49×49 square elements for the complete analysis over a truncated domain of $-8 \leq x_1 \leq 10$, $-9 \leq x_2 \leq 9$. Again the midpoint values of surface height are interpolated using the RBF implemented for the free surface curvature and unit normal to produce a smooth curve. The zero gradient far field condition was used throughout.

The flow is solved for a plane inclination angle of 45^o with inverse Bond number $B = 1$. Figure 4.11 compares centre line results for a radius of $a = 0.05$. As in Blyth and Pozrikidis [31] the asymptotic solution is found to over-predict the maximum displacement compared to the solution obtained by numerical analysis of the sphere. However the larger peak heights found from the current approach provides a closer fit between the asymptotic and numerical results. The centre lines of the asymptotic solutions using a RBF interpolation still over-predict the published results in Blyth and Pozrikidis [31] (their Fig 9a) utilizing FDAs, although the differences appear smaller than those for numerical results obtained. It is also noted that no limitations on the size of a are present for our numerical model. Figure 4.12 illustrates centre line solution for $a = 0.001$ with the asymptotic and numerical solutions giving near identical results. A small 1.5% difference in peak heights along the centre line is found, indicating consistency between the two models.

4.3.2 Large Free Surface Deflections

Results generated by removing the small amplitude free surface deflection approximation from Blyth and Pozrikidis [31] are produced in this section. A global RBF scheme is used for calculation of the free surface parameters, and implements the zero derivative far field conditions applied at the element nodes on the boundary of the domain. When using a large free surface deflection analysis, the free surface is meshed using triangular elements in preference to the rectangular elements used for the small free surface deflections. Mesh refinements are considered for a domain of $-6 \leq x_1 \leq 8$ and $-6 \leq x_2 \leq 6$ discretized

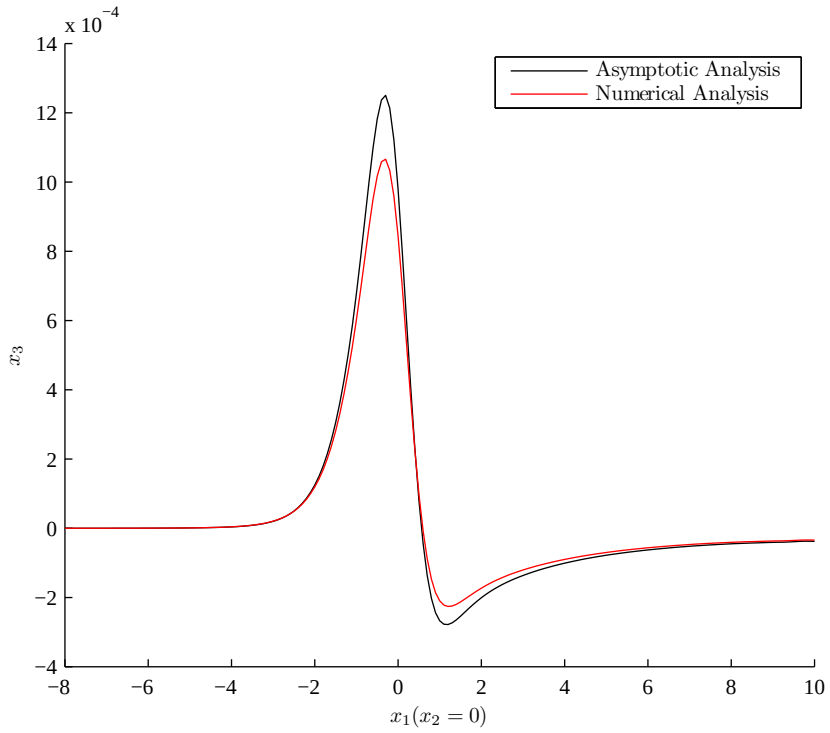

Figure 4.11: Centre line surface profiles using the assumption of small free surface deflection for flow over a sphere of radius $a = 0.05$ using an asymptotic and numerical analysis for the sphere.

by both 28×24 and 56×48 elements. A small hemispherical obstacle of radius 0.2 is considered and the flow is down a plane inclined at $\alpha = 45^o$ with an inverse Bond number $B = 1$. Centre line solutions indicating the profile for the 56×48 mesh, and the error between this and the coarser mesh are shown in figure 4.13.

The validity of the small free surface deflection assumption is analyzed by direct comparisons of results for large and small deflections, caused by large and small obstacles respectively. Again, a domain of $-6 \leq x_1 \leq 8$ and $-6 \leq x_2 \leq 6$ is considered for the free surface, discretized by 28×24 elements as found sufficient above. The small hemispherical obstacle has a radius of 0.2 and the large hemisphere a radius of 0.9. Both are discretized by successive subdivision into 256 geometrically linear elements. The flow is down a plane inclined at $\alpha = 45^o$ with an inverse Bond number $B = 1$. For direct comparison with earlier results, the near point singularity analysis is omitted, with numerical

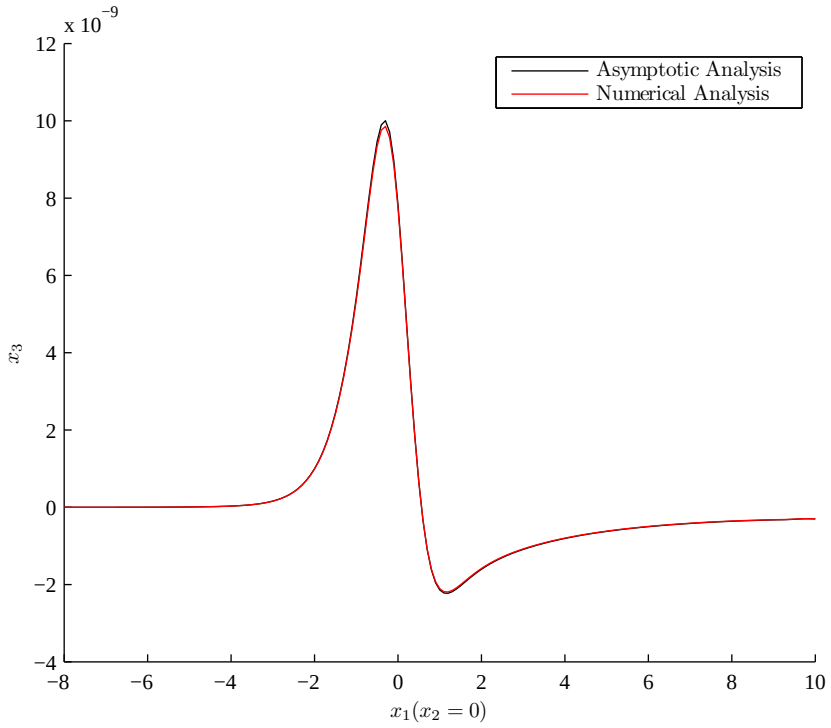

Figure 4.12: Centre line surface profiles using the assumption of small free surface deflection for flow over a sphere of radius $a = 0.001$ using an asymptotic and numerical analysis for the sphere. Both methods show near identical solutions.

integrations conducted via the 3-point Gaussian quadrature scheme for triangles.

Figure 4.14 shows the centre line solutions ($x_2 = 0$) for a small ($a = 0.2$) hemisphere. Results using the small deflection assumption are almost identical when compared to the complete analysis and as such it is a valid approximation for the flow profiles caused by small obstacles. The slight differences in solutions are found to completely disappear when the mesh resolutions are increased to 56×48.

Figure 4.15 illustrates the centre line solutions for a hemisphere of radius 0.9. The resulting free surface deflection is significant relative to the undisturbed film thickness and as such the limitation of a small free surface deflection is not appropriate, with noticeable difference between the two solutions produced. The approximated deflection

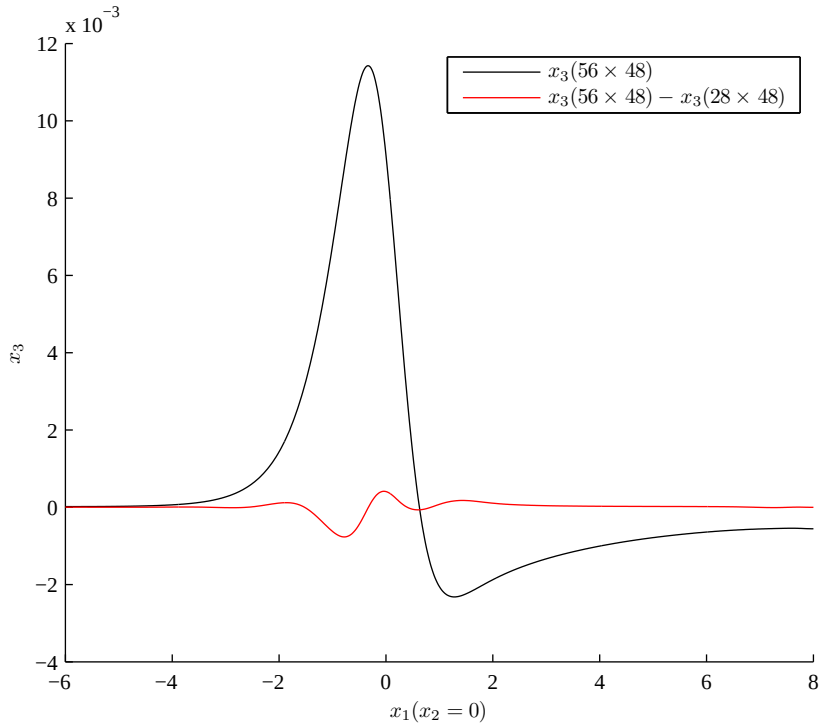

Figure 4.13: A centre line solution for flow over a hemispherical obstacle of radius $a = 0.2$, $B = 1$ and $\alpha = 45^o$, indicating the effects of mesh resolution on the film disturbance.

is shown to lag the full solution with both the peak height and trough depth underestimated. Again, when the mesh was refined to 56×48 elements, the general profiles shown were reproduced. The small deflection model produced no noticeable change in profile, whereas the full model introduced a minor (3%) reduction in peak height along the centre line, although the rest of the profile was identical. In the interests of computational time, the coarser mesh will be used throughout in the knowledge that the solution is sufficiently accurate.

Figure 4.16 shows the full free surface for flow over a hemisphere of radius $a = 0.9$, inverse Bond number $B = 1$ and plane inclination angle 45^o. The contours of the free surface deformation are also shown. This figure illustrates how a relatively large peak directly before the obstacle decays in a "horseshoe" shape with a shallow trough decaying slowly behind the obstacle.

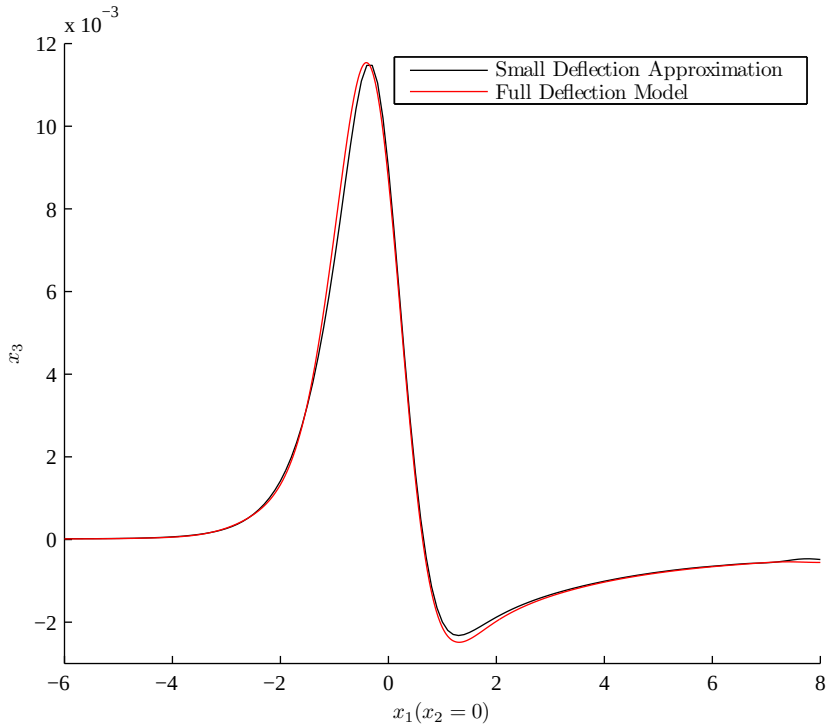

Figure 4.14: Comparison of centre line solutions for flow over a hemispherical obstacle with and without the small free surface deflection assumption. Flow parameters are $a = 0.2$, $B = 1$ and $\alpha = 45^o$.

Figure 4.17 illustrates the streamlines for flow over a hemisphere attached to an inclined plane at 45^o. The hemisphere has a radius of $a = 0.9$ and the flow has an inverse Bond number of $B = 1$. The two innermost streamlines move both outward, as well as over the hemisphere and streamline deflection reduces considerably further from the obstacle. It is noted that solutions show symmetry in the plane $x_2 = 0$.

Following Blyth and Pozrikidis [31], comparisons of the centre line solutions for a parameter analysis of the inverse Bond number and plane inclination angle is conducted. The obstacle is a hemisphere of radius $a = 0.9$ and discretized by 256 elements. A flow domain of $-8 \leq x_1 \leq 10$ and $-8 \leq x_2 \leq 8$ is considered with free surface meshes consisting of element distributions of 36×32. Again integration omits the near point singularity analysis and a 3-point Gaussian quadrature scheme is used.

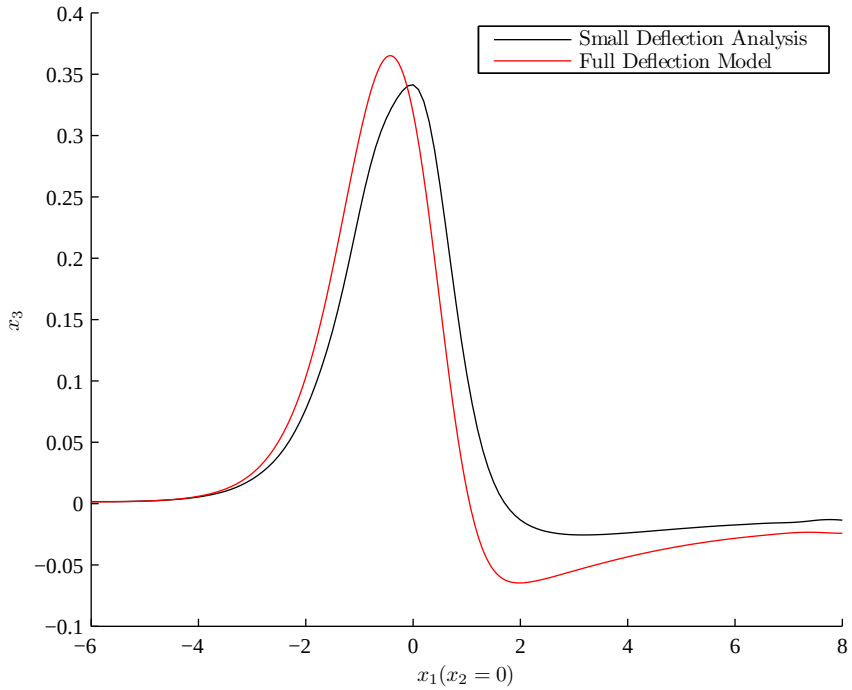

Figure 4.15: Comparison of centre line solutions for flow over a hemispherical obstacle with and without the small free surface deflection assumption. Flow parameters are $a = 0.9$, $B = 1$ and $\alpha = 45^o$.

Figure 4.18a indicates solutions for a range of inverse Bond numbers B and is comparable to the small deflection results of figure 4.7. Flow is down a 45^o plane and as expected increasing the inverse Bond number results in a flattening and smoothing of the interface. The peak is also seen to migrate slightly upstream. Within figure 4.18a, the far field condition appears not to be satisfied and this is a direct consequence of the size of the truncated domain used for calculation and the extended distances required for high surface tension flows to return fully to the undisturbed profile. However, the implementation of the zero derivative boundary condition helps retain consistent results without significant deflections caused by forcing an unrealistic far field condition. Figure 4.18b indicates the correlation between the maximum and minimum film height and inverse Bond number B corresponding to the results of figure 4.18a. Clearly the magnitude of the deflection from zero is reduced in both cases as B is increased, appearing to tend towards constant values for the maximum and minimum deflection. Peak height is af-

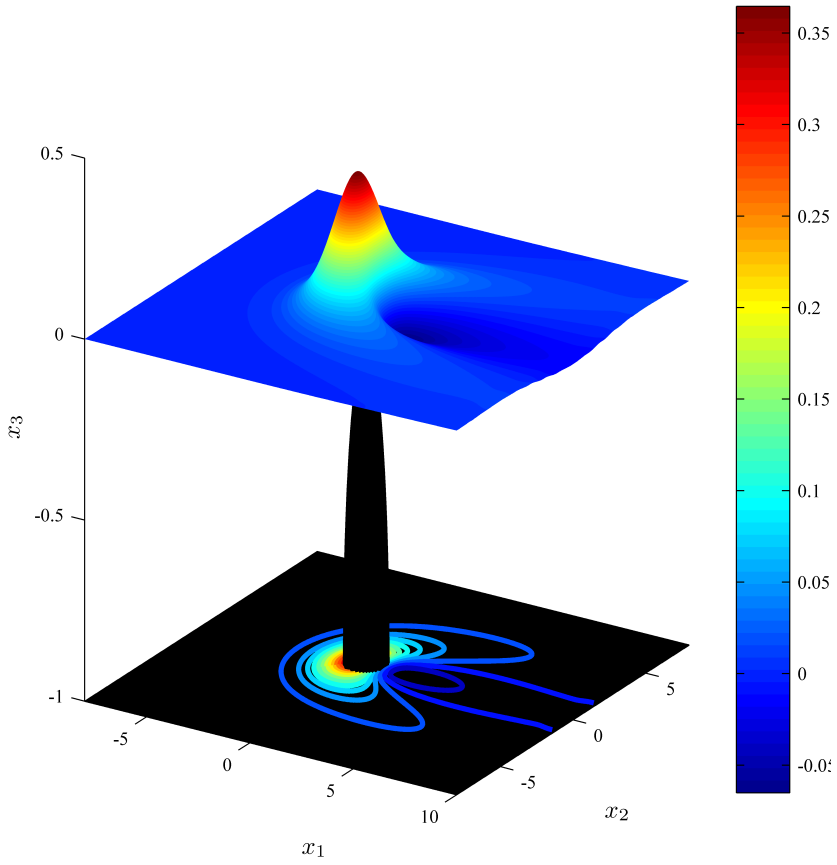

Figure 4.16: Three-dimensional solution profile for flow over a large hemisphere of radius $a = 0.9$. The plane is inclined at 45^o, and the inverse Bond number is 1.

fected more severely by the inverse Bond number when compared to the trough depth due to the sharper profile shape around the peak and larger value of curvature in this region.

Figure 4.19a indicates solutions for a range of plane inclination angles α and is comparable to the small deflection results in figure 4.8. Flow is for an inverse Bond number $B = 1$ and it is seen that increasing the inclination angle has the effect of increasing the peak size and decreasing the trough size behind the obstacle. The location of both the peak and trough is seen to migrate upstream as the angle is reduced, although the movement of the trough is most significant. Figure 4.19b indicates the correlation between

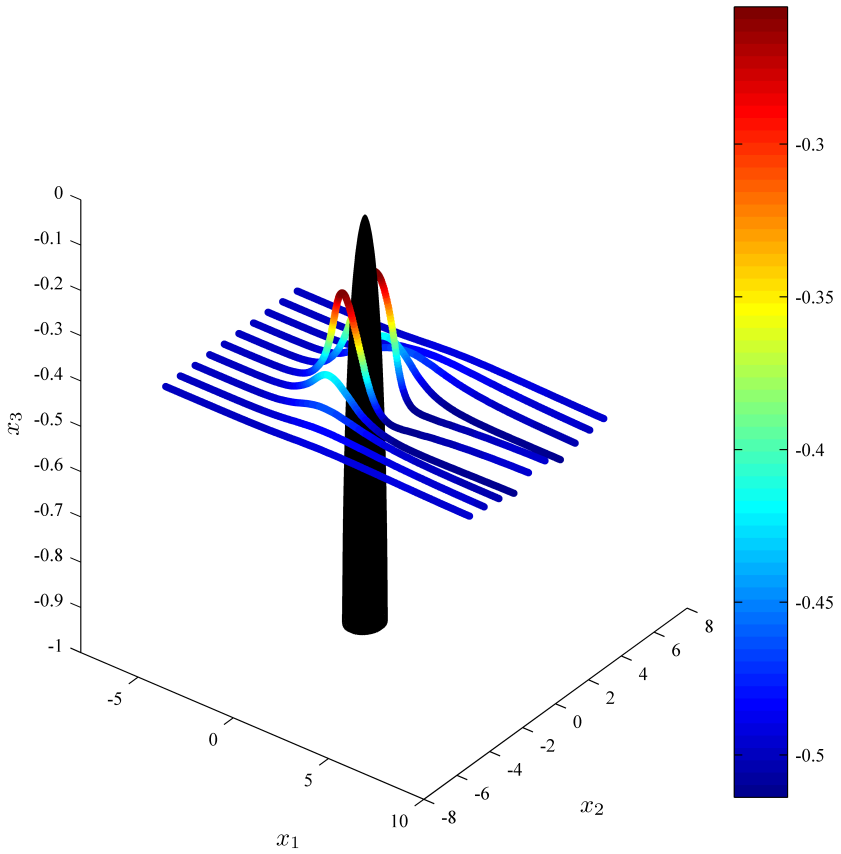

Figure 4.17: Pattern of streamlines starting at $x_3 = -0.5$ and upstream of the hemisphere for a range of x_2 locations. Flow is over a hemispherical obstacle of radius $a = 0.9$, on an inclined plane at $\alpha = 45^o$. The inverse Bond number of the flow is $B = 1$.

the maximum and minimum film height and the plane inclination angle α for solutions given in figure 4.19a. Both the peak and trough heights increase as the plane inclination angle is increased. Values of minimum film height increase slowly, and approximately linearly with plane angle. Initially, the maximum film height increases rapidly for small α. As the angle increases the maximum film height is seen to continue increasing, but at a progressively slower rate.

Typical solution profiles show how it is possible for obstacles larger than the undisturbed film to be contained fully within the fluid. The maximum possible obstacle size allowed

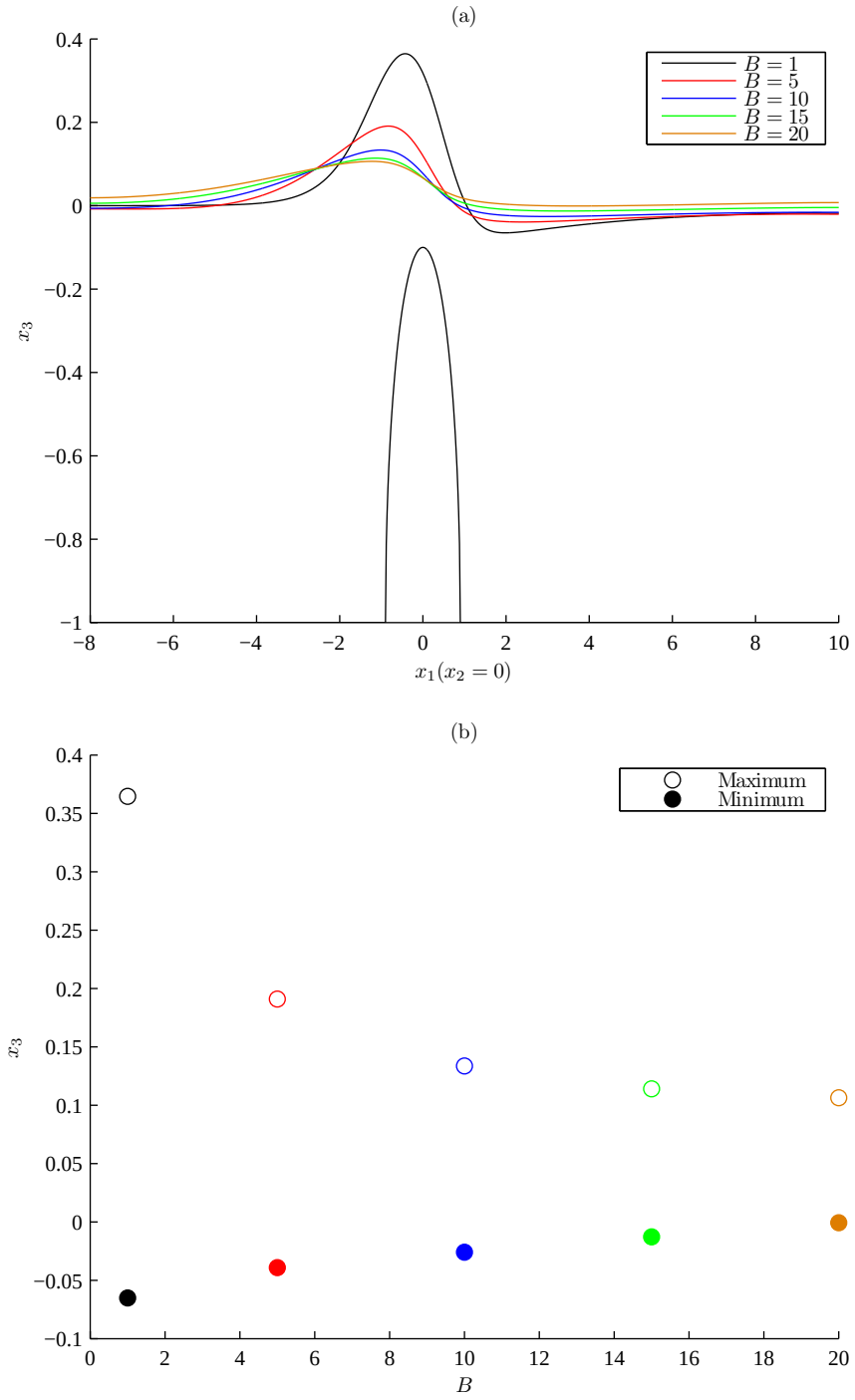

Figure 4.18: Solutions for flow over a large hemisphere of radius $a = 0.9$ attached to a plane inclined at 45^o showing a selection of inverse Bond numbers. Part (a) illustrates centre line solutions and (b) values of maximum and minimum film deflection as inverse Bond number changes.

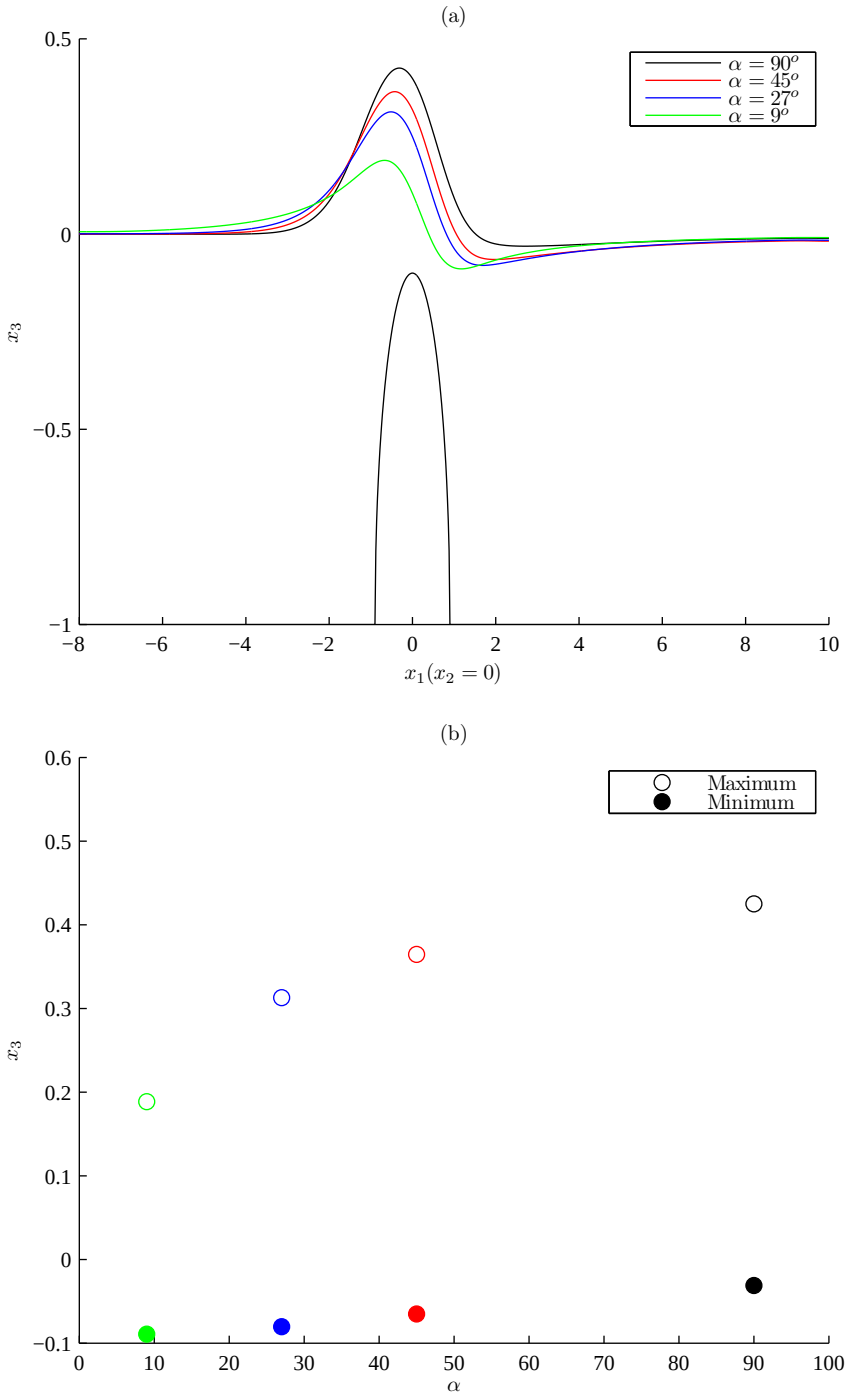

Figure 4.19: Solutions for flow over a large hemisphere of radius $a = 0.9$ showing a selection of wall inclinations. Part (a) illustrates centre line solutions and (b) values of maximum and minimum film deflection for changes in wall inclination. The flow has an inverse Bond number $B = 1$.

within the fluid is dependent on the inclination angle of the plane. Two cases are considered here, flow over large hemispherical obstacles on a shallow plane inclined at 5^o and a steep plane inclined at 90^o. For this analysis the hemispheres are discretized by 256 linear triangular elements. A flow domain of $-10 \leq x_1 \leq 10$ and $-8 \leq x_2 \leq 8$ is taken with free surface meshes consisting of an element distribution of 40×32. Numerical integration is conducted using the near point singularity approach outlined in § 4.2 and the zero derivative far field conditions are again applied within the global RBF analysis. Results are obtained by a simple parameter continuation analysis. A flow profile is found for an obstacle contained within the fluid. The obstacle is then increased in size (so that it is still within the fluid) and the new profile found from the starting point of the previous solution. This is continued until the obstacle is arbitrarily close to the free surface.

For flow down a plane inclined at 5^o the largest hemispherical obstacle containable within the Stokes flow has a radius $a = 1.028$. At this point intersection is imminent on the back edge of the obstacle where the film profile collapses towards its trough. A centre line profile for this obstacle size is shown in figure 4.20a, for a flow with a Bond number $Bo = 1$.

For flow down a plane inclined at 90^o the largest hemispherical obstacle containable within the film flow has a radius of $a = 1.92$. Interestingly unlike the case for a shallow plane this limitation is not caused by intersection of the obstacle and free surface, but rather by limitations on convergence of the model. This may be caused by the ill-conditioning effects present in the BIE due to the presence of near point singularities. These effects are more prevalent here than in the shallow plane analysis due to the extended region of near-point effects. Figure 4.20b illustrates the centre line solutions for this obstacle on a vertical plane ($\alpha = 90^o$) for flow with a Bond number $Bo = 1$.

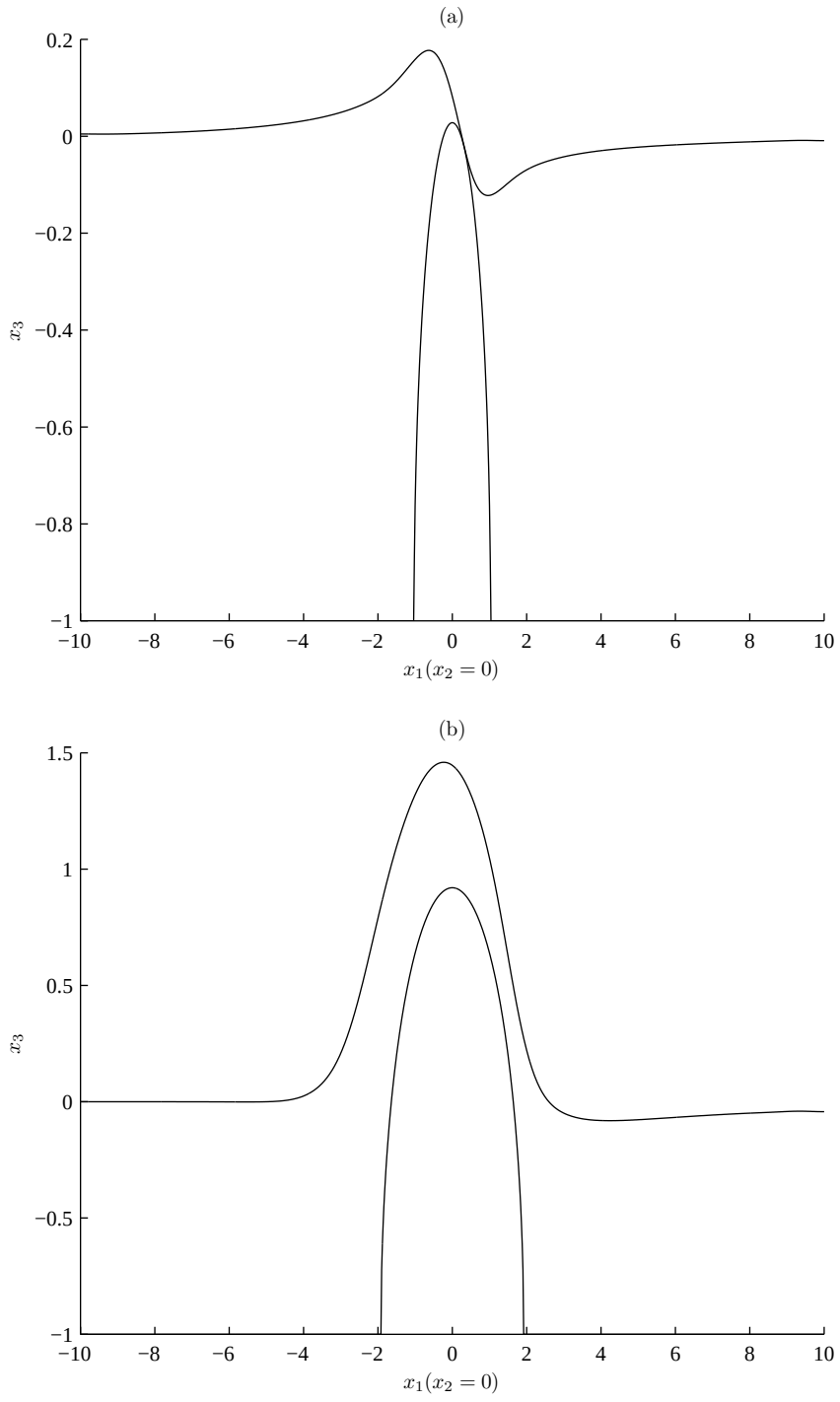

Figure 4.20: The centre line solution for flow over a large hemispherical obstacle contained fully within the Stokes flow down a (a) shallow plane inclined at 5^o where ($a = 1.028$) and (b) steep plane inclined at 90^o, where ($a = 1.92$). The Bond number of the flow is $Bo = 1.0$ in both cases.

Chapter 5

Stokes Flow Over Multiple Obstacles

The consideration of Stokes flow over multiple obstacles is a natural extension to the work outlined in Chapter 4, with § 5.1 modifying the single obstacle formulation to flow over an arbitrary number of obstacles. The numerical schemes used for solution of the formulation are identical to those given in § 4.2 using a radial basis function (RBF) analysis of the full free surface deflection. Modification is made to the free surface mesh, which is developed such that a refined region is present in the location of greatest deflection; details are specified in § 5.2. Solutions corresponding to flow over two and three hemispheres for a range of relative locations and flow parameters are presented in § 5.3.

5.1 Modification To Mathematical Formulation

This section considers the mathematical formulation for a thin film Stokes flow driven by gravity down an inclined plane over multiple obstacles attached to the plane. As in § 4.1 the flow variables are solved for disturbance and undisturbed components, yielding two boundary integral equations (BIEs) for solution over the obstacle and free surface.

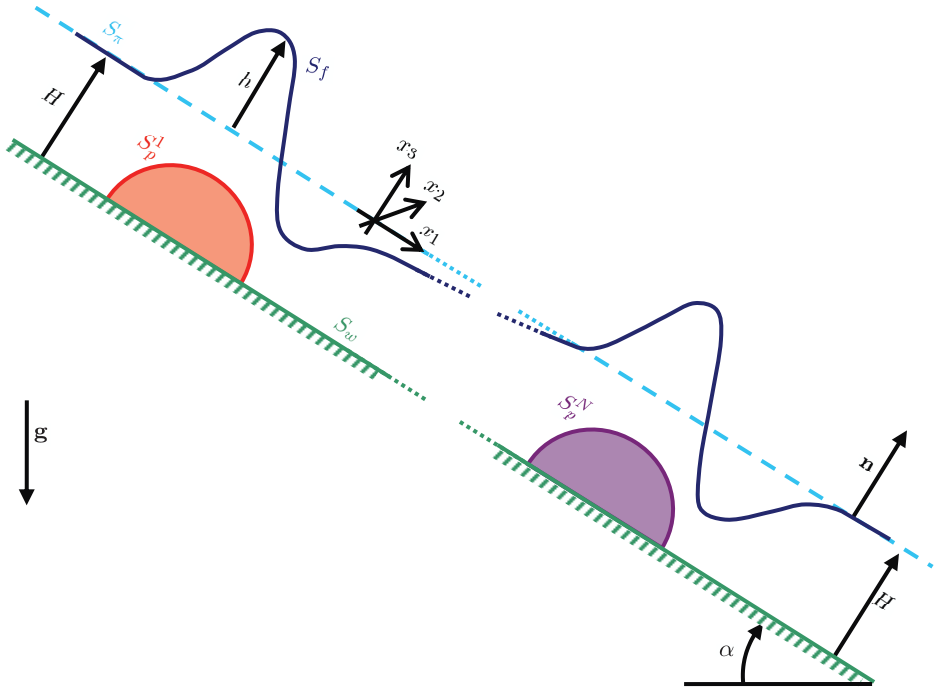

Figure 5.1: Two-dimensional cross section of a typical film profile over multiple obstacles.

A two-dimensional schematic for flow over N obstacles is shown in figure 5.1, where the disturbed free surface is denoted S_f and the wall is denoted S_w, and the wetted obstacle surface of the l^{th} obstacle is denoted S_p^l. The formulation of the governing equations follows that presented in § 4.1, although the no slip condition (4.1.6) is modified for each wetted obstacles surface, i.e.

$$u_i = 0 \qquad \mathbf{x} \in S_w \cup S_p^1 \cup S_p^2 \cup \ldots \cup S_p^N, \tag{5.1.1}$$

$$u_i^\delta = -u_i^\infty \qquad \mathbf{x} \in S_p^1 \cup S_p^2 \cup \ldots \cup S_p^N. \tag{5.1.2}$$

The BIE formulation is similar to earlier, except in this case extended to boundaries corresponding to multiple obstacles. The Stokes flow equations for the disturbance regime (equivalent to (4.1.28) for a single obstacle) can be represented exactly as the BIE given

in (5.1.3) over the fluid domain. This gives

$$c_{ij}(\mathbf{x}_0)u_i^\delta(\mathbf{x}_0) = \frac{1}{8\pi}\int\limits_{S_f\cup S_p^1\cup\ldots\cup S_p^N} G_{ij}^*(\mathbf{x},\mathbf{x}_0)f_i^\delta(\mathbf{x})\mathrm{d}S(\mathbf{x}) - \frac{1}{8\pi}\int\limits_{S_f\cup S_p^1\cup\ldots\cup S_p^N} u_i^\delta(\mathbf{x})T_{ijk}^*(\mathbf{x},\mathbf{x}_0)n_k(\mathbf{x})\mathrm{d}S(\mathbf{x}), \tag{5.1.3}$$

where $\mathbf{x}$ is the field point, and $\mathbf{x}_0$ any collocation point and the coefficient $c_{ij}(\mathbf{x}_0)$ is given by (4.1.30). For the N obstacle domains S_p^l, $l = 1,\ldots,N$ the undisturbed quantities satisfy the N BIEs

$$c_{ij}(\mathbf{x}_0)u_i^\infty(\mathbf{x}_0) = -\frac{1}{8\pi}\int\limits_{S_p^l} G_{ij}^*(\mathbf{x},\mathbf{x}_0)(f_i^\infty(\mathbf{x}) + Gn_i)\mathrm{d}S(\mathbf{x}) + \frac{1}{8\pi}\int\limits_{S_p^l} u_i^\infty(\mathbf{x})T_{ijk}^*(\mathbf{x},\mathbf{x}_0)n_k(\mathbf{x})\mathrm{d}S(\mathbf{x}), \tag{5.1.4}$$

for $l = 1,\ldots,N$, and is equivalent to (4.1.31) for $N = 1$.

The equivalent BIE to (4.1.34) for collocation over the free surface, is obtained by an identical procedure to § 4.1, yielding,

$$\frac{1}{2}u_j^\delta(\mathbf{x}_0) + \frac{1}{8\pi}\int\limits_{S_f} u_i^\delta(\mathbf{x})T_{ijk}^*(\mathbf{x},\mathbf{x}_0)n_k(\mathbf{x})\mathrm{d}S(\mathbf{x}) = \frac{1}{8\pi}\int\limits_{S_p^1\cup\ldots\cup S_p^N} G_{ij}^*(\mathbf{x},\mathbf{x}_0)\tilde{f}_i(\mathbf{x})\mathrm{d}S(\mathbf{x}) + \frac{1}{8\pi}\int\limits_{S_f} G_{ij}^*(\mathbf{x},\mathbf{x}_0)f_i^\delta(\mathbf{x})\mathrm{d}S(\mathbf{x}) \qquad \mathbf{x}_0 \in S_f. \tag{5.1.5}$$

Collocation over a specific wetted obstacle surface $\mathbf{x}_0 \in S_p^k$ for the BIE (5.1.4) has two possibilities; BIE (5.1.6) is applicable for $l = 1,\ldots,k-1,k+1,\ldots,N$,

$$\frac{1}{8\pi}\int\limits_{S_p^l} G_{ij}^*(\mathbf{x},\mathbf{x}_0)(f_i^\infty(\mathbf{x}) + Gn_i)\mathrm{d}S(\mathbf{x}) = \frac{1}{8\pi}\int\limits_{S_p^l} u_i^\infty(\mathbf{x})T_{ijk}^*(\mathbf{x},\mathbf{x}_0)n_k(\mathbf{x})\mathrm{d}S(\mathbf{x}), \tag{5.1.6}$$

and (5.1.7) is used for $l = k$,

$$\begin{aligned}\frac{1}{2}u_j^{\infty}(\mathbf{x}_0) = -\frac{1}{8\pi}\int\limits_{S_p^l} G_{ij}^*(\mathbf{x},\mathbf{x}_0)(f_i^{\infty}(\mathbf{x}) + Gn_i)\mathrm{d}S(\mathbf{x}) \\ = \frac{1}{8\pi}\int\limits_{S_p^l} u_i^{\infty}(\mathbf{x})T_{ijk}^*(\mathbf{x},\mathbf{x}_0)n_k(\mathbf{x})\mathrm{d}S(\mathbf{x}).\end{aligned} \tag{5.1.7}$$

The BIE (5.1.3) is applied on the obstacle S_p^k, with the no slip conditions (5.1.2) imposed to obtain

$$\begin{aligned}-\frac{1}{2}u_j^{\infty}(\mathbf{x}_0) = \frac{1}{8\pi}\int\limits_{S_f} G_{ij}^*(\mathbf{x},\mathbf{x}_0)f_i^{\delta}(\mathbf{x})\mathrm{d}S(\mathbf{x}) \\ -\frac{1}{8\pi}\int\limits_{S_f} u_i^{\delta}(\mathbf{x})T_{ijk}^*(\mathbf{x},\mathbf{x}_0)n_k(\mathbf{x})\mathrm{d}S(\mathbf{x}) \\ +\frac{1}{8\pi}\int\limits_{S_p^1\cup\ldots\cup S_p^N} G_{ij}^*(\mathbf{x},\mathbf{x}_0)f_i^{\delta}(\mathbf{x})\mathrm{d}S(\mathbf{x}) \\ +\frac{1}{8\pi}\int\limits_{S_p^1\cup\ldots\cup S_p^N} u_i^{\infty}(\mathbf{x})T_{ijk}^*(\mathbf{x},\mathbf{x}_0)n_k(\mathbf{x})\mathrm{d}S(\mathbf{x}).\end{aligned} \tag{5.1.8}$$

Combining BIEs (5.1.6) - (5.1.8) yields a BIE for collocation over the obstacle S_p^k as

$$\begin{aligned}\frac{1}{8\pi}\int\limits_{S_p^k} G_{ij}^*(\mathbf{x},\mathbf{x}_0)\tilde{f}_i(\mathbf{x})\mathrm{d}S(\mathbf{x}) \\ +\frac{1}{8\pi}\int\limits_{S_p^1\cup\ldots\cup S_p^{k-1}\cup S_p^{k+1}\cup\ldots\cup S_p^N} G_{ij}^*(\mathbf{x},\mathbf{x}_0)\tilde{f}_i(\mathbf{x})\mathrm{d}S(\mathbf{x}) \\ = -u_j^{\infty}(\mathbf{x}_0) - \frac{1}{8\pi}\int\limits_{S_f} G_{ij}^*(\mathbf{x},\mathbf{x}_0)f_i^{\delta}(\mathbf{x})\mathrm{d}S(\mathbf{x}) \\ +\frac{1}{8\pi}\int\limits_{S_f} u_i^{\delta}(\mathbf{x})T_{ijk}^*(\mathbf{x},\mathbf{x}_0)n_k(\mathbf{x})\mathrm{d}S(\mathbf{x}) \qquad \mathbf{x}_0 \in S_p^k,\end{aligned} \tag{5.1.9}$$

with this BIE holding for each $S_p^k, k = 1,\ldots,N$.

5.2 Modification Of Numerical Schemes

This section considers modifications to the numerical schemes used for a single obstacle Stokes flow analysis as outlined in § 4.2 for a multiple obstacle analysis. The solution

procedure follows the process outlined for the single obstacle model. Differences in the numerical scheme are limited to the implementation of the multiple obstacle boundary integral equations (BIEs), and improvements in the manner in which the free surface is meshed.

The numerical procedure for solving Stokes flow over multiple obstacles is similar to that for a single obstacle analysis (see § 4.2). The main difference occurs when implementing the obstacle BIEs (5.1.9). In this case, collocation takes place over all wetted obstacle surfaces $S_p^l, l = 1, \ldots, N$, and the resulting matrix problem is solved for all obstacles tractions $\tilde{f}_i$.

For flow over or around a single obstacle located at $(0, 0)$, appropriate far field conditions, were specified in chapter 4. For multiple obstacles, with centres separated by $(x_{1_{sep}}, x_{2_{sep}})$, the far field conditions are extended to $x_{1_{min}} - \frac{x_{1_{sep}}}{2} \leq x_1 \leq x_{1_{max}} + \frac{x_{1_{sep}}}{2}$ and $x_{2_{min}} - \frac{x_{2_{sep}}}{2} \leq x_2 \leq x_{2_{max}} + \frac{x_{2_{sep}}}{2}$.

Another modification of the earlier work is to implement a more refined free surface mesh in regions of large deformations instead of the uniform distribution used so far. In § 4.3, the free surface mesh was found sufficient to obtain solutions of reasonable accuracy. The mesh used was generated by first subdividing the flow domain into rectangular (ideally square) elements and then subdividing each of these by connection of their vertices into four triangular elements. However this mesh was also shown to produce 3% error in peak height when compared to a more refined mesh generated by the same technique.

Free surface meshes used in this chapter are refined in the region of the hemispheres. The mesh is initially discretized by rectangular elements defined by an inner element and outer element size. The outer square element is as found sufficient in § 4.3 and of size 1.0×1.0. The inner element is sized as the more refined mesh in section § 4.3 and of size 0.5×0.5. The transition region between the inner and outer uniform meshes involves a more complicated analysis. Input parameters involve the number of elements used to extend from the inner to the outer mesh and the scaling of these elements, so that they

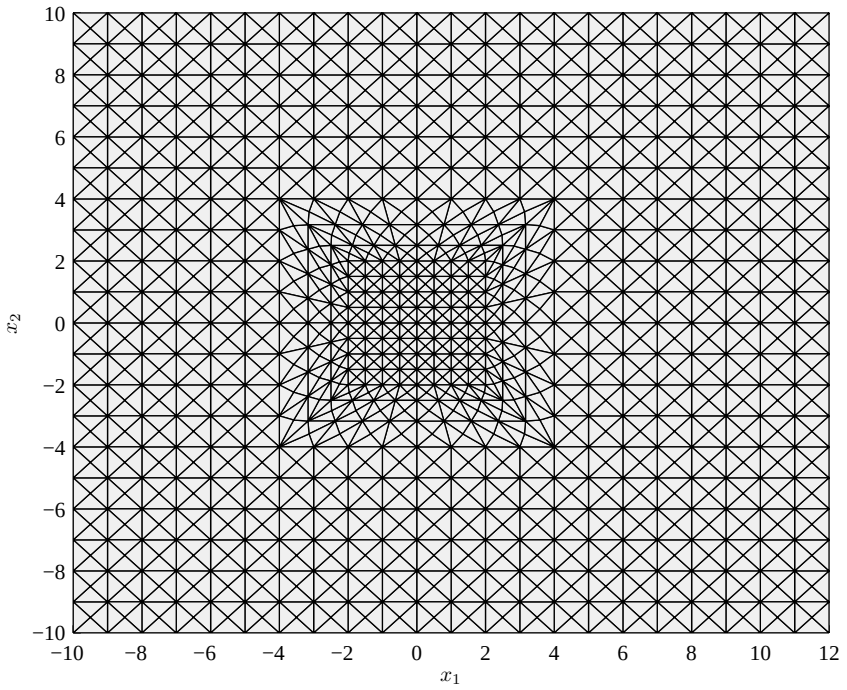

Figure 5.2: Typical free surface mesh for flow over an array of hemispheres.

can be biased towards the inner mesh. These parameters are chosen to give a reasonable conversion from the smaller, inner element size to the larger outer element size.

The size and shape of the inner mesh is also analyzed. The inner region is chosen to span the obstacles centres, and extend beyond this by a selected number of elements. However, to keep the transitional mesh of reasonable quality, the inner region should not become too long and thin and as such the ratio of x_1 coordinate mesh length to x_2 coordinate mesh length is tested and forced between $\frac{5}{4}$ and $\frac{4}{5}$ by adding more elements where necessary. Figure 5.2 illustrates a typical free surface mesh for flow over an array of hemispheres contained within $-1 \leq x_1 \leq 1$ and $-1 \leq x_2 \leq 1$. The inner mesh is extended for 2 elements in both the x_1 and x_2 direction beyond the centres of these obstacles.

For comparisons with flow over a single hemisphere, a similar mesh refinement process is conducted and results reproduced where necessary. In this case the obstacle is centred at $(0, 0)$ and the inner mesh spans a set distance in the $\pm x_1$ and $\pm x_2$ direction.

5.3 Solution Profiles For Flow Over Multiple Obstacles

Flow profiles over two and three hemispheres are considered in each of the following subsections. For flow over two hemispheres, a range of relative obstacle locations are investigated. For two hemispheres located in-line with the flow direction, a parameter analysis is considered, where effects of changing the inverse Bond number (4.3.1), plane inclination angle α, and hemisphere radius a are investigated. Hemispheres of a size that approach the free surface are also considered, and an analysis is made of how the gap between the free surface and obstacle is reduced by interaction of a wake on the flow over a downstream hemisphere.

5.3.1 Solutions For Flow Over Two Hemispheres

Flow over two hemispheres spaced symmetrically to the axis by a distance $(x_{1_{sep}}, x_{2_{sep}})$ are considered, with the hemisphere centres located at $x_1 = \pm\frac{x_{1sep}}{2}$ and $x_2 = \pm\frac{x_{2sep}}{2}$. Flow is fixed with a Bond number $Bo = 1.0$ and is down a plane inclined at $\alpha = 45^o$, with the two attached hemispheres having radius $a = 0.9$. Flow over a single obstacle located at $(0, 0)$ required far field locations $-6 \leq x_1 \leq 8$ and $-6 \leq x_2 \leq 6$ and for each dual obstacle analysis the far field is extended from these values as outlined in the previous section.

Figure 5.3 illustrates the centre line ($x_2 = 0$) profiles of the free surface in the direction of the upstream flow over two hemispheres in-line with the incident flow and with spacings $x_{1_{sep}} = 2, 4, 6, 8$. Dashed profiles indicate the equivalent flow over a single hemisphere at $(\pm\frac{x_{1sep}}{2}, 0)$. For all cases of obstacle separation, the deformation caused by the upstream hemisphere appears to reproduce closely the corresponding profile for a single obstacle. When the separation is large, the downstream hemisphere of the twin obstacle case reproduces closely the deformation caused by a single obstacle. This is because the wake decays after the upstream obstacle and the incident flow configuration to the downstream

obstacle approximates an undisturbed flow. As the obstacles are moved closer together the profile over the rear hemisphere is distorted more, with the peak decreasing and the trough increasing in amplitude. For $x_{1_{sep}} \geq 4$, the flow over the rear obstacle appears as a complete profile, rising from around the undisturbed flow height towards a peak and decaying behind the obstacle. For $x_{1_{sep}} = 2$, the profile fundamentally changes, and the flow over the rear obstacle begins during the collapse of the peak caused by the upstream obstacle. As such the peaks appear to be joined, with a small step down as flow passes between obstacles. A single, larger trough is formed downstream of the last obstacle, instead of behind each hemisphere in turn. This is confirmed by the contour plot in figure 5.6 for $x_{1_{sep}} = 2, x_{2_{sep}} = 0$.

Figure 5.4 shows the axis line ($x_1 = 0$) profiles of the free surface for flow over two hemispheres spaced perpendicular to the incoming flow direction. Dashed profiles correspond to flow over a single hemisphere at $(0, \pm\frac{x_{2_{sep}}}{2})$. The obstacle spacing and thus the flow profile is symmetric in each case about the line $x_2 = 0$. For large separations, the profiles over the two obstacles appear identical to that for a single obstacle. As the obstacles are moved closer, the outer regions of the flow profiles remain consistent with the corresponding single obstacle solution. For $x_{2_{sep}} \geq 4$, the inner region of the profiles merge, with the lowest surface point between hemispheres increasing from the undisturbed film height. In these cases the peak height above each hemisphere is of similar magnitude to the single hemisphere case. For $x_{2_{sep}} = 2$, the two profiles merge producing a single peak, much taller than that created for a single obstacle. The resultant cross-section flow profile appears as if the flow is interacting with a single larger obstacle. The contour plot in figure 5.6 for $x_{1_{sep}} = 0, x_{2_{sep}} = 2$ confirms this.

Figure 5.5 indicates the obstacle and film surface for the analysis of flow over two hemispheres separated by $x_{1_{sep}} = x_{2_{sep}} = 2$ and with centres located at $(-1, -1)$ and $(1, 1)$. The flow is incident to the leading hemisphere, and as the peak splits into a typical horseshoe shape, one of the raised ridges is incident to the downstream hemisphere. This thicker film region causes the peak over the rear hemisphere to be even taller, be-

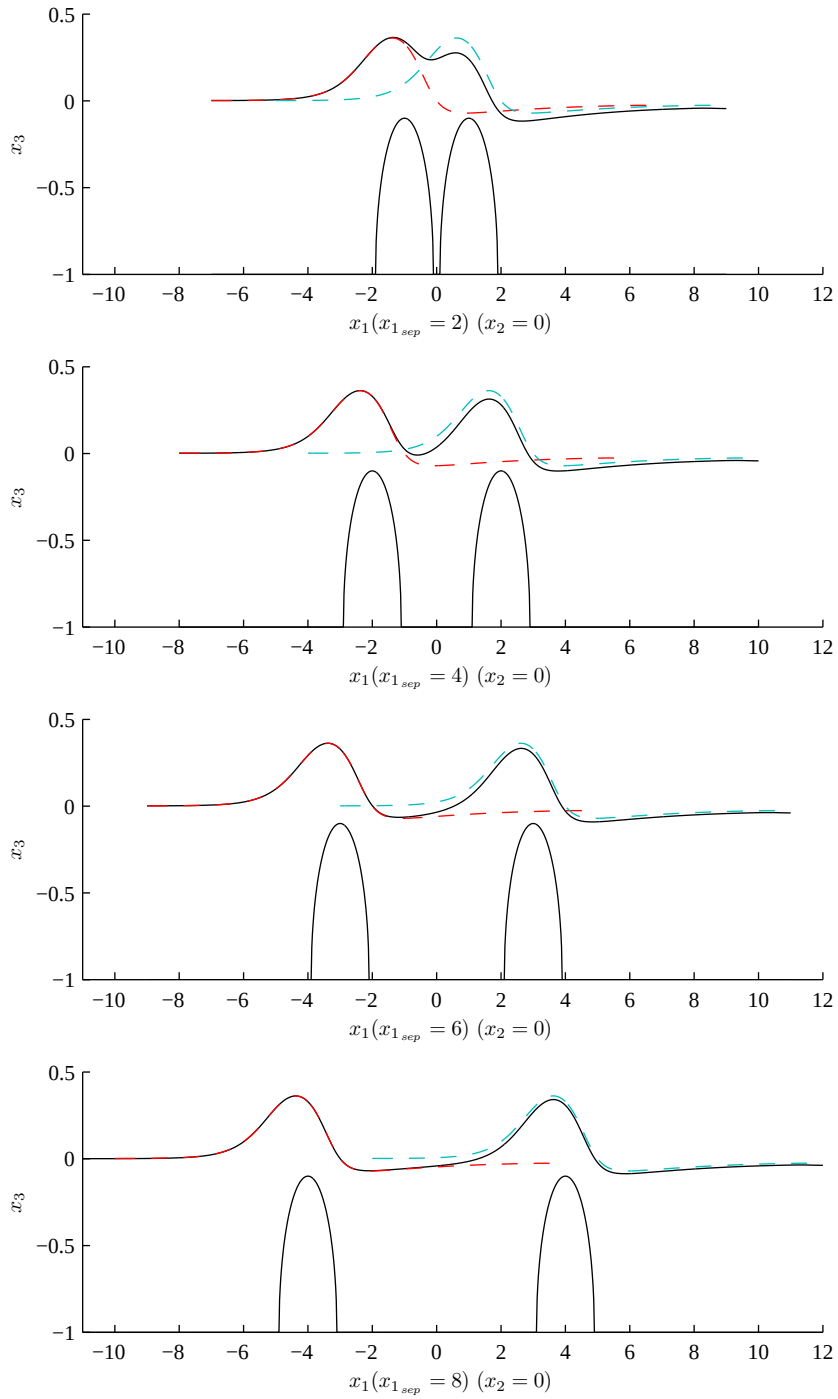

Figure 5.3: Centre line profiles for hemisphere separation distances $x_{1_{sep}} = 2, 4, 6,$ and 8 in line with the flow. Flow is over hemispheres of radius $a = 0.9$ and down a plane inclined at $\alpha = 45^o$. The Bond number of the flow is $Bo = 1.0$.

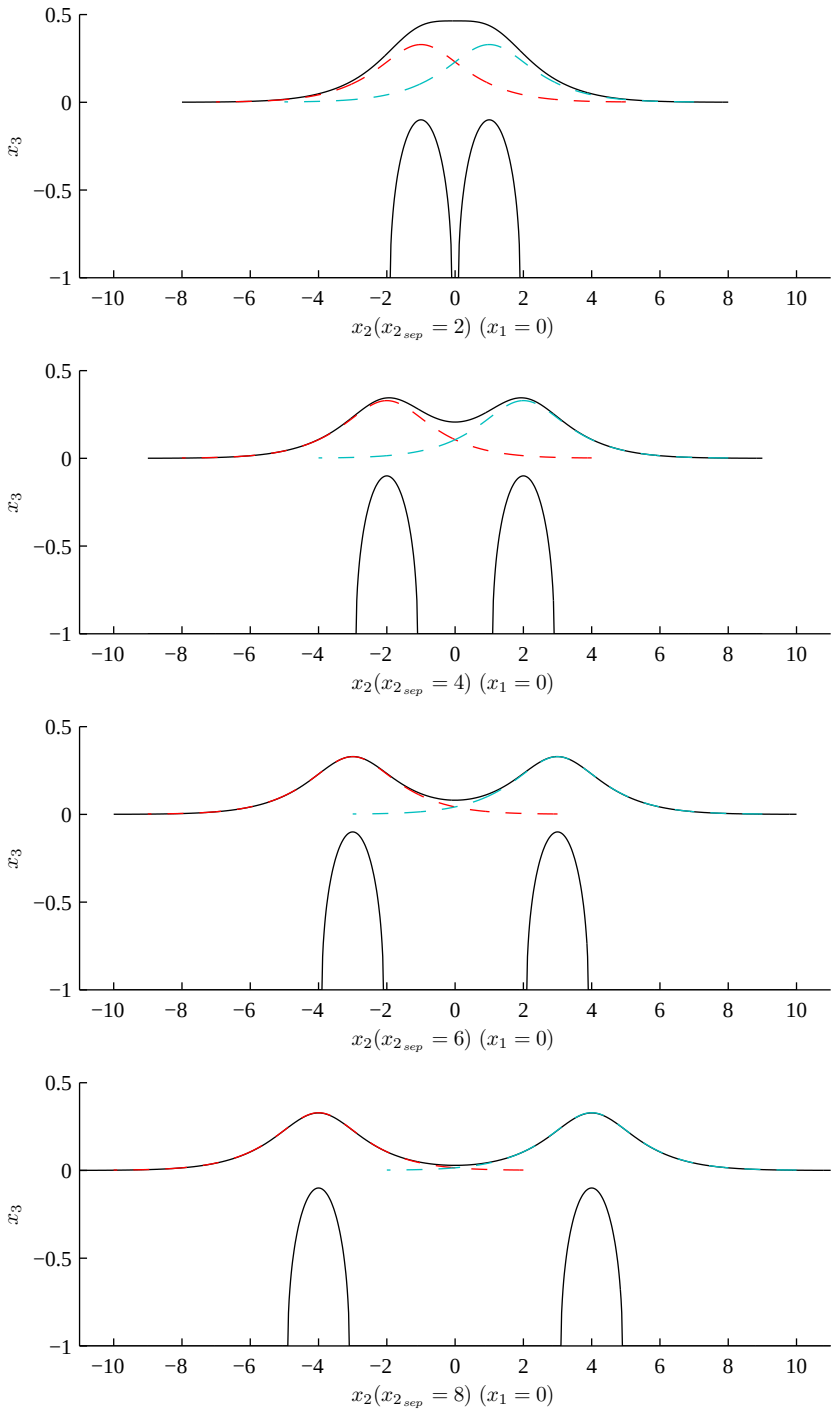

Figure 5.4: Centre line profiles for hemisphere separation distances $x_{2_{sep}} = 2, 4, 6$, and 8 perpendicular to the flow. Flow is over hemispheres of radius $a = 0.9$ and down a plane inclined at $\alpha = 45^o$. The Bond number of the flow is $Bo = 1.0$.

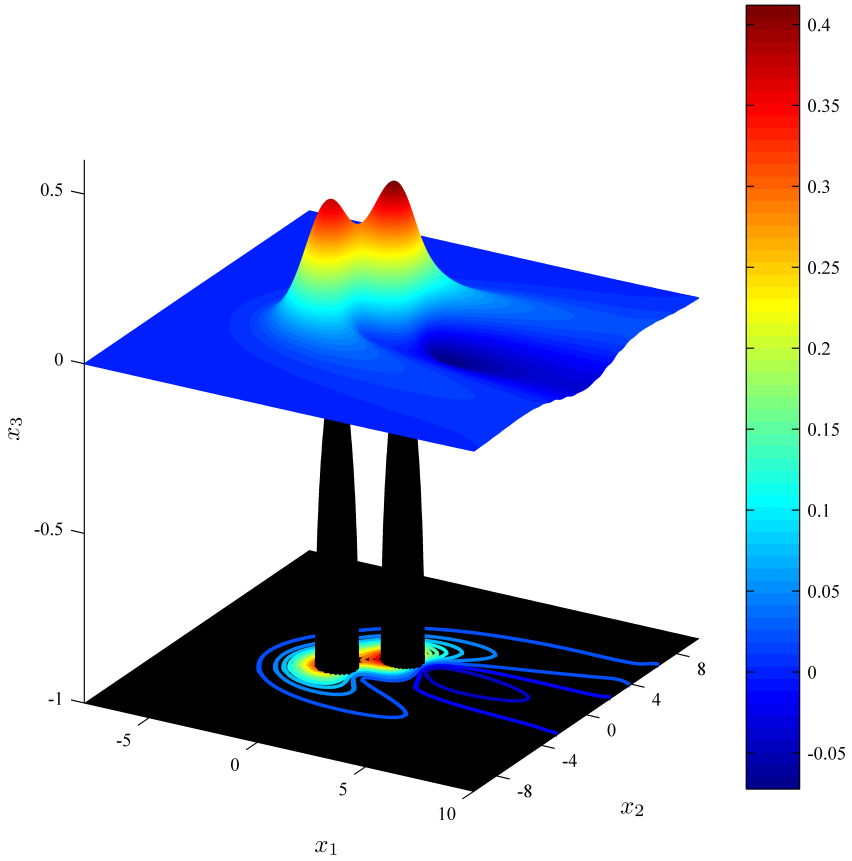

Figure 5.5: Three-dimensional solution profile for two hemispheres of radius $a = 0.9$, separated by $x_{1_{sep}} = 2, x_{2_{sep}} = 2$. The flow has a Bond number of $Bo = 1.0$, and is down a plane inclined at $\alpha = 45^o$

fore decaying in a typical fashion. The close proximity of the two obstacles allows most of the peaks to merge, with only the tips of the two deflections left independent. This is illustrated further by the contour plot in figure 5.6 for $x_{1_{sep}} = 2, x_{2_{sep}} = 2$.

Figure 5.6 shows three comparison contour plots for the obstacle configurations corresponding to figures 5.3, 5.4 and 5.5. Clearly, for $x_{1_{sep}} = 2, x_{2_{sep}} = 0$ the flow is symmetric in $x_2 = 0$ and the highest point on the free surface occurs just prior to the leading hemisphere. The peak is continued over the rear hemisphere and then collapses rapidly into a trough around $x_1 = 1.5$. This can also be seen in the centre line plot in figure 5.3. The contour plot for $x_{1_{sep}} = 0, x_{2_{sep}} = 2$ again illustrates the symmetry in $x_2 = 0$, with just a

single, wide peak occurring over $x_2 = 0$. This is also seen in figure 5.4. The peak decays rapidly into the trough just behind the line of the obstacles. However, the contour lines are disturbed downstream slightly along $x_2 = 0$ during the formation of the trough. In this case the flow is forced between the obstacles extending the peak region slightly. The contour plot for the two offset hemispheres of figure 5.5 does not show symmetry in the line $x_2 = 0$. In this case the peaks that occur due to the two obstacles can be clearly seen, with the downstream peak slightly larger. The rear hemisphere is clearly seen to lie in the decaying peak of the flow profile about the upstream hemisphere causing an extension to the distance that the raised ridge is noticed downstream.

A parameter investigation is conducted for flow over two hemispheres aligned with the incident flow and separated by $x_{1_{sep}} = 2$. The effects of changed inverse Bond number B, plane inclination angle α, and differential obstacle radii a is considered. Default values for the flow parameters include an inverse Bond number of $B = 1$, a plane inclination angle of $\alpha = 45^o$, and hemispheres of radii $a = 0.9$. In each case two parameters are chosen from above and the effects of altering the third analyzed.

Figure 5.7 illustrates the centre line ($x_2 = 0$) solutions for variations of inverse Bond number B. The increase in B, associated with an increase in surface tension forces, result in the flattening and smoothing of the profiles. For $B = 1$, the centre line profiles appear to oscillate as they pass from the first to the second hemisphere, forming two local peaks and a trough. The increase in B acts to smooth these local peaks which subsequently merge to form a single ridge that spans across the two obstacles. Consistent with the single obstacle analysis in § 4.3, the increase in inverse Bond number causes the height of the peak to reduce and for the disturbance to span a greater region upstream in the x_1 direction.

Figure 5.8 illustrates centre line ($x_2 = 0$) solutions for a range of plane inclination angles α with two local peaks occuring over each obstacle for all plane angles. The trough appears to shift slightly upstream, towards the back edge of the second hemisphere as

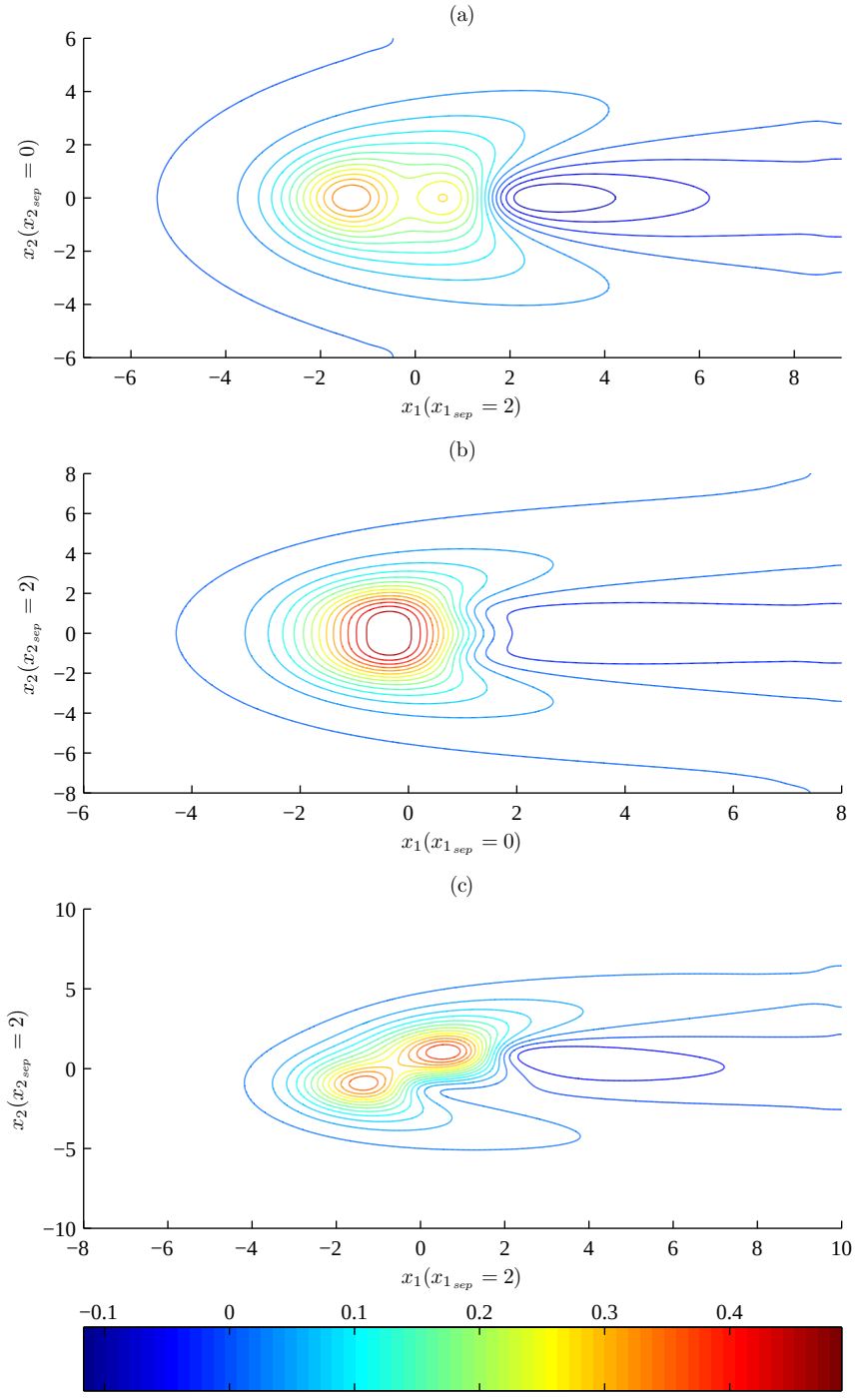

Figure 5.6: Contour plots for $(x_{1_{sep}}, x_{2_{sep}}) = (2,0), (0,2), (2,2)$. Flow is over two hemispheres of radius $a = 0.9$, attached to a plane inclined at $\alpha = 45^o$. The flow has a Bond number of $Bo = 1.0$.

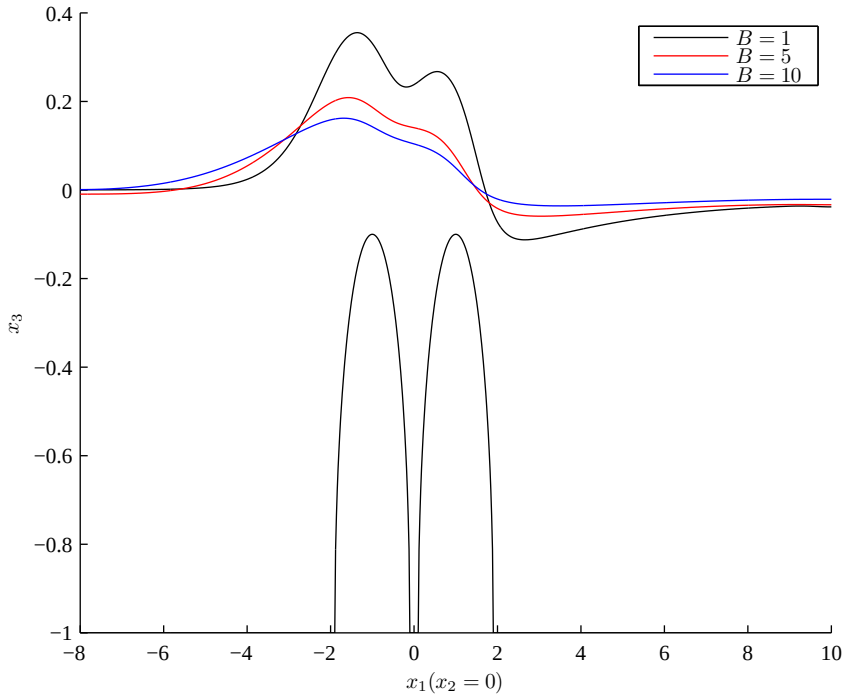

Figure 5.7: Centre line solution profiles for two hemispheres of radius $a = 0.9$, attached to a plane inclined at $\alpha = 45^o$ and separated by $x_{1_{sep}} = 2$. Results indicate the effect of varying the inverse Bond number B.

the plane angle is reduced. Consistent with the single obstacle case, the steeper the plane wall, the larger the peak that is formed.

Figure 5.9 gives the centre line ($x_2 = 0$) profiles for flow over two hemispheres separated by $x_{1_{sep}} = 2$ and with three differential radii; $a = 0.5, 1.3$, $a = 0.9, 0.9$, and $a = 1.3, 0.5$. When the obstacles are the same size ($a = 0.9, 0.9$), the flow exhibits two local peaks and a trough as the flow passes from the leading to the rear hemisphere. For the case of a small obstacle followed by a large obstacle ($a = 0.5, 1.3$) the flow appears to climb relatively slowly to a single peak over the downstream obstacle. For the case of a large obstacle followed by a small obstacle ($a = 1.3, 0.5$) the flow exhibits a large peak over the leading obstacle. However, in this case the formation of the trough shows a small kink over the rear obstacle. Interestingly the maximum peak heights for both cases of different sized hemispheres are approximately equal, and significantly greater than the

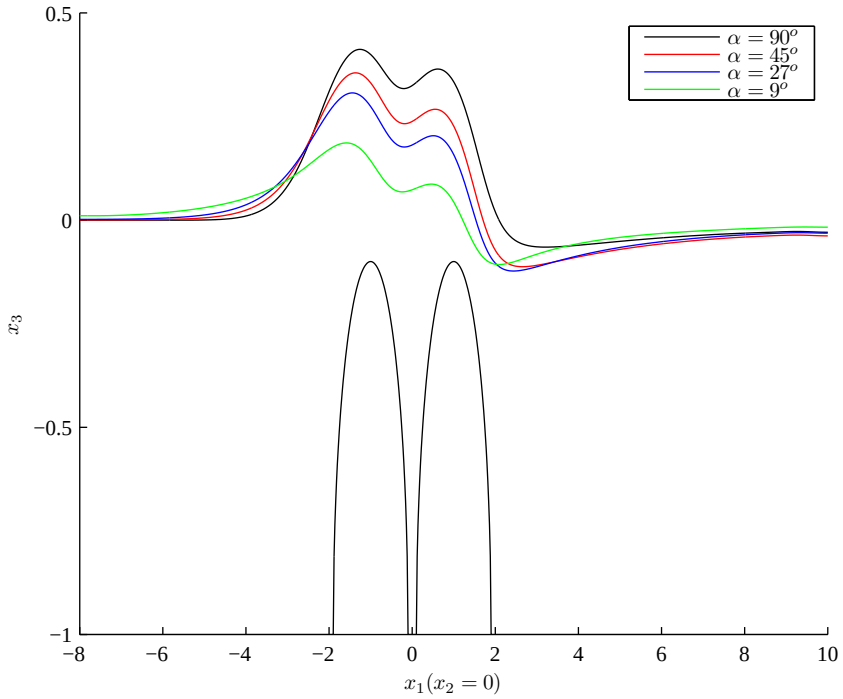

Figure 5.8: Centre line solution profiles for two hemispheres of radius $a = 0.9$ separated by $x_{1_{sep}} = 2$, showing the effect of varying the plane inclination angle α. The flow has an inverse Bond number of $B = 1.0$.

	Shallow ($\alpha = 5^o$) plane with $a = 1.05$	Steep ($\alpha = 90^o$) plane with $a = 1.60$
Single	0.0486	0.337
Double	0.0465	0.220

Table 5.1: Near point values (3.s.f.) for large hemispheres on shallow and steep planes.

case of equal hemisphere size; this suggests the peak height is strongly dependent on the maximum hemisphere radius. The corresponding film height for flow over a single hemisphere of radius $a = 1.3$ is provided allowing comparison with the dual hemisphere solutions. When the large hemisphere precedes the small hemisphere, flow over this obstacle shows negligible discrepancy to the single case. When the large hemisphere is the rear obstacle, a small difference to the single obstacle solution is present.

In § 4.3 it was found that the largest possible hemisphere containable within the fluid film was strongly dependent on the inclination of the plane. Profiles have been compared for

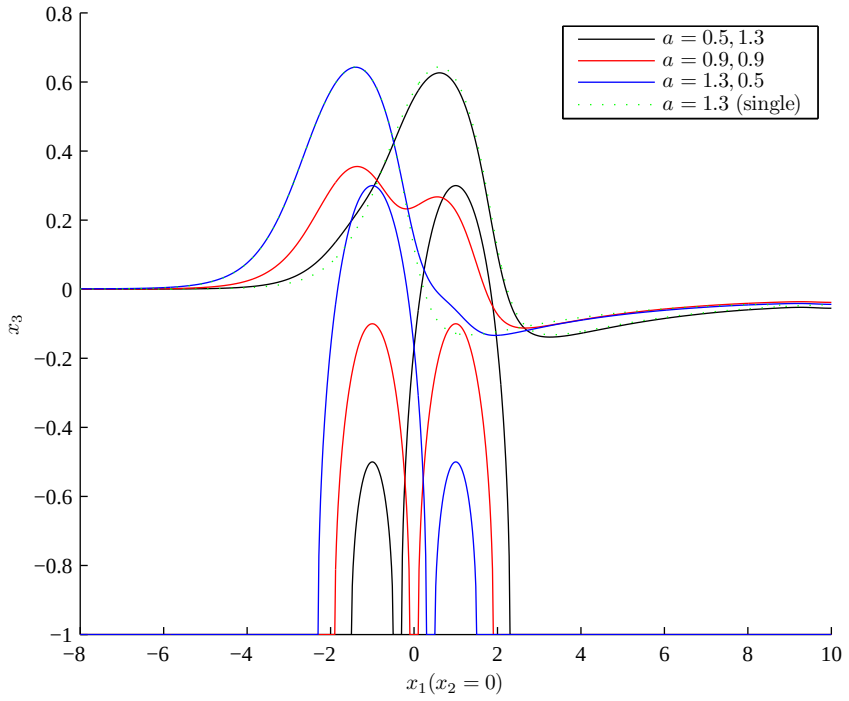

Figure 5.9: Centre line solution profiles for two hemispheres separated by $x_{1_{sep}} = 2$, indicating the effect of varying the two obstacles radii a. Flow is down a plane inclined at $\alpha = 45^o$, with an inverse Bond number $B = 1.0$. Dotted lines indicate a single hemisphere of radius $a = 1.3$.

a Bond number $Bo = 1$, and obstacle separation $x_{1_{sep}} = 4, x_{2_{sep}} = 0$. Table 5.1 indicates the smallest distance between the interpolated free surface and the obstacle for both a single and dual hemisphere configuration. Results on both the shallow and steep plane show this minimum distance is reduced when two obstacles are considered. For the shallow plane, hemispheres of radius $a = 1.05$ are modelled and only a minor reduction is noticed, as shown in figure 5.10a. For the steep plane, hemispheres of radius $a = 1.60$ are modelled and a significant reduction in the free surface/obstacle gap is found, as shown in figure 5.10b. It is noted that the results in § 4.3 are found using a different mesh for the same flow parameters as the results here, and this accounts for the small differences in solutions.

Centre line profiles for flow down a shallow plane corresponding to table 5.1 are shown

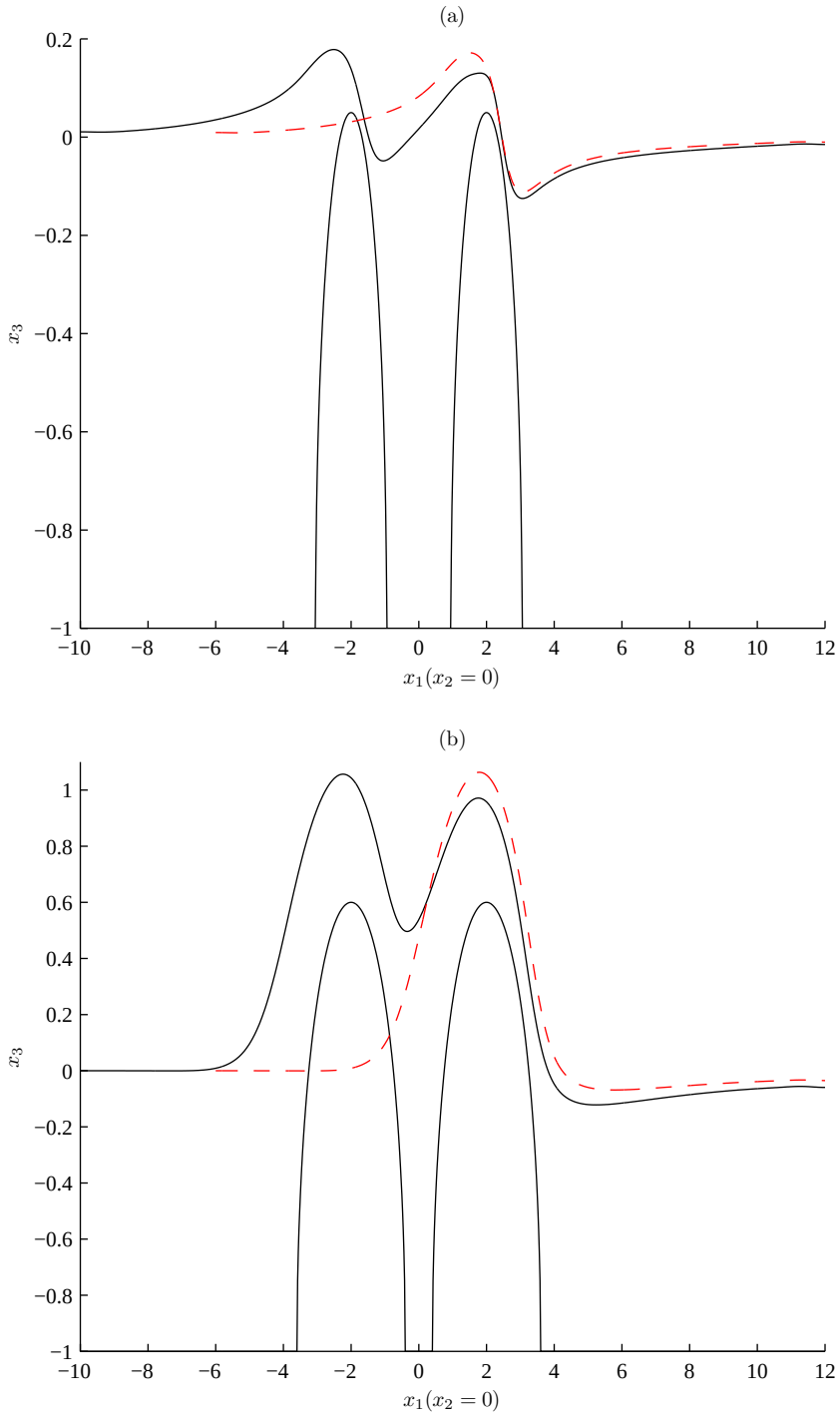

Figure 5.10: Centre line solution for flow over large hemispheres of radius (a) $a = 1.05$ attached to a shallow plane at $\alpha = 5^o$ (b) $a = 1.60$ attached to a steep plane at $\alpha = 90^o$. The Bond number of the flow in both cases is $Bo = 1.0$. Comparison is shown with a single hemisphere for both figures.

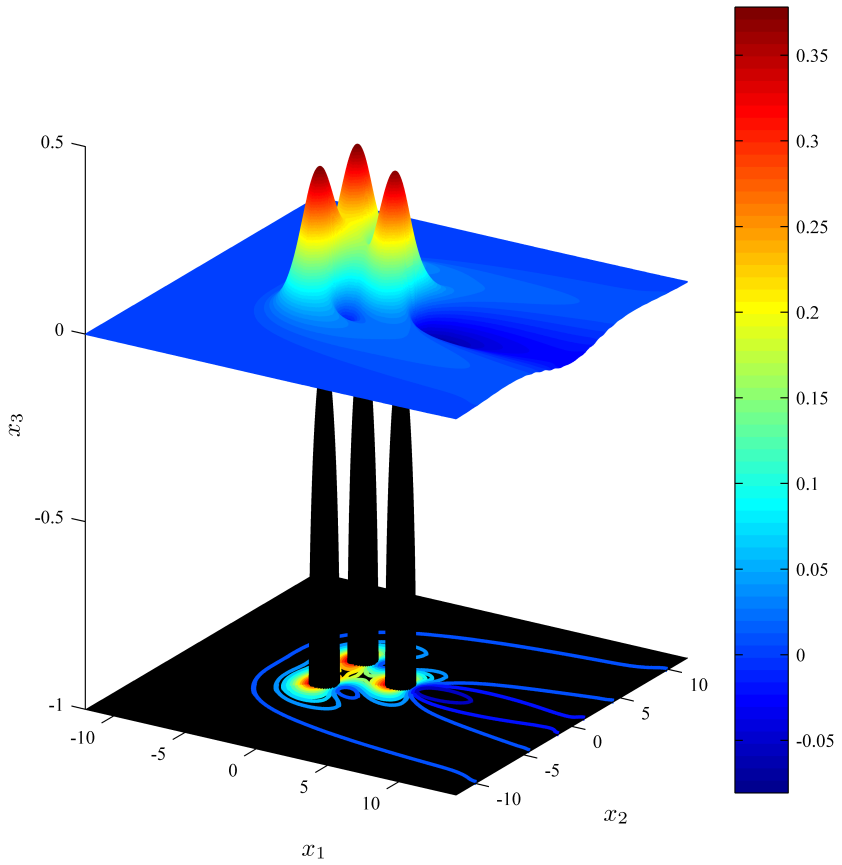

Figure 5.11: Three-dimensional solution profile for three hemispheres located at $(-2,-2)$, $(-2,2)$, $(2,0)$. The flow has a Bond number of $Bo = 1.0$, is down a plane inclined at $\alpha = 45^o$, and the hemispheres each have a radius of $a = 0.9$.

in figure 5.10a. Flow is down a plane inclined at $\alpha = 5^o$, and a minor reduction in the gap between the obstacle and free surface is found behind the rear hemisphere when compared with a single obstacle analysis. Centre line solutions for flow down a steep plane corresponding to the information in table 5.1 are shown in figure 5.10b. Flow is down a plane inclined at $\alpha = 90^o$, and a significant reduction in the near point values between the obstacle and free surface is found behind the rear hemispherical obstacle when compared with a single obstacle analysis.

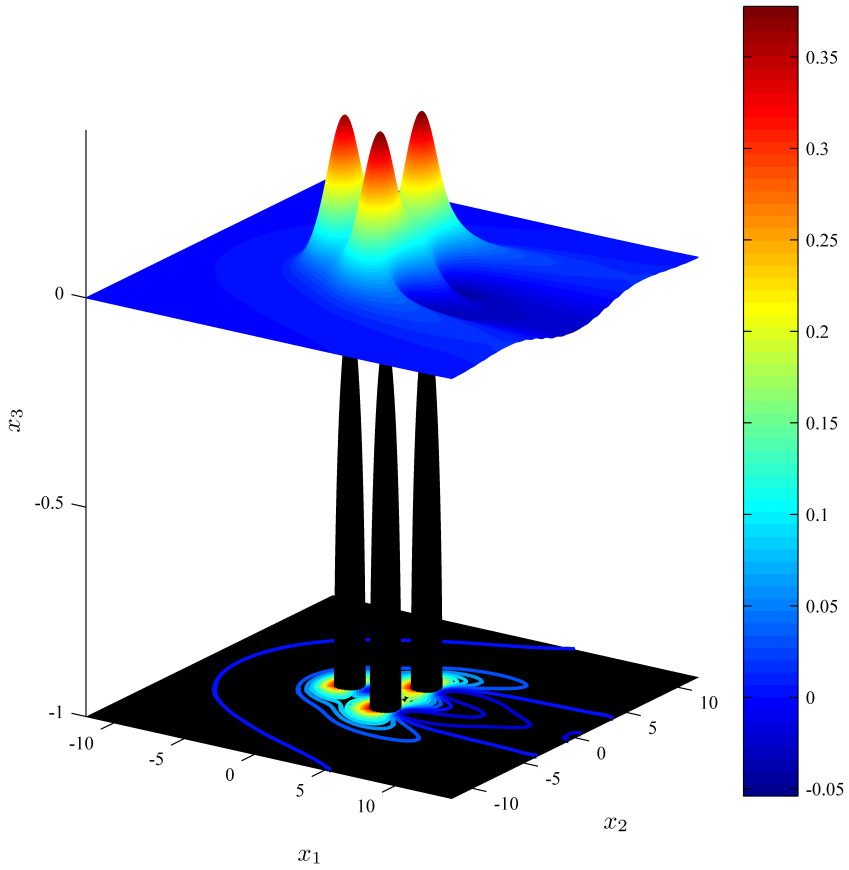

Figure 5.12: Three-dimensional solution profile for three hemispheres located at $(-2, 0)$, $(2, -2)$, $(2, 2)$. The flow has a Bond number of $Bo = 1.0$, is down a plane inclined at $\alpha = 45^o$, and the hemispheres each have a radius of $a = 0.9$.

5.3.2 Solutions For Flow Over Three Hemispheres

Illustration of flow over three hemispheres is now given for two obstacle configurations. Flow has a Bond number $Bo = 1$, all hemispheres have a radius of $a = 0.9$ and the plane is inclined at $\alpha = 45^o$. Obstacles are positioned in a symmetrical triangular array, with either a twin or single leading hemisphere configuration considered. A twin leading configuration is illustrated in figure 5.11 and consists of the upstream flow incident on two obstacles spaced perpendicularly to the flow direction with centres $(-2, -2), (-2, 2)$. This is followed by a trailing hemisphere centered at $(2, 0)$. The configuration shown in

figure 5.12 consists of the upstream flow incident on one obstacle centered at $(-2, 0)$ followed by two downstream hemispheres spaced perpendicularly to the flow direction with centres at $(2, -2), (2, 2)$. In both cases, three peaks are clearly seen just prior to each obstacle.

Chapter 6

Stokes Flow Around Obstacles

Flow profiles for thin film Stokes flow down an inclined plane over multiple obstacles in a range of configurations are considered. When these obstacles are increased in size they will eventually penetrate the film surface, leading to film flows around obstacles and adding another layer of complexity to the model. A contact angle constraint is imposed at the contact line within the radial basis function (RBF) interpolation, and the boundary integral equation (BIE) over the obstacle domain requires closing by addition of a top to the obstacle. Further details of the mathematical formulation are given in § 6.1. In addition, the obstacle requires re-meshing at each iteration, and a mesh must be generated for the top of the obstacle. Details of the numerical schemes implemented are given in § 6.2. Solution profiles for flow around single and multiple obstacles are produced in § 6.3, and the possibility of multiple solutions examined. These occur when a flow with fixed parameters may pass over or around an obstacle, and the resultant profile is dependent on the initial conditions. Multiple solutions are also examined in the case of two obstacles, to consider flow over then around an identical obstacle. All results shown in this chapter are for circular cylinders.

6.1 Mathematical Formulation

Stokes flow around obstacles adds an extra level of complexity to solving film flow problems compared to cases where the obstacles are fully submerged. Formulations in this section are developed from the consideration of flow over multiple obstacles in § 5.1. Modifications to the formulation involve the specification of an additional boundary condition imposing a contact angle at the free surface/obstacle intersections. In addition, solution of the integral equations for the undisturbed flow over the obstacle domains requires those domains to be closed. This is done by inclusion of an additional surface as the top of the obstacle.

For flow over N obstacles, no slip is imposed on each obstacle's wetted surface S_p^l, $l = 1, \ldots, N$ as defined in (5.1.1). In addition, a contact angle θ between the free surface and the obstacle boundary must be specified, which depends on the fluid/obstacle properties.

In two-dimensions, the contact angle at the point of intersection between two curves is well defined, and determined by the dot product between their corresponding tangent vectors. On the other hand, in three-dimensions the definition of the contact angle at a point on the contact curve of two intersecting surfaces is not uniquely specified since its value depends on how the contact point is approached from each surface. In some cases it is common to define the contact angle as a function of the unique angle between the normal vectors at a contact point.

In this work, as in the recent work by Sellier et al. [33], the following condition is imposed along the contact line at the obstacle surface

$$\frac{\partial h}{\partial x_i}\tilde{n}_i = \tan\left(\frac{\pi}{2} - \theta\right), \tag{6.1.1}$$

where $\tilde{n}_i$ is the outward unit normal of the obstacle and summation convention is applied.

Condition (6.1.1) is suitable to describe the contact line along the wall of a cylindrical

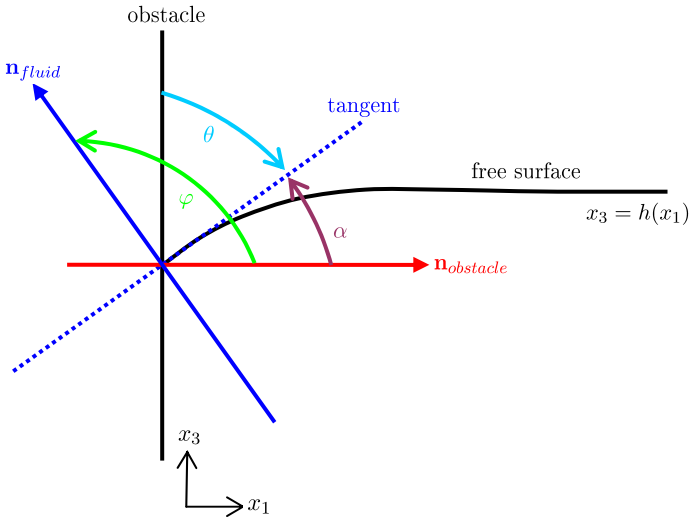

Figure 6.1: Schematic showing the two-dimensional definition of the contact angle.

obstacle with constant cross section, and located perpendicular to the undisturbed film profile, i.e. $\tilde{n}_3 = 0$. This condition is an extension to three-dimensions of the two-dimensional definition of the contact angle between a free surface and vertical wall, where the slope of the curve describing the free surface at the contact point is $\frac{\mathrm{d}h}{\mathrm{d}x_1} = \tan(\alpha) = \cot(\theta)$, and $\alpha = \frac{\pi}{2} - \theta$. The dot product of the normal vectors is $\cos(\varphi) = \cos(\pi - \theta) = -\frac{\mathrm{d}h}{\mathrm{d}x_1} / \sqrt{\left(\frac{\mathrm{d}h}{\mathrm{d}x_1}\right)^2 + 1}$, where the angle between the normal vectors is $\varphi = \frac{\pi}{2} + \alpha$, and therefore $\sin(\varphi) = 1/\sqrt{\left(\frac{\mathrm{d}h}{\mathrm{d}x_1}\right)^2 + 1}$. A schematic for the two-dimensional definition of the contact angle condition is shown in figure 6.1. Consequently, equation (6.1.1) gives the slope of the curve defined by the intersection between a normal plane to the cylinder, $\epsilon_{ijk}\tilde{n}_j\delta_{k3}$, and the free surface, at a contact point along the cylinder wall, i.e. the contact angle is a measure from the cylindrical wall to the free surface along a normal plane to the cylinder wall.

For flow around an obstacle, the integral formulation remains largely unchanged, but two additional terms are present in the boundary integral equations (BIEs). Figure 6.2 indicates a schematic of the nomenclature used for flow around a cylinder. The free surface is still labeled S_f along with the wetted obstacle surfaces S_p^l $l = 1, \ldots, N$. The obstacle domain is no longer closed solely by the wall S_w and the wetted obstacle surfaces

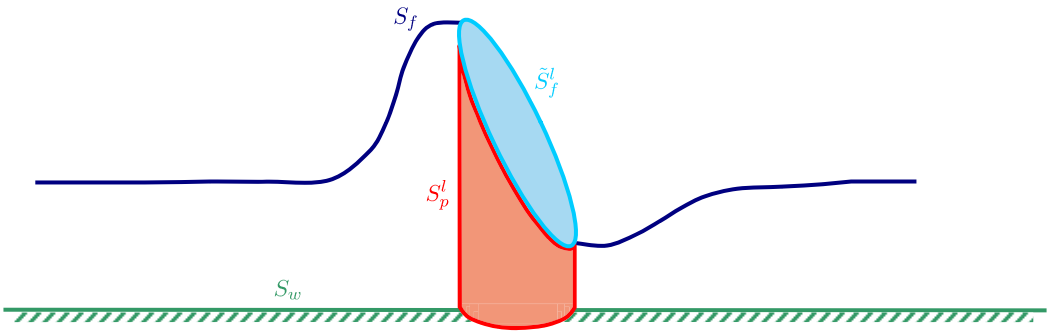

Figure 6.2: Schematic showing nomenclature for flow around the l^{th} cylinder.

S_p^l $l = 1, \ldots, N$, and thus virtual surfaces are introduced and labeled $\tilde{S}_f^l$.

To maintain the BIE formulation, (5.1.4) is modified to include integrals for the virtual surfaces $\tilde{S}_f^l$,

$$\begin{aligned} c_{ij}(\mathbf{x}_0)u_i^{\infty}(\mathbf{x}_0) = -\frac{1}{8\pi}\int\limits_{S_p^l \cup \tilde{S}_f^l} G_{ij}^*(\mathbf{x},\mathbf{x}_0)(f_i^{\infty}(\mathbf{x}) + Gn_i(\mathbf{x}))\mathrm{d}S(\mathbf{x}) \\ +\frac{1}{8\pi}\int\limits_{S_p^l \cup \tilde{S}_f^l} u_i^{\infty}(\mathbf{x})T_{ijk}^*(\mathbf{x},\mathbf{x}_0)n_k(\mathbf{x})\mathrm{d}S(\mathbf{x}). \end{aligned} \tag{6.1.2}$$

The BIE formulation for the disturbance variables over the fluid domain (5.1.3) is unchanged as the fluid film is not bounded by the virtual surfaces.

The term "virtual surface" is introduced as only the obstacle/fluid boundary S_p^l causes the film flow to deform. The resulting film profile is physically independent of the geometry of the virtual surface. The obstacle in all cases is bounded by the wall, the obstacle/fluid surface S_p^l, defined between the wall and the fluid/obstacle contact line, and the the virtual surface $\tilde{S}_f^l$. By similar derivations to those previously given in § 4.1 and § 5.1, two BIEs are derived, one collocated over the free surface S_f and one over the wetted obstacle surfaces S_p^l. The BIE used for collocating over the free surface (equivalent to

(5.1.5)) is

$$\begin{aligned}
\frac{1}{2}u_j^\delta(\mathbf{x}_0)+\frac{1}{8\pi}\int\limits_{S_f} u_i^\delta(\mathbf{x})T_{ijk}^*(\mathbf{x},\mathbf{x}_0)n_k(\mathbf{x})\mathrm{d}S(\mathbf{x}) \\
= \frac{1}{8\pi}\int\limits_{S_p^1\cup\ldots\cup S_p^N} G_{ij}^*(\mathbf{x},\mathbf{x}_0)\tilde{f}_i(\mathbf{x})\mathrm{d}S(\mathbf{x}) \\
+ \frac{1}{8\pi}\int\limits_{S_f} G_{ij}^*(\mathbf{x},\mathbf{x}_0)f_i^\delta(\mathbf{x})\mathrm{d}S(\mathbf{x}) \\
+ \frac{1}{8\pi}\int\limits_{\tilde{S}_f^1\cup\ldots\cup\tilde{S}_f^N} G_{ij}^*(\mathbf{x},\mathbf{x}_0)\left(f_i^\infty(\mathbf{x})+Gn_i(\mathbf{x})\right)\mathrm{d}S(\mathbf{x}) \\
- \frac{1}{8\pi}\int\limits_{\tilde{S}_f^1\cup\ldots\cup\tilde{S}_f^N} u_i^\infty(\mathbf{x})T_{ijk}^*(\mathbf{x},\mathbf{x}_0)n_k(\mathbf{x})\mathrm{d}S(\mathbf{x}) \qquad \mathbf{x}_0\in S_f.
\end{aligned} \tag{6.1.3}$$

For collocation of the obstacle surface a BIE (equivalent to (5.1.9)) is derived as

$$\begin{aligned}
\frac{1}{8\pi}\int\limits_{S_p^k} G_{ij}^*(\mathbf{x},\mathbf{x}_0)\tilde{f}_i(\mathbf{x})\mathrm{d}S(\mathbf{x}) + \frac{1}{8\pi}\int\limits_{S_p^1\cup\ldots\cup S_p^{k-1}\cup S_p^{k+1}\cup\ldots\cup S_p^N} G_{ij}^*(\mathbf{x},\mathbf{x}_0)\tilde{f}_i(\mathbf{x})\mathrm{d}S(\mathbf{x}) \\
= -u_j^\infty(\mathbf{x}_0) - \frac{1}{8\pi}\int\limits_{S_f} G_{ij}^*(\mathbf{x},\mathbf{x}_0)f_i^\delta(\mathbf{x})\mathrm{d}S(\mathbf{x}) \\
+ \frac{1}{8\pi}\int\limits_{S_f} u_i^\delta(\mathbf{x})T_{ijk}^*(\mathbf{x},\mathbf{x}_0)n_k(\mathbf{x})\mathrm{d}S(\mathbf{x}) \\
- \frac{1}{8\pi}\int\limits_{\tilde{S}_f^1\cup\ldots\cup\tilde{S}_f^N} G_{ij}^*(\mathbf{x},\mathbf{x}_0)\left(f_i^\infty(\mathbf{x})+Gn_i(\mathbf{x})\right)\mathrm{d}S(\mathbf{x}) \\
+ \frac{1}{8\pi}\int\limits_{\tilde{S}_f^1\cup\ldots\cup\tilde{S}_f^N} u_i^\infty(\mathbf{x})T_{ijk}^*(\mathbf{x},\mathbf{x}_0)n_k(\mathbf{x})\mathrm{d}S(\mathbf{x}) \qquad \mathbf{x}_0\in S_p.
\end{aligned} \tag{6.1.4}$$

In summary the steady, gravity driven Stokes flow down an inclined plane and around an obstacle is governed by solutions satisfying the BIEs (6.1.3) and (6.1.4), the kinematic condition (4.1.8) and the dynamic condition (4.1.7), along with the far field equations (4.1.5). As the obstacle protrudes through the free surface a contact line is present and the contact angle condition (6.1.1) is also required. Flows around obstacles are governed by: plane inclination angle α, the obstacle geometry, Bond number Bo and the contact angle θ.

6.2 Numerical Schemes

This section considers modifications to the numerical schemes used for a multiple obstacle Stokes flow analysis as outlined in § 5.2 for film flows around multiple obstacles. Developments in the numerical schemes involve meshing the circular cylindrical obstacles and free surface, along with incorporation of the contact angle constraint within the RBF interpolation of the free surface. Both of these are detailed later in respective subsections.

The iterative procedure for finding solutions to flow around multiple obstacles differs from that outlined for flow over an obstacle in § 4.2. The procedure used to obtain solutions in the present case of flow around multiple obstacles is defined below, with the unknown integral densities u_i^δ on S_f, and $\tilde{f}_i$ on $S_p^1 \cup \ldots \cup S_p^N$ obtained.

(i) Initially at the free surface elements mid-points $\mathbf{x}^m = (x_1^m, x_2^m)$, a film profile is defined by heights h with corresponding disturbance velocities u_i^δ.

(ii) The free surface heights h are interpolated using a radial basis function (RBF), incorporating the far field and contact angle condition, and used to find:

  (a) the heights at the nodal points of each free surface element $\mathbf{x}^n = (x_1^n, x_2^n)$;

  (b) the outward unit normal of the free surface at the element mid-points, $\mathbf{x}^m$;

  (c) the curvature of the free surface at the element mid-points, $\mathbf{x}^m$.

(iii) The contact line is found, and the wetted obstacle surface S_p^l is meshed from the wall S_w to the contact line. In addition a mesh for the top of the obstacle $\tilde{S}_f^l$ is also generated.

(iv) The disturbance boundary traction at the free surface element mid-points $\mathbf{x}^m$ is calculated by use of the dynamic condition (4.1.27).

(v) The obstacle boundary integral equations (BIEs) (6.1.4) are collocated over all

obstacles/fluid surfaces $S_p^k, k = 1, \ldots, N$ for tractions $\tilde{f}_i$. Solutions are obtained by using the boundary element method (BEM).

(vi) The free surface BIE (6.1.3) is collocated over S_f for the free surface disturbance velocities at each elements mid-points. It is noted that the height of the element mid-points are approximated within this BEM formulation by the average of the nodal point heights.

(vii) The kinematic condition (4.1.8) is applied with the current values of h and the calculated values of u_i^δ at element mid-points $\mathbf{x}^m$, to find an updated set of h defining the free surface.

(viii) The process is repeated from step 2 using the new film profile.

As outlined in chapter 4 for flow over an obstacle, the only place that the free surface height is approximated within the iterative solution procedure is for collocation over the free surface within the BEM. In all other calculations, the height at any mid element location is associated with the interpolated surface. This limitation is caused by implementing flat triangular elements within the BEM.

The numerical schemes required to solve the problem are now discussed. This includes forms for the meshes used for the free surface, and obstacle (including the wetted surface and the top of the obstacle), and the implementation of the RBF to evaluate the free surface position and various quantities such as curvature and unit normal, whilst constraining the contact angle (6.1.1). The BEM and near point integration schemes are implemented as described in § 4.2

6.2.1 Surface Discretizations

The obstacle/fluid boundaries, free surface, and virtual obstacle tops all require discretization. Circular cylinders are modelled throughout, satisfying the contact angle

constraint (6.1.1).

For circular cylindrical obstacles, the top edge of the cylinder was first considered with the circular perimeter of the cylinder discretized by a polygon of specified resolution and vertical lines subtended down its sides. In addition the height of the cylinder at each polygonal vertex was split evenly into a number of slices. The intersections of these two divisions form rectangular elements which were subdivided again into 4 triangular elements by connection of the diagonal vertices. Illustration of typical meshes for cylindrical cylinders are shown in figure 6.3. In cases for flow over and around a circular cylinder a form for the mesh on the top surface is required. The x_1x_2 element distribution of the top of the cylinder is generated by successive subdivision. This is slightly more complicated than the case of a hemisphere as it is only the outermost element sides that require translating onto the edge of the circle at each subdivision. At the end of the subdivision process the vertical position is defined depending on the case analyzed. For flow over a cylinder, each node is translated onto the sloped top of the cylinder, defined by its height at the upstream location $x_1 = -a$ and the downstream location $x_1 = a$. The height varies linearly in the x_1 direction between these two points. An example mesh for the cylinder in this case is shown in figure 6.3a. For flow around a cylinder, the top is defined by a RBF interpolation that also holds the normal gradients as zero on the outer edge of the cylinder. The functional values that require evaluation on the surface $\tilde{S}_f$ are calculated using an inward pointing normal as defined by the RBF interpolation. An example mesh for a cylinder with an interpolated top is shown in figure 6.3b.

Free surface meshes are modified from the earlier work considering flow over obstacles to allow the obstacle to penetrate the free surface. Formation of the meshes for both a single and multiple cylinder array is discussed below. In the case of a single cylinder the mesh is formed in a similar fashion to that outlined for the refined multiple hemisphere analysis in § 5.2. However, in the present case, there is no inner mesh and the transitional mesh is instead used to fit the discretized profile for the cylinder's contact line to the outer mesh. Again the outer mesh is constructed from elements of the size 1.0×1.0 as

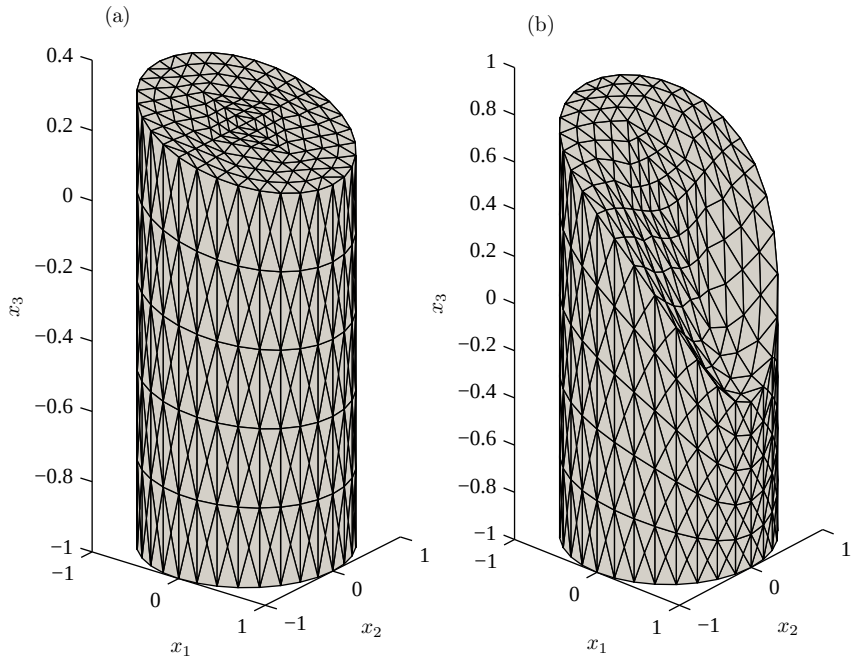

Figure 6.3: Typical mesh for a cylindrical obstacle, with (a) a truncated top and (b) an interpolated top.

found sufficient in earlier analysis. In each case the transitional mesh is formed by the input parameters of the number of elements used to extend from the cylinder wall to the outer mesh and the scaling of these elements. The choice of these parameters is made to give a reasonable conversion from the smaller, cylinder element size to the larger outer element size. A typical free surface mesh is shown in figure 6.4.

Free surface meshes for flow around multiple cylinders use alternative methods depending on the separation distance between the cylinders. If the cylinders are sufficiently far apart the mesh is formed by identical means to that outlined above, fitting the transitional meshes locally within the global outer mesh. However, if the transition meshes from each cylinder to the outer mesh overlap, then modification of this technique is required. An intermediate mesh with smaller element size than the outer mesh is defined. The cylinders are fitted to the intermediate mesh, and the intermediate mesh is then extended to the outer mesh in a similar way to the mesh formation for multiple hemispheres. Figure 6.5 indicates a typical free surface mesh for the case where flow is around 3 cylinders

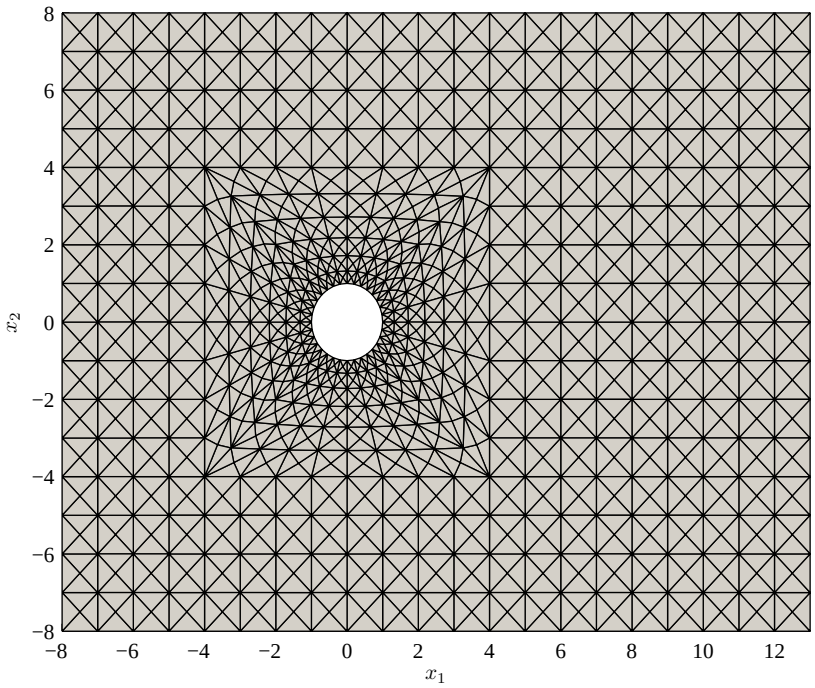

Figure 6.4: Typical free surface mesh for flow around a single cylinder of radius $a = 1.0$.

close to one another.

6.2.2 Radial Basis Function For Flow Around Cylinders

As for the case of flow over obstacles, a global Hermitian RBF interpolation of the fluid free surface is implemented. The RBF $\psi(\|\mathbf{x} - \boldsymbol{\xi}\|)$ allows incorporation of the far field derivative conditions and also the contact line condition for each obstacle that penetrates the free surface. As before the surface is interpolated using a thin plate spline RBF of the form $\psi = r^4 \log r$, where $r = \|\mathbf{x} - \boldsymbol{\xi}\|$, and is chosen to remove singularities of ψ at $r = 0$ for up to and including its third derivative. To guarantee invertibility, an additional polynomial of order 2 is required along with a homogeneous constraint condition.

The RBF can be used to constrain the free surface gradient at n far field points and n^{cl} contact line points. Surface displacements and derivatives $\frac{\partial h}{\partial x_1}$ and $\frac{\partial h}{\partial x_2}$ are represented

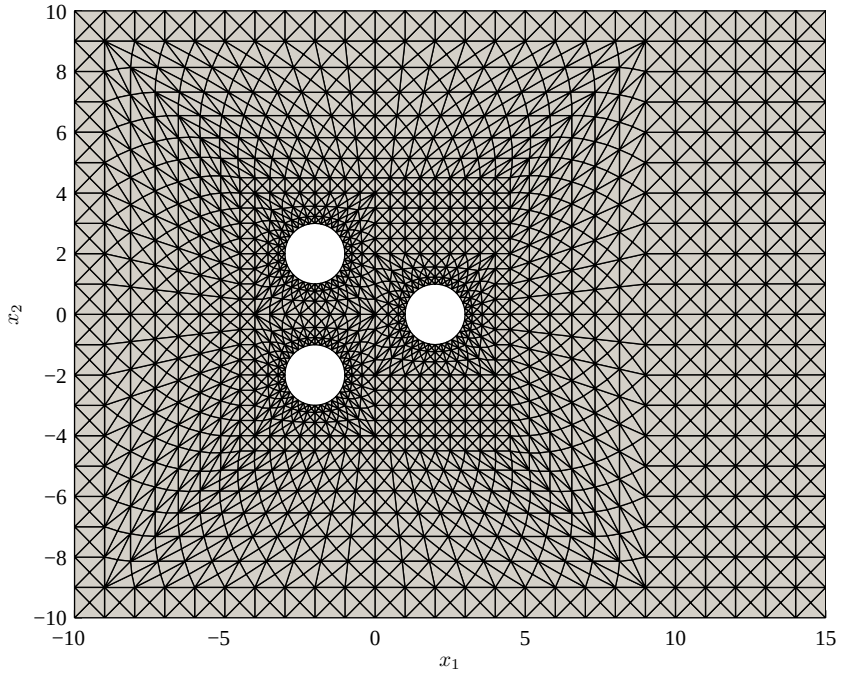

Figure 6.5: Typical free surface mesh for flow around multiple cylinder of radius $a = 1.0$.

by

$$h(x_1,x_2) = \sum_{j=1}^{N}\lambda_j\psi + \sum_{j=1}^{n}\lambda_{N+j}\frac{\partial\psi}{\partial\xi_1} + \sum_{j=1}^{n}\lambda_{N+n+j}\frac{\partial\psi}{\partial\xi_2} + \sum_{j=1}^{n^{cl}}\lambda_{N+n+n+j}\left(\tilde{n}_{\xi_1}\frac{\partial\psi}{\partial\xi_1} + \tilde{n}_{\xi_2}\frac{\partial\psi}{\partial\xi_2}\right) + P_2(\mathbf{x}), \tag{6.2.1}$$

$$\frac{\partial h}{\partial x_1} = \sum_{j=1}^{N}\lambda_j\frac{\partial\psi}{\partial x_1} + \sum_{j=1}^{n}\lambda_{N+j}\frac{\partial^2\psi}{\partial\xi_1\partial x_1} + \sum_{j=1}^{n}\lambda_{N+n+j}\frac{\partial^2\psi}{\partial\xi_2\partial x_1} + \sum_{j=1}^{n^{cl}}\lambda_{N+n+n+j}\left(\tilde{n}_{\xi_1}\frac{\partial^2\psi}{\partial\xi_1\partial x_1} + \tilde{n}_{\xi_2}\frac{\partial^2\psi}{\partial\xi_2\partial x_1}\right) + \frac{\partial P_2(\mathbf{x})}{\partial x_1}, \tag{6.2.2}$$

$$\frac{\partial h}{\partial x_2} = \sum_{j=1}^{N}\lambda_j\frac{\partial\psi}{\partial x_2} + \sum_{j=1}^{n}\lambda_{N+j}\frac{\partial^2\psi}{\partial\xi_1\partial x_2} + \sum_{j=1}^{n}\lambda_{N+n+j}\frac{\partial^2\psi}{\partial\xi_2\partial x_2} + \sum_{j=1}^{n^{cl}}\lambda_{N+n+n+j}\left(\tilde{n}_{\xi_1}\frac{\partial^2\psi}{\partial\xi_1\partial x_2} + \tilde{n}_{\xi_2}\frac{\partial^2\psi}{\partial\xi_2\partial x_2}\right) + \frac{\partial P_2(\mathbf{x})}{\partial x_2}. \tag{6.2.3}$$

The RBF interpolation forms a matrix representation $\tilde{h}_i = A_{ij}\lambda_j$ to be solved for the

unknowns λ_j. Matrix A_{ij} is given by,

$$A_{ij} = \begin{pmatrix} \psi & \frac{\partial\psi}{\partial\xi_1} & \frac{\partial\psi}{\partial\xi_2} & \tilde{n}_{\xi_1}\frac{\partial\psi}{\partial\xi_1} + \tilde{n}_{\xi_2}\frac{\partial\psi}{\partial\xi_2} & P_2 \\ \frac{\partial\psi}{\partial x_1} & \frac{\partial^2\psi}{\partial\xi_1\partial x_1} & \frac{\partial^2\psi}{\partial\xi_2\partial x_1} & \tilde{n}_{\xi_1}\frac{\partial^2\psi}{\partial\xi_1\partial x_1} + \tilde{n}_{\xi_2}\frac{\partial^2\psi}{\partial\xi_2\partial x_1} & \frac{\partial P_2}{\partial x_1} \\ \frac{\partial\psi}{\partial x_2} & \frac{\partial^2\psi}{\partial\xi_1\partial x_2} & \frac{\partial^2\psi}{\partial\xi_2\partial x_2} & \tilde{n}_{\xi_1}\frac{\partial^2\psi}{\partial\xi_1\partial x_2} + \tilde{n}_{\xi_2}\frac{\partial^2\psi}{\partial\xi_2\partial x_2} & \frac{\partial P_2}{\partial x_2} \\ A^1 & A^2 & A^3 & A^4 & A^5 \\ (P_2)^T & (\frac{\partial P_2}{\partial x_1})^T & (\frac{\partial P_2}{\partial x_2})^T & (A^5)^T & 0 \end{pmatrix}, \tag{6.2.4}$$

where terms A^1 - A^5 are given by,

$$A^1 = \tilde{n}_{x_1}\frac{\partial\psi}{\partial x_1} + \tilde{n}_{x_2}\frac{\partial\psi}{\partial x_2}, \tag{6.2.5}$$

$$A^2 = \tilde{n}_{x_1}\frac{\partial^2\psi}{\partial\xi_1\partial x_1} + \tilde{n}_{x_2}\frac{\partial^2\psi}{\partial\xi_1\partial x_2}, \tag{6.2.6}$$

$$A^3 = \tilde{n}_{x_1}\frac{\partial^2\psi}{\partial\xi_2\partial x_1} + \tilde{n}_{x_2}\frac{\partial^2\psi}{\partial\xi_2\partial x_2}, \tag{6.2.7}$$

$$A^4 = \tilde{n}_{x_1}\left(\tilde{n}_{\xi_1}\frac{\partial^2\psi}{\partial\xi_1\partial x_1} + \tilde{n}_{\xi_2}\frac{\partial^2\psi}{\partial\xi_2\partial x_1}\right) + \tilde{n}_{x_2}\left(\tilde{n}_{\xi_1}\frac{\partial^2\psi}{\partial\xi_1\partial x_2} + \tilde{n}_{\xi_2}\frac{\partial^2\psi}{\partial\xi_2\partial x_2}\right), \tag{6.2.8}$$

$$A^5 = \tilde{n}_{x_1}\frac{\partial P_2}{\partial x_1} + \tilde{n}_{x_2}\frac{\partial P_2}{\partial x_2}. \tag{6.2.9}$$

The obstacles unit normal at the point $\mathbf{x}^j$ is given by $\tilde{n}_{\mathbf{x}^j} = (\tilde{n}_{x_1^j}, \tilde{n}_{x_2^j})$, and the vector $\tilde{h}_i$ constructed from,

$$\tilde{h}_i = \begin{pmatrix} h & \frac{\partial h}{\partial x_1} & \frac{\partial h}{\partial x_2} & \tan\left(\frac{\pi}{2} - \theta\right) & 0 \end{pmatrix}^T. \tag{6.2.10}$$

The RBF yields the position of the element nodal points, the outward unit normal and the curvature.

A virtual top is generated to the obstacle that flow passes around, and this is also interpolated using a RBF. In this case the RBF is defined in terms of the contact line points, with the added constraint that the normal gradient of the cylinder around the contact line is zero. This analysis is a reduced version of the above problem (omitting the far field conditions, etc.) and no further details are presented. This interpolation

allows the inward unit normal to be found, necessary for evaluating the traction values on this surface, as used in BIEs (6.1.3) and (6.1.4).

6.3 Solution Profiles For Flow Around Obstacles

In this section results for flow around cylindrical obstacles on an inclined plane are presented. Results are initially shown for flow around a single cylinder on an inclined plane, with the possibility of solutions where both flow around and flow over an obstacle is valid, satisfying all requirements and demonstrating the possibilities of multiple solutions. Results for flow around multiple cylinders, and also the possibility of flow over, then around identical cylinders spaced in the direction of the incoming flow are presented.

6.3.1 Solutions For Flow Around Single Obstacles

Before results are produced, a mesh analysis was conducted on a free surface in the domain $-8 \leq x_1 \leq 10$ and $-8 \leq x_2 \leq 8$. The outer free surface mesh was based on 1.0×1.0 elements, found to be sufficient to describe large free surface deformations in chapter 4. Mesh considerations involve the number of vertical discretizations of the cylinder wall, and the resolution of the transitional mesh of the free surface connecting the cylinder to the outer meshes.

The obstacle discretization is governed by two key parameters, the circumferential discretization and the vertical discretization. Circumferentially, the cylinder is discretized 32 times, identical to that found optimal for the base of a hemisphere in earlier sections. Vertically, the cylinder was discretized into segments and profiles changed nominally with selection. Five vertical discretizations are used for the cylinder mesh, producing solutions which appear invariant to further refinement, and also helping to maintain the regularity of the mesh when large displacements are found between the upstream and

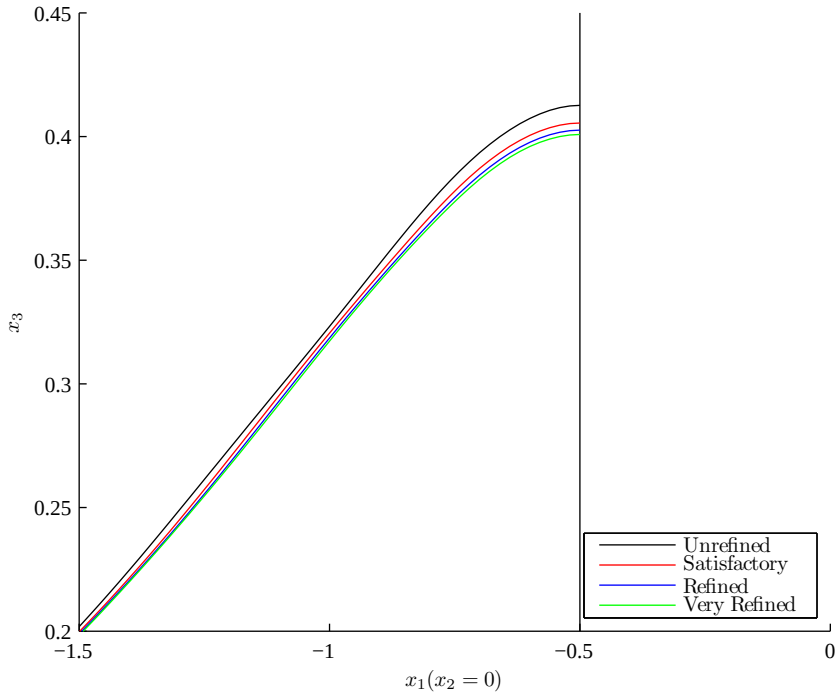

Figure 6.6: Centre line solution at the upstream edge of the cylinder indicating the transitional mesh resolutions described in table 6.1 for flow around a cylinder of radius $a = 0.5$.

downstream contact position on the obstacle.

The transitional mesh of the free surface involves a more complicated analysis. Input parameters involve the number of elements used to extend from the cylinder wall to the outer mesh and the scaling of these elements, so that they can be biased towards the cylinder wall. Four cases were considered with the number of elements and scaling values for each analysis shown in table 6.1. Solutions for these four transitional mesh resolutions are shown in figure 6.6.

All transitional mesh regimes are found to give accurate portrayals of the global flow profile. However, the effects of the contact line condition on the flow profile local to the cylinder is marginally affected by the transitional mesh resolutions used, especially for the case of an unrefined transitional discretization. As the mesh is progressively refined the solutions tend towards a converged solution. However, it is found that use of

	Number of Elements	Transitional Element Scaling Factor
Unrefined	4	0.60
Satisfactory	5	0.60
Refined	6	0.65
Very Refined	7	0.70

Table 6.1: Transitional free surface mesh regimes.

the "refined" mesh (see table 6.1 and figure 6.6) is adequate to accurately represent the flow regime around the cylinder and it is this transitional mesh resolution that is used throughout for cylinders of radius $a = 0.5$. For larger cylinders, the transitional mesh is changed but each time analyzed to maintain a similar resolution of elements as found sufficient for the $a = 0.5$ case considered here. For some results, the far field is extended to help maintain convergence and sufficient decay of the free surface disturbance.

Figure 6.7 shows the full free surface for flow around a cylinder of radius $a = 2.0$. The flow was down a plane inclined at $\alpha = 45^o$ and the film has a Bond number $Bo = 0.89$ corresponding to an inverse Bond number of 1 as defined in (4.3.1) and used by Blyth and Pozrikidis [31]. The contact angle at the cylinder walls was constrained to $\theta = 90^o$. A typical obstacle mesh can be seen in figure 6.3.

Figure 6.8 shows the streamlines for flow around a circular cylinder attached to a plane inclined at 45^o. The cylinder has a radius of $a = 0.5$ with a contact angle condition of $\theta = 90^o$ specified on the cylinder wall. The flow has an inverse Bond number of $B = 1$. Streamlines close to the cylinder are deflected upwards, as well as around the cylinder. In addition, as with the film profiles, solutions show symmetry about the plane $x_2 = 0$.

Figure 6.9a illustrates solutions for a range of inverse Bond numbers B. Flow is down a plane inclined at $\alpha = 45^o$ around a cylindrical obstacle of radius $a = 0.5$. The free surface/obstacle interface was modelled by a contact angle of $\theta = 90^o$. Increasing the inverse Bond number (i.e. raising the ratio of surface tension forces to gravitational

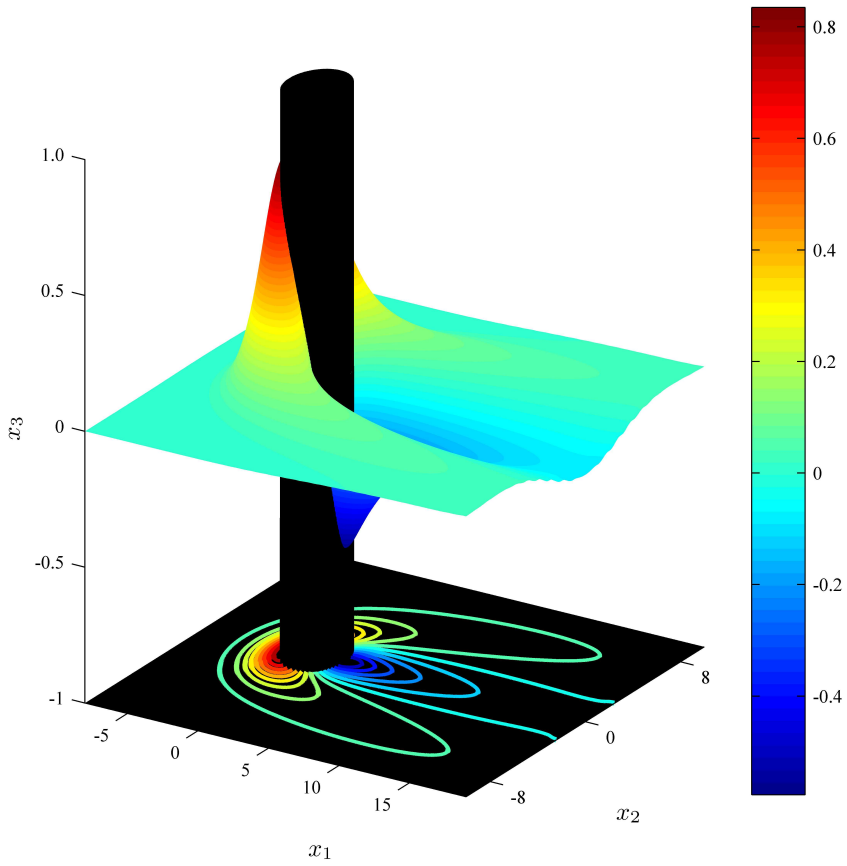

Figure 6.7: Three-dimensional solution profile for flow around a large cylinder of radius $a = 2.0$. The plane is inclined at $\alpha = 45^o$, the contact angle is set to $\theta = 90^o$ and the inverse Bond number is $B = 1$.

forces) results in a flattening of the centre line profiles. The far field truncation is extended for large B due to the large distances required for the free surface to return to a completely flat profile in these cases. In addition the deepest point behind the obstacle moves from the cylinder wall further downstream for the cases of large B. This is due to the relatively large upstream peak forcing fluid on the downstream edge of the obstacle up the cylinder wall due to the strength of the surface tension. Values of the maximum and minimum film deflection are given in figure 6.9b for a fixed geometry and indicate the dependence of film deflection on inverse Bond number B, corresponding to the results in figure 6.9a. Results show a similar trend to flow over a hemisphere, as shown in figure 4.18. As the the inverse Bond number increases, the amplitude of both

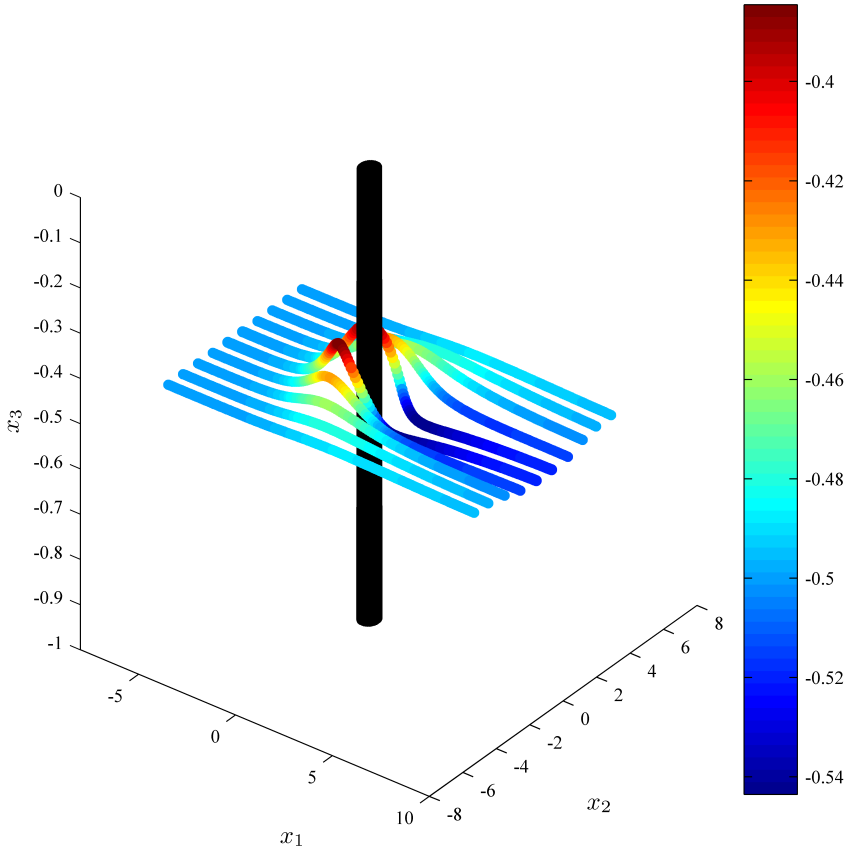

Figure 6.8: Pattern of streamlines starting at $x_3 = -0.5$ upstream of the cylinder and for a range of x_2 locations. Flow is around a circular cylinder of radius $a = 0.5$, on a plane inclined at $\alpha = 45^o$. The flow has an inverse Bond number of $B = 1$ and the contact angle is $\theta = 90^o$.

the peak and trough deflection decrease. The peak heights are affected more severely due to the higher curvature values in this region of the free surface. In addition, values for peak height and trough depth appear to tend towards constant values as B is increased.

Figure 6.10 shows the contact line profile around the cylinder wall for the range of inverse Bond numbers B depicted in figure 6.9. Raising the inverse Bond number flattens the flow profiles around the cylinder wall. Intersection of the contact line profiles occurs over a relatively small range of angular positions along the cylinder, between $0.67 - 1.06$ radians upstream of the position $x_1 = a$.

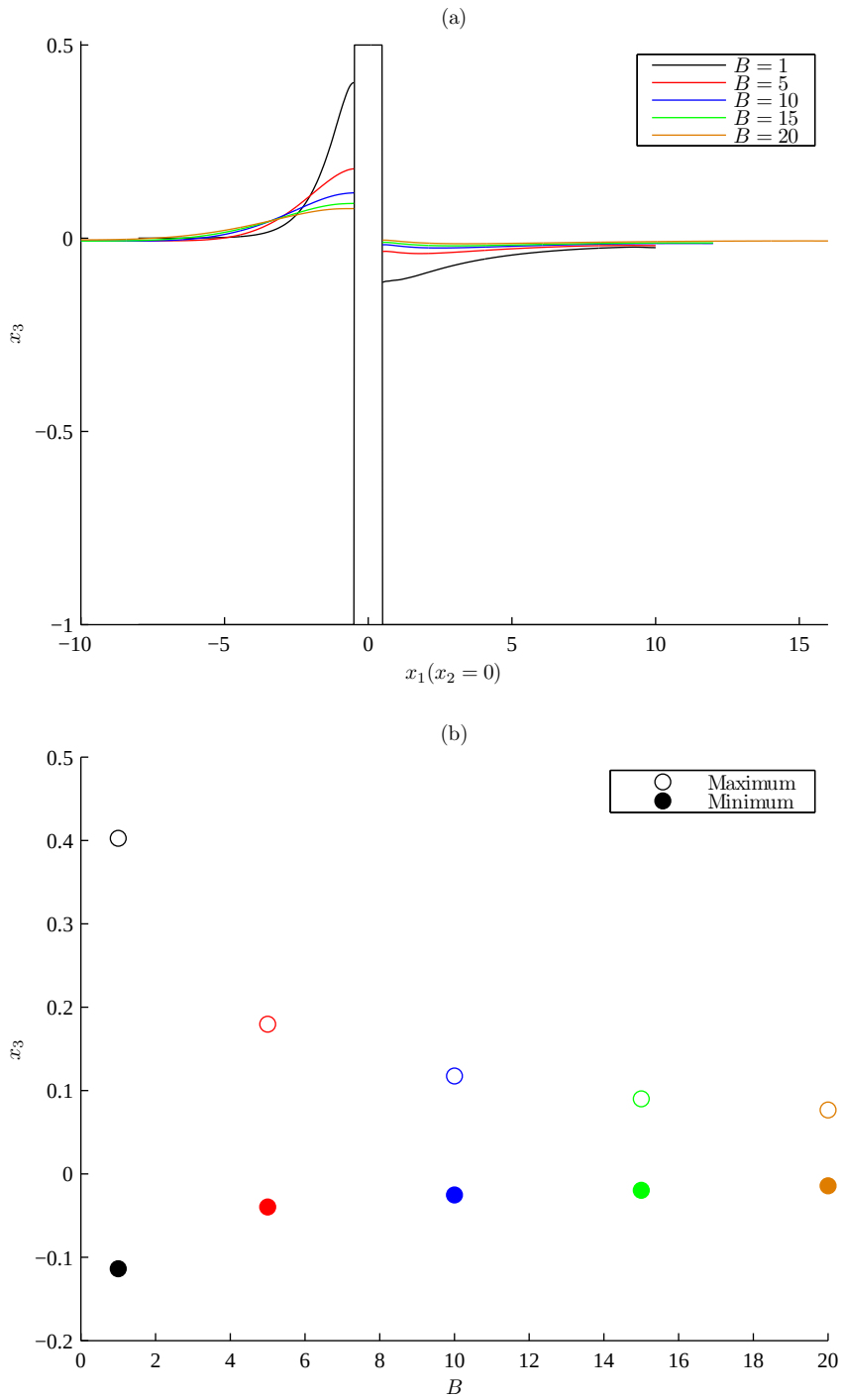

Figure 6.9: Solutions for flow at various inverse Bond number B, down an inclined plane at $\alpha = 45^o$ around a cylinder of radius $a = 0.5$ and contact angle $\theta = 90^o$. Part (a) shows centre line free surface elevations and (b) values of maximum and minimum deflection as inverse Bond number changes.

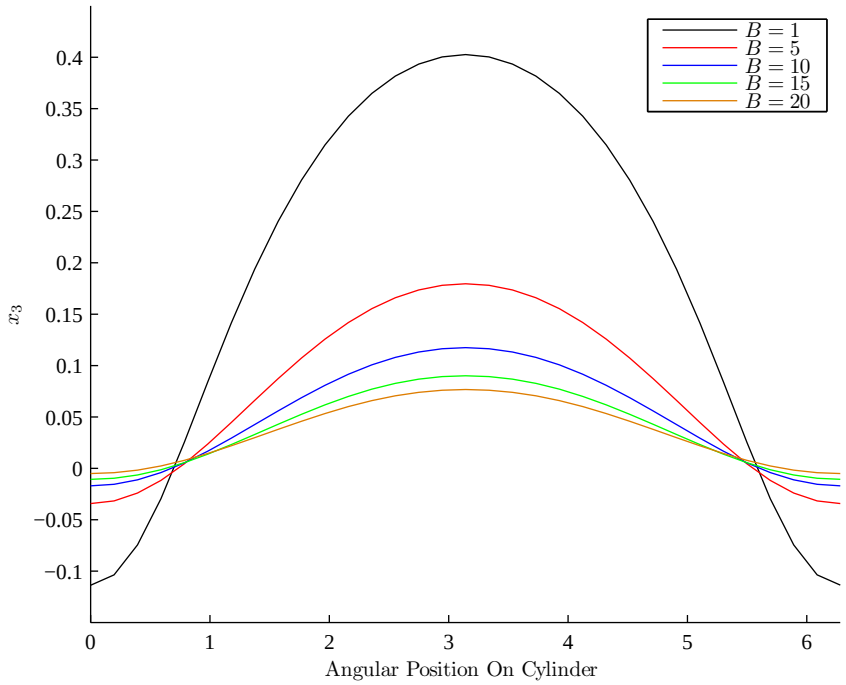

Figure 6.10: Contact line solutions for free surface deflections on a plane inclined at $\alpha = 45^o$ around a cylinder of radius $a = 0.5$. The flow has various values for inverse Bond number B. The contact angle at the cylinder wall is $\theta = 90^o$.

Figure 6.11a illustrates solutions for a range of plane inclination angles α. Flow is for an inverse Bond number $B = 1$ and around a cylindrical obstacle of radius $a = 0.5$. The free surface/obstacle interface was modelled by a contact angle of $\theta = 90^o$. Increasing the inclination angle results in a raising of the peak before the obstacle. The trough depth behind the obstacle varies depending on the wall angle used. This is in comparison with the earlier results for flow over hemispheres where a steeper plane inclination resulted in a shallower trough behind the obstacle. The peak location in front of the obstacle is unaffected by a decrease in plane angle. Figure 6.11b illustrates the dependence of maximum and minimum film height on plane inclination angle, α, as seen in figure 6.11a. The values of peak film height follow a similar trend to the results for flow over a hemisphere as shown in figure 4.19. As the plane angle is increased the maximum film height increases, but at a progressively slower rate. The minimum film height does not

follow the monotonic trend of figure 4.19; the trough is seen to initially deepen as the plane inclination is raised, before becoming progressively less shallow.

Figure 6.12 illustrates the contact line profile around the cylinder wall for the range of inclination angles depicted in figure 6.11. The steep planes cause a raise in the contact height upstream of the obstacle.

Figure 6.13a shows the smoothed centre line solutions for flow around a range of cylinders with varying radii. Flow is for an inverse Bond number $B = 1$ and down a plane inclined at $\alpha = 45^o$. The obstacle was chosen to be neutrally wetting, (i.e. the contact angle was $\theta = 90^o$). Increasing the cylinder radius results in a raising of the peak before the obstacle and a deepening of the trough behind it. This is a similar trend to that found earlier, and shown in figure 4.9. Figure 6.13b shows values of maximum and minimum film deflection for solutions shown in figure 6.13a, indicating the dependence of film deflection on cylinder radius, a. There is an approximately linear dependence for both cases, with the maximum film height increasing and the minimum film height decreasing, with cylinder radius.

Figure 6.14 illustrates the contact line profile around the cylinder wall for the range of cylinder radii depicted in figure 6.13. The large cylinders cause a rise in the contact height upstream of the obstacle and a lowering of the contact height downstream. Interestingly, intersection of the contact line profiles occurs at an approximately fixed angular position along the cylinder, between $0.94 - 0.98$ radians upstream of the position $x_1 = a$. Further refinement of the mesh around the cylinder may cause this range of angular position to diminish.

Figure 6.15a shows the smoothed centre line solutions for flow around a cylinder of radius 0.5. Flow is for an inverse Bond number $B = 1$ and down a plane inclined at $\alpha = 45^o$. The solutions show a range of wetting and non-wetting flow configurations corresponding to a range of contact angles θ. Decreasing the contact angle results in a raising of both the peak height before the obstacle and the trough behind it. In

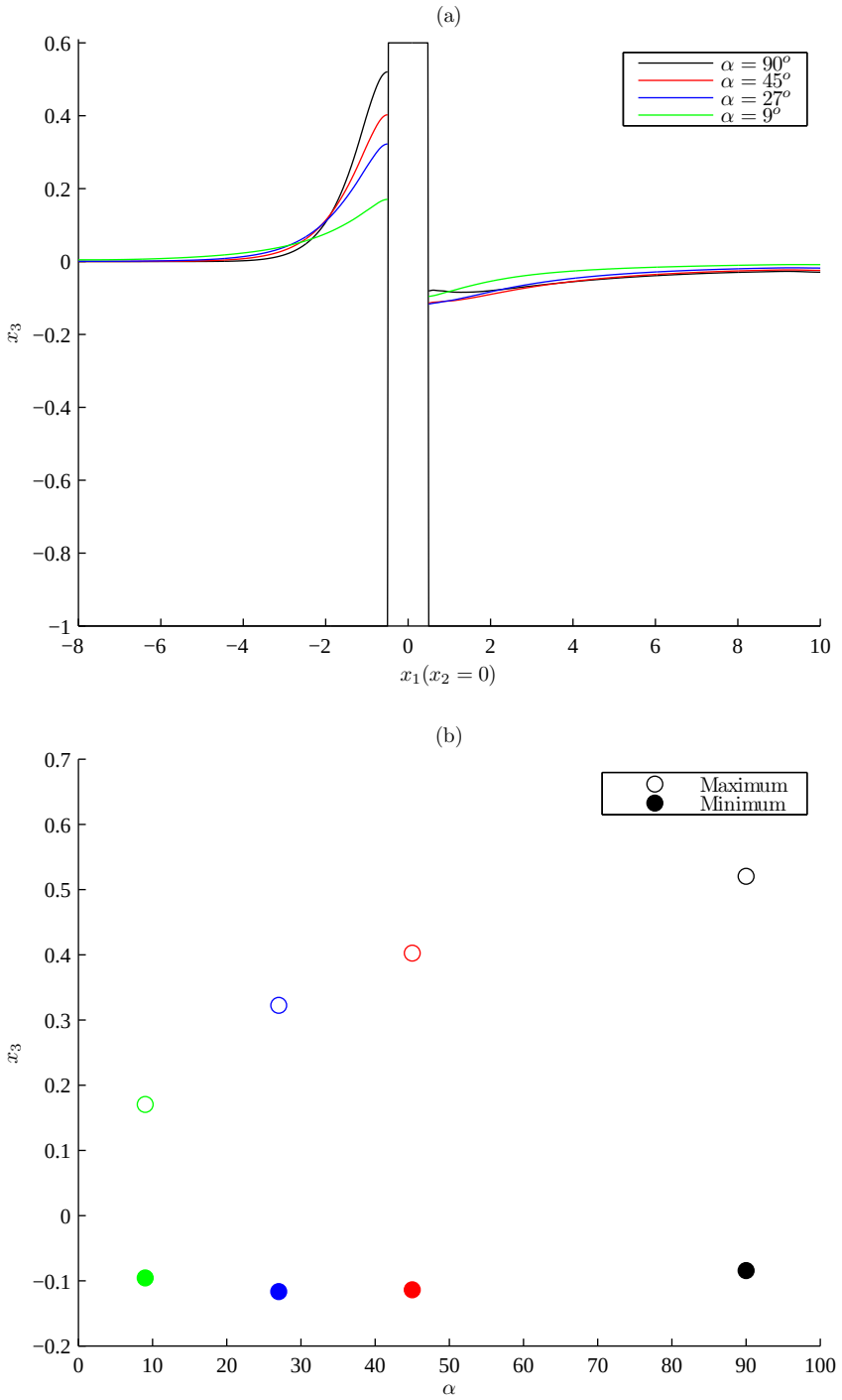

Figure 6.11: Solutions for flow around a cylinder of radius $a = 0.5$ and contact angle $\theta = 90^o$ with an inverse Bond number $B = 1$ and down a plane of various inclinations. Part (a) indicates the centre line solutions and (b) values of maximum and minimum deflection as the plane inclination changes.

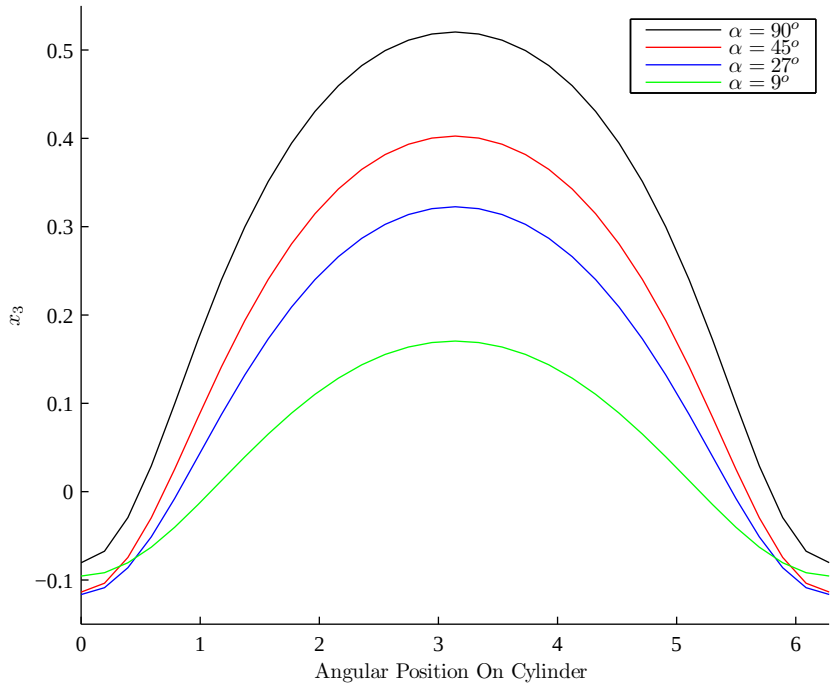

Figure 6.12: Contact line solutions for free surface deflections for flow down a plane at various inclination angles and around a cylinder of radius $a = 0.5$. The flow has an inverse Bond number of $B = 1$ and the contact angle at the cylinder wall is $\theta = 90^o$.

addition for wetting obstacles, maximum peak height occurs on the cylinder wall instead of a small distance from the cylinder. In contrast the non-wetting obstacles cause the minimum of the trough to occur at the cylinder instead of a small distance downstream of the obstacle. Figure 6.15b shows the trend of maximum and minimum film height for contact angle θ, with values corresponding to the results in figure 6.15a. Results show that for $\theta \leq 90^o$, the maximum heights decrease approximately linearly with increasing θ, and corresponds to film profiles where the peak occurs at the cylinder wall. Maximum heights for $\theta > 90^o$ decrease at a slower rate, corresponding to peak film heights occurring away from the cylinder wall. For $\theta < 90^o$ but increasing, the trough depth decreases at a slow rate, corresponding to cases where the film minimum occurs away from the cylinder wall. For $\theta \geq 90^o$, minimum heights decrease more quickly, and approximately linearly with increasing θ, corresponding to results where the film minimum occurs against the

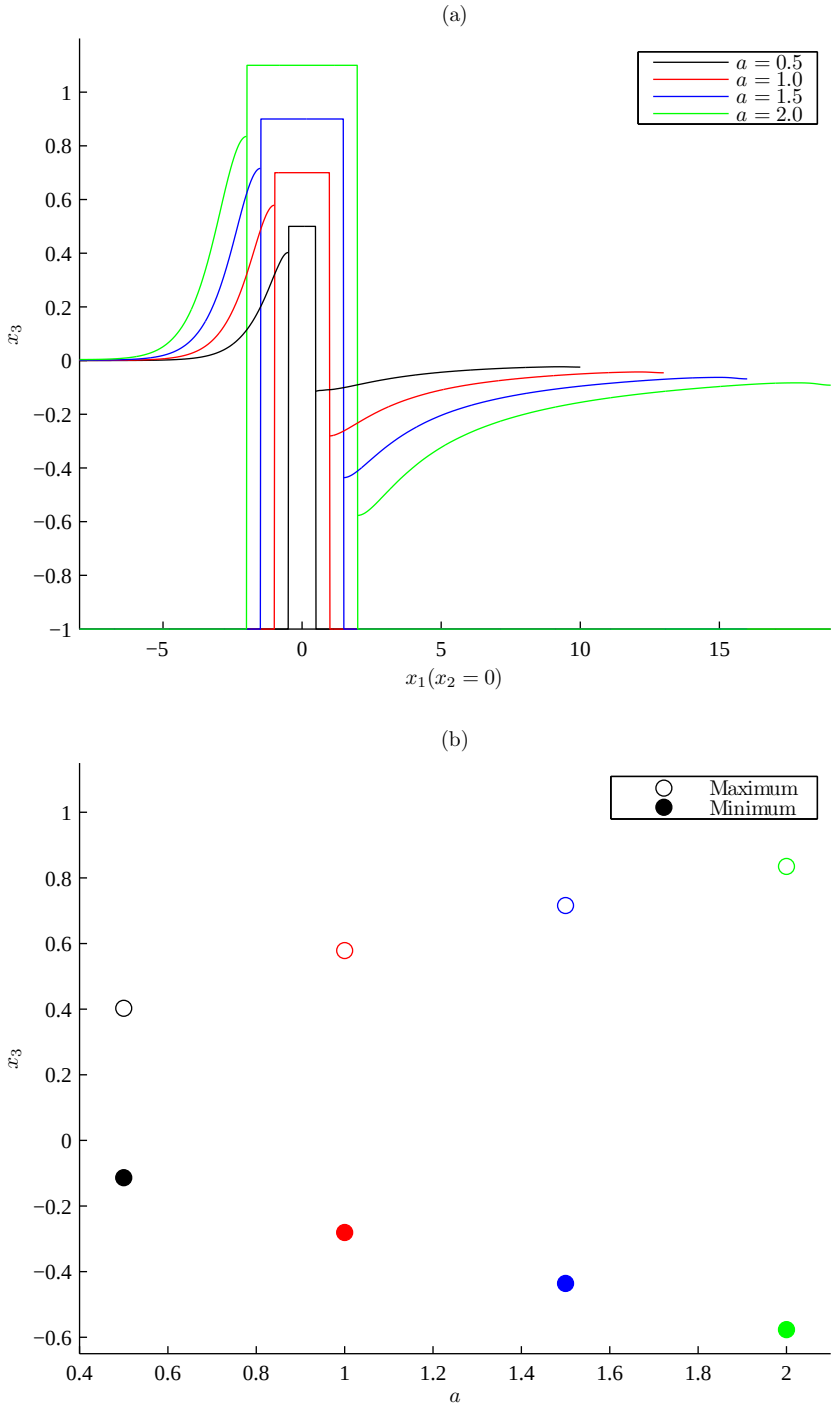

Figure 6.13: Solutions for flow around a cylinder of varying radius, with inverse Bond number $B = 1$, plane inclination of $\alpha = 45^o$ and contact angle of $\theta = 90^o$. Part (a) indicates the centre line solutions and (b) values of maximum and minimum deflection as cylinder radius changes.

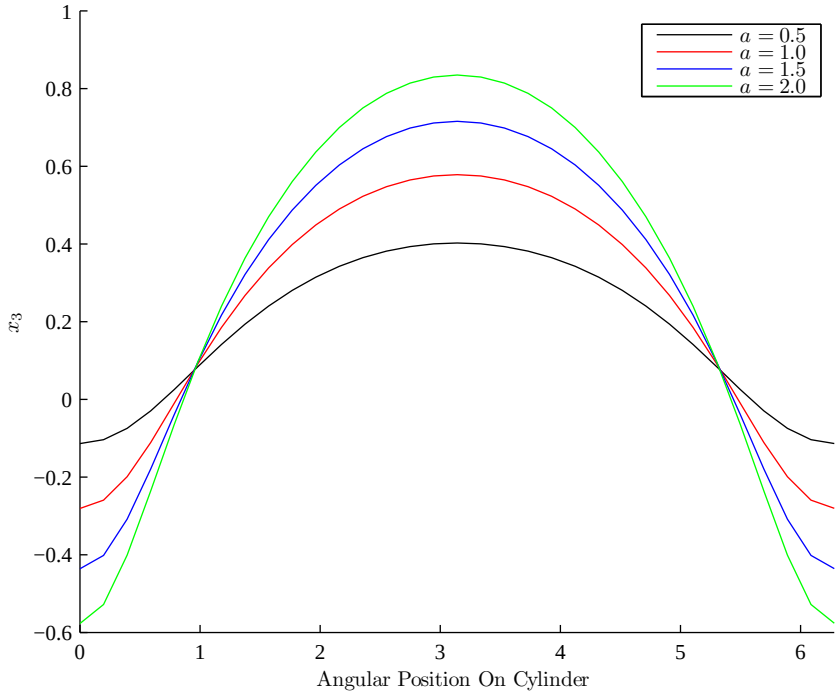

Figure 6.14: Contact line solutions for free surface deflections around a cylinder of varying radius, with inverse Bond number $B = 1$ and down a plane inclined at $\alpha = 45^o$. The contact angle at the cylinder wall is $\theta = 90^o$.

cylinder wall.

Figure 6.16 shows the contact line profiles around the cylinder wall for the range of contact angles depicted in figure 6.15. As the contact angle is raised, the contact line profile becomes sharper due to its greater effect downstream than upstream of the cylinder.

6.3.2 Multiple Solutions

The existence of multiple solutions for flow down a vertical plane will be demonstrated. Multiple solutions occur, when for the same flow parameters (i.e. Bond number, plane angle and obstacle geometry), flow can either exist completely submerging the obstacle or flowing around the obstacle. Take $\alpha = 90^o$, $Bo = 1$ and a cylinder radius $a = 0.5$, and for flow around a cylinder the static contact line angle is set at $\theta = 105^o$. The

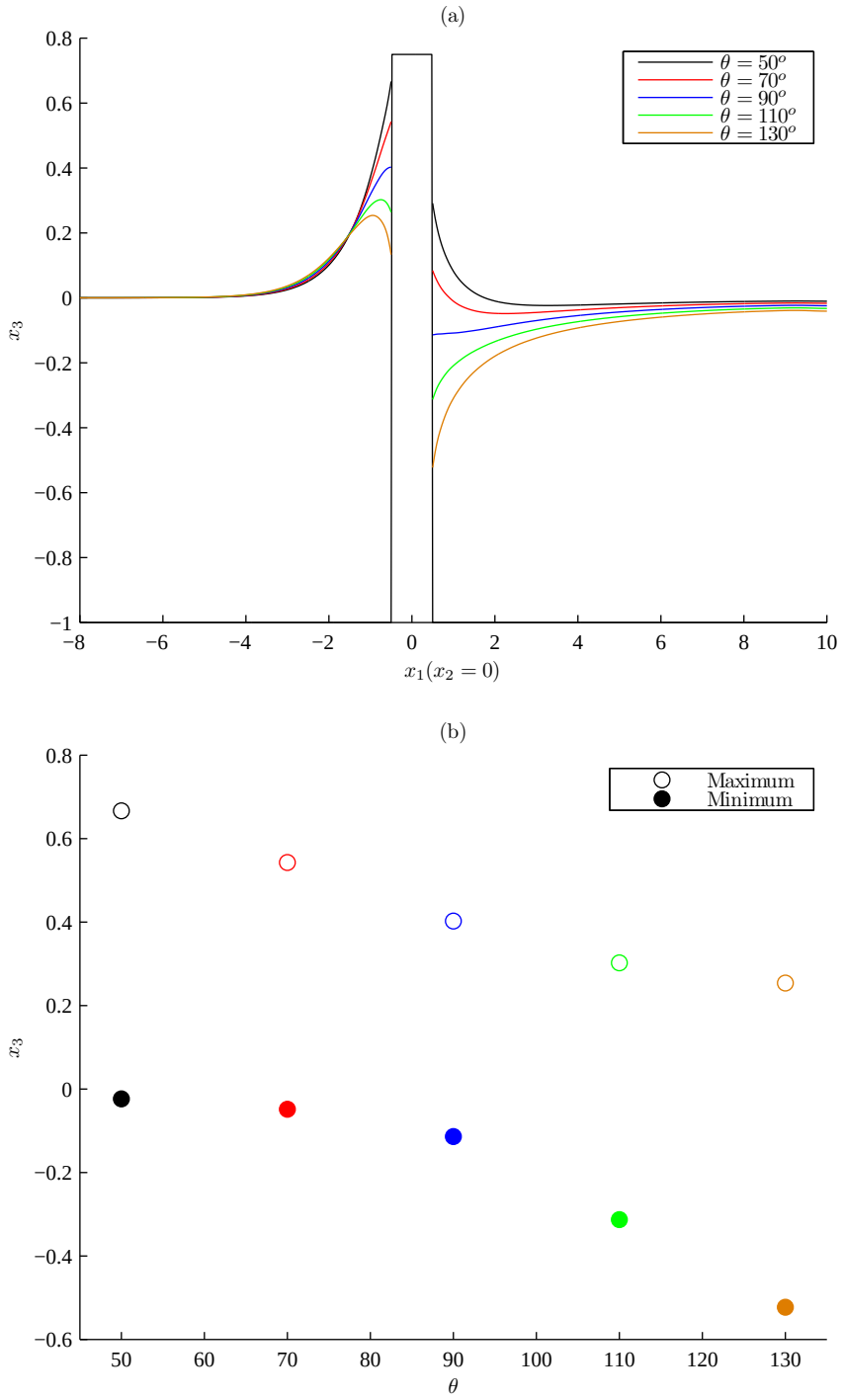

Figure 6.15: Solutions for various contact angles applied at the cylinder of radius $a = 0.5$ attached to a plane inclined at $\alpha = 45^o$. The flow has an inverse Bond number $B = 1$. Part (a) indicates the centre line solutions and (b) values of maximum and minimum deflection for various contact angles.

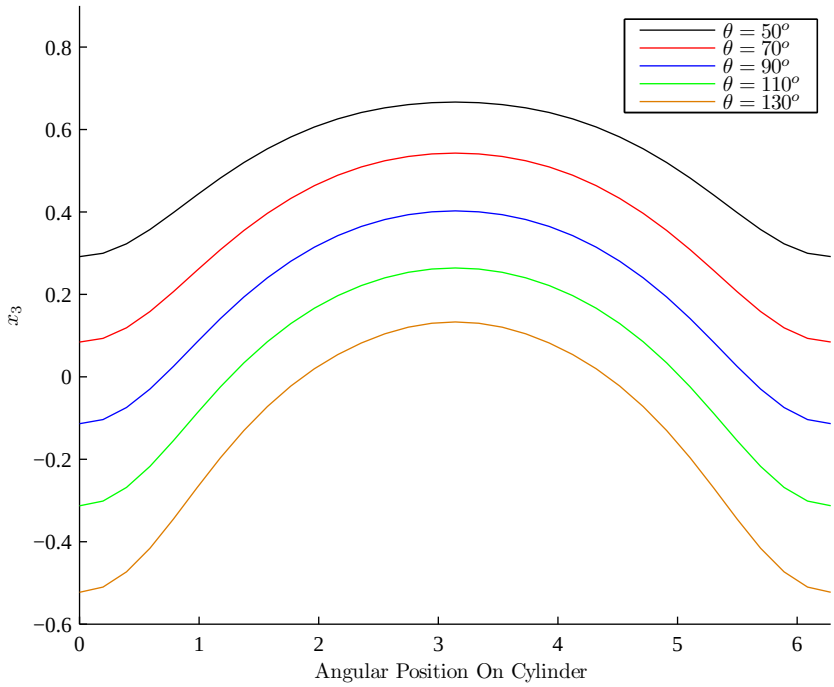

Figure 6.16: Contact line solutions for various contact angles at the cylinder wall. The free surface deflections are around a cylinder of radius $a = 0.5$ on an inclined plane at $\alpha = 45^o$ and the flow has an inverse Bond number $B = 1$.

free surface was solved in the domain $-8 \leq x_1 \leq 10$ and $-8 \leq x_2 \leq 8$ with the zero gradient far field conditions implemented. For the outer mesh, and for the complete flow-over mesh the surface was discretized into 36×32 elements (neglecting an inner refined region for the flow-over discretization). The previous transitional mesh for flow around the cylinder was retained, utilizing 6 elements with scaling factor 0.65. The cylinder was discretized by splitting the walls into five rows of elements, and the circumferential mesh (and top) of the cylinder was generated by four successive subdivisions. For flow over the cylinder, a parameter continuation method is adopted as for the case of large hemispherical obstacles already considered. This allows the cylinder to be increased above the undisturbed film height, allowing multiple solutions to be found.

Figure 6.17 indicates that the flow profile around a cylinder is below the top of the truncated cylinder used to obtain flows over a cylinder. The truncated cylinder varies

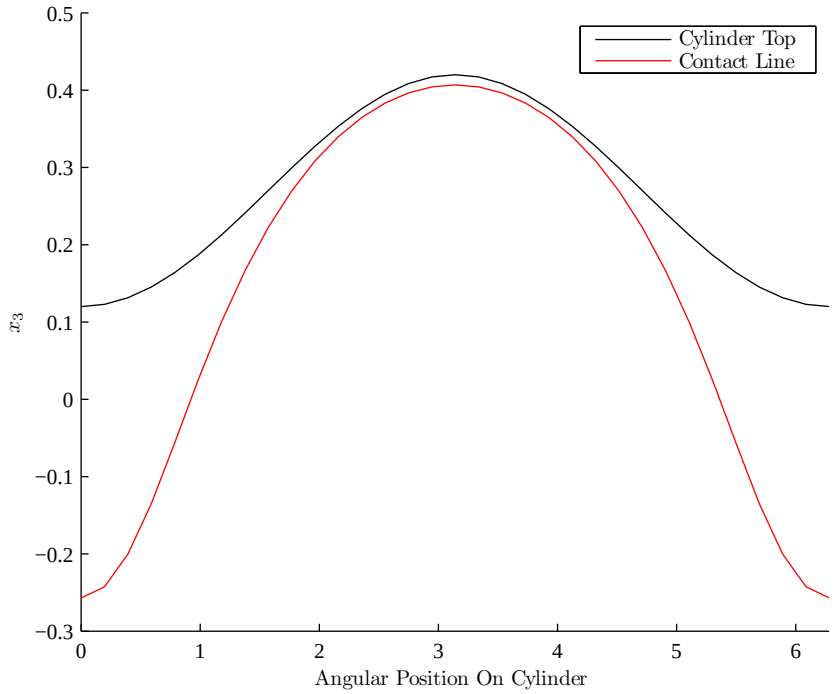

Figure 6.17: Comparison of the sloped cylinder top between $x_3 = 0.42$ and $x_3 = 0.12$, and contact line for flow around the cylinder of radius $a = 0.5$. The flow is down a vertical plane ($\alpha = 90^o$), with a Bond number $Bo = 1.0$, and a contact angle of $\theta = 105^o$.

linearly between $x_3 = 0.42$ and $x_3 = 0.12$. Thus multiple solutions exist for this set of flow parameters. Figure 6.18 indicates the corresponding centre line solutions for $x_2 = 0$ and $x_1 = 0$. The flow intersected by the obstacle is subject to a 105^o contact angle, and as such it is clearly seen that any more severely non-wetting obstacle can exhibit multiple solutions in this scenario.

For flow over or around a given cylinder, the existence of multiple solutions for varying flow parameters can be examined. Analysis is conducted for a cylinder of radius $a = 0.5$ with top sloped linearly in the x_1 direction between heights $x_3 = 0.3$ and $x_3 = 0.0$. The cylinder geometry is fixed and possible multiple solutions obtained for variations in the inverse Bond number B, and plane inclination angle α. For flow around the cylinder, three contact angles are analyzed, $\theta = 90^o, 105^o, 120^o$. Possible multiple solutions are

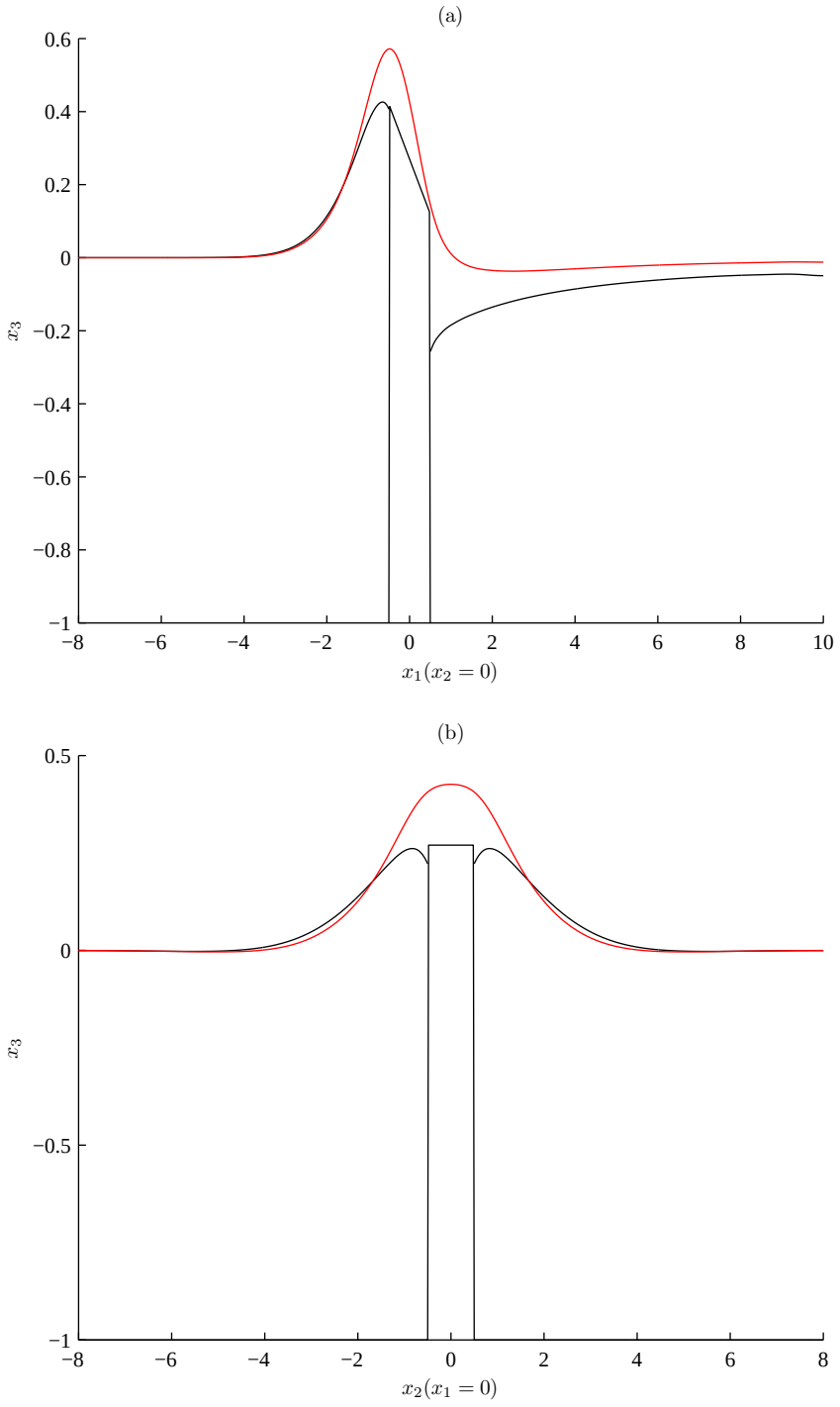

Figure 6.18: Centre line solutions in the (a) x_1 and (b) x_2 direction for flow over and around a cylinder of radius $a = 0.5$ and top sloped linearly between $x_3 = 0.42$ and $x_3 = 0.12$. The flow is down a vertical plane ($\alpha = 90^o$), with a Bond number $Bo = 1.0$ and the contact angle is $\theta = 105^o$.

characterized by the maximum film height of the fluid flow.

Figure 6.19 provides a map of solutions, characterized by maximum film height, for flow over or around the prescribed cylinder for variations in the inverse Bond number B. The plane inclination is fixed at $\alpha = 90^o$. Black lines indicate results for flow over the cylinder, and coloured lines results for flow around the cylinder for the three selected contact angles. Results are produced for the values of B indicated in the figure. For flow over the cylinder, an inverse Bond number of $B = 1$ is considered, and progressively increased. Numerical simulations are successful up to and including $B = 1.6$, with the numerical method found to fail within the region $1.6 < B \leq 2$. This is indicated in the figure by $| \rightarrow$ and is a consequence of the free surface impinging on the top of the truncated cylinder. For flow around the cylinder, results are obtained for $B = 5$, and the inverse Bond number is progressively reduced until the flow no longer remains below the top edge of the cylinder with failure indicated in the figure by $\leftarrow |$. For $\theta = 90^o$ results are obtained for $B \geq 3.5$, with failure in the region $3 \leq B < 3.5$ and for $\theta = 105^o$ results are found for $B \geq 1.6$, with failure in the region $1.2 \leq B < 1.6$. When a contact angle of $\theta = 120^o$ is used, results are obtained for all B considered. For values of $B \leq 1.6$, two distinct solution are possible corresponding to both flow over and flow around a circular cylinder of finite height. In all cases the regions of failure can be refined by evaluation of the flow at a greater number of inverse Bond numbers.

Figure 6.20 indicates the existence of possible twin solutions, characterized by maximum film height, for flow over or around the prescribed cylinder for variations in the plane inclination angle α. The inverse Bond number of the flow is constrained to $B = 1$. A black line indicates results obtained for flow over the cylinder, and coloured lines results for flow around the cylinder with the three different contact angles prescribed. Results are produced for the values of α indicated in the figure. When flow is over the cylinder, a plane inclination of $\alpha = 90^o$ is considered, and progressively reduced. Numerical simulations are successful for plane angles down to and including $\alpha = 54^o$, with failure of the numerical method in the region $45^o \leq \alpha < 54^o$. This is indicated in the figure

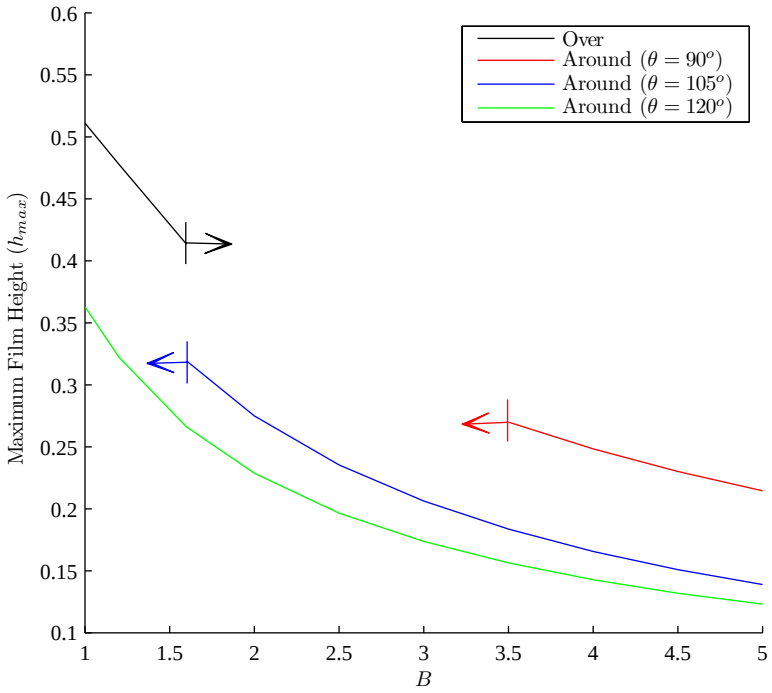

Figure 6.19: Map of possible solutions for flow down a vertical plane ($\alpha = 90^o$), over and around a cylinder of radius $a = 0.5$ with top sloped between $x_3 = 0.3$ and $x_3 = 0.0$. Results are illustrated by maximum film height, $h_{\max}$ at a given inverse Bond number B for three different contact angles.

by $\leftarrow |$ and is a consequence of the free surface impinging on the top of the truncated cylinder. For flow around the cylinder, results are obtained for $\alpha = 9^o$, and the plane is progressively steepened until the flow no longer remains below the top edge of the cylinder, with failure indicated in the figure by $| \rightarrow$. For $\theta = 90^o$ results are obtained for $\alpha \leq 18^o$ with failure in the region $18^o < \alpha \leq 27^o$ and for $\theta = 105^o$ results are produced for $\alpha \leq 36^o$ with failure within $36^o < \alpha \leq 45^o$. When a contact angle of $\theta = 120^o$ is used, results are obtained for all plane angles considered. For values of $\alpha \geq 54^o$ both solution for flow around and over the cylinder are obtained, identifying the possibility of multiple solutions. Refinement of the failure regions can be achieved by evaluation of flows at a greater number of plane inclination angles.

Failure to produce solutions in the cases considered in figures 6.19 and 6.20 corresponds

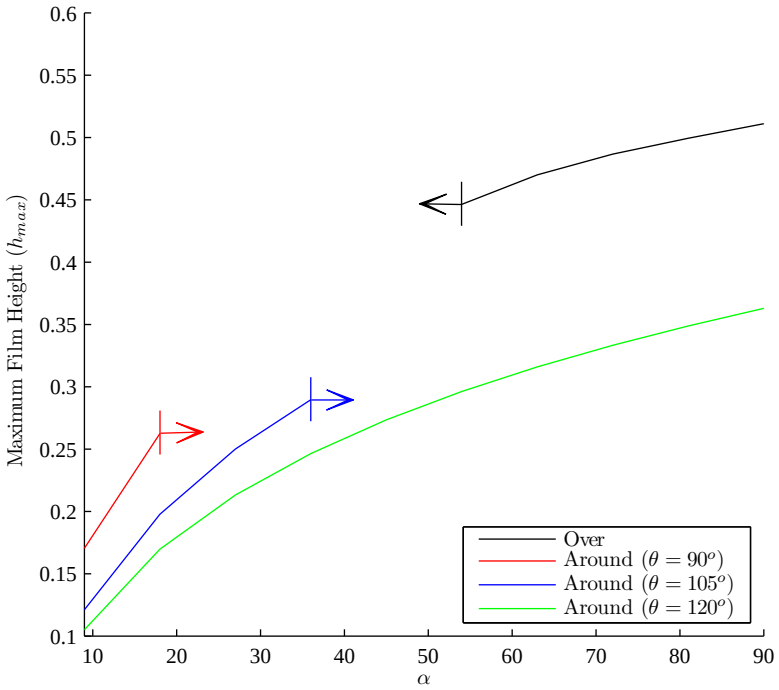

Figure 6.20: Map of possible solutions for flow with an inverse Bond number of $B = 1.0$, over and around a cylinder of radius $a = 0.5$ with top sloped between $x_3 = 0.3$ and $x_3 = 0.0$. Results illustrate maximum film height, $h_{\max}$ at a given plane inclination angle α, for three different contact angles.

to non-convergence of the iterative approach when finding the position of the contact line. As commented before, in the case of flow over the cylinder the solution breaks down when the free surface approaches the top surface of the cylinder given that in its formulation no contact condition is considered. On the other hand, the case of flow around the cylinder is more complex since as the film thickness grows the contact line can move from the cylinder wall to its top surface, with the possibility that the wall and part of the top are simultaneously wetted. The numerical formulation for flow around obstacles presented in this chapter, only considers cases where the contact line is defined along the cylinder wall (see comments given after equation (6.1.1)), and therefore the wetting of the top surface of the cylinder cannot be predicted. It appears that in the cases considered for flow around the cylinder, the breakdown of the solution occurs when the flow condition is such that the fluid tends to overcome the obstacle, partially wetting the top of the

cylinder (dry spot). The results reported in figures 6.19 and 6.20 are consistent with this condition; in the case of $\theta = 90^o$ the maximum film height is found at the contact line and consequently failure is expected when the maximum film height approaches the top of the cylinder, i.e. $h_{\max} \cong 0.3$, while in cases when $\theta > 90^o$ (non-wetting condition) the maximum film height is found inside the fluid domain, in front of the cylinder, with a smaller value at the contact line (see figures 6.15 and 6.16). Therefore, as reported in figures 6.19 and 6.20 for non-wetting conditions, it is possible to have a maximum film height larger than the cylinder height without submerging it.

The most significant feature observed in these results is the possibility of having multiple solutions, i.e. flow over and around the cylinder, given the same asymptotic upstream flow conditions when the cylinder wall has a non-wetting contact condition ($\theta > 90^o$) applied.

6.3.3 Solutions For Flow Around Two And Three Cylinders

This section considers the flow profiles for Stokes flow around two and three cylinders in a range of configurations. For flow around two cylinders, a range of relative obstacle locations are considered. For two cylinders lying in-line with the flow direction, a parameter analysis is considered, where effects of changing the inverse Bond number B, plane inclination angle α, cylinder radius a, and contact angle θ are investigated.

Comparison of flow around two cylinders, of equal radius $a = 1.0$ and spaced symmetrically with respect to the axis by $(x_{1_{sep}}, x_{2_{sep}})$ are considered with the cylinders centred on $(\pm\frac{x_{1sep}}{2}, \pm\frac{x_{2sep}}{2})$. Flow in each case has a Bond number $Bo = 1.0$ and is down a plane inclined at $\alpha = 45^o$. A contact angle condition of $\theta = 90^o$ is prescribed. Flow around a single cylinder located at $(0, 0)$ has far field locations $-8 \leq x_1 \leq 13$ and $-8 \leq x_2 \leq 8$ and this is extended similarly to that described in the previous chapter for flow over two hemispheres.

Figure 6.21 illustrates the centre line ($x_2 = 0$) profiles of surface elevation for flow around two cylinders in-line with the incident flow and with various spacings. Comparison profiles are given for flow around a single cylinder at $(\pm\frac{x_{1_{sep}}}{2}, 0)$. For all cases of obstacle separation, the flow profile generated by the upstream cylinder appears to be close to the profile for a single cylinder. When the separation is increased, flow around the downstream cylinder approximates more closely the deformation caused by a single obstacle. As the separation increases the wake decays after the leading cylinder and the incident flow configuration to the rear obstacle approaches that of an undisturbed flow. As the obstacles are moved closer together the peak height incident on the cylinder wall decreases. For $x_{1_{sep}} \geq 6$, the flow around the rear obstacle stems from the same location on the back edge of the upstream cylinder. The flow height on the back edge of the downstream cylinder is slightly reduced as the obstacles are brought closer together, although any changes are small. For $x_{1_{sep}} = 4$, the profile fundamentally changes, with the film height on the back edge of the upstream cylinder raised significantly, and the film height at the upstream edge of the rear cylinder lowered. The flow profile in this case is shown as a contour plot in figure 6.24, for $x_{1_{sep}} = 4$ and $x_{2_{sep}} = 0$.

Figure 6.22 shows the centre line ($x_1 = 0$) profiles for flow around two cylinders symmetrically positioned perpendicular to the incoming flow direction. Dashed profiles indicate the flow profiles around a single cylinder at $(0, \pm\frac{x_{2_{sep}}}{2})$. For large separations ($x_{2_{sep}} \geq 6$), the profiles around the double obstacle are accurately approximated by the flow profiles for two single obstacles, with the outer regions of the flow profiles remaining consistent with the corresponding single obstacle solution. The lowest free surface height in the merged inner region of the flow slowly increases from the undisturbed film height as the cylinders are brought closer together. For $x_{2_{sep}} = 4$, the outer regions of the flow profile differ from the corresponding single obstacle analysis, with a raised contact point on the cylinder wall. The film height of the inner region is raised significantly as the flow is forced through the small gap between the cylinders. A contour plot of this profile is shown in figure 6.24, for $x_{1_{sep}} = 0$ and $x_{2_{sep}} = 4$.

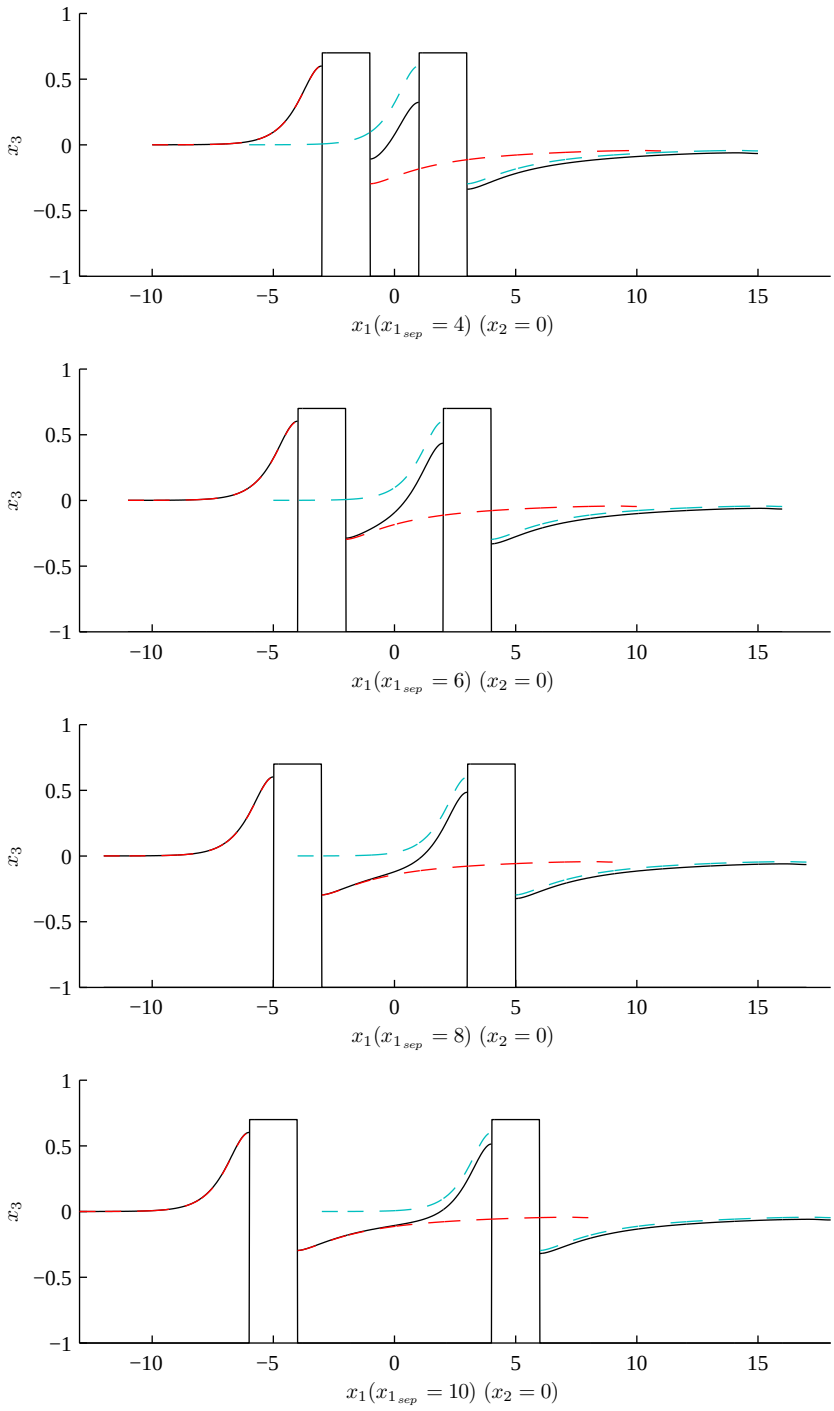

Figure 6.21: Centre line profiles for various cylinder separations $x_{1_{sep}}$ in line with the flow. The flow has a Bond number of $Bo = 1.0$, is down a plane inclined at $\alpha = 45^o$, and the cylinder has a radius of $a = 1.0$, and contact angle of $\theta = 90^o$.

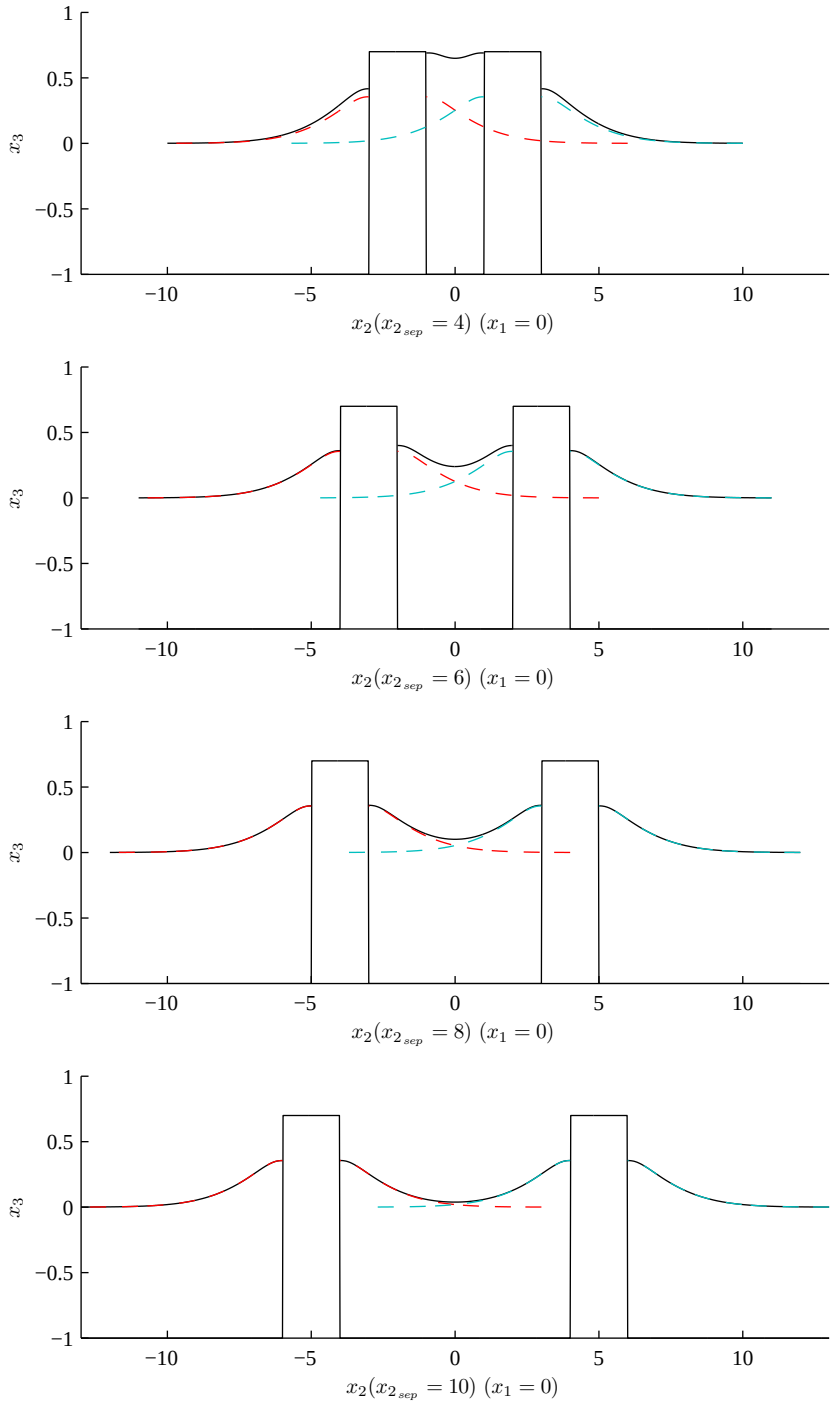

Figure 6.22: Centre line profiles for various cylinder separation distances $x_{2_{sep}}$ perpendicular to the flow. The flow has a Bond number of $Bo = 1.0$, is down a plane inclined at $\alpha = 45^o$, and the cylinder has a radius of $a = 1.0$ and contact angle of $\theta = 90^o$.

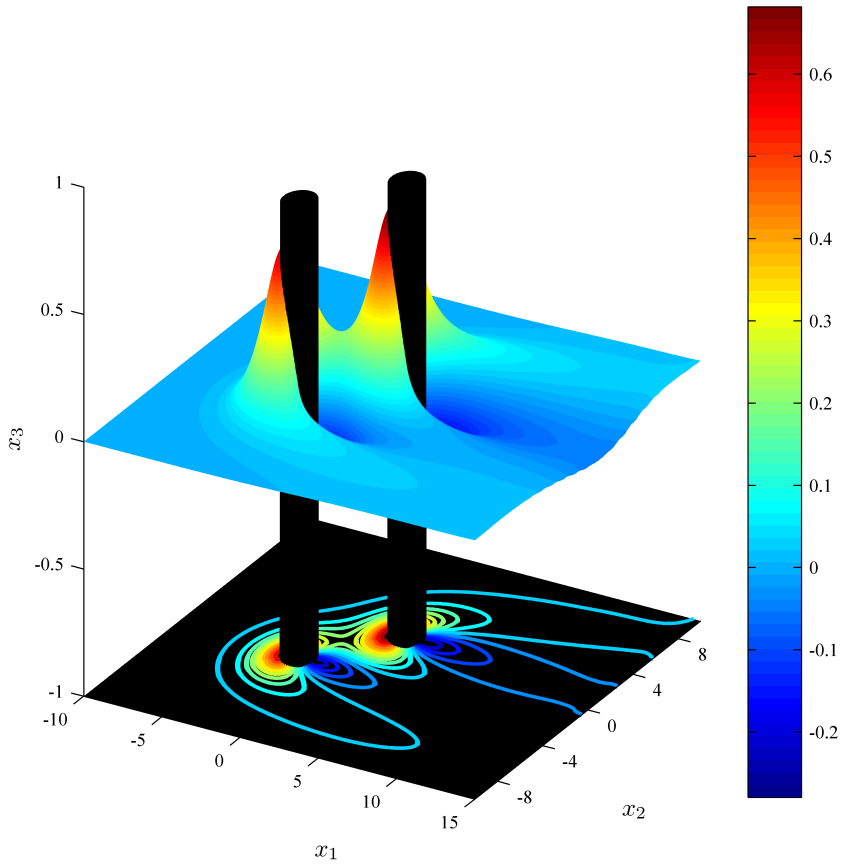

Figure 6.23: Three-dimensional solution profile for two cylinders separated by $x_{1_{sep}} = 4, x_{2_{sep}} = 4$. Flow parameters are; $Bo = 1.0$, $a = 1.0$, $\alpha = 45^o$, and $\theta = 90^o$.

Figure 6.23 shows the full free surface for the analysis of flow around two off-set cylinders separated by $x_{1_{sep}} = x_{2_{sep}} = 4$. The flow is incident to the first cylinder, and as the flow peak splits around the obstacle, one of these raised ridges is incident onto the downstream cylinder. This thicker film region causes the peak formed around the rear cylinder to increase, before decaying with a typical wake structure for a single cylinder. The individual profiles around each cylinder are sufficiently close to exhibit interaction with each other as is illustrated by the associated contour plot in figure 6.24.

Figure 6.24 illustrates three contour plots for the obstacle configurations corresponding to figures 6.21, 6.22 and 6.23. Taking $x_{1_{sep}} = 4, x_{2_{sep}} = 0$ the flow is symmetric about

$x_2 = 0$ and the highest points on the free surface occur on the upstream edge of the two cylinders. The rapid rise in film height is shown between the two cylinders as the trough from the leading cylinder develops into the peak of the downstream obstacle. The centre line plot for this flow can also be seen in figure 6.21. The contour plot for the case $x_{1_{sep}} = 0, x_{2_{sep}} = 4$ illustrates just a single, wide peak occurring and covering the leading edges of the two cylinders. The peak decays into a trough just behind each of the cylinders, with the raised flow forced between the cylinders decaying to the undisturbed film height further downstream. The contour plot for the non-symmetric case $x_{1_{sep}} = 4, x_{2_{sep}} = 4$ shows the contours of flow around two off-set cylinders with the downstream cylinder generating a slightly larger peak. The rear cylinder is seen to lie in the decaying peak of the upstream cylinder causing the range of this peak to extend further downstream.

A parameter analysis is conducted demonstrating the effects of altering the inverse Bond number B, plane inclination angle α, obstacle radii a, and contact angle θ. An inline configuration with $x_{1_{sep}} = 8$ is taken. Default values for the flow parameters include an inverse Bond number of $B = 1$, a plane inclination angle of $\alpha = 45^o$, circular cylinders of radius $a = 1.0$, and a contact angle condition of $\theta = 90^o$. In each case, three parameters are chosen from above and the effects of altering the fourth analyzed.

Figure 6.25 illustrates the surface elevation along the centre line ($x_2 = 0$) for variations in inverse Bond number, with an increase in B showing a flattening and smoothing of the profiles associated with an increase in surface tension. For $B = 1$, the centre line profiles undergo large variations in film height. The effects of increasing B is to raise the lowest points and lower the highest points of the film, minimizing the deformation of the free surface. In common with the single obstacle analysis shown in figure 6.9 and the earlier dual hemisphere analysis, the inverse Bond number causes the film disturbance to span a greater region upstream in the x_1 direction.

Figure 6.26 illustrates the centre line ($x_2 = 0$) surface elevations for changes in the plane

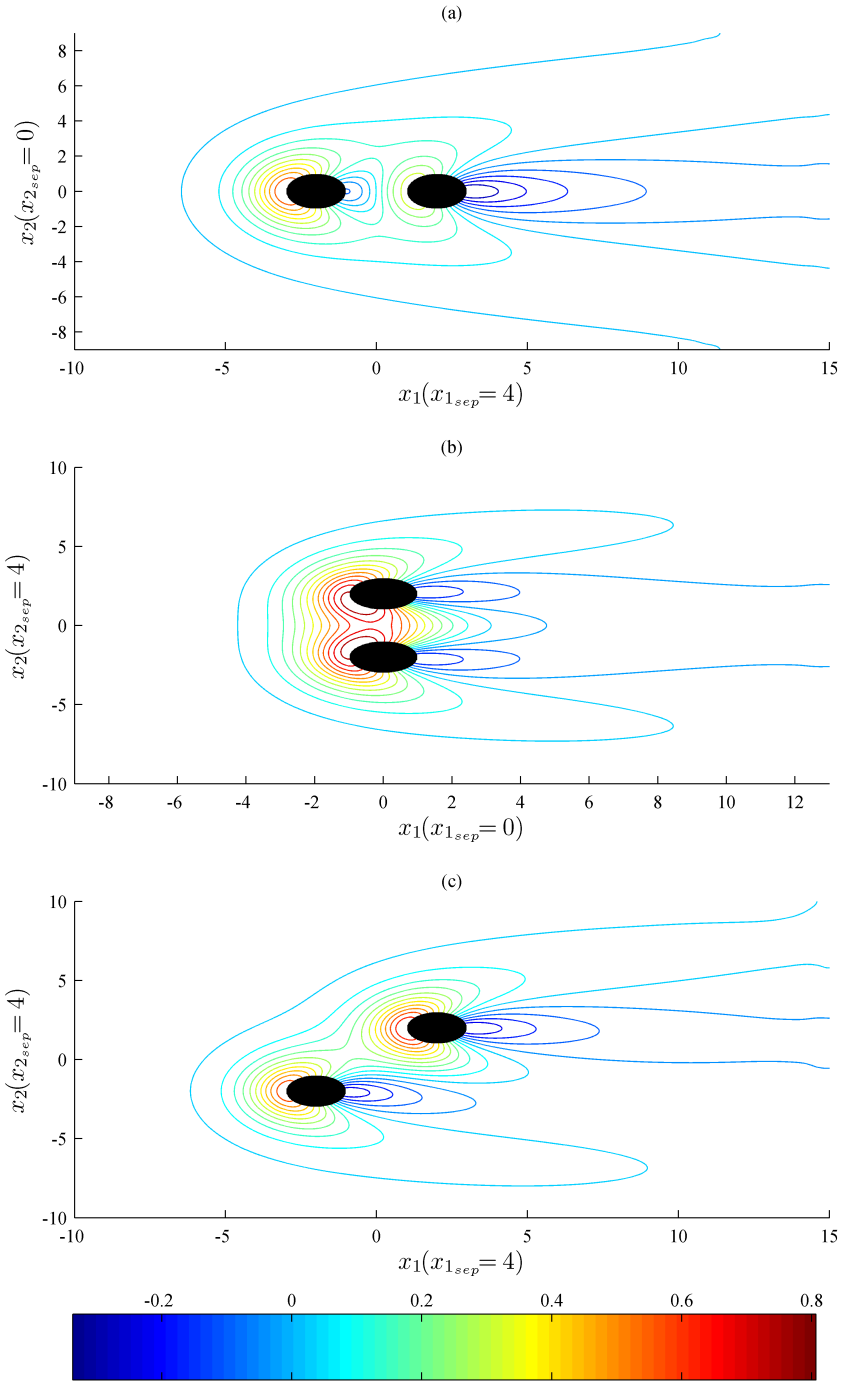

Figure 6.24: Contour plots for $(x_{1_{sep}}, x_{2_{sep}}) = (4,0), (0,4), (4,4)$, for flow around cylinders of radius $a = 1.0$. Other flow parameters are; $Bo = 1.0$, $\alpha = 45^o$, and $\theta = 90^o$.

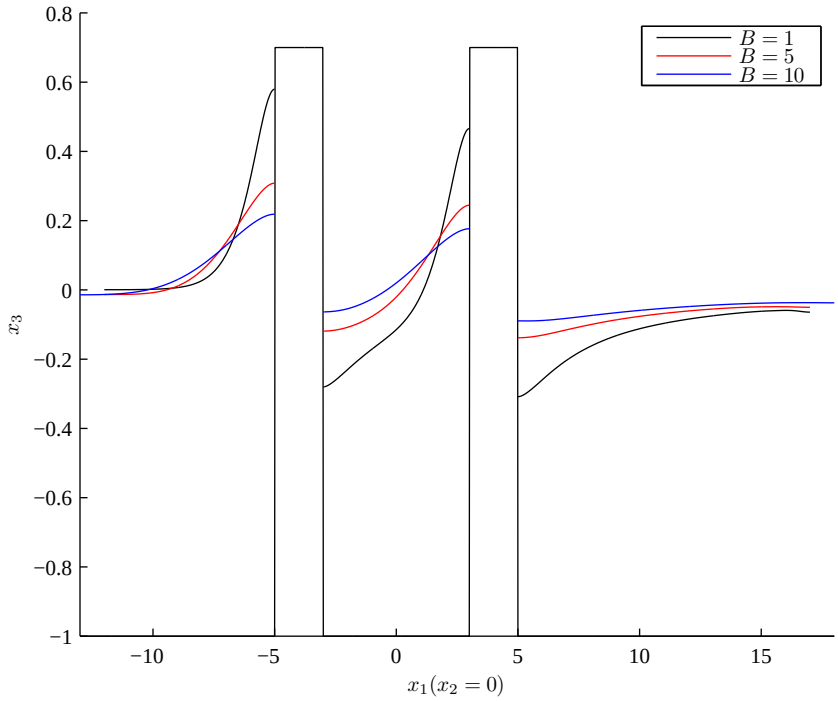

Figure 6.25: Centre line solution profiles for two cylinders separated by $x_{1_{sep}} = 8$, indicating the effects of varying the inverse Bond number B. The plane is inclined at $\alpha = 45^o$. The cylinder radius is $a = 1.0$, and a contact angle of $\theta = 90^o$ is used.

inclination angles α. It is noted that the steeper the plane wall, the larger the peak that is formed on the cylinders. Interestingly the larger cylinders analyzed here when compared to results shown in figure 6.11 show the film height on the downstream edge of the cylinder to be raised as the plane angle is decreased. This is in contrast to the single cylinder results which showed the downstream location to be close for all plane angles and not monotonic.

Figure 6.27 shows the centre line ($x_2 = 0$) profiles for variations in cylinder radius. Larger cylinders cause greater deformations of the free surface, with increasing peak and decreasing trough heights around the upstream cylinder. In addition, the trough of the downstream cylinder is lowered with increasing cylinder radius. The corresponding peak at the downstream cylinder for successive heights $a = 0.5, 1.0, 1.5$ is increased,

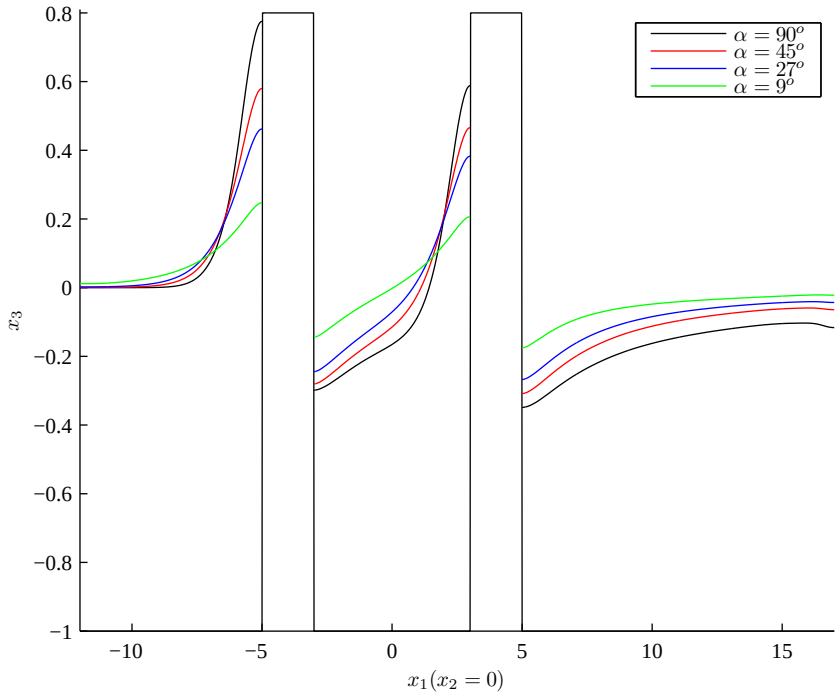

Figure 6.26: Centre line solution profiles for two cylinders separated by $x_{1_{sep}} = 8$, indicating the effects of varying the plane inclination angle α. The flow has an inverse Bond number of $B = 1.0$, and the cylinder radii are $a = 1.0$. The cylinder contact angle is $\theta = 90^o$.

however the peak height on the centre line associated with $a = 2.0$ is actually lower than the corresponding height for $a = 1.5$. In this latter case the deeper trough behind the upstream cylinder, associated with $a = 2.0$, forces the peak at the downstream cylinder to be reduced due to the large variation in film height necessary.

Figure 6.28 shows the centre line ($x_2 = 0$) profiles for variations in the contact angle at the cylinder/free surface interface. Results show the profiles are altered significantly depending on whether a wetting or non-wetting condition is applied at the cylinder. It is interesting to note the global effect of this local parameter variation. When a wetting condition is applied i.e. $\theta < 90^o$, the peaks maximize at the cylinder wall, and the minimum flow height is found a small distance from the cylinder. For non-wetting cylinders i.e. $\theta > 90^o$, the peak heights occur away from the cylinder wall and the flow

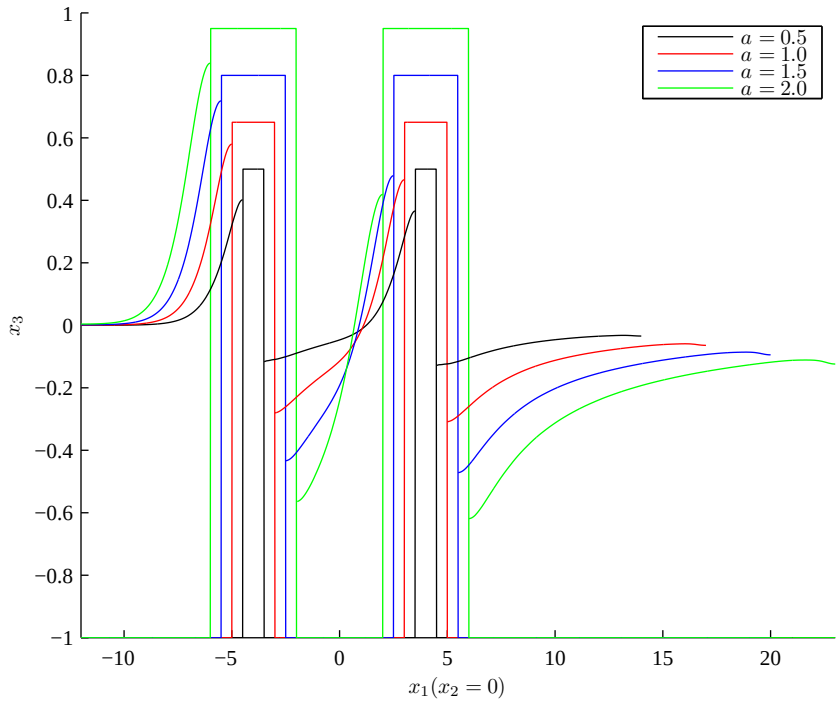

Figure 6.27: Centre line solution profiles for two cylinders separated by $x_{1_{sep}} = 8$, indicating the effects of varying the cylinders radii a. The flows inverse Bond number is $B = 1.0$, and the plane is inclined at $\alpha = 45^o$. The contact angle at the contact line is $\theta = 90^o$.

height minimizes at the point of contact. These results are consistent with the case of a single cylinder (see figure 6.15).

The flow around three cylinders in two geometrical configurations is considered. Flow is taken down a plane inclined at $\alpha = 45^o$ and has a Bond number $Bo = 1$. Flow is around circular cylinders of radius $a = 1.0$, with a contact angle condition of $\theta = 90^o$ applied. Cylinders are positioned in a symmetrical triangular array, with either a twin or single leading cylinder considered. A twin leading configuration is illustrated in figure 6.29 and consists of the upstream flow incident on two cylinders spaced perpendicularly to the flow direction at centres $(-2, -2), (-2, 2)$. This is followed by a trailing cylinder centered at $(2, 0)$. The configuration shown in figure 6.30 consists of the upstream flow incident on one obstacle centered at $(-2, 0)$ followed by two downstream cylinders spaced

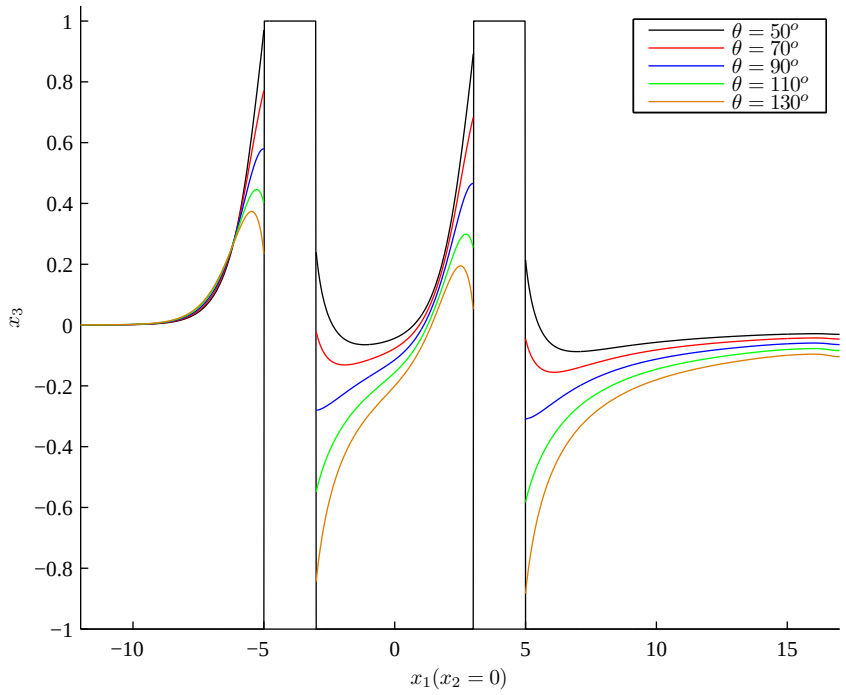

Figure 6.28: Centre line solution profiles for two cylinders separated by $x_{1_{sep}} = 8$, indicating the effects of varying the static contact line angle θ. The inverse Bond number is $B = 1.0$, the plane is inclined at $\alpha = 45^o$ and the cylinder radii is $a = 1.0$.

perpendicularly to the flow direction with centres at $(2, -2), (2, 2)$. For both cases, three peaks are clearly seen incident to the upstream edges of each cylinder.

6.3.4 Flow Over Then Around Identical Cylinders

The capability of the numerical method is demonstrated by considering the flow configuration of two identical cylinders, aligned in the direction of the flow, where the film passes over the leading cylinder, but due to the surface depression from its wake passes around the downstream cylinder. Flow is down a plane inclined at $\alpha = 90^o$, the cylinder radii is $a = 1.0$ and the flow has a Bond number of $Bo = 1.0$. For the rear cylinder, a contact angle is prescribed and minimized whilst still maintaining the flow to pass around the prescribed cylinder. The upstream cylinder top is sloped linearly in the direction of the

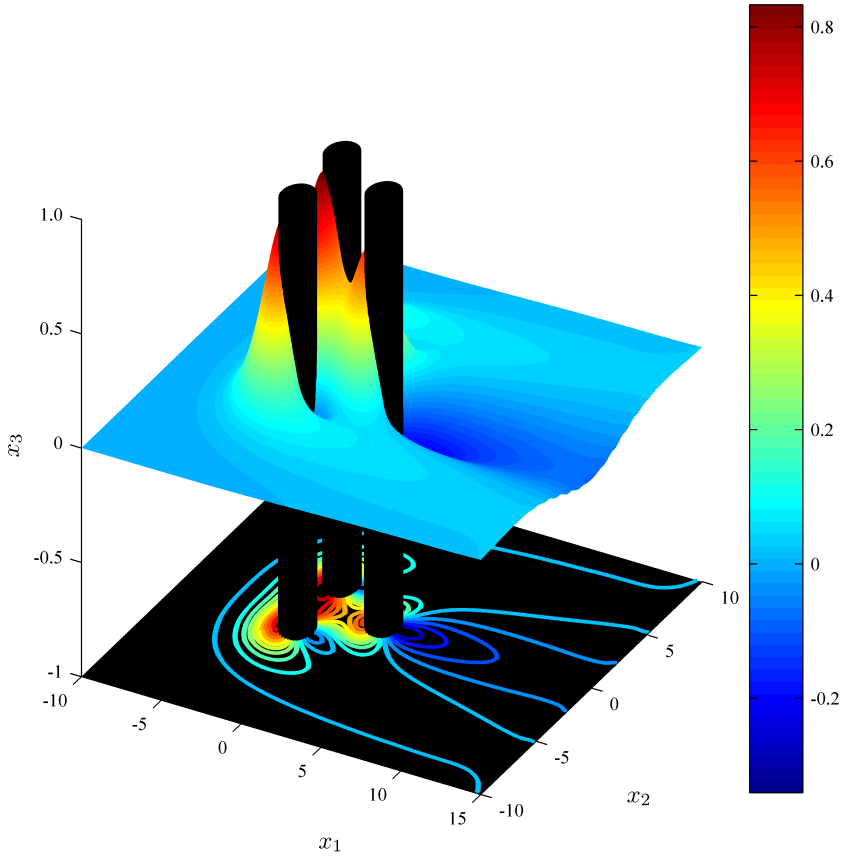

Figure 6.29: Three-dimensional solution profile for three cylinders located at $(-2, 2)$, $(-2, -2)$, $(2, 0)$. The Bond number of the flow is $Bo = 1.0$, the plane is inclined at $\alpha = 45^o$, and the cylinder radii and contact angle are $a = 1.0$ and $\theta = 90^o$ respectively.

flow and meshed as described earlier in this chapter.

This is an extension of the multiple solution work presented earlier. If the cylinders separation approaches ∞ in the x_1 direction, then the flow will fully return to its upstream form and the two profiles (over and around the cylinder) can be formed. As the obstacles are brought closer together the effects of the wake behind the upstream cylinder will act to relax the constraining contact angle condition necessary at the downstream cylinder.

A cylinder with a sloped top between $x_3 = 0.6$ at the upstream edge and $x_3 = 0.0$ at the downstream edge is considered. Flow profiles over and around a single cylinder,

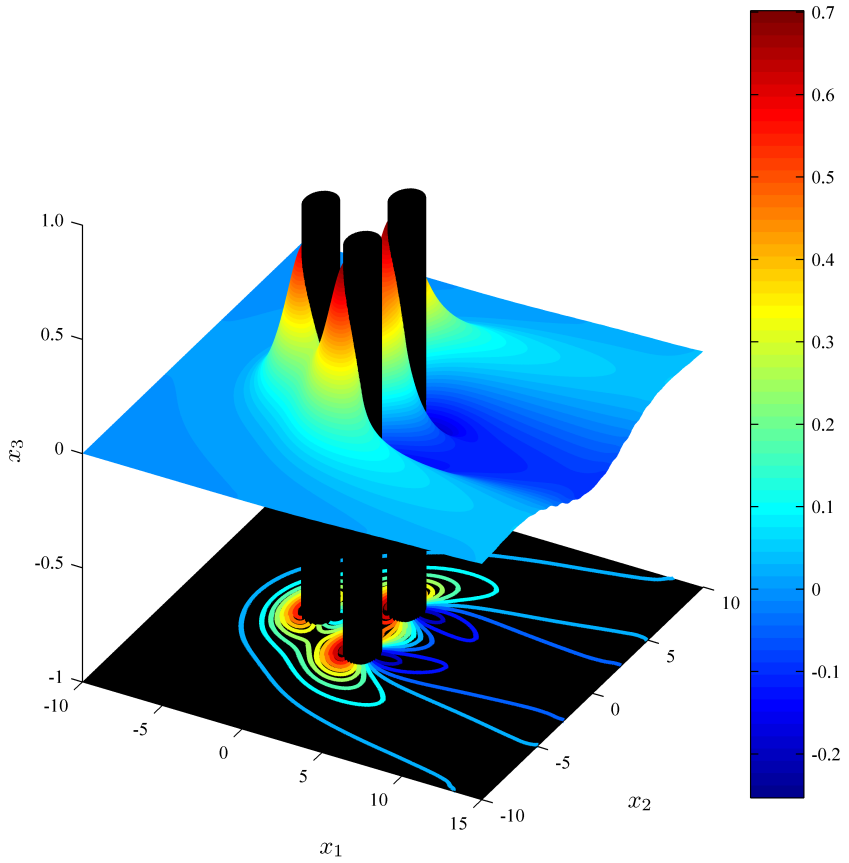

Figure 6.30: Three-dimensional solution profile for three cylinders located at $(-2, 2)$, $(-2, -2)$, $(2, 0)$. The Bond number of the flow is $Bo = 1.0$, and the plane is inclined at $\alpha = 45^o$. The cylinder radii are $a = 1.0$, and a contact angle of $\theta = 90^o$ is applied at each contact line.

corresponding to the theoretical case of infinitely spaced cylinders, and double obstacle solutions with spacings $x_{1_{sep}} = 8$ and $x_{1_{sep}} = 4$ are produced. In each case the contact angle θ is minimized whilst maintaining flow around the prescribed cylinder. Table 6.2 indicates the necessary minimum contact angle required to force flow around the downstream cylinder.

Figure 6.31 shows four solutions, the first two indicate the centre line solutions for a single obstacle analysis for flow over, and around the prescribed cylinder. For multiple solutions to be produced, the contact angle at the cylinder wall is constrained to $\theta \geq 111^o$. The final two centre lines indicate multiple solutions for flow over then around identical

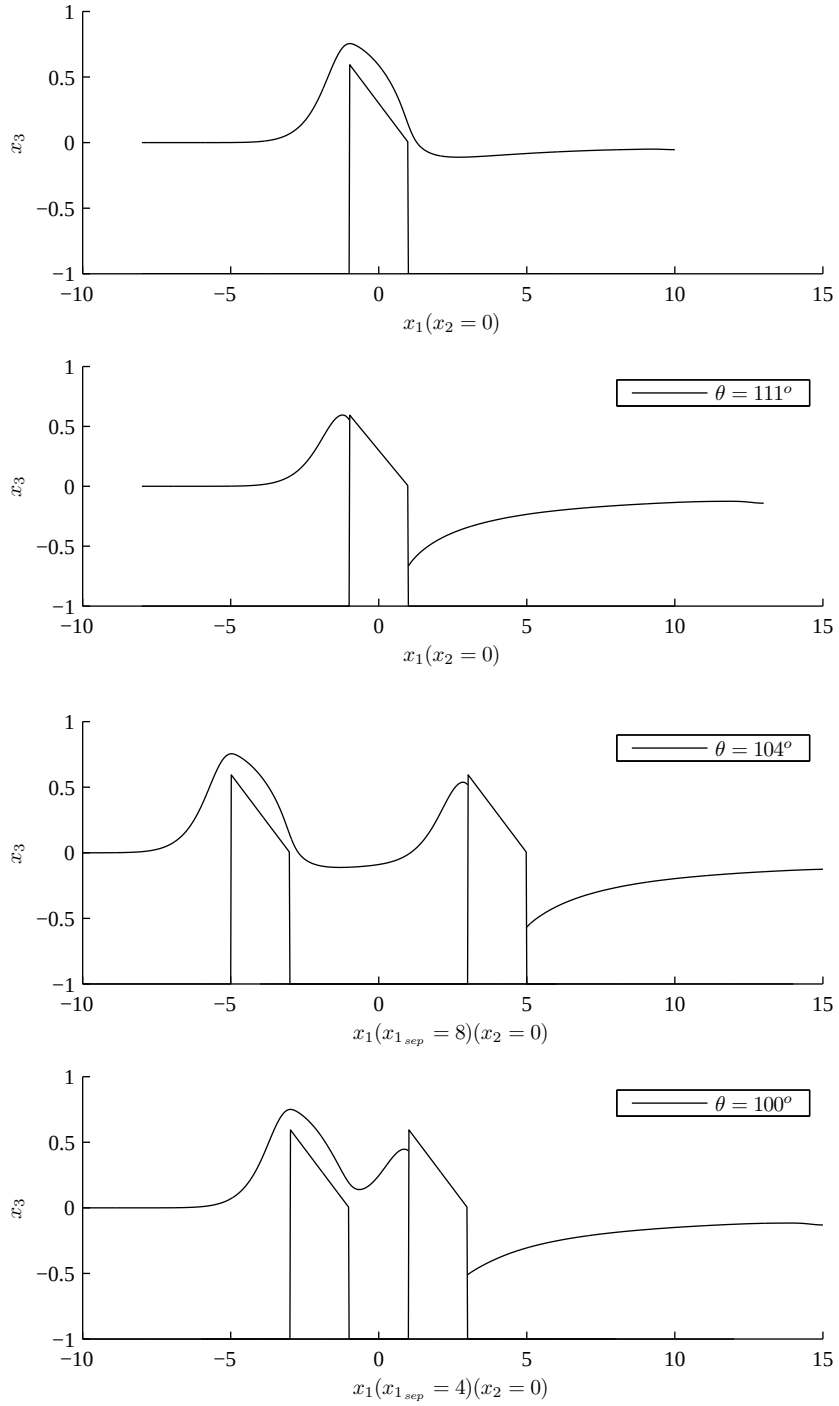

Figure 6.31: Centre line profiles for flow over and around a single cylinder and over then around two cylinders at finite separations. The contact angle is minimized whilst maintaining flow around the cylinder. Flow parameters are; $Bo = 1.0$, $\alpha = 90^o$, and $a = 1.0$.

$x_{1_{sep}}$	Minimum Contact Angle θ
∞	111^o
8	104^o
4	100^o

Table 6.2: Minimum contact angles required for flow to pass around the downstream cylinder, of radius $a = 1.0$ and top sloped linearly in the x_1 direction between $x_3 = 0.6$ and $x_3 = 0.0$

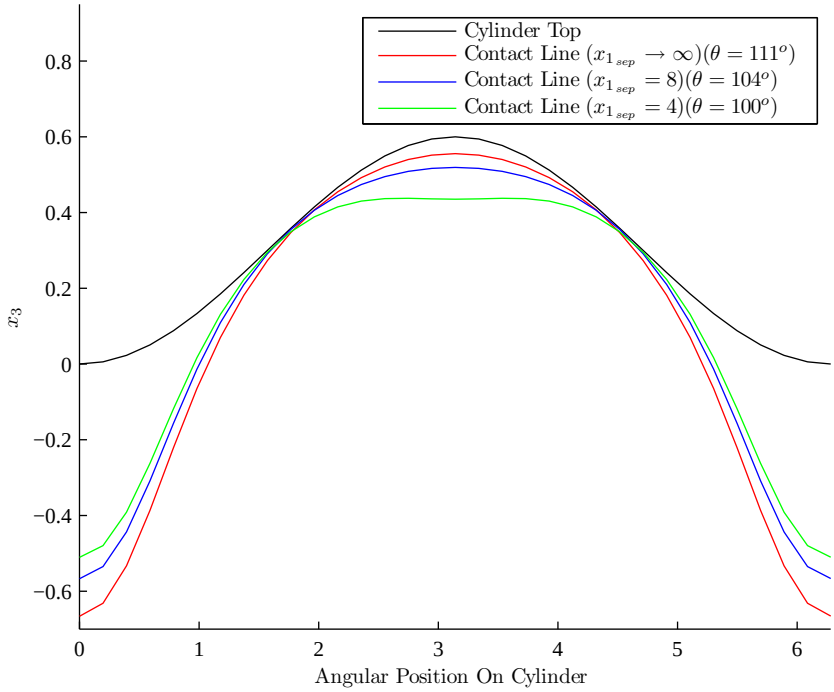

Figure 6.32: Contact line solutions for flow around each of the cylinders in figure 6.31, confirming that flow is always below the top of a cylinder of radius $a = 1.0$ with top sloped between $x_3 = 0.6$ and $x_3 = 0.0$. The flow has a Bond number of $Bo = 1.0$, and the plane is vertical ($\alpha = 90^o$).

cylinders spaced by finite separations $x_{1_{sep}} = 8$ and 4. As the cylinders are moved closer the profiles over each obstacle interact more severely and the contact angle condition necessary at the downstream cylinder is reduced.

Figure 6.32 illustrates the contact lines and cylinder top for the three scenarios for flow around a cylinder depicted in figure 6.31. Clearly in each case the flow profiles remain below the cylinder top, and in general as the cylinders are brought closer together, a flattening of the highest region of the profiles occurs.

Chapter 7

Small Inertial Effects Of Flow Over And Around Obstacles

Film profiles so far have been modelled using a Stokes flow approximation, and although typical film flows within a bearing chamber often have low Reynolds number, the effects of the convective term may still be relevant regarding the free surface and velocity profiles. This chapter considers small inertial effects for film flows both over and around circular cylinders.

Section 7.1 overviews existing literature for the analysis of flows at low Reynolds number. Within this literature, the validation of numerical schemes is usually conducted for flow in a lid-driven cavity. Due to the size of the three-dimensional film domain, an efficient numerical algorithm for evaluation of the convective term within the Navier Stokes equations is required. Section 7.2 considers flow in a three-dimensional lid-driven cavity for analysis of a computationally efficient numerical algorithm used to evaluate low Reynolds number flows. Solutions to the Navier-Stokes equations are found via the boundary element method (BEM) using an iterative technique. Conventional methods linearly approximate the convective term and solve for domain velocities and unknown boundary variables together. An alternative, more efficient approach where the convective term is evaluated directly from a previous estimate is considered, and the homogeneous and particular components of the flow are solved separately. In addition, to further

reduce the computational requirements of the flow problem, a local mass conservative interpolation for the velocity field is implemented. Section 7.3 considers the inertia effects for film flows over and around circular cylindrical obstacles, using the efficient numerical algorithms developed for the case of a lid-driven cavity.

7.1 Literature Review

The boundary element method (BEM) is a well established technique for solving Stokes flow problems. However difficulties occur when extending the formulation to the non-linear problem of finite Reynolds number flows. In these cases the integral representations contain domain integrals caused by the convective term, and the evaluation of these integrals is a major aspect of current research.

The domain integrals within the formulation can be solved effectively using techniques such as finite difference approximations (FDAs) and the finite element method (FEM). However these methods result in the loss of the boundary-only nature of the formulation. Methods have been developed which transform these domain integrals to the boundary, for example the dual reciprocity method (DRM) and the particular integrals technique (PIT) as developed by Nardini and Brebbia [43] and Ahmad and Banerjee [54] respectively. In the latter method, solutions are decomposed into a homogeneous and particular component satisfying the corresponding homogeneous and non-homogeneous partial differential equations (PDE). The particular solution fails to satisfy the boundary conditions of the problem, and thus the boundary conditions of the homogeneous PDE are modified to retain the original boundary conditions. The homogeneous PDE is solved by the corresponding integral equation with these new boundary conditions applied. This particular solution concept is used within the DRM but instead of solving for homogeneous and particular components separately, the domain integral is converted to boundary integrals by use of the divergence theorem. As the non-homogeneous convective term is unknown for this analysis, both the PIT and DRM approaches are numerically

equivalent.

The later work by Power and Botte [55] used a particular solution technique (PST) to solve low Reynolds number flow in a lid driven cavity. The formulation is based on the PIT approach, with the numerical procedure solving for the homogeneous and particular components separately. In addition an indirect BEM is used for solution of the homogeneous component. This PST method offered substantial benefits to the DRM and PIT models, reducing the computational cost of the numerical procedures.

When solving the Navier-Stokes equations, the nonlinear convective term requires accurate values for the derivatives of the velocity field. Conventional methods use a standard interpolation for the velocities, from which the derivatives can be found. However, these methods do not satisfy mass conservation causing inaccuracies, especially in regions of coarse mesh, or high velocity gradients. Use of a mass conservative interpolation was introduced by Florez and Power [56], and will be implemented throughout this chapter.

Solution of the Navier-Stokes equations using the DRM or other similar approaches often results in numerical schemes that require excessive computational requirements. Specifically, in cases where a mass conservative interpolation of the velocity field is used, both RAM and CPU time necessary to conduct the global radial basis function (RBF) interpolation may become prohibitive. Thus a local mass conservative RBF interpolation may be considered, with the possibility of significantly reducing the computational requirements. Local interpolations are discussed briefly in chapter 3, and Yamada et al. [57] show that despite the RBF interpolation being globally defined, it exhibits local behaviour when reconstructing the approximated function.

Reducing the computational requirements necessary for finding flow profiles at low Reynolds number is a priority. Thus, for the case of three-dimensional film flows at low Reynolds number, the PST approach is implemented. The following section develops the method for flow within a three-dimensional lid driven cavity with solutions produced in an iterative fashion. Initially a global mass conservative RBF interpolation

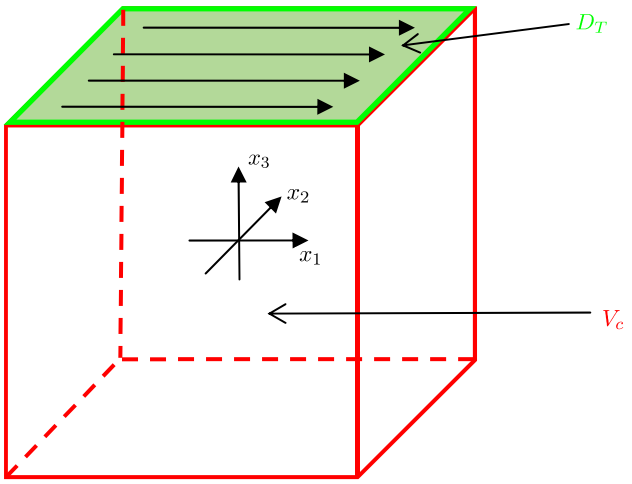

Figure 7.1: Schematic showing flow in a three-dimensional lid driven cavity.

is implemented. The particular solutions and BEM are solved together (as in the PIT) and separately (as in PST) at each iteration, and the effects on computational requirement reported. In the case of the PST solutions, a local RBF for the mass conservative velocity interpolation has also been implemented to further reduce the computational requirements of the problem.

7.2 Formulation And Numerical Schemes

For a large three-dimensional problem, conventional methods for extending Stokes flows solved using the boundary element method (BEM) to incorporate inertia effects can require prohibitively large computational resources. As a result, an efficient numerical algorithm for including the effects of low Reynolds number is developed, with validation considered for the case of a three-dimensional lid driven cavity.

Figure 7.1 illustrates a schematic of a three-dimensional lid driven cavity. The domain V_c is bounded by the surface $D = D_T \cup D_R$, where the top of the domain D_T has a prescribed velocity of unit speed in the x_1 direction. The edges of the domain are defined by $x_1 = \pm 0.5$, $x_2 = \pm 0.5$, and $x_3 = \pm 0.5$.

Flow within the cavity is governed by the usual incompressible equations for mass continuity (7.2.1) and Navier-Stokes (7.2.2),

$$\frac{\partial u_i}{\partial x_i} = 0, \tag{7.2.1}$$

$$-\frac{\partial p}{\partial x_i} + \frac{\partial^2 u_i}{\partial x_j^2} = Re\ u_j \frac{\partial u_i}{\partial x_j}, \tag{7.2.2}$$

subject to the no slip boundary conditions

$$u_i = \delta_{i1} \qquad \mathbf{x} \in D_T, \tag{7.2.3}$$

$$u_i = 0 \qquad \mathbf{x} \in D_R. \tag{7.2.4}$$

The inclusion of the convective term within a boundary integral formulation can take two forms, the dual reciprocity method [43] is first considered in the following subsection. The alternative homogeneous and particular solution approach [54] is then considered.

7.2.1 The Dual Reciprocity Method

The dual reciprocity method (DRM) as developed by Nardini and Brebbia [43] involves formulating the integral equations for the Navier-Stokes equations, and converting the domain integral for the convective term into boundary integrals. From the Lorentz reciprocal relation in chapter 2

$$u_j' \frac{\partial \sigma_{ij}}{\partial x_i} - u_j \frac{\partial \sigma_{ij}'}{\partial x_i} = \frac{\partial}{\partial x_i}(u_j' \sigma_{ij} - u_j \sigma_{ij}'). \tag{7.2.5}$$

Set,

$$u_i(\mathbf{x}) = \frac{1}{8\pi} G_{im}(\mathbf{x}, \mathbf{x}_0) b_m, \tag{7.2.6}$$

$$\sigma_{ik}(\mathbf{x}) = \frac{1}{8\pi} T_{imj}(\mathbf{x}, \mathbf{x}_0) b_m, \tag{7.2.7}$$

as in chapter 2, but in this case

$$\frac{\partial \sigma_{ij}}{\partial x_i} = B_j = Re\ u_k \frac{\partial u_j}{\partial x_k}, \tag{7.2.8}$$

instead of zero as for Stokes flow. Proceeding as before for Stokes flow, and substituting (7.2.6) - (7.2.8) into (7.2.5) yields

$$\begin{aligned}&\frac{\partial}{\partial x_i}\left(\frac{1}{8\pi}G_{jm}(\mathbf{x},\mathbf{x}_0)b_m\sigma_{ij}-u_j(\mathbf{x})\frac{1}{8\pi}T_{imj}(\mathbf{x},\mathbf{x}_0)b_m\right)\\&\qquad=\frac{1}{8\pi}G_{jm}(\mathbf{x},\mathbf{x}_0)b_mB_j-u_j(\mathbf{x})\left(-\delta(\mathbf{x}-\mathbf{x}_0)\delta_{jm}b_m\right).\end{aligned}\tag{7.2.9}$$

Dividing through by b_m and integrating over the domain V_c yields

$$\begin{aligned}&\int_{V_c}u_m(\mathbf{x})\delta(\mathbf{x}-\mathbf{x}_0)\mathrm{d}V(\mathbf{x})+\frac{1}{8\pi}\int_{V_c}G_{jm}(\mathbf{x},\mathbf{x}_0)B_j\mathrm{d}V(\mathbf{x})\\&\qquad=\int_D\left(\frac{1}{8\pi}G_{ij}(\mathbf{x},\mathbf{x}_0)\sigma_{ij}-\frac{1}{8\pi}u_j(\mathbf{x})T_{imj}(\mathbf{x},\mathbf{x}_0)\right)n_i(\mathbf{x})\mathrm{d}S(\mathbf{x}).\end{aligned}\tag{7.2.10}$$

Exchanging the variables such that $m\to j$, $j\to i$ and $i\to k$, and noting the symmetry properties of the stress tensor and greens function, yields the integral form for the full Navier-Stokes equations,

$$\begin{aligned}&u_j(\mathbf{x}_0)+\frac{1}{8\pi}\int_{V_c}G_{ij}(\mathbf{x},\mathbf{x}_0)B_i\mathrm{d}V(\mathbf{x})\\&\qquad=\frac{1}{8\pi}\int_D G_{ij}(\mathbf{x},\mathbf{x}_0)f_i(\mathbf{x})\mathrm{d}S(\mathbf{x})-\frac{1}{8\pi}\int_D u_i(\mathbf{x})T_{ijk}(\mathbf{x},\mathbf{x}_0)n_k(\mathbf{x})\mathrm{d}S(\mathbf{x}).\end{aligned}\tag{7.2.11}$$

This is identical to the Stokes integral equation, but for the additional domain integral, generated by the non-zero convective term in the governing equations. Accurate evaluation of this domain integral is necessary, and early methods involved a volume discretization of the domain. However, this loses the boundary only nature of the problem and a more attractive method is to convert the domain integral into corresponding boundary integrals.

Consider the interpolation of the convective term by a thin plate spline radial basis function (RBF), $\psi(\mathbf{x},\boldsymbol{\xi})$

$$B_i=\sum_{m=1}^{n}\beta_m^l\psi(\mathbf{x},\boldsymbol{\xi}_m)\delta_{il},\tag{7.2.12}$$

and the domain integral becomes

$$\int_{V_c}G_{ij}(\mathbf{x},\mathbf{x}_0)B_i\mathrm{d}V(\mathbf{x})=\sum_{m=1}^{n}\beta_m^l\int_{V_c}G_{ij}(\mathbf{x},\mathbf{x}_0)\psi(\mathbf{x},\boldsymbol{\xi}_m)\delta_{il}\mathrm{d}V(\mathbf{x}).\tag{7.2.13}$$

An auxiliary flow field $\left(\hat{u}_i^l(\mathbf{x},\boldsymbol{\xi}_m),\hat{p}^l(\mathbf{x},\boldsymbol{\xi}_m)\right)$ is defined by

$$\frac{\partial \hat{u}_i^l(\mathbf{x},\boldsymbol{\xi}_m)}{\partial x_i} = 0, \tag{7.2.14}$$

$$-\frac{\partial \hat{p}^l(\mathbf{x},\boldsymbol{\xi}_m)}{\partial x_i} + \frac{\partial^2 \hat{u}_i^l(\mathbf{x},\boldsymbol{\xi}_m)}{\partial x_j^2} = \psi(\mathbf{x},\boldsymbol{\xi}_m)\delta_{il}, \tag{7.2.15}$$

where solutions for $\left(\hat{u}_i^l(\mathbf{x},\boldsymbol{\xi}_m),\hat{p}^l(\mathbf{x},\boldsymbol{\xi}_m)\right)$ can be found from the corresponding interpolant $\psi(\mathbf{x},\boldsymbol{\xi}_m)$. The auxiliary traction is defined by

$$\hat{f}_i^l(\mathbf{x},\boldsymbol{\xi}_m) = \sigma_{ij}\left(\hat{u}_i^l(\mathbf{x},\boldsymbol{\xi}_m),\hat{p}^l(\mathbf{x},\boldsymbol{\xi}_m)\right) n_j(\mathbf{x}), \tag{7.2.16}$$

with the stress tensor defined as in (2.3.2).

The integral equation for the auxiliary flow field is

$$\begin{aligned}
&\hat{u}_i^l(\mathbf{x}_0,\boldsymbol{\xi}_m) + \frac{1}{8\pi}\int\limits_{V_c} G_{ij}(\mathbf{x},\mathbf{x}_0)\psi(\mathbf{x},\boldsymbol{\xi}_m)\mathrm{d}V(\mathbf{x}) \\
&\quad = \frac{1}{8\pi}\int\limits_{D} G_{ij}(\mathbf{x},\mathbf{x}_0)\hat{f}_i^l(\mathbf{x},\boldsymbol{\xi}_m)\mathrm{d}S(\mathbf{x}) - \frac{1}{8\pi}\int\limits_{D} \hat{u}_i^l(\mathbf{x},\boldsymbol{\xi}_m)T_{ijk}(\mathbf{x},\mathbf{x}_0)n_k(\mathbf{x})\mathrm{d}S(\mathbf{x}).
\end{aligned} \tag{7.2.17}$$

By using the interpolation (7.2.12) to represent the body term B_i, it follows that each component of the volume integral of its series representations is identical to those of (7.2.17), and can be eliminated to form an equation solely in terms of boundary integrals,

$$\begin{aligned}
&c_{ij}(\mathbf{x}_0)u_i(\mathbf{x}_0) \\
&\qquad = \frac{1}{8\pi}\int\limits_{D} G_{ij}(\mathbf{x},\mathbf{x}_0)f_i(\mathbf{x})\mathrm{d}S(\mathbf{x}) - \frac{1}{8\pi}\int\limits_{D} u_i(\mathbf{x})T_{ijk}(\mathbf{x},\mathbf{x}_0)n_k(\mathbf{x})\mathrm{d}S(\mathbf{x}) \\
&\qquad\quad + \sum_{m=1}^{n}\beta_m^l\left[c_{ij}(\mathbf{x}_0)\hat{u}_i^l(\mathbf{x}_0,\boldsymbol{\xi}_m) - \frac{1}{8\pi}\int\limits_{D} G_{ij}(\mathbf{x},\mathbf{x}_0)\hat{f}_i^l(\mathbf{x},\boldsymbol{\xi}_m)\mathrm{d}S(\mathbf{x})\right. \\
&\qquad\qquad \left. \frac{1}{8\pi}\int\limits_{D} \hat{u}_i^l(\mathbf{x},\boldsymbol{\xi}_m)T_{ijk}(\mathbf{x},\mathbf{x}_0)n_k(\mathbf{x})\mathrm{d}S(\mathbf{x})\right],
\end{aligned} \tag{7.2.18}$$

where $c_{ij}(\mathbf{x}_0)$ is the jump parameter. For solution of (7.2.18), expressions for the auxiliary flow field $\left(\hat{u}_i^l(\mathbf{x},\boldsymbol{\xi}_m),\hat{p}^l(\mathbf{x},\boldsymbol{\xi}_m)\right)$ (which can be found analytically) and the interpolation coefficients β_m^l are required.

7.2.2 Homogeneous And Particular Solutions

An alternative approach to formulating the Navier-Stokes equations in terms of a boundary only integral equation takes the form of considering homogeneous and particular solutions as in Ahmad and Banerjee [54]. This derivation can be used to obtain an identical governing equation to (7.2.18) for the DRM approach.

To proceed the solution variables are decomposed into homogeneous (superscript h) and particular (superscript p) components,

$$u_i = u_i^h + u_i^p, \tag{7.2.19}$$

$$p = p^h + p^p, \tag{7.2.20}$$

$$f_i = f_i^h + f_i^p. \tag{7.2.21}$$

Using (7.2.19) and (7.2.20), the governing equations and boundary conditions (7.2.1) - (7.2.4) are written in terms of homogeneous and particular components, with their solutions discussed below.

The homogeneous governing equations are,

$$\frac{\partial u_i^h}{\partial x_i} = 0, \tag{7.2.22}$$

$$-\frac{\partial p^h}{\partial x_i} + \frac{\partial^2 u_i^h}{\partial x_j^2} = 0, \tag{7.2.23}$$

representing Stokes flow within the cavity. By standard techniques for a direct formulation (7.2.22) - (7.2.23) can be rewritten exactly as a boundary integral equation (BIE) for the homogeneous velocities and tractions

$$\begin{aligned} &c_{ij}(\mathbf{x}_0)u_i^h(\mathbf{x}_0) \\ &\quad = \frac{1}{8\pi}\int_D G_{ij}(\mathbf{x},\mathbf{x}_0)f_i^h(\mathbf{x})\mathrm{d}S(\mathbf{x}) - \frac{1}{8\pi}\int_D u_i^h(\mathbf{x})T_{ijk}(\mathbf{x},\mathbf{x}_0)n_k(\mathbf{x})\mathrm{d}S(\mathbf{x}), \end{aligned} \tag{7.2.24}$$

where the coefficient $c_{ij}(\mathbf{x}_0)$ is the jump parameter. The boundary conditions applied

when solving the BIE (7.2.24) are

$$u_i^h = \delta_{i1} - u_i^p \qquad \mathbf{x} \in D_T, \tag{7.2.25}$$

$$u_i^h = -u_i^p \qquad \mathbf{x} \in D_R, \tag{7.2.26}$$

as the particular solution fails to satisfy any boundary condition.

The particular variables satisfy the governing equations,

$$\frac{\partial u_i^p}{\partial x_i} = 0, \tag{7.2.27}$$

$$-\frac{\partial p^p}{\partial x_i} + \frac{\partial^2 u_i^p}{\partial x_j^2} = Re\, u_j \frac{\partial u_i}{\partial x_j}, \tag{7.2.28}$$

and the convective term can be interpolated as in (7.2.12), with the auxiliary flow field $\left(\hat{u}_i^l(\mathbf{x}, \boldsymbol{\xi}_m), \hat{p}^l(\mathbf{x}, \boldsymbol{\xi}_m)\right)$ defined by (7.2.14) and (7.2.15). Particular solutions for the flow field can be evaluated if the auxiliary solution $\left(\hat{u}_i^l(\mathbf{x}, \boldsymbol{\xi}_m), \hat{p}^l(\mathbf{x}, \boldsymbol{\xi}_m)\right)$ and the coefficients β_m^l (given from B_i) are known and take the form,

$$u_i^p = \sum_{m=1}^{n} \beta_m^l \hat{u}_i^l(\mathbf{x}, \boldsymbol{\xi}_m), \tag{7.2.29}$$

$$p^p = \sum_{m=1}^{n} \beta_m^l \hat{p}^l(\mathbf{x}, \boldsymbol{\xi}_m), \tag{7.2.30}$$

$$f_i^p = \sum_{m=1}^{n} \beta_m^l \hat{f}_i^l(\mathbf{x}, \boldsymbol{\xi}_m). \tag{7.2.31}$$

The integral equation (7.2.18) for the DRM approach is obtained by substituting the homogeneous components in (7.2.24) for full and particular variables.

7.2.3 Construction Of The Convective Term And Auxiliary Flow Fields

Both of the above methods require the corresponding auxiliary solution for the RBF used to interpolate the convective term. In addition values for the convective term are also required. This can be achieved by using a mass conservative RBF interpolation for the velocities.

The convective term B_i is represented by interpolating the domain velocities with a RBF, and then using this interpolation to evaluate the derivatives of the velocity field. The interpolation is further constrained to satisfy mass conservation, as considered by Florez and Power [56]. A thin plate spline RBF of the form

$$\psi(\mathbf{x}, \boldsymbol{\xi}) = r^3, \tag{7.2.32}$$

is chosen, where $r = \| \mathbf{x} - \boldsymbol{\xi} \|$, and in this case a second order polynomial of the form

$$\begin{aligned} P_2 = \alpha_1^P + \alpha_2^P x_1 + \alpha_3^P x_2 + \alpha_4^P x_3 + \alpha_5^P x_1 x_2 \\ \alpha_6^P x_1 x_3 + \alpha_7^P x_2 x_3 + \alpha_8^P x_1^2 + \alpha_9^P x_2^2 + \alpha_{10}^P x_3^2, \end{aligned} \tag{7.2.33}$$

is required to guarantee invertibility, along with the appropriate homogeneous constraint condition.

The velocity field is represented by the Hermitian interpolation shown below

$$u_1 = \sum_{m=1}^{n} \alpha_m^1 \psi(\mathbf{x}, \boldsymbol{\xi}_m) + \sum_{m=1}^{n} \alpha_m^4 \frac{\partial \psi(\mathbf{x}, \boldsymbol{\xi}_m)}{\partial \xi_1} + P_2^1, \tag{7.2.34}$$

$$u_2 = \sum_{m=1}^{n} \alpha_m^2 \psi(\mathbf{x}, \boldsymbol{\xi}_m) + \sum_{m=1}^{n} \alpha_m^4 \frac{\partial \psi(\mathbf{x}, \boldsymbol{\xi}_m)}{\partial \xi_2} + P_2^2, \tag{7.2.35}$$

$$u_3 = \sum_{m=1}^{n} \alpha_m^3 \psi(\mathbf{x}, \boldsymbol{\xi}_m) + \sum_{m=1}^{n} \alpha_m^4 \frac{\partial \psi(\mathbf{x}, \boldsymbol{\xi}_m)}{\partial \xi_3} + P_2^3. \tag{7.2.36}$$

Corresponding derivatives of the velocity field are found by,

$$\frac{\partial u_i}{\partial x_j} = \sum_{m=1}^{n} \alpha_m^i \frac{\partial \psi(\mathbf{x}, \boldsymbol{\xi}_m)}{\partial x_j} + \sum_{m=1}^{n} \alpha_m^4 \frac{\partial \psi(\mathbf{x}, \boldsymbol{\xi}_m)}{\partial \xi_i \partial x_j} + \frac{\partial P_2^i}{\partial x_j}. \tag{7.2.37}$$

The mass conservative formulation forms the matrix problem $W_{3_{ij}} x_j = b_i$, where the first three rows of the matrix $W_{3_{ij}}$ in (7.2.38) consists of the velocity interpolations u_1, u_2 and u_3 as given by (7.2.34) - (7.2.36), collocated over n data points. The fourth row satisfies $\frac{\partial u_1}{\partial x_1} + \frac{\partial u_2}{\partial x_2} + \frac{\partial u_3}{\partial x_3} = 0$, corresponding to mass conservation and applied over the same n data points as the velocity interpolation. The final three rows describe the homogeneous constraint condition, required to guarantee invertibility of the interpolation

matrix. Thus, the matrix $W_{3_{ij}}$ takes the form of

$$W_{3_{ij}} = \begin{pmatrix} \psi & 0 & 0 & \frac{\partial \psi}{\partial \xi_1} & P_2^1 & 0 & 0 \\ 0 & \psi & 0 & \frac{\partial \psi}{\partial \xi_2} & 0 & P_2^2 & 0 \\ 0 & 0 & \psi & \frac{\partial \psi}{\partial \xi_3} & 0 & 0 & P_2^3 \\ \frac{\partial \psi}{\partial x_1} & \frac{\partial \psi}{\partial x_2} & \frac{\partial \psi}{\partial x_3} & \frac{\partial \psi}{\partial x_k \partial \xi_k} & \frac{\partial P_2^1}{\partial x_1} & \frac{\partial P_2^2}{\partial x_2} & \frac{\partial P_2^3}{\partial x_3} \\ \left(P_2^1\right)^T & 0 & 0 & \left(\frac{\partial P_2^1}{\partial x_1}\right)^T & 0 & 0 & 0 \\ 0 & \left(P_2^2\right)^T & 0 & \left(\frac{\partial P_2^2}{\partial x_2}\right)^T & 0 & 0 & 0 \\ 0 & 0 & \left(P_2^3\right)^T & \left(\frac{\partial P_2^3}{\partial x_3}\right)^T & 0 & 0 & 0 \end{pmatrix}, \tag{7.2.38}$$

which is of size $(4n+30) \times (4n+30)$, and summation convention is applied to the term $\frac{\partial \psi}{\partial x_k \partial \xi_k}$. The vector x_j takes the form

$$x_j = \begin{pmatrix} \alpha^1 & \alpha^2 & \alpha^3 & \alpha^4 & \alpha^{P^1} & \alpha^{P^2} & \alpha^{P^3} \end{pmatrix}^T, \tag{7.2.39}$$

and vector b_i the form

$$b_i = \begin{pmatrix} u_1 & u_2 & u_3 & \frac{\partial u_k}{\partial x_k} & 0 & 0 & 0 \end{pmatrix}^T, \tag{7.2.40}$$

where $\frac{\partial u_k}{\partial x_k} = 0$. Solution of this system allows the values of each velocity component to be found anywhere within the domain.

The auxiliary flow field is obtained by interpolating the convective term, and finding an analytical expression for the auxiliary velocity, pressure and traction from the interpolant. For interpolating the convective term (7.2.12), a thin plate spline RBF is used of the form

$$\psi(\mathbf{x}, \boldsymbol{\xi}) = r, \tag{7.2.41}$$

and again $r = \| \mathbf{x} - \boldsymbol{\xi} \|$. An additional first order polynomial

$$P_1 = \beta_1 + \beta_2 x_1 + \beta_3 x_2 + \beta_4 x_3, \tag{7.2.42}$$

along with a homogeneous constraint condition is necessary to guarantee invertibility of the system. This interpolation of the convective term requires the solution of the matrix-vector problem $W_{1_{ij}}\beta = \hat{b}_i$ where the matrix $W_{1_{ij}}$ is given by

$$W_{1_{ij}} = \begin{pmatrix} \psi & P_1 \\ (P_1)^T & 0 \end{pmatrix}, \tag{7.2.43}$$

of size $(n+4)\times(n+4)$, and the vector $\hat{b}_i$ is

$$\hat{b}_i = \begin{pmatrix} B & 0 \end{pmatrix}^T. \tag{7.2.44}$$

The auxiliary solutions to (7.2.14)and (7.2.15) are found by first representing the solution in terms of the potential $\phi(r)$,

$$\hat{u}_i^l(\mathbf{x}, \boldsymbol{\xi}_m) = \frac{\partial^2\phi(r)}{\partial x_k^2}\delta_{il} - \frac{\partial^2\phi(r)}{\partial x_i \partial x_l}, \tag{7.2.45}$$

which can be shown to satisfy conservation of mass (7.2.14). Substituting the expression (7.2.45) for $\hat{u}_i^l(\mathbf{x}, \boldsymbol{\xi}_m)$ into (7.2.15) yields

$$-\frac{\partial \hat{p}^l(\mathbf{x}, \boldsymbol{\xi}_m)}{\partial x_i} + \frac{\partial^4\phi(r)}{\partial x_k^4}\delta_{il} - \frac{\partial^4\phi(r)}{\partial x_i \partial x_l \partial x_k^2} = \psi(\mathbf{x}, \boldsymbol{\xi}_m)\delta_{il}. \tag{7.2.46}$$

The potential $\phi(r)$ is chosen to satisfy the non-homogeneous bi-harmonic equation

$$\frac{\partial^4\phi(r)}{\partial x_k^4} = \psi(r), \tag{7.2.47}$$

as the RBF can be written in terms of the radial distance, r. Correspondingly, the auxiliary pressure is given by

$$\hat{p}^l(\mathbf{x}, \boldsymbol{\xi}_m) = -\frac{\partial^3\phi(r)}{\partial x_l \partial x_k^2}, \tag{7.2.48}$$

and the traction is found by (7.2.16).

The potential $\phi(r)$ is found from equation (7.2.47), and the auxiliary velocity, pressure and traction can be found from (7.2.45), (7.2.48) and (7.2.16) respectively. The potential

and auxiliary flow field is also required for the first order polynomial (7.2.42). In this case, the data centre ξ_j is not relevant, and solutions are a function of the collocation node x_i only.

The auxiliary variables $\hat{u}_i^l$, $\hat{p}^l$, and $\hat{f}_i^l$ corresponding to $\psi = r$, $\psi = 1$, $\psi = x_1$, $\psi = x_2$, and $\psi = x_3$ are presented in Appendix C. It should be noted that although both $\hat{u}_i^l$ and $\hat{f}_i^l$ are required for film flow analysis, when considering a lid driven cavity, it is solely the velocity field which is of interest. As such, the particular pressures and tractions of the flow field are not required.

7.2.4 Numerical Techniques For Solving Low Reynolds Flow In A Lid Driven Cavity

Solution of the above formulations for the low Reynolds number flow in a lid driven cavity can take a range of iterative procedures. The conventional PIT approach involves writing the problem in a boundary only integral representation. The velocity field from the previous iteration is used to linearize the convective term and the numerical scheme forms a large matrix problem, solved at each iteration for the velocity field within the domain, and unknown values on the domain boundary (in this case boundary tractions). Details of the formulation are shown later.

Alternatively, the convective term can be approximated entirely from the previous iteration, and the particular solution evaluated explicitly. The boundary conditions of the integral equation for the homogeneous components can be updated and the homogeneous solution found throughout the domain. Although this particular solution technique (PST) as used by Power and Botte [55] is generally less convergent than the more traditional PIT, it is appealing due to the significant reduction in computational resources required. In addition, due to the simplification in explicitly finding the particular solution, it is possible to reduce the computational requirements of the mass conservative interpolation of the velocities further by means of a local interpolation. Details of this

Bounding Point	d_1	d_2	d_3	d_4	d_5	d_6	d_7	d_8
Bounding Value	0.7	0.3	0.2	0.15	0.1	0.05	0.02	0.01

Table 7.1: Boundary values used to determine which numerical integration approach to implement for the case of a lid driven cavity.

method are also considered.

For all numerical schemes, the BEM is implemented with constant elements. In addition, refinement of the numerical integration in cases with near-point singularities consists of a combination of the adaptive Gaussian integration algorithm and element subdivision approach outlined in chapter 4, with bounding values modified to those shown in table 7.1

Conventional Particular Integral Technique (PIT)

Within the PIT, the homogeneous BIE can be written in terms of the full velocity variables (7.2.19), yielding

$$\begin{aligned} &c_{ij}(\mathbf{x}_0)u_i(\mathbf{x}_0) \\ &=\frac{1}{8\pi}\int_D G_{ij}(\mathbf{x},\mathbf{x}_0)f_i^h(\mathbf{x})\mathrm{d}S(\mathbf{x}) - \frac{1}{8\pi}\int_D u_i(\mathbf{x})T_{ijk}(\mathbf{x},\mathbf{x}_0)n_k(\mathbf{x})\mathrm{d}S(\mathbf{x}) \\ &\quad + \sum_{m=1}^{n}\beta_m^l\left[c_{ij}(\mathbf{x}_0)\hat{u}_i^l(\mathbf{x}_0,\boldsymbol{\xi}_m) + \frac{1}{8\pi}\int_D \hat{u}_i^l(\mathbf{x},\boldsymbol{\xi}_m)T_{ijk}(\mathbf{x},\mathbf{x}_0)n_k(\mathbf{x})\mathrm{d}S(\mathbf{x})\right], \end{aligned} \tag{7.2.49}$$

in terms of the auxiliary velocities and it is left to find an approximation for β_m^l.

The matrix vector notation for the coefficients $\boldsymbol{\beta}$ is

$$\boldsymbol{\beta} = \mathbf{W}_1^{-1}\mathbf{B}, \tag{7.2.50}$$

where $\mathbf{W}_1$ is the interpolation matrix of the RBF (7.2.43). In addition the matrix vector notation for the mass conservative velocity interpolation is

$$\mathbf{u} = \mathbf{W}_3\boldsymbol{\alpha}, \tag{7.2.51}$$

where $\mathbf{W}_3$ is the interpolation matrix (7.2.38) and the derivatives of the velocity are defined by,

$$\frac{\partial \mathbf{u}}{\partial x_j} = \frac{\partial \mathbf{W}_3}{\partial x_j}\boldsymbol{\alpha}. \tag{7.2.52}$$

Using expression (7.2.52) coefficients $\boldsymbol{\beta}$ are defined by,

$$\boldsymbol{\beta} = \mathbf{W}_1^{-1}\tilde{\mathbf{U}}^j \frac{\partial \mathbf{W}_3}{\partial x_j}\mathbf{W}_3^{-1}\mathbf{u}, \tag{7.2.53}$$

where the term $\tilde{\mathbf{U}}^j$ is a matrix with j^{th} velocity component from the previous iteration on the leading diagonal. Clearly in solving the BIE (7.2.49), a large system of equations is produced covering all boundary and domain points, and requires solving at each iteration.

Efficient Implementation Of Particular Solution Techniques (PST)

Alternatively to the PIT method outlined above, a more computationally efficient PST approach can be developed by evaluating the particular solutions based entirely on the data from the previous iteration. The process is described in the following bullet points.

(i) Make an initial guess for the velocities within the domain, e.g. Stokes flow.

(ii) Calculate the mass conservative RBF interpolation for the domain velocities (7.2.38) to find the coefficients $\boldsymbol{\alpha}$.

(iii) Using (7.2.37) find the derivatives of the velocity field and evaluate the convective term $\mathbf{B}$.

(iv) Using the convective term, interpolate using (7.2.12) to find β_m^l.

(v) Particular velocities within the domain can be found and are given by (7.2.29).

(vi) The boundary conditions to the homogeneous solution are updated using the particular solutions.

(vii) The homogeneous solution is found using the BIE (7.2.24) for unknown boundary values.

(viii) The BIE is then implemented to find the homogeneous velocities within the domain.

(ix) The homogeneous and particular velocities are combined, convergence is tested and the procedure is repeated from step (ii) if necessary.

The advantage of the PST over the conventional PIT is the reduction in computational requirements. In the PIT a large system of equations is generated during each iteration which then require solving. In this analysis a smaller system (based on either the unknown boundary quantities or domain points) is formed. In addition, the matrix components of this system are unchanged throughout the iterations. Thus a LUD decomposition can be generated initially, and then used at each iteration to obtain the solution with a modified right-hand-side to the matrix vector problem.

The computational requirements associated with the evaluation of the mass conservative velocity interpolation (7.2.38) can be further reduced. The matrix is large and of size $(4n+30)\times(4n+30)$, where n is the number of interpolation points within the domain. By using a local RBF interpolation, the problem can be reduced to n matrices of size $(4n_l+30)\times(4n_l+30)$, where n_l is the number of local interpolation points and $n_l \ll n$. Typically $n_l \sim 30$ for this analysis and the RBF interpolation is constructed from the closest n_l data points to the global point of interest. Further details of local RBF interpolations are given in chapter 3

7.2.5 Flow Profiles For A Lid Driven Cavity

This subsection considers solutions for flow in a three-dimensional lid driven cavity at a selection of Reynolds numbers. As the boundary velocities to the domain are known, a regular array of interpolation points are used throughout the domain and boundary for

the mass conservative velocity, and inertia interpolations. These interpolations are used to find the particular velocities at the collocation points of the BEM and the internal domain points. In all test cases 3456 triangular boundary elements and 2197 interpolation points are used. Initially comparison of the PIT using a global mass conservative interpolation and the PST using both the global and local mass conservative interpolations is made. Analysis for both the computational time and peak RAM requirements of the formulations is conducted. The use of a local interpolation introduces an additional approximation in the analysis, and the accuracy of the local interpolation and the choice of n_l is considered. Following this analysis, results are presented for the three-dimensional lid driven cavity, giving good agreement with previously published results.

Comparison Of Methods

The computational performance of the three numerical methods are compared when solving for the velocity field in a lid driven cavity at $Re = 100$. In all cases the iterative loop requires an under-relaxation factor for convergence. For the PIT an under-relaxation factor of 0.8 was found optimum; for the global PST, a value of 0.5 was used and for the local PST, 0.6 was required. In each case the under-relaxation value was found optimum to the nearest tenth. For the local interpolation, the number of points used was minimized, whilst avoiding a singular interpolation matrix, and in this case 27 points was found as the minimum. Figure 7.2 indicates the computational requirements of peak RAM and run time for each numerical method. Clearly using the global PST over the PIT produces significant advantages in terms of computational resources required. The RAM required reduces from 6.5GB to 4GB, and the run time is over 20 times faster. Moving to the local RBF interpolation gives further reduction in computational resources required. Peak RAM reduces to under 3.5GB, and the simulation time is halved again from the global PST. Clearly a significant reduction in the computational requirements of the problem is made when adopting the PST over a more conventional PIT approach.

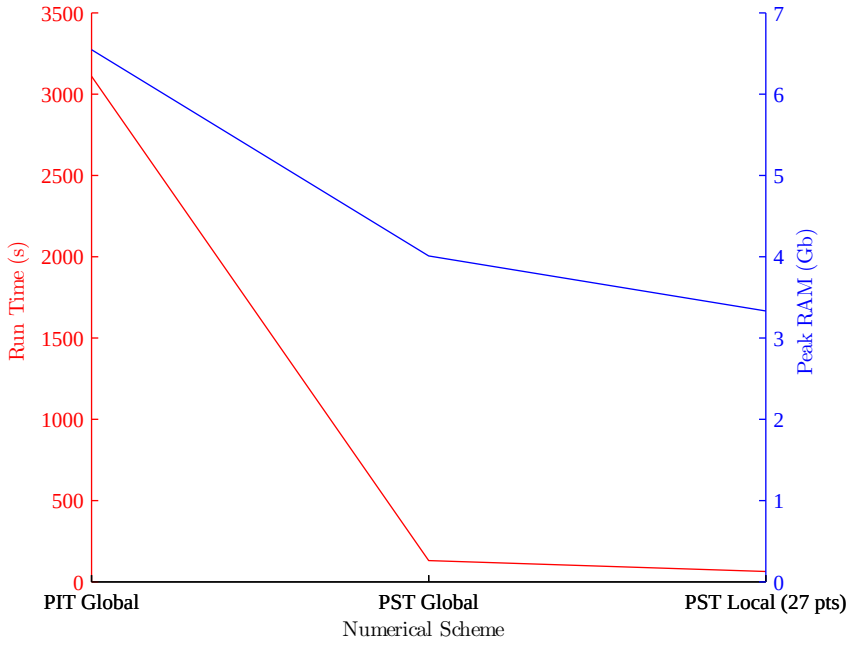

Figure 7.2: Comparison of computational performance of the numerical schemes for flow in a lid driven cavity at $Re = 100$.

Although the global forms of the PIT and PST approaches solve identical systems of equations (albeit by different means), the local mass conservative velocity interpolation introduces an additional approximation into the formulation. The accuracy of this approximation can be improved by increasing the number of local points used, however this increases the computational requirements, acting to negate the advantage gained by using this interpolation. Figure 7.3 illustrates the maximum L^2 norm over all data points in the velocity field for the difference between the PIT velocity vector and those obtained by the PST. The global PST method solves an identical system of equations to the global PIT approach, and as predicted the solution is identical. The introduction of the local mass conservative RBF interpolation introduces an additional approximation, whose accuracy is shown to increase with increasing size of the local domain. However, this is at the expense of computational speed, and eventually the solution run time will become greater than that for the global approach.

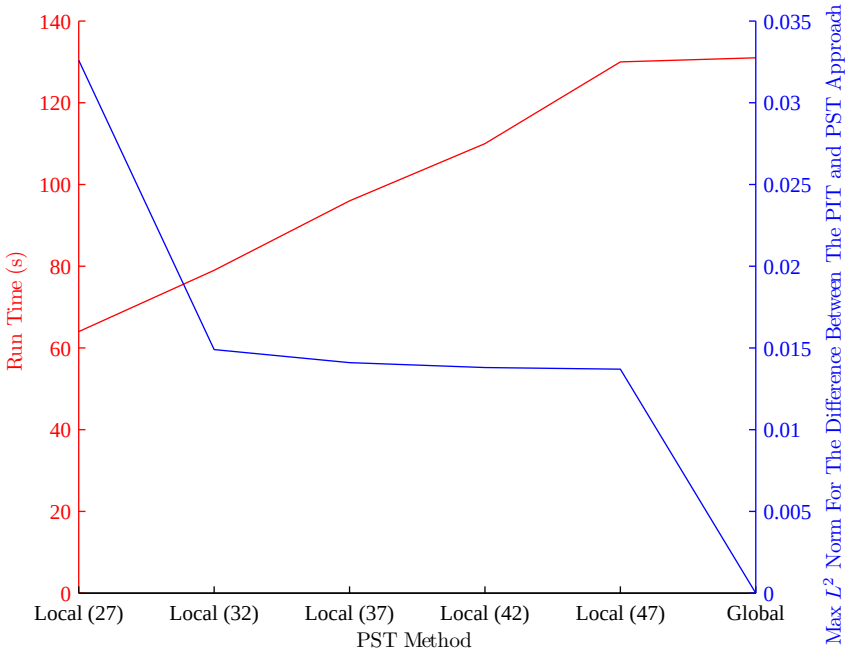

Figure 7.3: Results of the accuracy attained by a local RBF interpolation, for flow in a lid driven cavity at $Re = 100$.

Solutions At A Range Of Reynolds Numbers

Solutions for the vector fields within the cavity are shown at $Re = 0$, $Re = 100$ and $Re = 200$ using the local RBF interpolation for 32 points. Figure 7.4 illustrates the velocity field on the centre plane ($x_2 = 0$) for Stokes flow and a low Reynolds number flow ($Re = 100$) in a three-dimensional lid driven cavity. Qualitatively, these profiles are as expected from previous studies and an increase in Reynolds number moves the vortex towards the right hand corner of the cavity.

However for quantitative analysis, Figure 7.5 is produced, presenting the centre line solution for the velocity component u_{x_1} in the x_3 direction ($x_1 = x_2 = 0$) and velocity component u_{x_3} in the x_1 direction ($x_2 = x_3 = 0$) for $Re = 0$, $Re = 100$ and $Re = 200$. Comparison of these profiles can be made with published results, for example Yang et al. [58]. Figure 7.5a for u_{x_1} in the x_3 direction illustrates excellent agreement with previously published results at $Re = 100$. Figure 7.5b produces a small discrepancy from

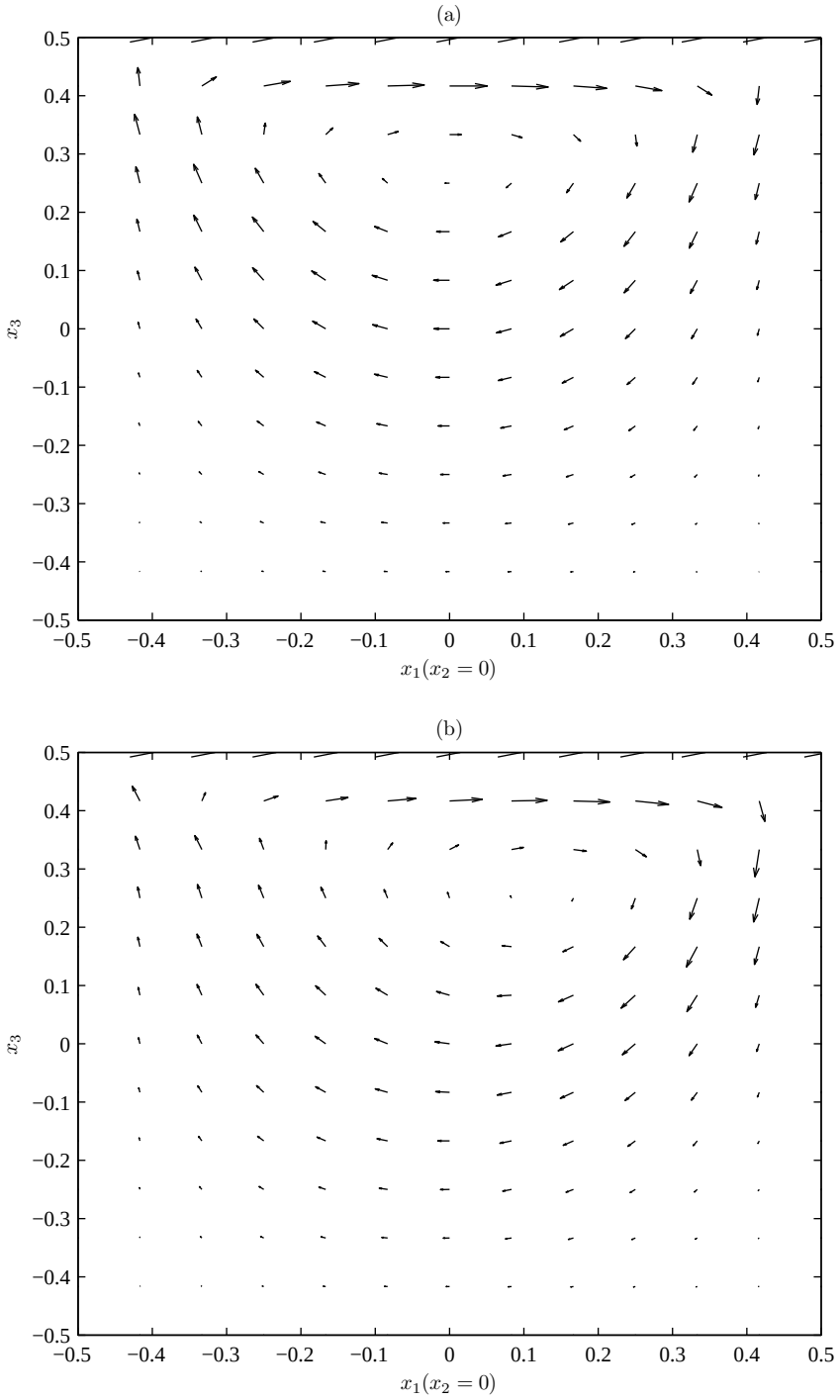

Figure 7.4: Centre plane solution of flow in a three-dimensional lid driven cavity for (a) Stokes flow ($Re = 0$) and (b) $Re = 100$.

published results for u_{x_3} in the x_1 direction at $Re = 100$. Here the prediction for the vertical velocity is slightly greater between $-0.2 < x_1 < 0.4$ than the equivalent profile in [58].

7.3 Low Reynolds Number Film Flows

This section considers the inertial effects on flows over and around circular cylinders at low Reynolds number. An overview of the mathematical formulation for the case of film flow at finite Reynolds number is initially presented. Following this, a numerical approach is developed based on the optimal scheme developed for a three-dimensional lid driven cavity in § 7.2. Finally results are presented indicating the effects of low Reynolds number on the film profile generated.

7.3.1 Formulation Of Low Reynolds Number Film Flows

The mathematical formulation is presented for film flow down an inclined plane and around an obstacle at finite Reynolds number. However, the formulation can be reduced to flow over a single cylinder by omission of the contact line condition and the "dry" top of the cylinder $\tilde{S}_f$. Figure 7.6 indicates a schematic for flow around a cylinder. This is similar to that presented in figure 6.2, with the edges of the domain now marked as S_e.

The flow is governed by mass continuity (7.3.1) and Navier-Stokes equation (7.3.2),

$$\frac{\partial u_i}{\partial x_i} = 0, \tag{7.3.1}$$

$$-\frac{\partial p}{\partial x_i} + \frac{\partial G}{\partial x_i} + \frac{\partial^2 u_i}{\partial x_j^2} = Re\, u_j \frac{\partial u_i}{\partial x_j}, \tag{7.3.2}$$

where $G = -2(x_3 \cot\alpha - x_1)$ is the gravitational driving components as in the Stokes case considered previously. A summary of the various surfaces defined in figure 7.6 are given in table 7.2. By using the characteristic scales defined in table 4.1, the following

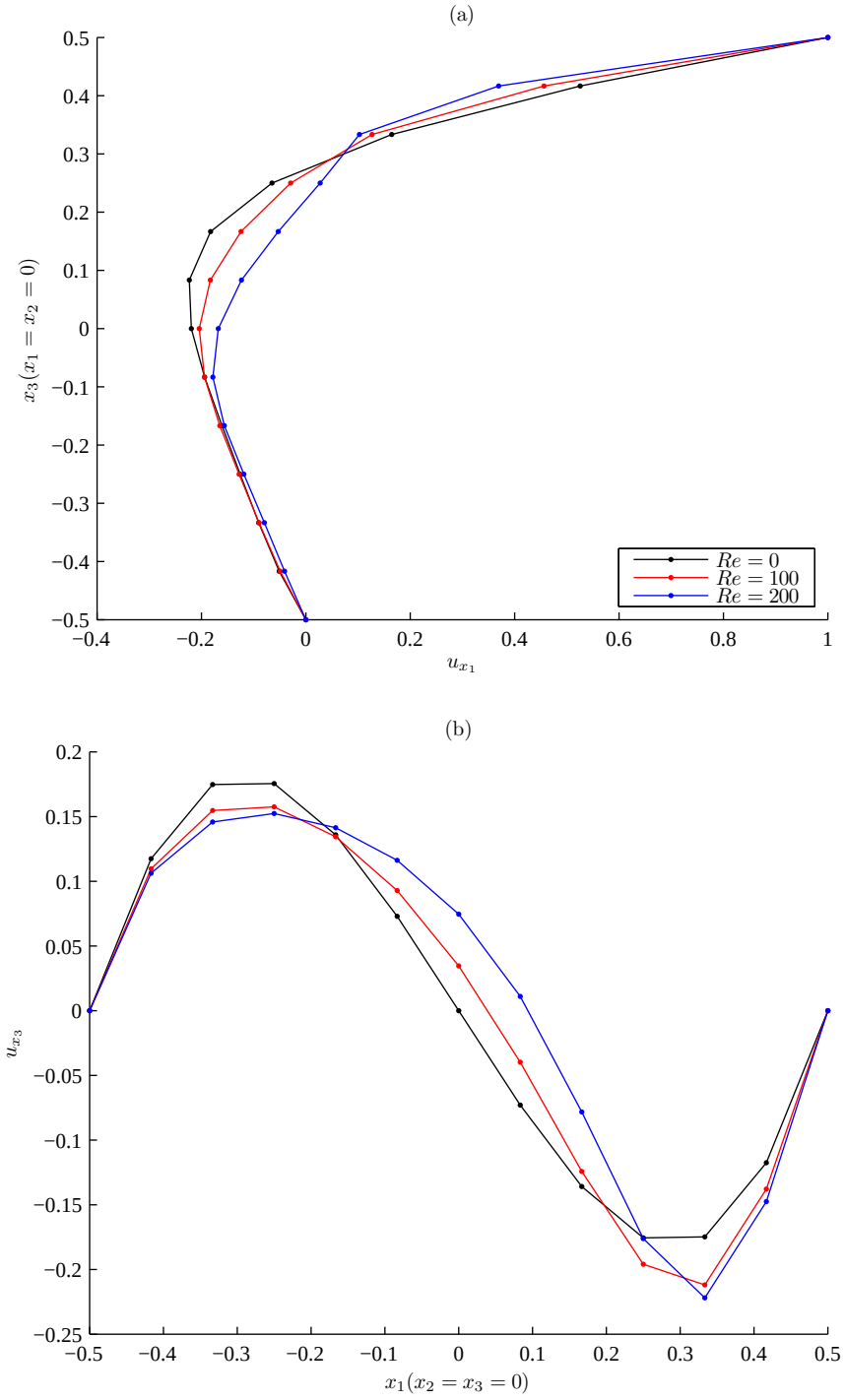

Figure 7.5: Centre line solution at $Re = 0$, $Re = 100$ and $Re = 200$ for flow in a three-dimensional lid driven cavity showing (a) velocity component u_{x_1} in the x_3 direction ($x_1 = x_2 = 0$) and (b) velocity component u_{x_3} in the x_1 direction ($x_2 = x_3 = 0$).

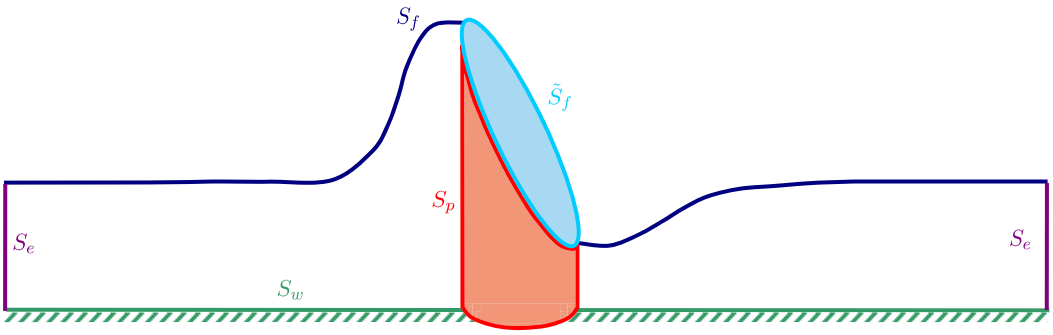

Figure 7.6: Schematic showing nomenclature for flow around a cylinder at finite Reynolds number. In this case the edges of the domain are denoted S_e.

S_f	Free surface
$\tilde{S}_f$	Cylinder top
S_p	Wetted cylinder surface
S_e	Edges to the domain
S_w	Wall

Table 7.2: Definition of surface nomenclature.

expression for the Reynolds number can be found,

$$Re = \frac{H^3 g \sin\alpha}{2\nu^2}. \tag{7.3.3}$$

The film flow is subject to the following boundary conditions

$$u_i = 0 \quad \mathbf{x} \in S_w, S_p, \tag{7.3.4}$$

$$\frac{\partial x_i}{\partial t} n_i = u_j n_j \quad \mathbf{x} \in S_f, \tag{7.3.5}$$

$$f_i = -\frac{4}{Bo} \kappa n_i \quad \mathbf{x} \in S_f, \tag{7.3.6}$$

$$\frac{\partial h}{\partial x_i} n_i = \tan\left(\frac{\pi}{2} - \theta\right) \quad \mathbf{x} \in S_f \cap S_p. \tag{7.3.7}$$

No slip on the wall and wetted obstacle surface is defined by (7.3.4), the kinematic and dynamic condition are defined by (7.3.5) - (7.3.6) respectively and applied on the free surface. Finally, (7.3.7) is the contact line constraint.

As for Stokes flow analysis, the solution variables are decomposed into disturbance (superscript δ) and an asymptotic regime (superscript ∞),

$$u_i = u_i^\delta + u_i^\infty, \tag{7.3.8}$$

$$p = p^\delta + p^\infty, \tag{7.3.9}$$

$$f_i = f_i^\delta + f_i^\infty. \tag{7.3.10}$$

The undisturbed governing equations are (7.3.11) - (7.3.12)

$$\frac{\partial u_i^\infty}{\partial x_i} = 0, \tag{7.3.11}$$

$$-\frac{\partial p^\infty}{\partial x_i} + \frac{\partial G}{\partial x_i} + \frac{\partial^2 u_i^\infty}{\partial x_j^2} = 0, \tag{7.3.12}$$

where (p^∞, u_i^∞) is the flow field associated with Stokes flow down an inclined plane in the absence of obstacles. As in earlier analysis, the solutions for the asymptotic flow field are,

$$u_i^\infty = (1 - x_3^2)\delta_{i1}, \tag{7.3.13}$$

$$p^\infty = -2x_3 \cot\alpha, \tag{7.3.14}$$

$$f_i^\infty = 2x_3(n_i \cot\alpha - n_3\delta_{i1} - n_1\delta_{i3}). \tag{7.3.15}$$

It is also noted that this solution of u_i^∞ satisfies $u_j^\infty \frac{\partial u_i^\infty}{\partial x_j} = 0$, and (p^∞, u_i^∞) is also the solution of the full Navier-Stokes equations for flow down an inclined plane in the absence of obstructions.

The far field conditions for the flow problem require the free surface disturbance to tend to zero far from the obstacle, and the film velocity, pressure and boundary tractions to return to those of an undisturbed film. Thus the far field constraints are:

$$h, \frac{\partial h}{\partial x_1}, \frac{\partial h}{\partial x_2} \rightarrow 0 \quad \mathbf{x} \rightarrow \pm\infty, \tag{7.3.16}$$

$$u_i \rightarrow u_i^\infty \quad \mathbf{x} \rightarrow \pm\infty, \tag{7.3.17}$$

$$p \rightarrow p^\infty \quad \mathbf{x} \rightarrow \pm\infty, \tag{7.3.18}$$

$$f_i \rightarrow f_i^\infty \quad \mathbf{x} \rightarrow \pm\infty. \tag{7.3.19}$$

The disturbance governing equations are (7.3.20) - (7.3.21)

$$\frac{\partial u_i^\delta}{\partial x_i} = 0, \tag{7.3.20}$$

$$-\frac{\partial p^\delta}{\partial x_i} + \frac{\partial^2 u_i^\delta}{\partial x_j^2} = Re\, u_j \frac{\partial u_i}{\partial x_j}, \tag{7.3.21}$$

subject to the following boundary and far field conditions

$$u_i^\delta = 0 \quad \mathbf{x} \in S_w, \tag{7.3.22}$$

$$u_i^\delta = -u_i^\infty \quad \mathbf{x} \in S_p, \tag{7.3.23}$$

$$f_i^\delta = f_i - f_i^\infty \quad \mathbf{x} \in S_f, \tag{7.3.24}$$

$$u_i^\delta = 0 \quad \mathbf{x} \in S_e, \tag{7.3.25}$$

$$f_i^\delta = 0 \quad \mathbf{x} \in S_e, \tag{7.3.26}$$

For solution, the disturbance regime is decomposed further into a homogeneous (superscript h) and particular (superscript p) components,

$$u_i^\delta = u_i^{h\delta} + u_i^{p\delta}, \tag{7.3.27}$$

$$p^\delta = p^{h\delta} + p^{p\delta}, \tag{7.3.28}$$

$$f_i^\delta = f_i^{h\delta} + f_i^{p\delta}, \tag{7.3.29}$$

The homogeneous solutions are governed by the following expressions for mass conservation and Stokes equation

$$\frac{\partial u_i^{h\delta}}{\partial x_i} = 0, \tag{7.3.30}$$

$$-\frac{\partial p^{h\delta}}{\partial x_i} + \frac{\partial^2 u_i^{h\delta}}{\partial x_j^2} = 0, \tag{7.3.31}$$

and the particular solutions satisfies

$$\frac{\partial u_i^{p\delta}}{\partial x_i} = 0, \tag{7.3.32}$$

$$-\frac{\partial p^{p\delta}}{\partial x_i} + \frac{\partial^2 u_i^{p\delta}}{\partial x_j^2} = Re\, u_j \frac{\partial u_i}{\partial x_j}. \tag{7.3.33}$$

The particular solutions fails to satisfy any boundary conditions. As such the boundary conditions for the homogeneous components of the disturbance regime are modified to account for the particular solution. Thus the homogeneous disturbance regime is solved for the boundary conditions

$$u_i^{h\delta} = -u_i^{p\delta} \quad \mathbf{x} \in S_w, \tag{7.3.34}$$

$$u_i^{h\delta} = -u_i^{p\delta} - u_i^{\infty} \quad \mathbf{x} \in S_p, \tag{7.3.35}$$

$$f_i^{h\delta} = f_i - f_i^{p\delta} - f_i^{\infty} \quad \mathbf{x} \in S_f, \tag{7.3.36}$$

$$u_i^{h\delta} = -u_i^{p\delta} \quad \mathbf{x} \in S_e, \tag{7.3.37}$$

$$f_i^{h\delta} = -f_i^{p\delta} \quad \mathbf{x} \in S_e. \tag{7.3.38}$$

Hence, terms on the wall and at the edges of the domain that were identically zero for the Stokes flow analysis now require evaluation.

The Boundary Integral Equations

A boundary integral equation (BIE) for the asymptotic flow quantities inside the obstacle domain is,

$$\begin{aligned} c_{ij}(\mathbf{x}_0)u_i^{\infty}(\mathbf{x}_0) = -\frac{1}{8\pi} &\int\limits_{S_p \cup \tilde{S}_f \cup S_w} G_{ij}^*(\mathbf{x},\mathbf{x}_0)\tilde{f}_i^{\infty}(\mathbf{x})\mathrm{d}S(\mathbf{x}) \\ &+\frac{1}{8\pi} \int\limits_{S_p \cup \tilde{S}_f \cup S_w} u_i^{\infty}(\mathbf{x})T_{ijk}^*(\mathbf{x},\mathbf{x}_0)n_k(\mathbf{x})\mathrm{d}S(\mathbf{x}), \end{aligned} \tag{7.3.39}$$

where the unit normal is taken to point out of the fluid, and thus into the obstacle domain and $\tilde{f}_i^{\infty}(\mathbf{x}) = f_i^{\infty}(\mathbf{x}) + Gn_i$. Correspondingly the BIE for the homogeneous disturbance quantities over the fluid domain is,

$$\begin{aligned} c_{ij}(\mathbf{x}_0)u_i^{h\delta}(\mathbf{x}_0) = \frac{1}{8\pi} &\int\limits_{S_f \cup S_p \cup S_w \cup S_e} G_{ij}^*(\mathbf{x},\mathbf{x}_0)f_i^{h\delta}(\mathbf{x})\mathrm{d}S(\mathbf{x}) \\ &- \frac{1}{8\pi} \int\limits_{S_f \cup S_p \cup S_w \cup S_e} u_i^{h\delta}(\mathbf{x})T_{ijk}^*(\mathbf{x},\mathbf{x}_0)n_k(\mathbf{x})\mathrm{d}S(\mathbf{x}). \end{aligned} \tag{7.3.40}$$

The Lorentz-Blake Green's functions yield $G^*_{ij}(\mathbf{x},\mathbf{x}_0) = 0 \quad \mathbf{x} \in S_w$ and also for the asymptotic solution $u_i^\infty = 0 \quad \mathbf{x} \in S_w$. Thus equations (7.3.39) and (7.3.40) become

$$\begin{aligned} c_{ij}(\mathbf{x}_0)u_i^\infty(\mathbf{x}_0) = -\frac{1}{8\pi}\int\limits_{S_p\cup\tilde{S}_f} G^*_{ij}(\mathbf{x},\mathbf{x}_0)\tilde{f}_i^\infty(\mathbf{x})\mathrm{d}S(\mathbf{x}) \\ +\frac{1}{8\pi}\int\limits_{S_p\cup\tilde{S}_f} u_i^\infty(\mathbf{x})T^*_{ijk}(\mathbf{x},\mathbf{x}_0)n_k(\mathbf{x})\mathrm{d}S(\mathbf{x}), \end{aligned} \tag{7.3.41}$$

and

$$\begin{aligned} c_{ij}(\mathbf{x}_0)u_i^{h\delta}(\mathbf{x}_0) = \frac{1}{8\pi}\int\limits_{S_f\cup S_p\cup S_e} G^*_{ij}(\mathbf{x},\mathbf{x}_0)f_i^{h\delta}(\mathbf{x})\mathrm{d}S(\mathbf{x}) \\ -\frac{1}{8\pi}\int\limits_{S_f\cup S_p\cup S_w\cup S_e} u_i^{h\delta}(\mathbf{x})T^*_{ijk}(\mathbf{x},\mathbf{x}_0)n_k(\mathbf{x})\mathrm{d}S(\mathbf{x}), \end{aligned} \tag{7.3.42}$$

respectively.

Collocation Over The Free Surface

When collocating over the free surface, the BIE for the asymptotic flow regime within the obstacle becomes

$$\begin{aligned} \frac{1}{8\pi}\int\limits_{S_p\cup\tilde{S}_f} G^*_{ij}(\mathbf{x},\mathbf{x}_0)\tilde{f}_i^\infty(\mathbf{x})\mathrm{d}S(\mathbf{x}) \\ = \frac{1}{8\pi}\int\limits_{S_p\cup\tilde{S}_f} u_i^\infty(\mathbf{x})T^*_{ijk}(\mathbf{x},\mathbf{x}_0)n_k(\mathbf{x})\mathrm{d}S(\mathbf{x}), \end{aligned} \tag{7.3.43}$$

and the disturbance BIE becomes

$$\begin{aligned} \frac{1}{2}u_j^{h\delta}(\mathbf{x}_0) + \frac{1}{8\pi}\int\limits_{S_f} u_i^{h\delta}(\mathbf{x})T^*_{ijk}(\mathbf{x},\mathbf{x}_0)n_k(\mathbf{x})\mathrm{d}S(\mathbf{x}) \\ = \frac{1}{8\pi}\int\limits_{S_f} G^*_{ij}(\mathbf{x},\mathbf{x}_0)f_i^{h\delta}(\mathbf{x})\mathrm{d}S(\mathbf{x}) + \frac{1}{8\pi}\int\limits_{S_p\cup S_e} G^*_{ij}(\mathbf{x},\mathbf{x}_0)f_i^{h\delta}(\mathbf{x})\mathrm{d}S(\mathbf{x}) \\ -\frac{1}{8\pi}\int\limits_{S_p\cup S_w\cup S_e} u_i^{h\delta}(\mathbf{x})T^*_{ijk}(\mathbf{x},\mathbf{x}_0)n_k(\mathbf{x})\mathrm{d}S(\mathbf{x}). \end{aligned} \tag{7.3.44}$$

Combining the BIEs (7.3.43) and (7.3.44) yields,

$$\begin{aligned}
&\frac{1}{2}u_j^{h\delta}(\mathbf{x}_0) + \frac{1}{8\pi}\int\limits_{S_f} u_i^{h\delta}(\mathbf{x})T_{ijk}^*(\mathbf{x},\mathbf{x}_0)n_k(\mathbf{x})\mathrm{d}S(\mathbf{x}) \\
&\quad= \frac{1}{8\pi}\int\limits_{S_f} G_{ij}^*(\mathbf{x},\mathbf{x}_0)f_i^{h\delta}(\mathbf{x})\mathrm{d}S(\mathbf{x}) + \frac{1}{8\pi}\int\limits_{S_e} G_{ij}^*(\mathbf{x},\mathbf{x}_0)f_i^{h\delta}(\mathbf{x})\mathrm{d}S(\mathbf{x}) \\
&\quad- \frac{1}{8\pi}\int\limits_{S_e} u_i^{h\delta}(\mathbf{x})T_{ijk}^*(\mathbf{x},\mathbf{x}_0)n_k(\mathbf{x})\mathrm{d}S(\mathbf{x}) + \frac{1}{8\pi}\int\limits_{\tilde{S}_f} G_{ij}^*(\mathbf{x},\mathbf{x}_0)\tilde{f}_i^{\infty}(\mathbf{x})\mathrm{d}S(\mathbf{x}) \\
&\quad- \frac{1}{8\pi}\int\limits_{\tilde{S}_f} u_i^{\infty}(\mathbf{x})T_{ijk}^*(\mathbf{x},\mathbf{x}_0)n_k(\mathbf{x})\mathrm{d}S(\mathbf{x}) - \frac{1}{8\pi}\int\limits_{S_w} u_i^{h\delta}(\mathbf{x})T_{ijk}^*(\mathbf{x},\mathbf{x}_0)n_k(\mathbf{x})\mathrm{d}S(\mathbf{x}) \\
&\quad+ \frac{1}{8\pi}\int\limits_{S_p} G_{ij}^*(\mathbf{x},\mathbf{x}_0)\left(\tilde{f}_i^{\infty}(\mathbf{x}) + f_i^{h\delta}(\mathbf{x})\right)\mathrm{d}S(\mathbf{x}) \\
&\quad- \frac{1}{8\pi}\int\limits_{S_p} (u_i^{\infty}(\mathbf{x}) + u_i^{h\delta}(\mathbf{x}))T_{ijk}^*(\mathbf{x},\mathbf{x}_0)n_k(\mathbf{x})\mathrm{d}S(\mathbf{x}),
\end{aligned} \tag{7.3.45}$$

and using the prescribed boundary conditions this becomes

$$\begin{aligned}
&\frac{1}{2}u_j^{h\delta}(\mathbf{x}_0) + \frac{1}{8\pi}\int\limits_{S_f} u_i^{h\delta}(\mathbf{x})T_{ijk}^*(\mathbf{x},\mathbf{x}_0)n_k(\mathbf{x})\mathrm{d}S(\mathbf{x}) \\
&\quad= \frac{1}{8\pi}\int\limits_{S_f} G_{ij}^*(\mathbf{x},\mathbf{x}_0)f_i^{h\delta}(\mathbf{x})\mathrm{d}S(\mathbf{x}) - \frac{1}{8\pi}\int\limits_{S_e} G_{ij}^*(\mathbf{x},\mathbf{x}_0)f_i^{p\delta}(\mathbf{x})\mathrm{d}S(\mathbf{x}) \\
&\quad+ \frac{1}{8\pi}\int\limits_{S_e} u_i^{p\delta}(\mathbf{x})T_{ijk}^*(\mathbf{x},\mathbf{x}_0)n_k(\mathbf{x})\mathrm{d}S(\mathbf{x}) + \frac{1}{8\pi}\int\limits_{\tilde{S}_f} G_{ij}^*(\mathbf{x},\mathbf{x}_0)\tilde{f}_i^{\infty}(\mathbf{x})\mathrm{d}S(\mathbf{x}) \\
&\quad- \frac{1}{8\pi}\int\limits_{\tilde{S}_f} u_i^{\infty}(\mathbf{x})T_{ijk}^*(\mathbf{x},\mathbf{x}_0)n_k(\mathbf{x})\mathrm{d}S(\mathbf{x}) + \frac{1}{8\pi}\int\limits_{S_w} u_i^{p\delta}(\mathbf{x})T_{ijk}^*(\mathbf{x},\mathbf{x}_0)n_k(\mathbf{x})\mathrm{d}S(\mathbf{x}) \\
&\quad+ \frac{1}{8\pi}\int\limits_{S_p} G_{ij}^*(\mathbf{x},\mathbf{x}_0)\hat{f}_i(\mathbf{x})\mathrm{d}S(\mathbf{x}) + \frac{1}{8\pi}\int\limits_{S_p} u_i^{p\delta}(\mathbf{x})T_{ijk}^*(\mathbf{x},\mathbf{x}_0)n_k(\mathbf{x})\mathrm{d}S(\mathbf{x}),
\end{aligned} \tag{7.3.46}$$

for collocation over the free surface S_f, where $\hat{f}_i(\mathbf{x}) = \tilde{f}_i^{\infty}(\mathbf{x}) + f_i^{h\delta}(\mathbf{x})$. Equation (7.3.46) defines unknown velocities $u_i^{h\delta}$ at the free surface for given particular $(u_i^{p\delta}, p^{p\delta})$, and far field $(u_i^{\infty}, p^{\infty})$ solutions along with surface tractions on the wetted surface of the obstacle.

Collocation Over The Wetted Obstacle Surface

For collocation over the wetted obstacle surface, the BIE corresponding to the asymptotic regime over the obstacle domain takes the form

$$\begin{aligned}\frac{1}{2}u_j^{\infty}(\mathbf{x}_0) = -\frac{1}{8\pi}\int\limits_{S_p\cup\tilde{S}_f} G_{ij}^*(\mathbf{x},\mathbf{x}_0)\tilde{f}_i^{\infty}(\mathbf{x})\mathrm{d}S(\mathbf{x}) \\ + \frac{1}{8\pi}\int\limits_{S_p\cup\tilde{S}_f} u_i^{\infty}(\mathbf{x})T_{ijk}^*(\mathbf{x},\mathbf{x}_0)n_k(\mathbf{x})\mathrm{d}S(\mathbf{x}),\end{aligned} \tag{7.3.47}$$

and the disturbance BIE the form

$$\begin{aligned}\frac{1}{2}u_j^{h\delta}(\mathbf{x}_0) &= \frac{1}{8\pi}\int\limits_{S_f} G_{ij}^*(\mathbf{x},\mathbf{x}_0)f_i^{h\delta}(\mathbf{x})\mathrm{d}S(\mathbf{x}) \\ &- \frac{1}{8\pi}\int\limits_{S_f} u_i^{h\delta}(\mathbf{x})T_{ijk}^*(\mathbf{x},\mathbf{x}_0)n_k(\mathbf{x})\mathrm{d}S(\mathbf{x}) + \frac{1}{8\pi}\int\limits_{S_p\cup S_e} G_{ij}^*(\mathbf{x},\mathbf{x}_0)f_i^{h\delta}(\mathbf{x})\mathrm{d}S(\mathbf{x}) \\ &- \frac{1}{8\pi}\int\limits_{S_p\cup S_w\cup S_e} u_i^{h\delta}(\mathbf{x})T_{ijk}^*(\mathbf{x},\mathbf{x}_0)n_k(\mathbf{x})\mathrm{d}S(\mathbf{x}).\end{aligned} \tag{7.3.48}$$

Rearranging (7.3.47) and (7.3.48) for the obstacle tractions, and combining yields

$$\begin{aligned}\frac{1}{8\pi}\int\limits_{S_p} G_{ij}^*(\mathbf{x},\mathbf{x}_0)\left(\tilde{f}_i^{\infty}(\mathbf{x}) + f_i^{h\delta}(\mathbf{x})\right)\mathrm{d}S(\mathbf{x}) &= \frac{1}{2}u_j^{h\delta}(\mathbf{x}_0) - \frac{1}{2}u_j^{\infty}(\mathbf{x}_0) \\ &- \frac{1}{8\pi}\int\limits_{S_f} G_{ij}^*(\mathbf{x},\mathbf{x}_0)f_i^{h\delta}(\mathbf{x})\mathrm{d}S(\mathbf{x}) + \frac{1}{8\pi}\int\limits_{S_f} u_i^{h\delta}(\mathbf{x})T_{ijk}^*(\mathbf{x},\mathbf{x}_0)n_k(\mathbf{x})\mathrm{d}S(\mathbf{x}) \\ &- \frac{1}{8\pi}\int\limits_{S_e} G_{ij}^*(\mathbf{x},\mathbf{x}_0)f_i^{h\delta}(\mathbf{x})\mathrm{d}S(\mathbf{x}) + \frac{1}{8\pi}\int\limits_{S_e} u_i^{h\delta}(\mathbf{x})T_{ijk}^*(\mathbf{x},\mathbf{x}_0)n_k(\mathbf{x})\mathrm{d}S(\mathbf{x}) \\ &- \frac{1}{8\pi}\int\limits_{\tilde{S}_f} G_{ij}^*(\mathbf{x},\mathbf{x}_0)\tilde{f}_i^{\infty}(\mathbf{x})\mathrm{d}S(\mathbf{x}) + \frac{1}{8\pi}\int\limits_{\tilde{S}_f} u_i^{\infty}(\mathbf{x})T_{ijk}^*(\mathbf{x},\mathbf{x}_0)n_k(\mathbf{x})\mathrm{d}S(\mathbf{x}) \\ &+ \frac{1}{8\pi}\int\limits_{S_w} u_i^{h\delta}(\mathbf{x})T_{ijk}^*(\mathbf{x},\mathbf{x}_0)n_k(\mathbf{x})\mathrm{d}S(\mathbf{x}) \\ &+ \frac{1}{8\pi}\int\limits_{S_p} (u_i^{h\delta}(\mathbf{x}) + u_i^{\infty}(\mathbf{x}))T_{ijk}^*(\mathbf{x},\mathbf{x}_0)n_k(\mathbf{x})\mathrm{d}S(\mathbf{x}),\end{aligned} \tag{7.3.49}$$

and using the prescribed boundary conditions this BIE becomes

$$\begin{aligned}
\frac{1}{8\pi}\int_{S_p} G^*_{ij}(\mathbf{x},\mathbf{x}_0)\hat{f}_i(\mathbf{x})\mathrm{d}S(\mathbf{x}) &= -\frac{1}{2}u_j^{p\delta}(\mathbf{x}_0) - u_j^{\infty}(\mathbf{x}_0) \\
&- \frac{1}{8\pi}\int_{S_f} G^*_{ij}(\mathbf{x},\mathbf{x}_0)f_i^{h\delta}(\mathbf{x})\mathrm{d}S(\mathbf{x}) + \frac{1}{8\pi}\int_{S_f} u_i^{h\delta}(\mathbf{x})T^*_{ijk}(\mathbf{x},\mathbf{x}_0)n_k(\mathbf{x})\mathrm{d}S(\mathbf{x}) \\
&+ \frac{1}{8\pi}\int_{S_e} G^*_{ij}(\mathbf{x},\mathbf{x}_0)f_i^{p\delta}(\mathbf{x})\mathrm{d}S(\mathbf{x}) - \frac{1}{8\pi}\int_{S_e} u_i^{p\delta}(\mathbf{x})T^*_{ijk}(\mathbf{x},\mathbf{x}_0)n_k(\mathbf{x})\mathrm{d}S(\mathbf{x}) \\
&- \frac{1}{8\pi}\int_{\tilde{S}_f} G^*_{ij}(\mathbf{x},\mathbf{x}_0)\tilde{f}_i^{\infty}(\mathbf{x})\mathrm{d}S(\mathbf{x}) + \frac{1}{8\pi}\int_{\tilde{S}_f} u_i^{\infty}(\mathbf{x})T^*_{ijk}(\mathbf{x},\mathbf{x}_0)n_k(\mathbf{x})\mathrm{d}S(\mathbf{x}) \\
&- \frac{1}{8\pi}\int_{S_w} u_i^{p\delta}(\mathbf{x})T^*_{ijk}(\mathbf{x},\mathbf{x}_0)n_k(\mathbf{x})\mathrm{d}S(\mathbf{x}) \\
&\quad - \frac{1}{8\pi}\int_{S_p} u_i^{p\delta}(\mathbf{x})T^*_{ijk}(\mathbf{x},\mathbf{x}_0)n_k(\mathbf{x})\mathrm{d}S(\mathbf{x}),
\end{aligned} \tag{7.3.50}$$

for collocation over the wetted obstacle surface S_p. Equation (7.3.50) defines the unknown boundary tractions $\hat{f}_i$ on the wetted obstacle surface for given particular $(u_i^{p\delta}, p^{p\delta})$, and far field $(u_i^{\infty}, p^{\infty})$ solutions along with free surface velocities given by the previous BIE (7.3.46).

Alternatively, the solutions can be found by considering the homogeneous and particular components first, then solving for the disturbance and undisturbed homogeneous components. Using this method, results produced by the numerical scheme are identical to those generated by the above formulation.

7.3.2 Solution Techniques For Low Reynolds Number Film Flows

This subsection considers the numerical techniques used to solve the film flow problem outlined above. An iterative approach is used to solve the governing equations at each free surface position. In addition an accurate numerical model is required to evaluate the particular solutions, and this is based on the particular solution techniques (PST) outlined in § 7.2.

Iterative Technique

The iterative technique used to solve the governing equations for a three-dimensional lid driven cavity as considered in § 7.2 is developed for the case of finite Reynolds number film flow. The method uses the PST model, solving for homogeneous and particular solutions independently, and iterating to convergence. Clearly this iterative model is evaluated for each free surface location, which itself is progressively iterated towards a steady state profile, emphasizing the need for an efficient technique.

The following indicates the iterative solution technique for the full film flow problem.

(i) Produce an initial guess for the film profile heights h of the free surface, and the domain velocity profile (usually use velocities from a Stokes flow analysis).

(ii) Use a Hermitian radial basis function (RBF) interpolation to generate values for the free surface curvature and outward unit normal.

  (a) Using the guessed velocity profile, implement a mass conservative RBF interpolation to obtain the inertia component.

  (b) Interpolate the inertia component using a RBF to find the corresponding coefficients.

  (c) Find the corresponding particular solutions to the disturbance flow regime.

  (d) Solve the BIEs (together) for the boundary traction on the wetted obstacle surface S_p, and homogeneous disturbance velocities on the free surface S_f.

  (e) Using the BIE, find the homogeneous component of the disturbance velocities within the domain.

  (f) Combine homogeneous and particular solutions of the disturbance regime and the asymptotic velocities to obtain the full velocity profile throughout the domain.

  (g) Repeat from (a) as required until convergence is reached.

(iii) Use the converged velocity profile to update the free surface profile.

(iv) If the movement of the free surface is sufficiently small, then a steady-state profile is found, alternative repeat from step (ii), using the new free surface location. In addition, the initial guess for the domain velocities is made by a mass conservative velocity interpolation, based on the converged velocities at the end of the previous free surface iteration.

A key difference to the Stokes flow analysis in earlier chapters, is that the BIEs are solved together during the PST iteration, where previously the two BIEs have been solved separately. This improves the convergence of the PST method.

The Boundary Element Method

The boundary element method (BEM) is applied similarly to the Stokes flow case to evaluate the boundary integrals in (7.3.46) and (7.3.50), using constant functional, flat triangular elements throughout. However, four extra integrals are present when compared to the Stokes case. These are,

(i) The double-layer potential over the wetted obstacle surface S_p.

(ii) The double-layer potential over the wall (external to the obstacle) S_w.

(iii) The single-layer potential over the edges of the domain S_e.

(iv) The double-layer potential over the edges of the domain S_e.

Point (i) above is simple to incorporate as the obstacle mesh is already discretized to evaluate the single-layer potential. However, point (ii) above requires a mesh for the wall, outside of the obstacle footprint, and points (iii) - (iv) need a mesh for the edges of the domain. The x_1x_2 distribution of elements for the wall discretization are identical

to the free surface analysis for flow around a cylinder, but with $x_3 = -1$. The far field element on both the free surface and wall meshes match, and are connected using a column of elements. These are generated similarly to the side elements of cylindrical obstacles, with first quadrilateral elements being formed, and then each of these being divided further into four triangular elements. Typical meshes for flow over a cylinder are shown in figure 7.7. Figure 7.7a indicates the meshes that were previously used for the Stokes analysis (S_f, S_p), and figure 7.7b shows the additional meshes required for the finite Reynolds number analysis (S_w, S_e).

Particular Solution

The particular solution is obtained using a particular solution technique (PST) as outlined in § 7.2. Both global and local mass conservative velocity interpolations are used to evaluate the convective term throughout the domain.

When interpolating the convective term to evaluate the particular solutions, it is noted that the flow field in the far field ($x_1, x_2 \to \infty$) should return to the asymptotic regime $p \to p^\infty$ and $u_i \to u_i^\infty$, satisfying $u_j \frac{\partial u_i}{\partial x_j} = 0$. The edges of the domain are a truncation of the full far field condition, and to help accuracy in implementing this condition, additional points are taken just outside of the discretized flow domain where the convective term is set to 0. The convective term is then interpolated over all domain and additional points.

It is also possible to decompose the convective term into its component disturbance and asymptotic parts,

$$B_i = u_j^\delta \frac{\partial u_i^\infty}{\partial x_j} + u_j^\infty \frac{\partial u_i^\delta}{\partial x_j} + u_j^\delta \frac{\partial u_i^\delta}{\partial x_j}, \qquad u_j^\infty \frac{\partial u_i^\infty}{\partial x_j} = 0. \tag{7.3.51}$$

Expressions for the asymptotic velocity field are known analytically, and a mass conservative interpolation of the disturbance velocities is required to find the derivative $\frac{\partial u_i^\delta}{\partial x_j}$. However, in practice it is found optimum to interpolate the full velocities and evaluate

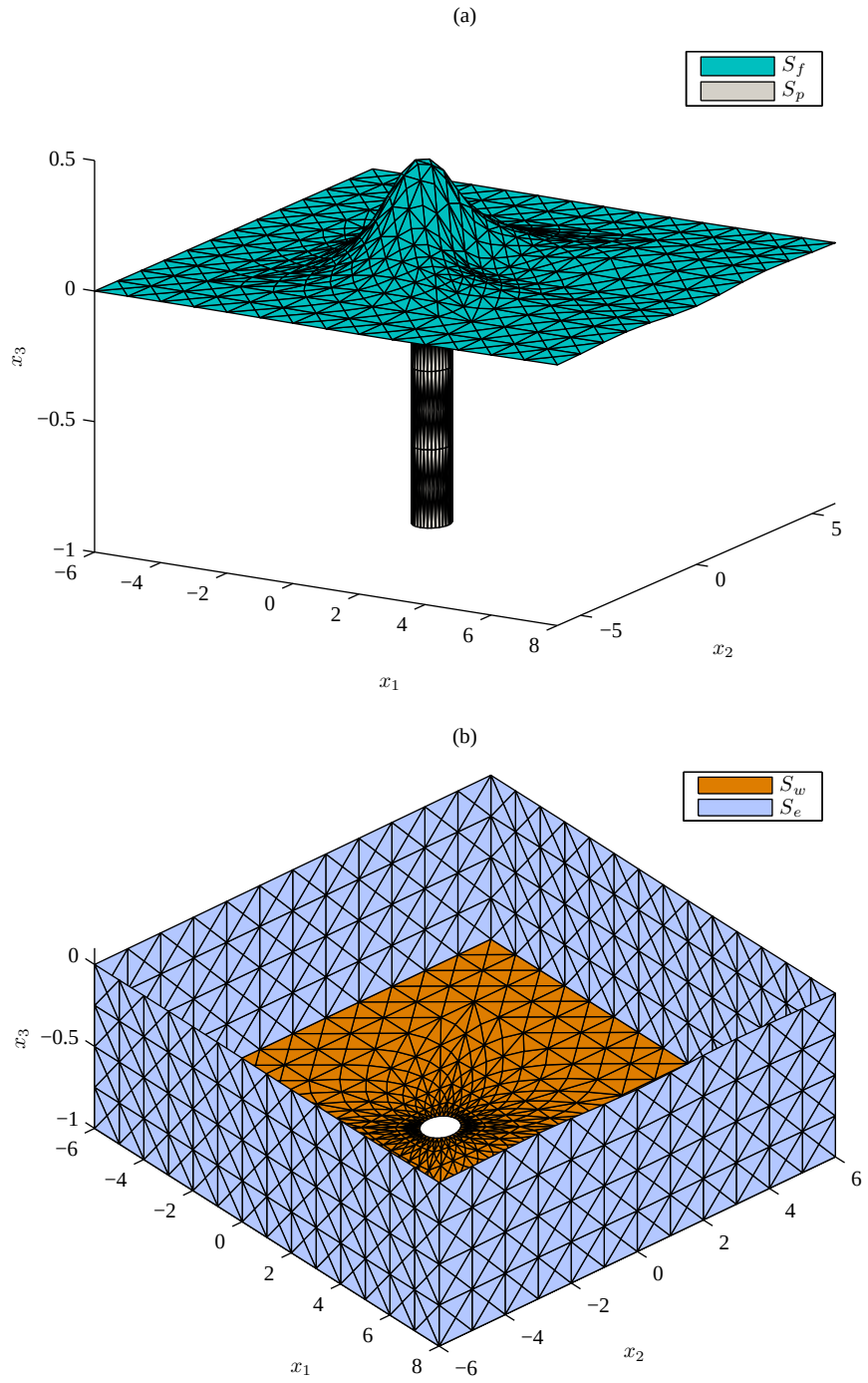

Figure 7.7: Typical meshes required for a finite Reynolds number model, where (a) indicates the meshes used previously for a Stokes flow analysis for film flow over a cylinder, and (b) the additional meshes required due to the more complex formulation for non-zero Re.

B_i directly.

Using the numerical schemes and formulation outlined, solution profiles for film flow over and around circular cylinders at finite Reynolds number are produced and shown in the following subsection.

7.3.3 Low Reynolds Film Profiles Obstructed By Obstacles

This subsection considers film flow down an inclined plane both over and around cylindrical obstacles. Examination of the full three-dimensional film profile for both flow over and around an obstacle, along with comparison with Stokes flow solutions is considered. Solutions are produced using the numerical techniques outlined earlier in this chapter, with results initially generated with a global mass conservative RBF interpolation of the velocities. This subsection of results concludes by considering a local velocity interpolation and comparing its accuracy with the global analysis.

Flow over a circular cylindrical obstacle is considered for an inverse Bond number of $B = 1$, and down an inclined plane at $\alpha = 45^o$. The cylinder has a radius of $a = 0.5$ with a flat top at $x_3 = -0.1$. Figure 7.8 indicates the full three-dimensional film profiles at a Reynolds number $Re = 3$. Results indicate a profile similar to that of Stokes flow over a cylinder, with a large upstream peak being formed above the obstacle, collapsing downstream into a shallow trough. The peak is seen to decay in a typical "horseshoe" fashion, illustrated further by the contours of the film profile as shown on the inclined wall. As expected, figure 7.8 also illustrates a symmetric solution in the plane $x_2 = 0$.

For flow over a cylinder, comparison is made for solutions at a range of Reynolds number. Figure 7.9 illustrates the centre line solutions ($x_2 = 0$) for film flow with identical parameters to those outlined for figure 7.8, namely $B = 1$, $\alpha = 45^o$, $a = 0.5$ with cylinder top located at $x_3 = -0.1$. Solutions are produced for Stokes flow ($Re = 0$), $Re = 1.5$ and $Re = 3$. All of the centre line profiles are similar, with an upstream peak and a

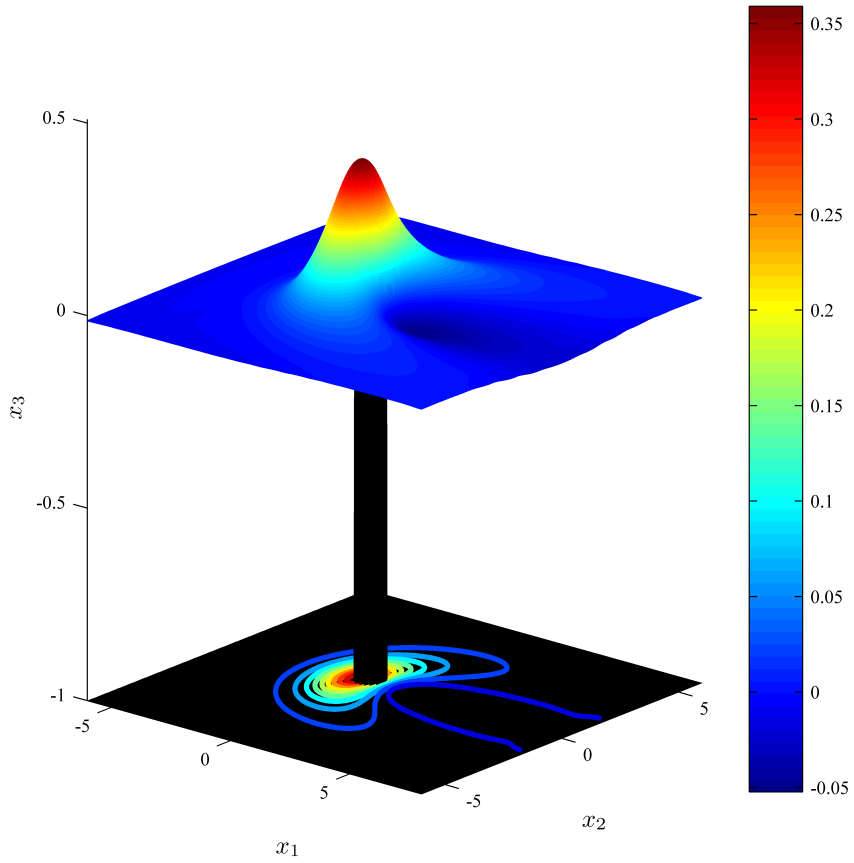

Figure 7.8: Three-dimensional profile for film flow down an inclined plane at $\alpha = 45^o$, and over a cylinder of radius $a = 0.5$ with flat top at $x_3 = -0.1$. The flow has non-dimensional parameters $B = 1$ and $Re = 3$.

shallow downstream trough. Clearly as the Reynolds number is increased, the height of the peak is increased, with the trough behind the obstacle becoming slightly deeper. For $Re > 3$, solutions become numerical unstable, with the PST method failing to converge, and thus it is not possible to find film profiles at greater Reynolds numbers.

Flow around a circular cylindrical obstacle is considered for an inverse Bond number of $B = 1$, and down an inclined plane at $\alpha = 45^o$. The cylinder has a radius of $a = 0.5$, with a contact angle of $\theta = 90^o$ applied along the contact line of the flow. Figure 7.10 shows the full three-dimensional film profile at a $Re = 3$ for the above set of parameters. As expected, the resulting film profile is symmetric. A large peak is formed at the

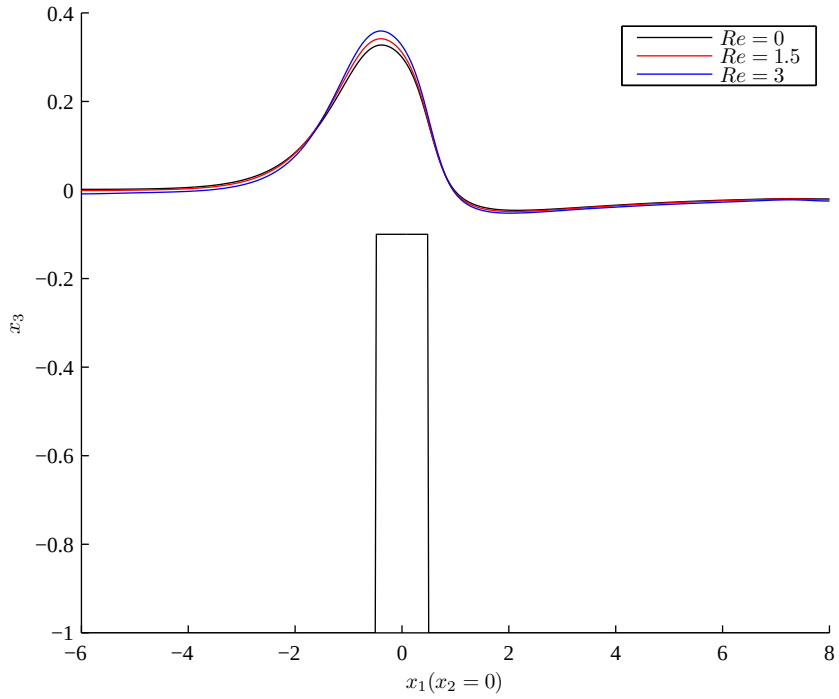

Figure 7.9: Centre line solutions comparing film flow down an inclined plane at $\alpha = 45^o$, and over a cylinder of radius $a = 0.5$ with flat top at $x_3 = -0.1$ for a range of Reynolds numbers. The flow has an inverse bond number of $B = 1$.

upstream edge of the cylinder, decaying around the obstacle and forming a trough on the downstream edge of the cylinder. Contours on the inclined wall illustrate the "horseshoe" shape of the decaying film profile.

A comparison of centre line solutions for film flow around a cylinder and at a range of Reynolds number is shown in figure 7.11. Flow parameters are identical to those used for figure 7.10, with $B = 1$, $\alpha = 45^o$, $a = 0.5$ and $\theta = 90^o$. Solutions are presented for three Reynolds number, $Re = 0$, $Re = 1.5$, and $Re = 3$. Results indicate an increase in the peak height and a deepening of the trough as the Reynolds number is increased. As for flow over a cylinder, for $Re > 3$, the PST method is unstable, and film profiles cannot be found at greater Reynolds numbers.

Results so far have been produced using a global mass conservative velocity interpolation.

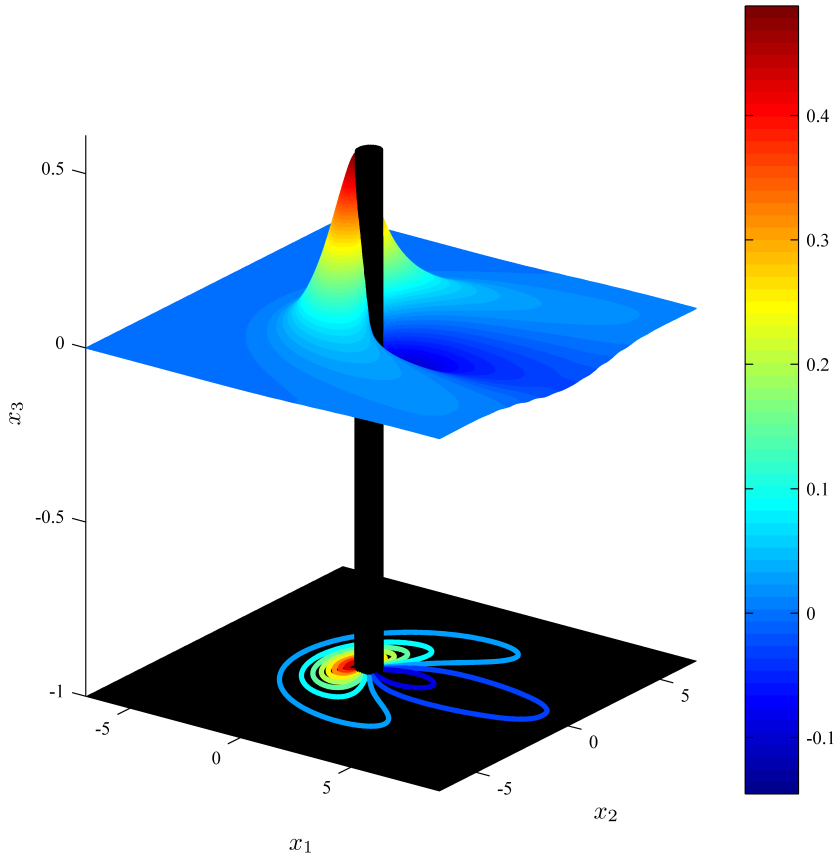

Figure 7.10: Three-dimensional profile for film flow down an inclined plane at $\alpha = 45^o$, and around a cylinder of radius $a = 0.5$ with contact angle $\theta = 90^o$. The flow has non-dimensional parameters $B = 1$ and $Re = 3$.

As for the case of a lid driven cavity in § 7.2, reductions in both the CPU time and RAM requirements necessary for the global analysis may be found by implementing a local interpolation with a suitable number of points. A comparison between the global and local schemes is considered for flow with an inverse Bond number $B = 1$, and down a plane inclined at $\alpha = 45^o$ with an attached circular cylinder of radius $a = 0.5$. For the flow over analysis, the cylinder is truncated at $x_3 = -0.1$, and for the flow around analysis a contact angle constraint of $\theta = 90^o$ implemented. All results are found at a Reynolds number of $Re = 3$.

When implementing a local interpolation, less computational resources are required when

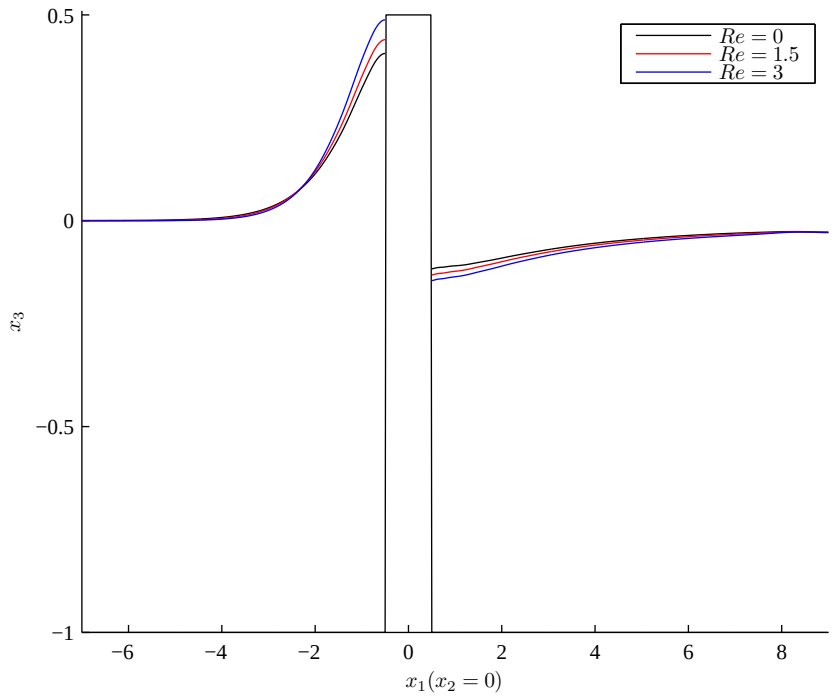

Figure 7.11: Centre line solutions comparing film flow down an inclined plane at $\alpha = 45^o$, around a cylinder of radius $a = 0.5$ with contact angle $\theta = 90^o$ for a range of Reynolds numbers. The flow has an inverse bond number of $B = 1$.

fewer local points are chosen. However, when insufficient points are used in the local interpolation, several problems may be experienced with the numerical schemes. If the number of local points is reduced too severely, then the rate of convergence of the free surface profile is found to reduce, resulting in significantly more iterations and the possibility of longer overall run-times. Alternatively, the PST method can fail completely, with no flow solution obtained. Therefore, care needs to be taken in choosing an optimum number of local interpolation points, and simulations using both 45 and 51 points have been considered throughout the following analysis.

Table 7.3 lists the computational performance of global and local schemes (using 45 and 51 points) for both flow over and flow around a circular cylinder. Solutions are iterated from an undisturbed free surface, with a Stokes flow velocity profile assumed.

Flow Over	Av. Film Iteration (s)	# Iterations	Peak Ram (Gb)
Global	31.9	789	3.7
Local (51 pts)	34.6	788	3.4
Local (45 pts)	30.4	821	3.1
Flow Around	Av. Film Iteration (s)	# Iterations	Peak Ram (Gb)
Global	40.0	1408	4.3
Local (51 pts)	41.9	1264	3.9
Local (45 pts)	Simulation Fails, PST Diverges		

Table 7.3: Average free surface iteration time and peak ram requirements for both a global and local velocity interpolation.

The domain interpolation use approximately 1200 points for the flow over analysis and 1300 points for the flow around analysis (with exact numbers depending on the film profile at any iteration). For this number of domain points, the use of 51 local points slightly increases the average run-time of a free surface iteration, and decreases the peak RAM requirements of the simulation when compared to a global scheme. In future, as computational resources are increased the number of domain points may also be increased, and the use of a local interpolation with 51 points should offer significant benefits. The models have also been evaluated using 45 local interpolation points. For flow over, the simulation converges but requires additional iterations to a global and 51 point local scheme. For flow around, no solution is found with the PST diverging during the analysis. Difference in the success of the two models at 45 local points is due to the differing representation of the domain points throughout the fluid.

Figure 7.12 indicates the centre line solutions for flow down an inclined plane both over and around a circular cylinder corresponding to the flow parameters used in table 7.3. Comparison is made between the global mass conservative velocity interpolation and a local interpolation using 51 points. Flow over solutions are illustrated in figure 7.12a with flow around solutions in figure 7.12b. In both cases, results show minimal difference between the global and local interpolation.

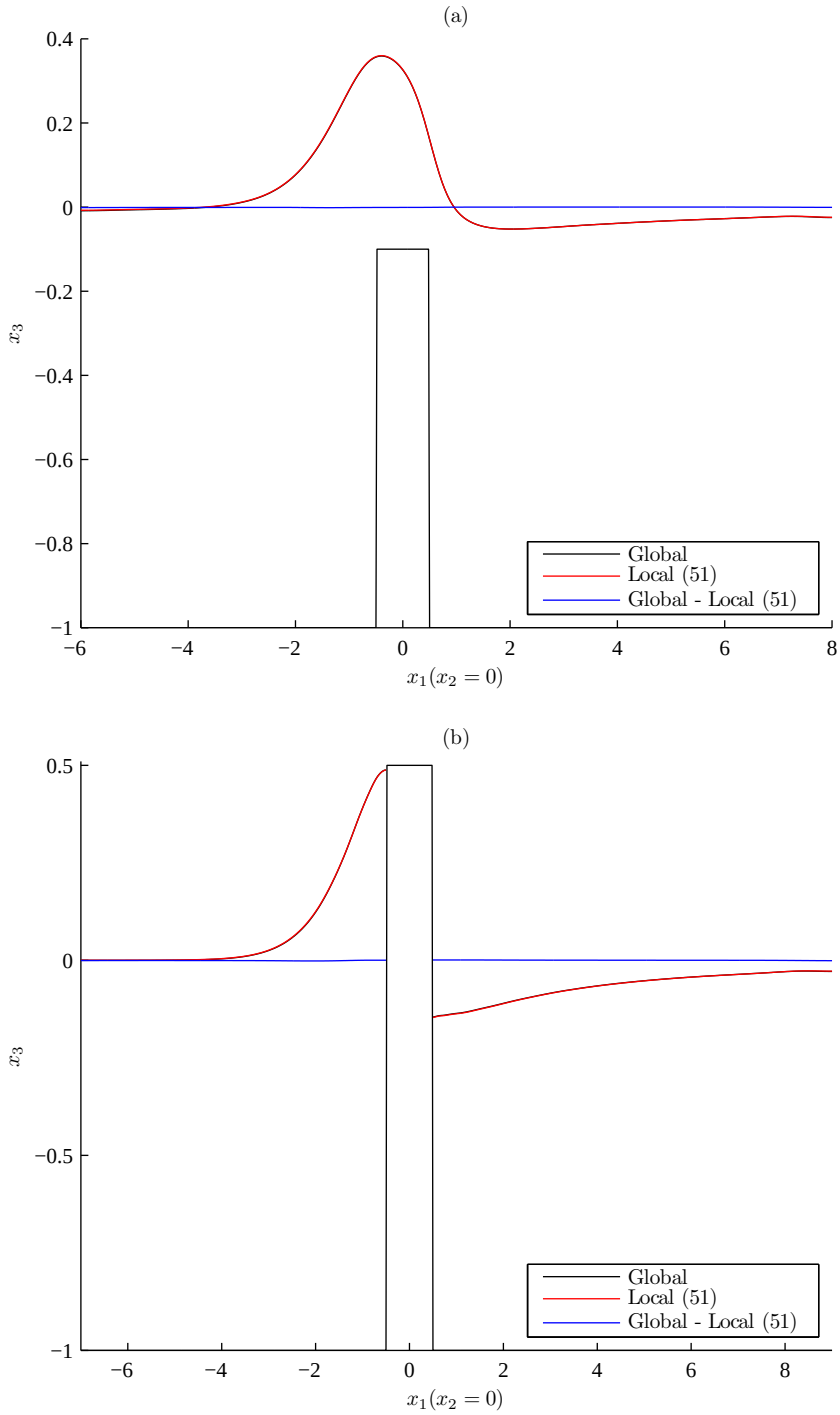

Figure 7.12: Comparison of a global and local (51 points) velocity interpolation for film flow obstructed by a cylinder of radius $a = 0.5$, with $B = 1$, $\alpha = 45^o$ and $Re = 3$. Part (a) indicates flow over the cylinder with top at $x_3 = -0.1$ and (b) flow around the cylinder with contact angle $\theta = 90^o$.

Chapter 8

Summary And Conclusions

Oil films are used in aero-engine bearing chambers to cool and transport heat away from bearings and walls within the oil system. If there is insufficient thickness of oil on the chamber wall, then oil degradation, coking and potentially oil fires can occur. Prediction of film behaviour is impaired as bearing chambers include complex geometries such as obstacles that can significantly affect the local behaviour of the oil film. The bearing chamber is a hostile environment for experimental analysis and measurement of the oil films interaction with obstructions is difficult. This thesis has considered the numerical modelling of the interaction of thin films with obstacles. Methods and results are provided for single or multiple obstacles which may or may not penetrate the free surface.

Numerical solutions for three-dimensional Stokes flow down an inclined plane over and around multiple obstacles have been developed and solutions found by the boundary element method (BEM). Initially chapter 4 considers flow profiles using the small free surface deflection by Blyth and Pozrikidis [31]. A global radial basis function (RBF) is used throughout to better evaluate the reduced form of the free surface curvature and outward unit normal. Comparisons are made to the finite difference approximations (FDA) used by [31], with results indicating a reduction in mesh dependency for the RBF approach. For flow over an obstacle, the film profile is governed by three parameters; inverse Bond number, plane inclination angle, and hemisphere radius. A parameter

analysis for each of these quantities is also produced using the small free surface deflection assumption. Flow profiles over asymptotically small obstacles, such as considered by Pozrikidis and Thoroddsen [29], have been reproduced and shown to give excellent agreement with simulations incorporating the full obstacle.

Chapter 4 also extends the small free surface deflection assumption by Blyth and Pozrikidis [31] by using a global RBF interpolation to accurately determine free surface quantities such as curvature and unit normal for larger surface deflections. Comparisons with the small free surface deflection assumption indicate consistency of results for small disturbances generated by small hemispheres ($a \sim 20\%$ of film height). For larger deformations generated by larger obstacles, solutions using the small deflection assumption become inconsistent with the full analysis. This illustrates the need for removing this restriction for more general, large obstructions. Streamlines and a parameter analysis for variations in inverse Bond number and plane inclination are also conducted using this full analysis. For large hemispheres fully contained within the fluid, it is found that the Stokes flow can support obstacles larger than the undisturbed free surface. The maximum size of hemisphere is strongly dependent on the inclination of the plane.

The single obstacle analysis is extended to a more general formulation for flow over arbitrary multiple obstacles in chapter 5. Flows over two, large hemispheres have been analyzed, with variations in the obstacle locations considered. The effects of separating the obstacles in-line with the flow has been illustrated, and flow profiles shown to return to those associated with a single obstacle in the case of large separations. In addition obstacles spaced perpendicular to the incoming flow have been modelled. In this case, when the obstacles are located close to one another, the flow reacts to the obstacle as if there is one large obstruction to the flow. A significantly larger peak is formed, spanning both obstacles when compared to the cases of moderate and large separations. Finally two hemispheres spaced diagonally to each other are considered, situating the downstream hemisphere in the decaying peak of the upstream obstacle, illustrating a non-symmetric solution. For obstacles aligned in the direction of the flow, a parameter

study was conducted to investigate the effects of varying the inverse Bond number, plane inclination angle and hemisphere radius. Flow over two hemispheres that approach the film surface have also been modelled, and the effects of placing the downstream obstacle in the wake of the upstream hemisphere considered. The wake from the upstream obstacle on both a shallow and a steep plane is shown to reduce the minimum gap between the free surface and obstacle when compared to a sole obstruction. Finally, flows over three hemispheres were modelled, with solutions obtained for two obstacle configurations based on a triangular array. Restrictions on obtaining flow over more obstacles is due to computational resources.

Chapter 6 extends the formulation further to consider flow around single and multiple circular cylinders. The incorporation of a contact angle condition within the RBF was required. For flow around a single cylinder streamline plots are produced along with a parameter study. For flow around obstacles, there are four governing parameters; inverse Bond number, plane inclination angle, cylinder radius and contact angle. A comparison of flow over and around a truncated cylinder indicates the possibility of dual solutions and indicates the steady state flow profile in this case is dependent on the initial conditions prescribed and not uniquely by the parameters of the flow field. Finally, the possibility of multiple solutions occurring for variations in the underlying flow parameters is confirmed, with results characterized by the maximum film height. It is shown that for a sufficiently large contact angle, results can be forced around a truncated cylinder for a chosen set of flow parameters, resulting in dual solutions.

Flows around multiple circular cylinders are also considered in chapter 6. Flow around two circular cylinders, with various obstacle locations were analyzed. As for flow over multiple hemispheres, the effects of separating the obstacles in line with the flow have been illustrated, and flow profiles shown to return to those associated with a single obstacle in the case of large separations. For obstacles spaced perpendicular to the incoming flow and in close proximity, the film profile between the cylinders becomes significantly raised when compared to cylinders at greater separation distances. Finally the non-

symmetric situation of two cylinders spaced diagonally to each other was modelled, with the downstream cylinder situated in the decaying peak of the upstream obstacle. When the cylinders were aligned in the direction of the flow, a parameter study was conducted to investigate the effects of varying the inverse Bond number, plane inclination angle, cylinder radius and contact angle. Flow solutions around three cylinders were also considered, with two obstacle configurations based on the triangular array with different symmetrical orientations to the flow direction. Finally, the versatility of the numerical approach is demonstrated with the analysis of flow over then around two identical cylinders spaced in the direction of the flow. The effect of the wake caused by the upstream cylinder was also considered, and shown to allow the contact angle at the downstream cylinder to be relaxed. As the obstacles are moved closer, the effects of the wake are strengthened and the contact angle condition can be lowered further.

The above formulations utilize a Stokes flow approximation for the analysis of free surface film flows over and around obstacles. The effects of inertia in these flow problems may be significant, particularly for dry-out, and the incorporation of the convective term of the Navier-Stokes equations was considered in chapter 7. However, the films flows have awkward geometries which require very efficient numerical algorithms to effectively include the convective term into the integral formulation used for the earlier analysis. Development of these efficient numerical algorithms was first conducted for the common test problem of flow in a three-dimensional lid driven cavity. This thesis evaluates a formulation for low Reynolds number flows using the BEM to solve the homogeneous solution, whilst formulating a particular solution using a RBF interpolation. Unlike conventional formulations such as the particular integral technique (PIT), which linearize the convective term and solves for domain velocities and unknown boundary tractions together, a method which solves the particular and homogeneous components separately, called the particular solution technique (PST) has been implemented. In addition, a local mass conservative interpolation for the velocity field has been introduced to further reduce the necessary computational resources. This local interpolation is an approximation to the

global analysis, with the accuracy of this method also considered. Solutions for $Re = 0$, $Re = 100$ and $Re = 200$ are produced by this PST approach using a fraction of the computational resources that would be required by the conventional PIT.

Chapter 7 uses the optimized numerical scheme developed for the lid-driven cavity test case and modest computational resources to evaluate low Reynolds number flows over and around cylindrical obstacles. Solutions are produced using both a global and local mass conservative interpolation for the velocity field. Results are obtained for Reynolds number up to $Re = 3$, beyond which difficulties with convergence of the numerical schemes was found. However, at $Re = 3$, changes in the film profile were observed, with the film peak increasing, just before the obstacle, and the trough decreasing behind the obstruction.

8.1 Future Work

The following possible areas of future work are of particular interest:

- The need remains for extended numerical analysis of flow over and around obstacles, and stems from oil film flows within bearing chambers, and the complex support structures which exist. Bearing chambers also include sump regions, and numerical analysis of flow over three-dimensional trenches and dips would be of interest.
- In a bearing chamber, the oil film is driven by surface shear forces as well as gravity. The effects of including surface shear from the air flow could be considered.
- The effects of perturbations to the free surface profile could be analyzed. This would be of particular relevance to the multiple solution analysis, determining which of the two possible solutions (over or around) is most prevalent when subjected to perturbations to the incoming flow.

- The oil film within the bearing chamber is used to cool the chamber wall. The effects of heat transfer from the wall to the thin oil film could also be considered.
- The analysis could be extended to consider the curvature of a realistic bearing chamber geometry, instead of a localized flow down an inclined plane.
- In chapter 7 the method outlined for incorporating the inertia effects is convergent for low Reynolds number. Further development and modification to the numerical schemes implemented, and increased computational resources may allow convergence for higher Reynolds number.

Appendix A

Lorentz-Blake Greens Functions

The Lorentz-Blake Greens functions for flow bounded by an infinite plane at $x_3 = w$ are reproduced for our co-ordinate system from Blyth and Pozrikidis [31] and shown below. The field point is given by $\mathbf{x} = (x_1, x_2, x_3)$ and the singularity point by $\mathbf{x}_0 = (x_{0_1}, x_{0_2}, x_{0_3})$.

A.1 Lorentz-Blake Velocity Greens Function

The Lorentz-Blake Velocity Greens function, $G^*_{ij}(\mathbf{x}, \mathbf{x}_0)$ is given by,

$$G^*_{ij}(\mathbf{x}, \mathbf{x}_0) = G^{ST}_{ij}(\hat{\mathbf{x}}) - G^{ST}_{ij}(\hat{\mathbf{X}}) + 2h_0^2 G^D_{ij}(\hat{\mathbf{X}}) - 2h_0 G^{SD}_{ij}(\hat{\mathbf{X}}), \tag{A.1.1}$$

where G^{ST}_{ij} is the free-space velocity Greens function or Stokeslet, and

$$G^{ST}_{ij}(\mathbf{x}) = \frac{\delta_{ij}}{|\mathbf{x}|} + \frac{x_i x_j}{|\mathbf{x}|^3}, \tag{A.1.2}$$

$$G^D_{ij}(\mathbf{x}) = \pm\left(\frac{\delta_{ij}}{|\mathbf{x}|^3} - 3\frac{x_i x_j}{|\mathbf{x}|^5}\right), \tag{A.1.3}$$

$$G^{SD}_{ij}(\mathbf{x}) = x_3 G^D_{ij}(\mathbf{x}) \pm \frac{\delta_{j3}x_i - \delta_{i3}x_j}{|\mathbf{x}|^3}, \tag{A.1.4}$$

where a minus corresponds to $j = 3$ and a plus for $j = 1, 2$. Also,

$$h_0 = x_{0_3} - w, \tag{A.1.5}$$

$$\hat{\mathbf{x}} = \mathbf{x} - \mathbf{x}_0, \tag{A.1.6}$$

$$\hat{\mathbf{X}} = \mathbf{x} - \mathbf{x}_0^{IM}, \tag{A.1.7}$$

$$\mathbf{x}_0^{IM} = (x_{0_1}, x_{0_2}, 2w - x_{0_3}). \tag{A.1.8}$$

A.2 Lorentz-Blake Pressure Greens Function

The Lorentz-Blake Pressure Greens function, $P_i^*(\mathbf{x}, \mathbf{x}_0)$ is given by,

$$P_i^*(\mathbf{x}, \mathbf{x}_0) = -2\left[\frac{X_i}{|\mathbf{X}|^3} + \frac{Y_i}{|\mathbf{Y}|^3} 2Y_i \left(-\frac{1}{|\mathbf{Y}|^3} + 3\frac{Y_3^2}{|\mathbf{Y}|^5}\right) 2h \left(-\frac{\delta_{i3}}{|\mathbf{Y}|^3} + 3\frac{Y_3 Y_i}{|\mathbf{Y}|^5}\right)\right], \tag{A.2.1}$$

where

$$h = x_3 - w, \tag{A.2.2}$$

$$\mathbf{X} = \mathbf{x}_0 - \mathbf{x}, \tag{A.2.3}$$

$$\mathbf{Y} = \mathbf{x}_0 - \mathbf{x}^{IM}, \tag{A.2.4}$$

$$\mathbf{x}^{IM} = (x_1, x_2, 2w - x_3). \tag{A.2.5}$$

A.3 Lorentz-Blake Stress Greens Function

The Lorentz-Blake Stress Greens function, $T_{ijk}^*(\mathbf{x}, \mathbf{x}_0)$ is given by,

$$T_{ijk}^*(\mathbf{x}, \mathbf{x}_0) = T_{ijk}^{ST}(\hat{\mathbf{x}}) - T_{ijk}^{ST}(\hat{\mathbf{X}}) + 2h_0^2 T_{ijk}^D(\hat{\mathbf{X}}) - 2h_0 T_{ijk}^{SD}(\hat{\mathbf{X}}), \tag{A.3.1}$$

where T_{ijk}^{ST} is the free-space stress Greens function, and

$$T_{ijk}^{ST}(\mathbf{x}) = 6\frac{x_i x_j x_k}{|\mathbf{x}|^5}, \tag{A.3.2}$$

$$T_{ijk}^{D}(\mathbf{x}) = \pm 6\left(-\frac{\delta_{ik}x_j + \delta_{ij}x_k + \delta_{kj}x_i}{|\mathbf{x}|^5} + 5\frac{x_i x_j x_k}{|\mathbf{x}|^7}\right), \tag{A.3.3}$$

$$T_{ijk}^{SD}(\mathbf{x}) = x_3 T_{ijk}^{D}(\mathbf{x}) \pm 6\left(\frac{\delta_{ik}x_j x_3 - \delta_{j3}x_i x_k}{|\mathbf{x}|^5}\right), \tag{A.3.4}$$

where a minus corresponds to $j = 3$ and a plus for $j = 1, 2$. Also h_0, $\hat{\mathbf{x}}$, $\hat{\mathbf{X}}$, $\mathbf{x}_0^{IM}$ are defined by (A.1.5) - (A.1.8) respectively.

Appendix B

Integrating Dirac's Delta Function

B.1 Integrating Over A Hemisphere

It is known from the standard properties of Dirac's delta function that its integral over a domain that contains the singularity (see Figure B.1) will result in 1, whilst its integral over a domain that omits the singularity will result in 0.

The scenario when the point $\mathbf{x}_0$ lies directly upon the bounding smooth surface D of the arbitrary control volume V_c is considered. First, however we note how the delta function has a radial argument and that its value is zero everywhere except at the singularity, where it is infinite. Consider two spheres, drawn with radius a and b respectively and

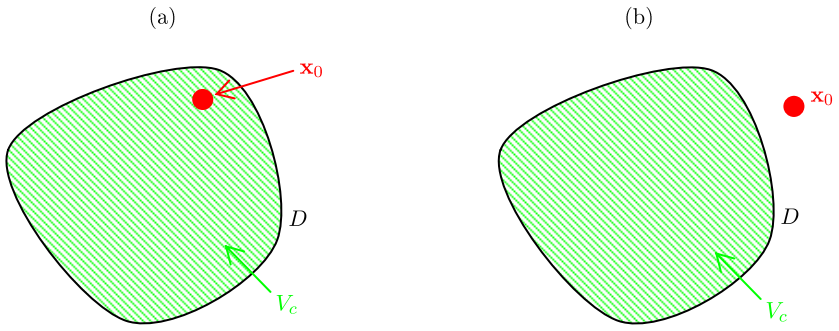

Figure B.1: Two illustrations indicating a control volume and singularity, (a) inside the control volume and (b) outside the control volume.

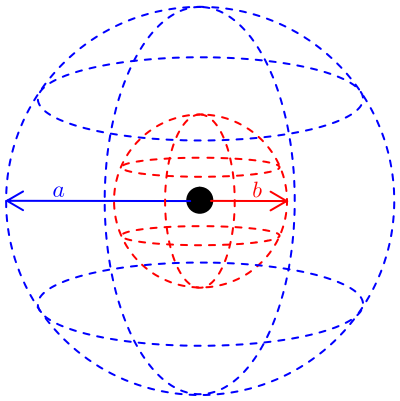

Figure B.2: Illustration indicating the effect of integrating the Dirac delta function centred on two spheres of different radii. The smaller sphere has radius b and the larger sphere radius a.

with $a > b > 0$, centred about the singularity point. It is clear that integrating the delta function over the larger sphere will have the same result as integrating over the smaller sphere, however small the radius b of this smaller sphere becomes - see Figure B.2.

If the singularity point is now considered to coincide with an arbitrarily shaped smooth boundary D that describes the control volume V_c, then by drawing a sphere of radius $\gamma \ll 1$ centred on the singularity it is intuitively obvious that the part of the boundary D within the sphere will tend to a flat plane in the limit of γ tending to zero.

Any flat plane that intersects a sphere, whilst passing through its centre, will split the sphere into two equal hemispheres. As contributions to the integral from Dirac's delta function are only dependent on radius then the orientation of the bisecting plane becomes insignificant and,

$$\begin{aligned} \int_{\text{SPHERE}} \delta(\mathbf{x}-\mathbf{x}_0)\mathrm{d}V(\mathbf{x}) &= 2 \int_{\text{HEMISPHERE}} \delta(\mathbf{x}-\mathbf{x}_0)\mathrm{d}V(\mathbf{x}) \\ &= 1. \end{aligned} \tag{B.1.1}$$

Giving the final result,

$$\begin{aligned}\int_{V_c} \delta(\mathbf{x}-\mathbf{x}_0)\mathrm{d}V(\mathbf{x}) &= \int_{\text{HEMISPHERE}} \delta(\mathbf{x}-\mathbf{x}_0)\mathrm{d}V(\mathbf{x}) \\ &= \frac{1}{2},\end{aligned} \tag{B.1.2}$$

as required.

B.2 Integrating Over A Boundary Corner

The case of a singularity placed at a corner of the boundary D is considered, with Dirac's delta function integrated over the control volume V_c contained by D. As shown in section B.1, the value of the integral is solely dependent on the shape of the boundary infinitely close to the singularity. Extending this local boundary shape into free-space allows the calculation of the *solid angle* of the boundary corner. Drawing a unit sphere around the singularity will result in an intersection of the extended local boundary shape and the sphere. This contour will map out a surface area on the sphere, Ω, known as the solid angle. The solid angle takes values between 0 and 4π, with a value of 2π representing the hemisphere in the above analysis and 4π representing the entire surface of the sphere. The units of solid angle is *steradians*.

From an extension of the previous argument, the integral over a proportion of a spheres surface (e.g. $\Omega/4\pi$) is equal to the same proportion multiplied by the integral over the whole sphere. Thus the integral over a control volume bounded by D , which has the singularity located at a boundary corner with solid angle Ω, has value

$$\begin{aligned}\int_{V_c} \delta(\mathbf{x}-\mathbf{x}_0)\mathrm{d}V(\mathbf{x}) &= \frac{\Omega}{4\pi}\int_{\text{SPHERE}} \delta(\mathbf{x}-\mathbf{x}_0)\mathrm{d}V(\mathbf{x}) \\ &= \frac{\Omega}{4\pi}.\end{aligned} \tag{B.2.1}$$

Appendix C

Auxiliary Solutions To A Thin Plate Spline Radial Basis Function

When using the dual reciprocity method (DRM) to solve flows at finite Reynolds number, the convective term may be incorporated into the analysis by use of a radial basis function (RBF) interpolation. For a given choice of RBF, auxiliary solutions for the velocity $\hat{u}_i^l$, pressure $\hat{p}^l$, and traction $\hat{f}_i^l$ are required and can be found analytically. The method for obtaining these solutions is outlined in Chapter 7, and results for the thin plate spline RBF $\psi(\mathbf{x}, \boldsymbol{\xi}) = r$ along with additional first order polynomial $P_1 = \beta_1 + \beta_2 x_1 + \beta_3 x_2 + \beta_4 x_3$ are shown below.

$$\psi = r, \qquad r = \| \mathbf{x} - \boldsymbol{\xi} \|, \tag{C.0.1}$$

$$\hat{u}_i^l = \frac{5}{72} r^3 \delta_{il} - \frac{1}{24} r (x_i - \xi_i)(x_l - \xi_l), \tag{C.0.2}$$

$$\hat{p}^l = -\frac{1}{4} r (x_l - \xi_l), \tag{C.0.3}$$

$$\begin{aligned} \hat{f}_i^l = \Bigg[& \frac{1}{6} r (x_j - \xi_j)\delta_{il} + \frac{1}{6} r (x_i - \xi_i)\delta_{jl} + \frac{1}{6} r (x_l - \xi_l)\delta_{ij} \\ & - \frac{1}{24 r} (x_i - \xi_i)(x_j - \xi_j)(x_l - \xi_l) \Bigg] n_j(\mathbf{x}). \end{aligned} \tag{C.0.4}$$

$$\psi = x_1, \tag{C.0.5}$$

$$\begin{aligned}
\hat{u}_i^l =& \frac{1}{10}\left(x_1^3 + x_2^2 x_1 + x_3^2 x_1\right)\delta_{il} \\
&- \frac{1}{280}\left(4x_1^3\left[5\delta_{1i}\delta_{1l} + \delta_{2i}\delta_{2l} + \delta_{3i}\delta_{3l}\right]\right. \\
&+ 4x_2^3\left[\delta_{1i}\delta_{2l} + \delta_{2i}\delta_{1l}\right] + 4x_3^2\left[\delta_{1i}\delta_{3l} + \delta_{3i}\delta_{1l}\right] \\
&+ 12x_1^2 x_2\left[\delta_{1i}\delta_{2l} + \delta_{2i}\delta_{1l}\right] + 12x_1^2 x_3\left[\delta_{1i}\delta_{3l} + \delta_{3i}\delta_{1l}\right] \\
&+ 4x_2^2 x_1\left[3\delta_{2i}\delta_{2l} + 3\delta_{1i}\delta_{1l} + \delta_{3i}\delta_{3l}\right] + 4x_3^2 x_1\left[3\delta_{3i}\delta_{3l} + 3\delta_{1i}\delta_{1l} + \delta_{2i}\delta_{2l}\right] \\
&+ 4x_2^2 x_3\left[\delta_{1i}\delta_{3l} + \delta_{3i}\delta_{1l}\right] + 4x_3^2 x_2\left[\delta_{1i}\delta_{2l} + \delta_{2i}\delta_{1l}\right] \\
&\left.+ 8x_1 x_2 x_3\left[\delta_{3i}\delta_{2l} + \delta_{2i}\delta_{3l}\right]\right),
\end{aligned} \tag{C.0.6}$$

$$\hat{p}^l = -\frac{1}{10}\left[3x_1^2\delta_{1l} + x_2^2\delta_{1l} + x_3^2\delta_{1l} + 2x_2x_1\delta_{2l} + 2x_3x_1\delta_{3l}\right], \tag{C.0.7}$$

$$\begin{aligned}
\hat{f}_i^l = \Bigg[& \frac{1}{10}\left(3x_1^2\delta_{1l} + x_2^2\delta_{1l} + x_3^2\delta_{1l} + 2x_2x_1\delta_{2l} + 2x_3x_1\delta_{3l}\right)\delta_{ij} \\
&+ \frac{1}{10}\left(3x_1^2\delta_{1j} + x_2^2\delta_{1j} + x_3^2\delta_{1j} + 2x_2x_1\delta_{2j} + 2x_3x_1\delta_{3j}\right)\delta_{il} \\
&+ \frac{1}{10}\left(3x_1^2\delta_{1i} + x_2^2\delta_{1i} + x_3^2\delta_{1i} + 2x_2x_1\delta_{2i} + 2x_3x_1\delta_{3i}\right)\delta_{jl} \\
&- \frac{12}{140}x_1^2\left[5\delta_{1i}\delta_{1j}\delta_{1l} + \delta_{2i}\delta_{1j}\delta_{2l} + \delta_{3i}\delta_{1j}\delta_{3l}\right. \\
&\qquad \left.+\delta_{1i}\delta_{2j}\delta_{2l} + \delta_{2i}\delta_{2j}\delta_{1l} + \delta_{3i}\delta_{3j}\delta_{1l} + \delta_{1i}\delta_{3j}\delta_{3l}\right] \\
&- \frac{4}{140}x_2^2\left[3\delta_{1i}\delta_{2j}\delta_{2l} + 3\delta_{2i}\delta_{2j}\delta_{1l} + 3\delta_{2i}\delta_{1j}\delta_{2l}\right. \\
&\qquad \left.+3\delta_{1i}\delta_{1j}\delta_{1l} + \delta_{1i}\delta_{3j}\delta_{3l} + \delta_{3i}\delta_{3j}\delta_{1l} + \delta_{3i}\delta_{1j}\delta_{3l}\right] \\
&- \frac{4}{140}x_3^2\left[3\delta_{3i}\delta_{1j}\delta_{3l} + 3\delta_{3i}\delta_{3j}\delta_{1l} + 3\delta_{1i}\delta_{3j}\delta_{3l}\right. \\
&\qquad \left.+3\delta_{1i}\delta_{1j}\delta_{1l} + \delta_{2i}\delta_{1j}\delta_{2l} + \delta_{2i}\delta_{2j}\delta_{1l} + \delta_{1i}\delta_{2j}\delta_{2l}\right] \\
&- \frac{8}{140}x_1x_2\left[3\delta_{1i}\delta_{1j}\delta_{2l} + 3\delta_{1i}\delta_{2j}\delta_{1l} + 3\delta_{2i}\delta_{2j}\delta_{2l}\right. \\
&\qquad \left.+3\delta_{2i}\delta_{1j}\delta_{1l} + \delta_{2i}\delta_{3j}\delta_{3l} + \delta_{3i}\delta_{3j}\delta_{2l} + \delta_{3i}\delta_{2j}\delta_{3l}\right] \\
&- \frac{8}{140}x_1x_3\left[3\delta_{1i}\delta_{3j}\delta_{1l} + 3\delta_{1i}\delta_{1j}\delta_{3l} + 3\delta_{3i}\delta_{3j}\delta_{3l}\right. \\
&\qquad \left.+3\delta_{3i}\delta_{1j}\delta_{1l} + \delta_{3i}\delta_{2j}\delta_{2l} + \delta_{2i}\delta_{3j}\delta_{2l} + \delta_{2i}\delta_{2j}\delta_{3l}\right] \\
&- \frac{8}{140}x_2x_3\left[\delta_{2i}\delta_{3j}\delta_{1l} + \delta_{2i}\delta_{1j}\delta_{3l} + \delta_{3i}\delta_{2j}\delta_{1l}\right. \\
&\qquad \left.\left.+\delta_{3i}\delta_{1j}\delta_{2l} + \delta_{1i}\delta_{3j}\delta_{2l} + \delta_{1i}\delta_{2j}\delta_{3l}\right]\right] n_j(\mathbf{x}).
\end{aligned} \tag{C.0.8}$$

$$\psi = x_2, \tag{C.0.9}$$

$$\begin{aligned}
\hat{u}_i^l =& \frac{1}{10}\left(x_2^3 + x_1^2 x_2 + x_3^2 x_2\right)\delta_{il} \\
&- \frac{1}{280}\left(4x_2^3\left[5\delta_{2i}\delta_{2l} + \delta_{1i}\delta_{1l} + \delta_{3i}\delta_{3l}\right]\right. \\
&+ 4x_1^3\left[\delta_{2i}\delta_{1l} + \delta_{1i}\delta_{2l}\right] + 4x_3^2\left[\delta_{2i}\delta_{3l} + \delta_{3i}\delta_{2l}\right] \\
&+ 12x_2^2 x_1\left[\delta_{2i}\delta_{1l} + \delta_{1i}\delta_{2l}\right] + 12x_2^2 x_3\left[\delta_{2i}\delta_{3l} + \delta_{3i}\delta_{2l}\right] \\
&+ 4x_1^2 x_2\left[3\delta_{1i}\delta_{1l} + 3\delta_{2i}\delta_{2l} + \delta_{3i}\delta_{3l}\right] + 4x_3^2 x_2\left[3\delta_{3i}\delta_{3l} + 3\delta_{2i}\delta_{2l} + \delta_{1i}\delta_{1l}\right] \\
&+ 4x_1^2 x_3\left[\delta_{2i}\delta_{3l} + \delta_{3i}\delta_{2l}\right] + 4x_3^2 x_1\left[\delta_{2i}\delta_{1l} + \delta_{1i}\delta_{2l}\right] \\
&\left.+8x_2 x_1 x_3\left[\delta_{3i}\delta_{1l} + \delta_{1i}\delta_{3l}\right]\right),
\end{aligned} \tag{C.0.10}$$

$$\hat{p}^l = -\frac{1}{10}\left[3x_2^2\delta_{2l} + x_1^2\delta_{2l} + x_3^2\delta_{2l} + 2x_1x_2\delta_{1l} + 2x_3x_2\delta_{3l}\right], \tag{C.0.11}$$

$$\begin{aligned}
\hat{f}_i^l = &\left[\frac{1}{10}\left(3x_2^2\delta_{2l} + x_1^2\delta_{2l} + x_3^2\delta_{2l} + 2x_1x_2\delta_{1l} + 2x_3x_2\delta_{3l}\right)\delta_{ij}\right. \\
&+ \frac{1}{10}\left(3x_2^2\delta_{2j} + x_1^2\delta_{2j} + x_3^2\delta_{2j} + 2x_1x_2\delta_{1j} + 2x_3x_2\delta_{3j}\right)\delta_{il} \\
&+ \frac{1}{10}\left(3x_2^2\delta_{2i} + x_1^2\delta_{2i} + x_3^2\delta_{2i} + 2x_1x_2\delta_{1i} + 2x_3x_2\delta_{3i}\right)\delta_{jl} \\
&- \frac{12}{140}x_2^2\left[5\delta_{2i}\delta_{2j}\delta_{2l} + \delta_{1i}\delta_{2j}\delta_{1l} + \delta_{3i}\delta_{2j}\delta_{3l}\right. \\
&\qquad\left.+\delta_{2i}\delta_{1j}\delta_{1l} + \delta_{1i}\delta_{1j}\delta_{2l} + \delta_{3i}\delta_{3j}\delta_{2l} + \delta_{2i}\delta_{3j}\delta_{3l}\right] \\
&- \frac{4}{140}x_1^2\left[3\delta_{2i}\delta_{1j}\delta_{1l} + 3\delta_{1i}\delta_{1j}\delta_{2l} + 3\delta_{1i}\delta_{2j}\delta_{1l}\right. \\
&\qquad\left.+3\delta_{2i}\delta_{2j}\delta_{2l} + \delta_{2i}\delta_{3j}\delta_{3l} + \delta_{3i}\delta_{3j}\delta_{2l} + \delta_{3i}\delta_{2j}\delta_{3l}\right] \\
&- \frac{4}{140}x_3^2\left[3\delta_{3i}\delta_{2j}\delta_{3l} + 3\delta_{3i}\delta_{3j}\delta_{2l} + 3\delta_{2i}\delta_{3j}\delta_{3l}\right. \\
&\qquad\left.+3\delta_{2i}\delta_{2j}\delta_{2l} + \delta_{1i}\delta_{2j}\delta_{1l} + \delta_{1i}\delta_{1j}\delta_{2l} + \delta_{2i}\delta_{1j}\delta_{1l}\right] \\
&- \frac{8}{140}x_2x_1\left[3\delta_{2i}\delta_{2j}\delta_{1l} + 3\delta_{2i}\delta_{1j}\delta_{2l} + 3\delta_{1i}\delta_{1j}\delta_{1l}\right. \\
&\qquad\left.+3\delta_{1i}\delta_{2j}\delta_{2l} + \delta_{1i}\delta_{3j}\delta_{3l} + \delta_{3i}\delta_{3j}\delta_{1l} + \delta_{3i}\delta_{1j}\delta_{3l}\right] \\
&- \frac{8}{140}x_2x_3\left[3\delta_{2i}\delta_{3j}\delta_{2l} + 3\delta_{2i}\delta_{2j}\delta_{3l} + 3\delta_{3i}\delta_{3j}\delta_{3l}\right. \\
&\qquad\left.+3\delta_{3i}\delta_{2j}\delta_{2l} + \delta_{3i}\delta_{1j}\delta_{1l} + \delta_{1i}\delta_{3j}\delta_{1l} + \delta_{1i}\delta_{1j}\delta_{3l}\right] \\
&- \frac{8}{140}x_1x_3\left[\delta_{1i}\delta_{3j}\delta_{2l} + \delta_{1i}\delta_{2j}\delta_{3l} + \delta_{3i}\delta_{1j}\delta_{2l}\right. \\
&\qquad\left.\left.+\delta_{3i}\delta_{2j}\delta_{1l} + \delta_{2i}\delta_{3j}\delta_{1l} + \delta_{2i}\delta_{1j}\delta_{3l}\right]\right] n_j(\mathbf{x}).
\end{aligned} \tag{C.0.12}$$

$$\psi = x_3, \tag{C.0.13}$$

$$\begin{aligned}
\hat{u}_i^l =& \frac{1}{10}\left(x_3^3 + x_2^2 x_3 + x_1^2 x_3\right)\delta_{il} \\
&- \frac{1}{280}\left(4x_3^3\left[5\delta_{3i}\delta_{3l} + \delta_{2i}\delta_{2l} + \delta_{1i}\delta_{1l}\right]\right. \\
&+ 4x_2^3\left[\delta_{3i}\delta_{2l} + \delta_{2i}\delta_{3l}\right] + 4x_1^2\left[\delta_{3i}\delta_{1l} + \delta_{1i}\delta_{3l}\right] \\
&+ 12x_3^2 x_2\left[\delta_{3i}\delta_{2l} + \delta_{2i}\delta_{3l}\right] + 12x_3^2 x_1\left[\delta_{3i}\delta_{1l} + \delta_{1i}\delta_{3l}\right] \\
&+ 4x_2^2 x_3\left[3\delta_{2i}\delta_{2l} + 3\delta_{3i}\delta_{3l} + \delta_{1i}\delta_{1l}\right] + 4x_1^2 x_3\left[3\delta_{1i}\delta_{1l} + 3\delta_{3i}\delta_{3l} + \delta_{2i}\delta_{2l}\right] \\
&+ 4x_2^2 x_1\left[\delta_{3i}\delta_{1l} + \delta_{1i}\delta_{3l}\right] + 4x_1^2 x_2\left[\delta_{3i}\delta_{2l} + \delta_{2i}\delta_{3l}\right] \\
&\left.+ 8x_3 x_2 x_1\left[\delta_{1i}\delta_{2l} + \delta_{2i}\delta_{1l}\right]\right),
\end{aligned} \tag{C.0.14}$$

$$\hat{p}^l = -\frac{1}{10}\left[3x_3^2\delta_{3l} + x_2^2\delta_{3l} + x_1^2\delta_{3l} + 2x_2x_3\delta_{2l} + 2x_1x_3\delta_{1l}\right], \tag{C.0.15}$$

$$\begin{aligned}
\hat{f}_i^l = \Bigg[& \frac{1}{10}\left(3x_3^2\delta_{3l} + x_2^2\delta_{3l} + x_1^2\delta_{3l} + 2x_2x_3\delta_{2l} + 2x_1x_3\delta_{1l}\right)\delta_{ij} \\
&+ \frac{1}{10}\left(3x_3^2\delta_{3j} + x_2^2\delta_{3j} + x_1^2\delta_{3j} + 2x_2x_3\delta_{2j} + 2x_1x_3\delta_{1j}\right)\delta_{il} \\
&+ \frac{1}{10}\left(3x_3^2\delta_{3i} + x_2^2\delta_{3i} + x_1^2\delta_{3i} + 2x_2x_3\delta_{2i} + 2x_1x_3\delta_{1i}\right)\delta_{jl} \\
&- \frac{12}{140}x_3^2\left[5\delta_{3i}\delta_{3j}\delta_{3l} + \delta_{2i}\delta_{3j}\delta_{2l} + \delta_{1i}\delta_{3j}\delta_{1l}\right. \\
&\qquad \left.+\delta_{3i}\delta_{2j}\delta_{2l} + \delta_{2i}\delta_{2j}\delta_{3l} + \delta_{1i}\delta_{1j}\delta_{3l} + \delta_{3i}\delta_{1j}\delta_{1l}\right] \\
&- \frac{4}{140}x_2^2\left[3\delta_{3i}\delta_{2j}\delta_{2l} + 3\delta_{2i}\delta_{2j}\delta_{3l} + 3\delta_{2i}\delta_{3j}\delta_{2l}\right. \\
&\qquad \left.+3\delta_{3i}\delta_{3j}\delta_{3l} + \delta_{3i}\delta_{1j}\delta_{1l} + \delta_{1i}\delta_{1j}\delta_{3l} + \delta_{1i}\delta_{3j}\delta_{1l}\right] \\
&- \frac{4}{140}x_1^2\left[3\delta_{1i}\delta_{3j}\delta_{1l} + 3\delta_{1i}\delta_{1j}\delta_{3l} + 3\delta_{3i}\delta_{1j}\delta_{1l}\right. \\
&\qquad \left.+3\delta_{3i}\delta_{3j}\delta_{3l} + \delta_{2i}\delta_{3j}\delta_{2l} + \delta_{2i}\delta_{2j}\delta_{3l} + \delta_{3i}\delta_{2j}\delta_{2l}\right] \\
&- \frac{8}{140}x_3x_2\left[3\delta_{3i}\delta_{3j}\delta_{2l} + 3\delta_{3i}\delta_{2j}\delta_{3l} + 3\delta_{2i}\delta_{2j}\delta_{2l}\right. \\
&\qquad \left.+3\delta_{2i}\delta_{3j}\delta_{3l} + \delta_{2i}\delta_{1j}\delta_{1l} + \delta_{1i}\delta_{1j}\delta_{2l} + \delta_{1i}\delta_{2j}\delta_{1l}\right] \\
&- \frac{8}{140}x_3x_1\left[3\delta_{3i}\delta_{1j}\delta_{3l} + 3\delta_{3i}\delta_{3j}\delta_{1l} + 3\delta_{1i}\delta_{1j}\delta_{1l}\right. \\
&\qquad \left.+3\delta_{1i}\delta_{3j}\delta_{3l} + \delta_{1i}\delta_{2j}\delta_{2l} + \delta_{2i}\delta_{1j}\delta_{2l} + \delta_{2i}\delta_{2j}\delta_{1l}\right] \\
&- \frac{8}{140}x_2x_1\left[\delta_{2i}\delta_{1j}\delta_{3l} + \delta_{2i}\delta_{3j}\delta_{1l} + \delta_{1i}\delta_{2j}\delta_{3l}\right. \\
&\qquad \left.+\delta_{1i}\delta_{3j}\delta_{2l} + \delta_{3i}\delta_{1j}\delta_{2l} + \delta_{3i}\delta_{2j}\delta_{1l}\right]\Bigg] n_j(\mathbf{x}).
\end{aligned} \tag{C.0.16}$$

$$\psi = 1, \qquad r = \| \mathbf{x} \|, \tag{C.0.17}$$

$$\hat{u}_i^l = \frac{2}{15} r^2 \delta_{il} - \frac{1}{15} x_i x_l, \tag{C.0.18}$$

$$\hat{p}^l = -\frac{1}{3} x_l, \tag{C.0.19}$$

$$\hat{f}_i^l = \left[\frac{1}{5} x_i \delta_{jl} + \frac{1}{5} x_j \delta_{il} + \frac{1}{5} x_l \delta_{ij} \right] n_j(\mathbf{x}). \tag{C.0.20}$$

References

[1] C. Eastwick, K. Simmons, K. Huebner, C. Young, B. Azzopardi, and R. Morrison. Film flow around bearing chamber support structures. *Proceedings of ASME Turbo Exp 2005: Power for Land, Sea and Air*, Nevada, June 6-9, 2005.

[2] S. Wittig, A. Glahn, and J. Himmelsbach. Influence of high rotational speeds on heat transfer and oil film thickness in aero-engine bearing chambers. *Journal of Engineering for Gas Turbines and Power*, 116(2):395–401, 1994.

[3] A. Glahn and S. Wittig. Two-phase air/oil flow in aero engine bearing chambers: Characterization of oil film flows. *Journal of Engineering for Gas Turbines and Power*, 118(3):578–583, 1996.

[4] M. Farrall, S. Hibberd, K. Simmons, and D. Giddings. Prediction of air/oil exit flows in a commercial aero-engine bearing chamber. *Proceedings of the Institution of Mechanical Engineers, Part G: Journal of Aerospace Engineering*, 220(3):197–202, 2006.

[5] M. Farrall, K. Simmons, S. Hibberd, and P. Gorse. A numerical model for oil film flow in an aeroengine bearing chamber and comparison to experimental data. *Journal of Engineering for Gas Turbines and Power*, 128(1):111–117, 2006.

[6] M. Farrall, S. Hibberd, and K. Simmons. The effect of initial injection conditions on the oil droplet motion in a simplified bearing chamber. *Journal of Engineering for Gas Turbines and Power*, 130(1):012501–7, 2008.

[7] O.A. Kabov. Heat transfer from a small heater to a falling liquid film. *Heat Transfer Research*, 27(1):221–226, 1996.

[8] O.A. Kabov and I.V. Marchuk. Infrared study of the liquid film flowing on surface with nonuniform heat flux distribution. *Heat Transfer Research*, 29(6):544–562, 1998.

[9] O.A. Kabov, B. Scheid, I.A. Sharina, and J.C. Legros. Heat transfer and rivulet structures formation in a falling thin liquid film locally heated. *International Journal of Thermal Sciences*, 41(7):664–672, 2002.

[10] S. Shetty and R.L. Cerro. Spreading of a liquid point source over a complex surface. *Industrial & Engineering Chemistry Research*, 37(2):626–635, 1998.

[11] K. Argyriadi, M. Vlachogiannis, and V. Bontozoglou. Experimental study of inclined film flow along periodic corrugations: The effect of wall steepness. *Physics of Fluids*, 18(1):012102, 2006.

[12] L.E. Stillwagon and R.G. Larson. Leveling of thin films over uneven substrates during spin coating. *Physics of Fluids A*, 2(11), 1990.

[13] L.M. Peurrung and D.B. Graves. Film thickness profiles over topography in spin coating. *Journal of The Electrochemical Society*, 138(7):2115–2124, 1991.

[14] M.M.J. Decré and J.-C. Baret. Gravity-driven flows of viscous liquids over two-dimensional topographies. *Journal of Fluid Mechanics*, 487:147–166, 2003.

[15] B.S. Shiralkar and R.T. Lahey. The effect of obstacles on a liquid film. *Journal of Heat Transfer*, pages 528–533, 1973.

[16] J.M. Skotheim, U.W.E. Thiele, and B. Scheid. On the instability of a falling film due to localized heating. *Journal of Fluid Mechanics*, 475:1–19, 2003.

[17] B. Scheid, A. Oron, P. Colinet, U. Thiele, and J.C. Legros. Nonlinear evolution of nonuniformly heated falling liquid films. *Physics of Fluids*, 14(12):4130–4151, 2002.

[18] C.Y. Wang. Liquid film flowing slowly down a wavy incline. *AIChE Journal*, 27(2): 207–212, 1981.

[19] C. Pozrikidis. The flow of a liquid film along a periodic wall. *Journal of Fluid Mechanics*, 188:275–300, 1988.

[20] C. Pozrikidis. Effect of surfactants on film flow down a periodic wall. *Journal of Fluid Mechanics*, 496:105–127, 2003.

[21] N.A. Malamataris and V. Bontozoglou. Computer aided analysis of viscous film flow along an inclined wavy wall. *Journal of Computational Physics*, 154(2):372–392, 1999.

[22] S. Kalliadasis, C. Bielarz, and G.M. Homsy. Steady free-surface thin film flows over topography. *Physics of Fluids*, 12(8):1889–1898, 2000.

[23] A. Mazouchi and G.M. Homsy. Free surface stokes flow over topography. *Physics of Fluids*, 13(10):2751–2761, 2001.

[24] E.B. Hansen. Free surface stokes flow over an obstacle. In *Boundary Elements VIII*, Tokyo, Japan, 1986.

[25] E.B. Hansen. Stokes flow of a fluid layer over an obstacle on a tilted plane. *Mathematical and Computer Modelling*, 15:195–193, 1991.

[26] N.H. Shuaib. *Numerical simulation of thin film flow including surface shear and gravitational effects*. PhD thesis, University of Nottingham, 2004.

[27] M. Hayes, G. O'Brien, and J.H. Lammers. Green's function for steady flow over a small two-dimensional topography. *Physics of Fluids*, 12(11):2845–2858, 2000.

[28] P.H. Gaskell, P.K. Jimack, M. Sellier, H.M. Thompson, and M.C.T. Wilson. Gravity-driven flow of continuous thin liquid films on non-porous substrates with topography. *Journal of Fluid Mechanics*, 509(1):253–280, 2004.

[29] C. Pozrikidis and S.T. Thoroddsen. The deformation of a liquid film flowing down an inclined plane wall over a small particle arrested on the wall. *Physics of Fluids A*, 3(11):2546–2558, 1991.

[30] Y.C. Lee, H.M. Thompson, and P.H. Gaskell. An efficient adaptive multigrid algorithm for predicting thin film flow on surfaces containing localised topographic features. *Computers & Fluids*, 36:838–855, 2007.

[31] M.G. Blyth and C. Pozrikidis. Film flow down an inclined plane over a three-dimensional obstacle. *Physics of Fluids*, 18(5):052104–14, 2006.

[32] M. Sellier. The flow of a thin liquid film past a cylinder. In *COMSOL Users Conference 2006*, pages 151–154, Frankfurt, 2006.

[33] M. Sellier, Y.C. Lee, H.M. Thompson, and P.H. Gaskell. Thin film flow on surfaces containing arbitrary occlusions. *Computers & Fluids*, 38(1):171–182, 2009.

[34] C. Pozrikidis. *A Practical Guide to Boundary Element Methods with the Software Library BEMLIB*. Chapman & Hall/CRC, Florida, 2002.

[35] H. Power and L.C. Wrobel. *Boundary Integral Methods in Fluid Mechanics*. Computational Mechanics Publications, Southampton, 1995.

[36] C. Pozrikidis. *Introduction to Theoretical and Computational Fluid Dynamics*. Oxford University Press, New York, 1997.

[37] C. Pozrikidis. *Boundary integral and singularity methods for linearized viscous flow*. Cambridge University Press, Cambridge, 1992.

[38] D.J. Acheson. *Elementary Fluid Mechanics*. Oxford University Press, New York, 2003.

[39] H. Ockendon and J.R. Ockendon. *Viscous Flow*. Cambridge Texts in Applied Mathematics. Cambridge University Press, New York, 1995.

[40] R. Franke. Scattered data interpolation: Tests of some method. *Mathematics of Computation*, 38(157):181–200, 1982.

[41] A. La Rocca, A. Hernandez Rosales, and H. Power. Radial basis function hermite collocation approach for the solution of time dependent convection-diffusion problems. *Engineering Analysis with Boundary Elements*, 29(4):359–370, 2005.

[42] A. La Rocca and H. Power. A double boundary collocation hermitian approach for the solution of steady state convection-diffusion problems. *Computers & Mathematics with Applications*, 55(9):1950–1960, 2008.

[43] D. Nardini and C.A. Brebbia. A new approach to free vibration analysis using boundary elements. *Applied Mathematical Modelling*, 7(3):157–162, 1983.

[44] M.A. Golberg and C.S. Chen. *Discrete projection methods for integral equations*. Computational Mechanics Publication, Southampton, 1997.

[45] M.J.D. Powell. The uniform convergence of thin plate spline interpolation in two dimensions. *Numerische Mathematik*, 68(1):107–128, 1994.

[46] W.R. Madych and S.A. Nelson. Multivariate interpolation and conditionally positive definite functions. ii. *Mathematics of Computation*, 54(189):211–230, 1990.

[47] R. Schaback. Multivariate interpolation and approximation by translates of a basis function. In C.K. Chui and L.L. Schumaker, editors, *Approximation theory VIII*. World Scientific Publishing Co., Inc., 1995.

[48] M.E. O'Neill. A sphere in contact with a plane wall in a slow linear shear flow. *Chemical Engineering Science*, 23(11):1293–1298, 1968.

[49] G. Krishnasamy, F.J. Rizzo, and Y. Liu. Boundary integral equations for thin bodies. *International Journal for Numerical Methods in Engineering*, 37:107–121, 1994.

[50] J.C. Lachat and J.O. Watson. Effective numerical treatment of boundary integrations: A formulation for three-dimensional elastostatics. *International Journal for Numerical Methods in Engineering*, 10(5):991–1005, 1976.

[51] K.A. Hayami. *Projection transformation method for near singular surface boundary element integrals (Lecture Notes in Engineering)*, volume 73. Springer-Verlag, Berlin, 1992.

[52] Y.Mi and M.H. Aliabadi. Taylor expansion algorithm for integration of 3d near-hypersingular integrals. *Communications in Numerical Methods in Engineering*, 12 (1):51, 1996.

[53] V. Cutanda, P.M. Juhl, and F. Jacobsen. On the modelling of narrow gaps using standard boundary element method. *Journal of the Acoustical Society of America*, 109(4):1296–1303, 2001.

[54] S. Ahmad and P.K. Banerjee. Free vibration analysis by bem using particular integrals. *Journal of Engineering Mechanics*, 112(7):682–695, 1986.

[55] H. Power and V. Botte. An indirect boundary element method for solving low reynolds number navier-stokes equations in a three-dimensional cavity. *International Journal for Numerical Methods in Engineering*, 41(8):1485–1505, 1998.

[56] W.F. Florez and H. Power. Drm multidomain mass conservative interpolation approach for the bem solution of the two-dimensional navier-stokes equations. *Computers and Mathematics with Applications*, 43(3-5):457–472, 2002.

[57] T. Yamada, L.C. Wrobel, and H. Power. On the convergence of the dual reciprocity boundary element method. *Engineering Analysis with Boundary Elements*, 13(3): 291–298, 1994.

[58] J.-Y. Yang, S.-C. Yang, Y.-N. Chen, and C.-A. Hsu. Implicit weighted eno schemes for the three-dimensional incompressible navier-stokes equations. *Journal of Computational Physics*, 146(1):464–487, 1998.